

Investigating the Requirement of *Clrn2* for Mammalian Hearing

A thesis presented for the degree of Doctor of Philosophy (DPhil)

Hilary Term, 2021

Lucy Alannah Dunbar

Department of Biochemistry, Wolfson College, University of Oxford

Mammalian Genetics Unit, MRC Harwell Institute

Supervisors: Dr Mike Bowl (Mammalian Genetics Unit, MRC Harwell Institute)

Professor Steve Brown (Mammalian Genetics Unit, MRC Harwell Institute)

Professor Matthew Whitby (Department of Biochemistry, University of Oxford)

Word count: 37072



Abstract

Investigating the Requirement of *Clrn2* for Mammalian Hearing

Lucy Alannah Dunbar

Cochlear inner and outer hair cells are the functional units of mammalian hearing. At their apex, specialised microvilli known as stereocilia are arranged in three rows of ascending height, and the mechano-electrical transduction (MET) channels, crucial for converting sound-induced fluid waves into electrical signals, reside at the top of the two shorter rows. Each MET channel is tethered to the adjacent stereocilia in a taller row via a tip link, which mechanically gates the channel upon deflection of the stereocilia bundle. The genetic mechanisms involved in the development and maintenance of the hair bundle are poorly understood.

The Harwell Ageing Screen utilised an unbiased forward genetics approach in mice to identify *Clrn2* as a novel deafness gene. *Clrn2* encodes the clarin-2 protein, a small glycoprotein constituting 232 residues, exhibiting four transmembrane domains. At this time there were no publications relating to the function of clarin-2. However, its paralogue *Clrn1* is the causative gene in Usher Syndrome type 3A, a rare genetic condition characterised by combined deafness and blindness.

Following complementation testing, which confirmed *Clrn2*'s requirement for hearing, comprehensive auditory phenotyping of the $Clrn2^{clarniet}$ mouse (characterised by a W4STOP mutation encoding a severely truncated clarin-2 peptide) revealed a profound, early-onset, progressive auditory deficit. *Clrn2* was therefore confirmed as critical for hearing in mouse. More recently, two separate studies have reported *CLRN2* to be associated with adult hearing function and the cause of hearing loss in a consanguineous Iranian family.

Utilising the *clarinet* mutant, ultrastructural analysis and electrophysiological studies demonstrate that while the hair bundle begins to develop normally in the early postnatal stages, the two shorter 'transducing' outer hair cell stereocilia rows regress before the onset of hearing. To further investigate the role of clarin-2 in the postnatal cochlea, an additional two novel mutants were generated using CRISPR/Cas9 technology: $Clrn2^{del629}$, whereby *Clrn2*'s critical second exon is constitutively deleted; and $Clrn2^{fl}$, in which exon 2 is floxed by *loxP* sites, allowing its conditional deletion. Morphological and functional investigations of the $Clrn2^{fl};Myo15^{cre}$ mouse revealed that expression of hair cell-specific *Clrn2* in the early postnatal stages only of development is sufficient to maintain the normal architecture of the hair bundle, but results in a severe auditory phenotype that is slower to progress than that of the $Clrn2^{clarinet}$ or $Clrn2^{del629}$ mutant.

The results presented in this thesis have demonstrated *Clrn2* as essential for mammalian hearing, being crucial for the maintenance of auditory hair bundle integrity and function. Furthermore, these investigations have suggested a critical role for clarin-2 in maintenance of the MET channel current, and implicate clarin-2 as an interacting partner of the MET channel complex. These findings further elaborate upon the genetic landscape of mammalian hearing, and remove *Clrn2* from the 'ignorome' of genes with unknown biological function.

Acknowledgements

Over the course of my DPhil, I have had the privilege of working with some truly amazing people; without you all, this thesis would not have been possible.

Firstly, huge thanks go to my supervisors: Dr Mike Bowl, Professor Steve Brown and Professor Matthew Whitby, for your guidance over the last four and a half years. To Mike in particular for everything you have taught me, and for always having an open door.

I am incredibly thankful to the members of sensorineural hearing loss team and the wider deafness group, past and present – in particular Carlos Aguilar, Jamie Lee, Sherri Newton and Andy Parker. You have taught me how to be a good scientist. I will miss our Deafness Days, but look forward to reuniting over tapas and sangria in the future! To my fellow Harwell PhD students – thank you for reminding me that postgraduate life is anything but boring.

I am in debt to all the dedicated staff at the Mary Lyon Centre – especially Lucie Vizor and Ward 4, Jackie Harrison and Ward 5, and Sara Wells, for taking good care of my mice. Thanks also go to the core facilities at Harwell including GEMS, Histology, the Molecular and Cellular Biology team and Jeremy Sanderson in Bioimaging (riding in the ferret through the Oxfordshire countryside is a highlight of my time at Harwell).

The support from our external collaborators throughout my DPhil has been invaluable. Special thanks go to Professor Aziz El-Amraoui at the Institut Pasteur, and Professor Walter Marcotti at the University of Sheffield, and their colleagues who contributed their expertise and discussions to my project.

Thanks also go the Medical Research Council, the University of Oxford Department of Biochemistry, Wolfson College, the Genetics Society, the Galton Institute, and the Association for Research in Otolaryngology whose generous funding and grants allowed not only for my research to take place, but for the wonderful opportunity to attend several international meetings.

To Ruby, for years of friendship and laughter on tap. To Sam, for unwavering patience and encouragement. And finally to my parents, Dulcie and Graham, and my brother, Nicholas – your support is immeasurable and words cannot express how lucky I am to have you. This thesis is dedicated to you.

Statement of Contributions

The *clarinet* mutant was originally identified by Dr Joanne Dorning, Carlos Aguilar and Dr Prashanthini Shanthakumar, MRC Harwell Institute, as part of the Harwell Ageing Screen. The Bioinformatics team aligned and analysed the whole genome sequencing data to identify lesions within the *clarinet* critical interval. Preliminary phenotyping of the MPC-169 cohort and qRT-PCR experiments were performed by Dr Philomena Mburu, MRC Harwell Institute.

The *Clrn2*^{del629} and *Clrn2*^{fl} mice were generated by the Molecular and Cellular Biology team at MRC Harwell Institute. Genotyping was performed by the Genotyping, Expression and Mutation Screens core facility at MRC Harwell Institute.

Selected capturing and pseudo-colouring of micrographs, stereocilia height measurements and isolated immunolabelling experiments were carried out by Dr Andrew Parker, Carlos Aguilar and Dr Sherylanne Newton, respectively (as indicated in figure legends and/or corresponding text), at MRC Harwell Institute. Tissue cutting and processing for H&E sections was performed by the Histology team at MRC Harwell Institute.

Electroretinogram recordings, behavioural tests and selected swim tests on *clarinet* mice were performed and interpreted by Dr Pranav Patni and Professor Aziz El-Amraoui at the Institut Pasteur in Paris.

Electrophysiology recordings were undertaken and interpreted by Dr Laura Corns, Dr Stuart Johnson, Adam Carlton, Anna Underhill and Professor Walter Marcotti at the University of Sheffield.

All other work was undertaken by me.

Publications

DUNBAR, L. A., PATNI, P., AGUILAR, C., MBURU, P., CORNS, L., WELLS, H. R., DELMAGHANI, S., PARKER, A., JOHNSON, S., WILLIAMS, D., ESAPA, C. T., SIMON, M. M., CHESSUM, L., NEWTON, S., DORNING, J., JEYARAJAN, P., MORSE, S., LELLI, A., CODNER, G. F., PEINEAU, T., GOPAL, S. R., ALAGRAMAM, K. N., HERTZANO, R., DULON, D., WELLS, S., WILLIAMS, F. M., PETIT, C., DAWSON, S. J., BROWN, S. D., MARCOTTI, W., EL-AMRAOUI, A. & BOWL, M. R. 2019. Clarin-2 is essential for hearing by maintaining stereocilia integrity and function. ***EMBO Molecular Medicine,*** 11, e10288.

VONA, B., MAZAHERI, N., LIN, S.-J., **DUNBAR, L. A.**, MAROOFIAN, R., AZAIEZ, H., BOOTH, K. T., VITRY, S., RAD, A., RÜSCHENDORF, F., VARSHNEY, P., FOWLER, B., BEETZ, C., ALAGRAMAM, K. N., MURPHY, D., SHARIATI, G., SEDAGHAT, A., HOULDEN, H., PETREE, C., VIJAYKUMAR, S., SMITH, R. J. H., HAAF, T., EL-AMRAOUI, A., BOWL, M. R., VARSHNEY, G. K. & GALEHDARI, H. 2021. A biallelic variant in CLRN2 causes non-syndromic hearing loss in humans. ***Human Genetics***.

Meetings

Poster presentation: *clarinet* is required for maintenance of stereocilia and essential for hearing. ***Modeling Hearing and Balance Disorders in Mice: The HEAR@JAX Workshop***, The Jackson Laboratory, Bar Harbour, Maine, USA, 25th September 2018.

Poster presentation: Clarin-2 is Required for Maintenance of Mechanotransducing Stereocilia and Essential for Hearing. ***The Association for Research in Otolaryngology 42nd Annual MidWinter Meeting***, Baltimore, Maryland, USA, 10th February 2019.

Podium presentation (Mammalian Genome 1st prize for Best Overall Presentation): Clarin-2 is essential for hearing by maintaining stereocilia integrity and function. ***The Mammalian Genetics & Development Workshop***, UCL Institute of Child Health, London, UK, 3rd December 2019.

Table of Contents

Abstract i
Acknowledgements ii
Statement of Contributions iii
Publications iv
Meetings v
Table of Contents vi
Table of Figures x
Table of Tables xiv
Abbreviations xv

Chapter 1: Introduction 1
1.1 Peripheral auditory system 1
1.1.1 Outer and middle ear 2
1.1.2 Inner Ear 3
1.1.3 Organ of Corti 4
1.1.4 Supporting cells 5
1.1.5 Hair cells 5
1.1.6 Stereocilia 7
1.1.7 Stereocilia mechano-electrical transduction and maintenance 9
1.1.8 Molecular identity of the MET channel 10
1.1.9 Ribbon synapses and innervation of the cochlea 11
1.1.10 Sound transduction 13
1.2 Central auditory system 14
1.3 Development of the inner ear 15
1.3.1 Hair bundle development 16
1.4 Vestibular system 17
1.5 Hearing loss 18
1.5.1 Conductive hearing loss 20
1.5.2 Sensorineural hearing loss 21
1.5.3 Hair cell regeneration 21
1.5.4 Age-related hearing loss (AHL) 22
1.5.5 Hearing loss and cognitive decline 23
1.5.6 Tinnitus 23
1.5.7 Noise exposure and other environmental factors 24

1.6 Mouse models of human disease 25
1.6.1 Genetic manipulation in mice 26
1.6.2 The mouse as a model for hearing loss 28
1.6.3 Auditory and vestibular phenotyping of mouse models 29
1.7 Forward and reverse genetics screens 31
1.7.1 Use of ENU in mutagenesis-driven screens 31
1.7.2 Harwell Ageing Screen 32
1.7.3 MPC-169 34
1.8 *Clrn2* 36
1.8.1 Usher Syndrome 36
1.9 PhD hypothesis and research aims 38
Chapter 2: Materials and Methods 40
2.1 Mice 40
2.1.1 Husbandry 40
2.1.2 Generation of mouse cohorts 40
2.1.3 Genotyping 43
2.2 Auditory phenotyping 50
2.2.1 Click box 50
2.2.2 Auditory Brainstem Response (ABR) 50
2.2.3 Distortion Product Otoacoustic Emissions 51
2.3 Vestibular phenotyping 52
2.3.1 Behavioural studies 52
2.3.2 Swim test 52
2.4 Electroretinogram recordings 53
2.5 Electrophysiological studies 54
2.5.1 Mechano-electrical transduction current recordings 54
2.5.2 Patch clamp recordings 55
2.6 Scanning electron microscopy 55
2.7 Immunohistochemistry 57
2.7.1 Immunolabelling of whole-mounts 57
2.7.2 Immunolabelling of vibratome sections 59
2.8 Histology 60
2.9 RT-PCR 60
2.10 Statistical analyses 61
Chapter 3: Characterisation of the *clarinet* mouse model 62
3.1 Introduction 62

3.2 Results 63
3.2.1 Generation of a second *Clrn2* (*Clrn2*^{del629}) allele 63
3.2.2 Complementation test 66
3.2.3 *clarinet* viability and body weight 70
3.2.4 *clarinet* ABR time course 72
3.2.5 *clarinet* distortion product otoacoustic emission testing 75
3.2.6 Gross cochlear morphology 77
3.2.7 Changes in *clarinet* hair bundle structure over time 78
3.2.8 Longitudinal vestibular phenotyping 85
3.2.9 Electroretinogram response 87
3.2.10 Synaptic labelling 88
3.2.11 Electrophysiological properties of cochlear hair cells 89
3.2.12 Ultrastructural analyses of adult *clarinet* auditory hair bundles 94
3.3 Discussion 95
Chapter 4: Spatial and temporal expression and localisation of *Clrn2*/clarin-2 97
4.1 Introduction 97
4.2 Results 98
4.2.1 Visualisation of single-cell RNA-seq data 98
4.2.2 Immunolabelling of whole mounts 101
4.2.3 Immunolabelling of vibratome-cut cochlear sections 103
4.3 Discussion 107
Chapter 5: Separating the prenatal and postnatal requirement of *Clrn2* 111
5.1 Introduction 111
5.2 Results 114
5.2.1 *Clrn2*^{del629} auditory phenotype 114
5.2.2 Ultrastructural analysis of the *Clrn2*^{del629} mutant 119
5.2.3 Design and generation of a conditional *Clrn2* knockout mouse 120
5.2.4 Hair cell-specific deletion of *Clrn2* causes hearing loss 122
5.2.5 Ultrastructural analyses of *Clrn2*$^{fl/fl}$;*Myo15*$^{cre/+}$ mice 125
5.2.6 Electrophysiological properties of *Clrn2*-deficient immature hair cells 126
5.2.7 Temporal deletion of *Clrn2* 127
5.3 Discussion 129
Chapter 6: Discussion 131
6.1 Introduction 131
6.1.1 *Clrn2* is required for mammalian hearing 131
6.1.2 Constitutive deletion of *Clrn2*'s second exon 133

6.1.3 Sub-cellular localisation of *Clrn2*/clarin-2 134
6.1.4 Postnatal hair cell-specific *Clrn2* mutation and possible roles for clarin-2 136
6.2 Other *Clrn2* mutants 139
6.2.1 *Clrn2* IMPC mutant mouse phenotype 139
6.2.2 *clrn2* in zebrafish 141
6.3 *Clrn2* mutants phenocopy other mutants with disrupted hair bundles 142
6.4 The role of *CLRN2* in human hearing 146
6.4.1 Human aged-related hearing difficulty may be associated with *CLRN2* 146
6.4.2 Recessive *CLRN2* mutations in an Iranian family 148
6.5 Future directions 149
6.5.1 Exploring the differential requirement of *Clrn2* in the two hair cell types 149
6.5.2 Assessing localisation and interacting partners with a *Clrn2*^{tag} mouse 150
6.5.3 Noise challenging of *Clrn2* heterozygous mutants 151
6.6 Implications for therapeutic intervention 152
6.7 Concluding remarks 153
Chapter 7: References 154

Table of Figures

Figure 1.1: Overview of the human ear. 2
Figure 1.2: The cochlea. (A) Cross section of a single turn of the cochlea 3
Figure 1.3: Representative pseudo-coloured scanning electron micrograph (SEM) images of stereocilia on top of an (A) OHC and (B) IHC from a wild type mouse at postnatal day 16 (P16). 7
Figure 1.4: Schematic diagram of stereocilia MET channel complex proteins. 10
Figure 1.5: Depolarised IHCs convert mechanical vibrations into electrical signals. 14
Figure 1.6: Schematic diagram of the bilateral ascending auditory pathway from the cochlea to the auditory cortex including auditory structures within the brainstem (1), midbrain (2), and cortex (3). 15
Figure 1.7: Schematic diagram of sequential stages of avian hair bundle development. 17
Figure 1.8: Representative audiograms for a patient with conductive hearing loss in the left ear (A) and sensorineural hearing loss in the right ear (B) 20
Figure 1.9: The hearing range of laboratory animals compared with that of humans 28
Figure 1.10: An ABR waveform from a wild type mouse displaying the summating potential (SP) and the first five peaks, in response to a 60 dB SPL stimulus. 30
Figure 1.11: Affected mice in the MPC-169 pedigree exhibit early-onset, severe hearing loss. 34
Figure 1.12: SNP mapping and whole genome sequencing of mouse pedigree MPC169. 35
Figure 1.13: Preliminary analysis of MPC-169 and *Clrn2* inner ear transcripts. 36
Figure 1.14: Predicted structure of wild type mouse clarin-2 protein 38
Figure 2.1: Generation of additional *Clrn2* mutants using CRISPR/Cas9 technology and a long single-stranded (lssDNA) donor approach. 41
Figure 2.2: Examples of normalised melting peaks for homozygous (grey), heterozygous (red) and wild type (blue) *clarinet* samples, using the LightScanner unlabelled probe genotyping technique 44
Figure 2.3: Example of copy number counting assay results for the genotyping of $Clrn2^{del629}$ samples. 47
Figure 2.4: Equations used to measure stereocilia heights from scanning electron micrographs 57
Figure 3.1: Schematic representation of mouse wild type ($Clrn2^{+}$) and $Clrn2^{del629}$ mutant allele, generated through CRISPR/Cas9 genome editing. 64
Figure 3.2: RT-PCR analysis and sequencing of P21 $Clrn2^{del629}$ cochlear ducts. 66
Figure 3.3: $Clrn2^{w4stop/del629}$ mice exhibit profound auditory dysfunction. 67
Figure 3.4: Scanning electron micrographs from control $Clrn2^{del629/+}$ and compound heterozygous $Clrn2^{w4stop/del629}$ cochleae at P28. 69
Figure 3.5: The $Clrn2^{clarinet}$ mutation does not affect viability. 70
Figure 3.6: Averaged body weights at P16 suggest that the $Clrn2^{clarinet}$ mutation does not affect body weight at this time point, in either males or females 71
Figure 3.7: Genotype-averaged body weights suggest that the $Clrn2^{clarinet}$ mutation does not significantly affect body weight gain during development, in either males or females 72
Figure 3.8: Averaged ABR thresholds in *clarinet* mice demonstrate an early-onset, progressive hearing loss at all frequencies tested. 73
Figure 3.9: Averaged ABR thresholds for P21 *clarinet* mice with mutants separated by sex 74
Figure 3.10: Representative ABR waveforms recorded in response to a click stimulus for P21 wild type, heterozygous and homozygous *clarinet* mice 75
Figure 3.11: $Clrn2^{clarinet/clarinet}$ mice fail to produce normal DPOAE responses 75

Figure 3.12: Histological assessment of P20 *Clrn2*$^{clarinet/clarinet}$ mid-modiolar cochlear sections indicates normal gross morphology. 77
Figure 3.13: Representative scanning electron micrographs of cochlear hair cells indicate no gross patterning issues in the sensory epithelium of P16 *Clrn2*$^{clarinet/clarinet}$ mice in comparison to *Clrn2*$^{+/+}$ and *Clrn2*$^{clarinet/+}$ controls 79
Figure 3.14: Pseudo-coloured scanning electron micrographs of individual OHC and IHC mid-cochlear bundles show *Clrn2*$^{clarinet/clarinet}$ stereocilia morphology is to wild type controls at P16. 80
Figure 3.15: Pseudo-coloured scanning electron micrographs of individual OHC and IHC mid-cochlear bundles show *Clrn2*$^{clarinet/clarinet}$ stereocilia architecture is comparable, at a gross morphological level, to wild type controls at P8. 82
Figure 3.16: Distribution of individual measures across genotypes shows shorter *clarinet* OHC, but not IHC stererocilia at both P8 and P16. 84
Figure 3.17: Swim testing at P28 and P60 indicates the *clarinet* mutation does not cause early-onset vestibular function 85
Figure 3.18: Longitudinal swim testing of *clarinet* mice at MRC Harwell Institute indicates vestibular dysfunction 86
Figure 3.19: Electroretinogram (ERG) responses from representative control *Clrn2*$^{clarinet/+}$ (grey) and mutant *Clrn2*$^{clarinet/clarinet}$ (red) mice 87
Figure 3.20: P21 *clarinet* mice display the correct number and localisation of pre- and post-synaptic densities in their IHCs 88
Figure 3.21: MET channel currents in immature clarinet hair bundles. 90
Figure 3.22: Potassium currents recorded in adult *clarinet* (red) mice indicate the correct functional maturation of OHCs, but not IHCs, when compared to heterozygous controls (grey) 93
Figure 3.23: Pseudo-coloured scanning electron micrographs of individual OHC and IHC mid-cochlear bundles show *Clrn2*$^{clarinet/clarinet}$ stereocilia morphology is distinguishable from wild type and heterozygous controls at P28. 94
Figure 4.1: Preliminary immunolabelling of P20 wild type whole mount tissues appears to show clarin-2 localisation in the stereocilia of IHCs and OHCs. 98
Figure 4.2: Visualisation of single cell RNA-seq data for *Clrn2* in mouse cochlear epithelium from Kolla et al., 2020. 99
Figure 4.3: Visualisation of single cell RNA-seq data for *Clrn2* in P2 mouse cochlear cell groups from Kubota et al., 2021 100
Figure 4.4: Immunolabelling of P8 wild type C57BL/6J sensory epithelium with Rb61 anti-clarin-2 (red) shows non-specific staining of inner and outer hair cells at both 1:50 (top panel) and 1:100 dilutions (bottom panel) 102
Figure 4.5: Immunolabelling of postnatal wild type whole mount tissue with Abcam anti-clarin-2 antibody shows non-specific staining of sensory epithelium 103
Figure 4.6: Immunofluorescence image of P30 mouse organ of Corti, showing clarin-2 localisation in hair cell bodies. 104
Figure 4.7: Atlas anti-clarin-2 antibody staining (green) on vibratome sections from wild type P30 cochlea appears to target tissue non-specifically (top and middle panels), but a secondary only control sample demonstrates specific staining of the inner and outer hair cell stereocilia (bottom panel) 105
Figure 4.8: Different configurations of primary and secondary antibodies, and phalloidin markers, does not improve Atlas anti-clarin-2 signal 106
Figure 4.9: Mouse clarin-2 protein. 109
Figure 4.10: clarin-1 and clarin-2 peptide sequence alignment. 110

Figure 5.1: Regional plot of P-values for single nucleotide polymorphism (SNP) association with hearing difficulty around the *CLRN2* gene locus on chromosome 4 113
Figure 5.2: The *Clrn2*^{del629} mutation does not affect survival 115
Figure 5.3: Averaged body weights at P21 suggest that the *Clrn2*^{del629} mutation does not affect the pre-weaning growth of male or female mutant mice. 116
Figure 5.4: Averaged ABR thresholds are elevated in P21 *Clrn2*^{del629} mice at all frequencies tested. 116
Figure 5.5: Isolated averaged ABR thresholds of *Clrn2* mutants at P21 indicates that *Clrn2*$^{del629/del629}$ (solid triangle) hearing loss is slightly more severe than the *Clrn2*$^{clarinet/clarinet}$ (open triangle) phenotype 117
Figure 5.6: Averaged DPOAE responses in P28 *Clrn2*^{del629} mice are reduced at lower frequencies. .. 118
Figure 5.7: Ultrastructural analysis demonstrates abnormal hair bundle architecture in *Clrn2*^{del629} homozygous mice 119
Figure 5.8: Schematic representation of mouse wild type (*Clrn2*$^{+}$) and *Clrn2*^{fl} mutant alleles, generated through CRISPR/Cas9 genome editing.. 121
Figure 5.9: Schematic representation of a breeding strategy for generating a conditional *Clrn2* mutant. 122
Figure 5.10: Averaged ABR thresholds are elevated in *Clrn2*$^{fl/fl}$*;Myo15*$^{cre/+}$ mice at all frequencies tested. 123
Figure 5.11: Isolated averaged ABR thresholds of *Clrn2* mutants at P21 and P28 indicates that *Clrn2*$^{fl/fl}$*;Myo15*$^{cre/+}$ (solid triangle) hearing loss progresses more slowly than the *Clrn2*$^{clarinet/clarinet}$ (open triangle) phenotype 124
Figure 5.12: SEM ultrastructural analysis of *Clrn2*$^{fl/fl}$*;Myo15*$^{cre/+}$ hair bundles at P42 demonstrate normal OHC stereocilia that resemble those of the *Clrn2*$^{fl/fl}$*;Myo15*$^{+/+}$ controls (top panels) 125
Figure 5.13: MET channel current is comparable between control and *Clrn2*$^{fl/fl}$*;Myo15*$^{cre/+}$ mice. 127
Figure 6.1: Biochemically known interactions between proteins in the USH interactome..... 132
Figure 6.2: Evoked ABR thresholds in *Clrn2*$^{em1(IMPC)J}$ mice at 14 weeks. 140
Figure 6.3: Schematic representation of the proposed MET channel complex, the tip link and the upper tip link density 144
Figure 6.4: Human and mouse clarin-2 amino acid sequence alignment..... 147

Table of Tables

Table 1.1: Selected key genes for hair bundles. 8
Table 1.2: Classification of hearing loss. 18
Table 1.3: Overview of Harwell Ageing Screen phenotyping pipeline. 33
Table 1.4: Characteristics of the genes and encoded proteins in the *Clrn* family in the mouse. 37
Table 2.1: sgRNAs used in the generation of the *Clrn2*^{fl} mouse 42
Table 2.2: lssDNA donor sequence (1,049 nucleotides) used in the generation of the additional *Clrn2* mutants 42
Table 2.3: Expected genotyping ratios when using wild type and mutant assays in conjunction 45
Table 2.4: Oligonucleotide sequences used in the *Clrn2*^{del629} wild type genotyping assay 45
Table 2.5: Oligonucleotide sequences used in the *Clrn2*^{del629} mutant genotyping assay 46
Table 2.6: Oligonucleotide sequences used in the *Clrn2*^{fl} wild type genotyping assay 47
Table 2.7: Oligonucleotide sequences used in the *Clrn2*^{fl} mutant genotyping assay 48
Table 2.8: Oligonucleotide sequences used in the *Myo15*^{cre} wild type genotyping assay 48
Table 2.9: Oligonucleotide sequences used in the *Myo15*^{cre} mutant genotyping assay 48
Table 2.10: Oligonucleotide sequences used to verify Cre recombination at *loxP* sites in the wild type assay 49
Table 2.11: Oligonucleotide sequences used to verify Cre recombination at *loxP* sites in the mutant assay 49
Table 2.12: Score and corresponding behaviour of mice undergoing the swim test. 53
Table 2.13: Summary of antibodies and conditions employed in clarin-2 immunofluorescence experiments on cochlear tissues 58
Table 3.1: Exact p values for ABR and DPOAE phenotyping of clarinet animals 76

Abbreviations

A – adenine

ABR – auditory brainstem response

ahl – age-related hearing loss

AMPA – α-amino-3-hydroxy-5-methylisoxazole-4- proprionic acid

ANOVA – analysis of variance

Atoh1 – Atonal homolog 1

BLAST – Basic Local Alignment Search Tool

BMP – bone morphogenetic protein

bp – base pair

BSA – bovine serum albumin

C – cytosine

Ca^{2+} – calcium ion

Cas – CRISPR-associated

Cdh – cadherin

CRISPR – Clustered Regularly Interspaced Short Palindromic Repeats

dB SPL – decibels sound pressure level

DAPI – 4',6-diamidino-2-phenylindole

dpf – days post fertilisation

DCs – Deiters' cells

DEXA – dual energy X-ray analysis

DPOAE – distortion product otoacoustic emission

DV – driver voltage

ECG – electrocardiogram

EDTA – ethylenediaminetetraacetic acid

E – embryonic day

ENU – *n*-ethyl-*n*-nitrosourea

ERG – electroretinography

ER – estrogen receptor

F-actin – filamentous action

FGF – fibroblast growth factor

G – guanine

gEAR – gene Expression Analysis Resource

GJB2 – gap junction beta 2

GWAS – genome-wide association study

H&E – haematoxylin and eosin

HDR – homology-directed repair

HET – heterozygous

HOM – homozygous

hpf – hours post fertilisation

Hz – hertz

IHC – inner hair cell

IMPC – International Mouse Phenotyping Consortium

IPGTT – intraperitoneal glucose tolerance test

K^+ – potassium ion

kb – kilobase

kDA – kilodaltons

kHz – kilohertz

LD – linkage disequilibrium

LHFPL5 – Lipoma HMGIC fusion partner-like 5

LOC – lateral olivary complex

lssDNA – long single-stranded DNA

M – molar

Mb – megabase

MET – mechano-electrical transduction

MIB – microinjection buffer

MOC – medial olivary complex

MRI – magnetic resonance imaging

mRNA – messenger RNA

ms – millisecond

mV – millivolts

n – number

nA – nanoampere

NHEJ – non-homologous end joining

NIHL – noise-induced hearing loss

OHC – outer hair cell

OM – otitis media

P – postnatal day

P_0 – open resting probability

PAM – protospacer adjacent motif

PB – phosphate buffer

PBS – phosphate buffered saline

PBST – phosphate buffered saline with Tween

Pcdh – protocadherin

PFA – paraformaldehyde

PTS – permanent threshold shift

RNID – Royal National Institute for Deaf

RP – retinitis pigmentosa

RT – room temperature

s.e.m. – standard error of the mean

SEM – scanning electron microscopy

s.d. – standard deviation

SGN – spiral ganglion neuron

sgRNA – single guide RNA

SHIRPA – SmithKline Beecham, Harwell, Imperial College and Royal London Hospital phenotype assessment

scRNA-seq – single-cell RNA sequencing

SNP – single nucleotide polymorphism

SOC – superior olivary complex

Sox – SRY-related HMG box

SP – summating potential

ssODNs – single-stranded oligodeoxynucleotides

T – thymine

TARP – transmembrane AMPA receptor regulatory protein

TMC – transmembrane channel like

TMHS – tetraspan membrane protein of hair cell stereocilia

TMIE – transmembrane inner ear

Trp – tryptophan

tSNE – t-distributed stochastic neighbor embedding

TTS – temporary threshold shift

USH – Usher Syndrome

UTR – untranslated region

V – volts

V_m – resting membrane potential

VsEP – vestibular sensory-evoked potential

WT – wild type

Chapter 1: Introduction

The mammalian auditory system is capable of detecting and deciphering sound waves in the surrounding environment. The majority of the process occurs in the cochlea, a tiny structure located close to the brain. The successful detection and processing of the external signal relies on a chain of events, each of which is sophisticated, intricate and organised to optimise its function. Consequently, the human auditory system can recognise sounds in the range of 20 to 20,000 hertz (Hz). Due to its complexity and fragility, however, the system is particularly vulnerable to both physical damage and genetic variation, some of which cannot be reversed. This damage can result in hearing loss of varying severity. Increased understanding of the molecular genetics of mammalian hearing will allow a genetic diagnosis for patients with hearing difficulty, and ultimately aid the development of therapeutic interventions for hearing loss.

1.1 Peripheral auditory system

The mammalian auditory system can broadly be categorised into the peripheral and central auditory systems. The peripheral auditory system is responsible for the detection and transduction of external sounds.

1.1.1 Outer and middle ear

The peripheral auditory system is subdivided into three regions: the outer, middle and inner ear (Figure 1.1). The outer ear consists of the pinna, the visible portion of the ear, which is shaped to funnel sound waves from the surrounding environment down the ear canal, or auditory meatus. The sound waves are focused onto the tympanic membrane, or eardrum, which forms the barrier between the outer and middle ears. The eardrum is thin, conical and asymmetric in shape, and its function is to convert sound energy into acoustic vibrations, which are passed onto the ossicles (Fay et al., 2006), the three middle ear bones known as the malleus, incus and stapes. The surface area of the eardrum is many times that of the stapes, enabling concentration of the sound wave energy. The ossicles, in vibrating consecutively, act as an impedance transformer and deliver the sound energy to the fluid-filled inner ear, which is separated from the middle ear by the oval window of the cochlea. The footplate of the stapes vibrates against the oval window, which in turn causes vibrations in the adjacent fluid of the inner ear (Thomson and Madani, 2014). The oval window is one of two openings from the middle ear to the inner ear; the other is the round window. Additionally, the development of negative pressure in the middle ear is prevented by the opening of the Eustachian tube (leading to

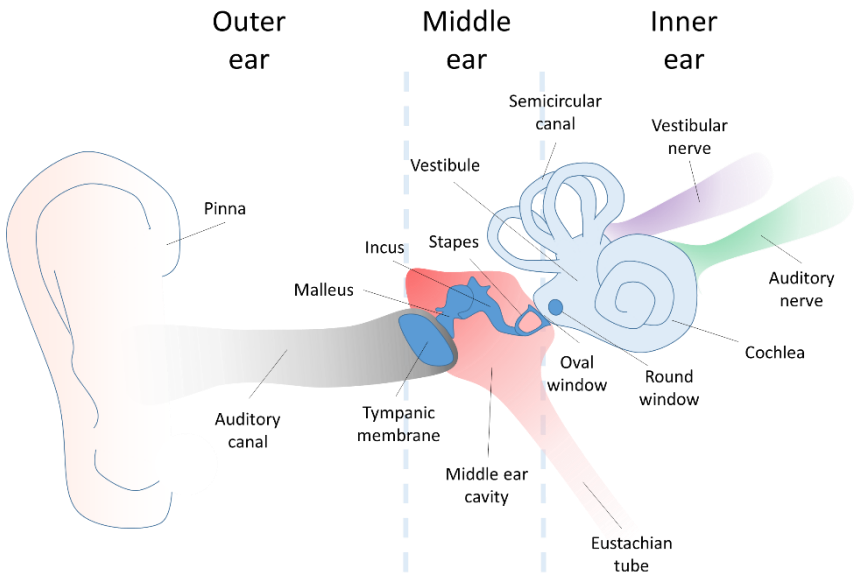

Figure 1.1: Overview of the human ear. Sound from the environment is funnelled by the pinna down the auditory canal, where it strikes the tympanic membrane, causing it to vibrate. This vibration is passed onto the ossicles (malleus, incus and stapes), which is in turn passed to the cochlea at the oval window, which is connected to the stapes.

the nasopharynx), which is controlled by contraction of the surrounding muscle, and allows for ventilation of the cavity (Van Heerbeek et al., 2002).

1.1.2 **Inner Ear**

The inner ear is surrounded by a wall known as the bony labyrinth. The labyrinth houses the cochlea and the vestibular system, the functional elements of the inner ear responsible for auditory transduction and balance respectively.

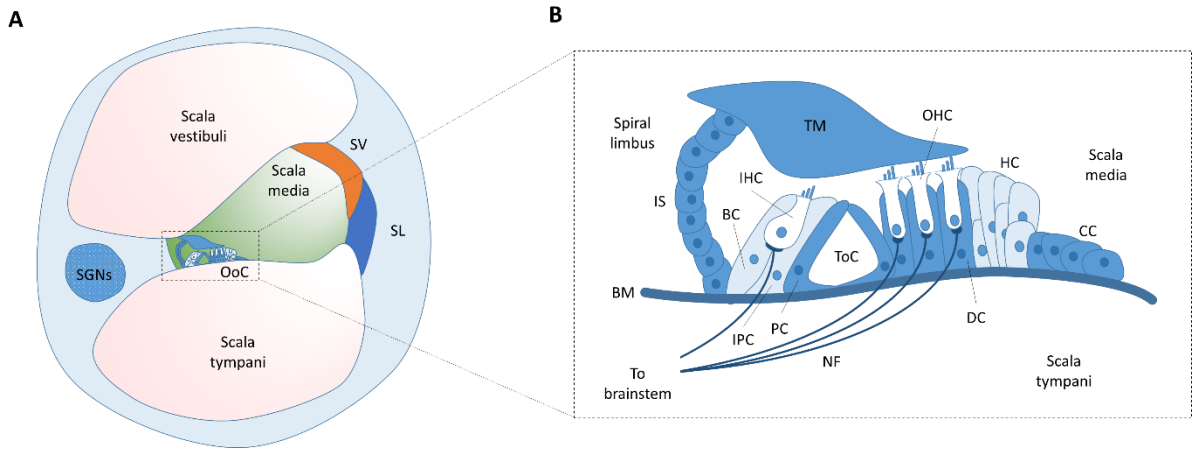

Figure 1.2: The cochlea. (A) Cross section of a single turn of the cochlea. The cochlea contains three chambers: the scala vestibuli and tympani, which are filled with perilymph, and the scala media, filled with endolymph. Reissner's membrane separates the scala vestibuli from the scala media. The basilar membrane, on which the organ of Corti resides, separates the scala media from the scala tympani. **(B) Sound transduction occurs at the organ of Corti.** The organ of Corti resides in the scala media atop of the basilar membrane. Surrounding the three rows of OHCs and one row of IHCs are four types of supporting cells. IHCs – inner hair cell; OHC – outer hair cell; PC – pillar cell; ToC – tunnel of Corti; DC – Deiters' cell; HC – Hensen cell; CC – Claudius cell; NF – nerve fibres; IPC – inner phalangeal cell; BC – Border cell; IS – inner sulcus; BM – basilar membrane; TM – tectorial membrane; SGNs – spiral ganglion neurons; SL – spiral ligament; SP – spiral limbus; SV – stria.

The spiral-shaped cochlea, from the Greek for '*snail*', resides in the temporal bone of the skull and consists of three adjacent membranous tubes (Figure 1.2A) coiled around a bony axis, the modiolus, and enclosed in the otic capsule. The upper and lower chambers, the scala vestibuli and the scala tympani respectively, are filled with perilymph that is rich in sodium ions (Na^+) and low in potassium ions (K^+) which is typical of an extracellular fluid; yet this composition is reversed in the endolymph of the scala media (Smith et al., 1954). The endolymph is produced by the stria vascularis, which is

located on the lateral wall of the scala media and maintains the endolymph's ionic composition. The endocochlear potential, a product of this, is maintained through K^+ transport across the lateral wall (Adachi et al., 2013) at around +80 millivolts (mV), and is essential for auditory function (Tasaki and Spyropoulos, 1959). Reissner's membrane separates the scala vestibuli from the scala media. The basilar membrane is located at the bottom of the scala media, and separates it from the scala tympani below. The length of the basilar membrane in mammals is positively correlated with body weight (Robles and Ruggero, 2001).

1.1.3 Organ of Corti

Residing on the surface of the basilar membrane is the organ of Corti, the structure responsible for the transduction of sound energy arriving from the oval window (Figure 1.2B). The organ of Corti harbours the sensory hair cells, which are surrounded by supporting cells and sit below the tectorial membrane. The hair cells are arranged in a consistent pattern along the basilar membrane, in a configuration of three rows of outer hair cells (OHCs) and one row of inner hair cells (IHCs). Protruding from the apical surface of the hair cells are specialised actin-filled microvilli known as stereocilia (Flock and Cheung, 1977).

A strip of extracellular matrix known as the tectorial membrane is positioned above the organ of Corti, and its underside is in direct contact with the tips of OHC stereocilia. When portions of the basilar membrane vibrate, hair cells residing at that region are lifted towards the tectorial membrane. The basilar membrane is wide and flexible at the apex of the cochlea, and narrow and more rigid at the basal end. The spatial arrangement of hair cells is such that hair cells in a specific location on the basilar membrane respond best optimally to vibrations of a given frequency, with high frequency vibrations detected best at the base of the cochlea and conversely low frequency vibrations detected best at the apex of the cochlea. This phenomenon is known as tonotopic organisation, first described in detail by Békésy and Wever (1960).

1.1.4 **Supporting cells**

Surrounding the hair cells at the centre of the organ of Corti are several distinct subtypes of supporting cell (Figure 1.2B). Deiters' cells (DCs) are found under, and extend between, the OHCs, while the IHCs are surrounded by the inner phalangeal cells and Border cells. Separating the inner and outer hair cells are the pillar cells, which meet to form a lumen known as the tunnel of Corti. Next to DCs are Hensen's cells, which are in turn adjacent to Claudius cells. The inner sulcus, adjacent to the Border cells, provides further stabilisation for the IHCs. The supporting cells are connected to hair cells by adherens and tight adherens junctions.

The supporting cells perform a number of critical functions important for the maintenance of hair cells and hearing. Crucially, they provide structural integrity for the organ of Corti and the hair cells. Microtubules in pillar cells and DCs ensure they provide rigid support for the hair cells (Slepecky et al., 1995). Furthermore, they maintain the homeostatic environment within the scala media for proper function of the hair cells (Ramírez-Camacho et al., 2006). Supporting cells are also thought to phagocytose damaged or dead hair cells from the sensory epithelium while maintaining its integrity, as demonstrated in a study using guinea pigs: Abrashkin et al. (2006) found prestin (an OHC-specific protein) inside the cell bodies of supporting cells following hair cell insult. Finally, there is evidence of multiple supporting cell subtypes spontaneously regenerating into hair cells in the neonatal mouse cochlea (McGovern et al., 2019).

1.1.5 **Hair cells**

The auditory hair cells of the cochlea are the functional units of hearing. There are approximately 12,000 OHCs and 3,500 IHCs per human cochlea (Dallos, 1992), in comparison with 2,500 OHCs and 750 IHCs in the mouse cochlea (Ehret and Frankenreiter, 1977). Mammals are born with all of their hair cells, but these are gradually lost over time as mammalian cochlear hair cells are unable to regenerate, unlike those of some lower vertebrates. As such, cellular damage that leads to hair cell death will lead to permanent hearing loss. (Groves, 2010)

The IHCs, distinguishable from OHCs by their pear-shaped appearance, are the sensory cells chiefly involved in the perception of sound. They achieve this by transducing the mechanical vibrations transferred from the basilar membrane into electrical signals, which travel via the ascending (afferent) neuronal pathway to the auditory cortex in the brain for processing by the central auditory system.

The OHCs, cylindrical in shape, are responsible for the amplification and 'fine-tuning' of the vibrational signal arriving from the oval window. The OHCs act as the 'cochlear amplifier', in which they generate force to drive a positive feedback loop and amplify the travelling wave (Gold and Gray, 1948). They are also the origin of otoacoustic emissions, self-generated sounds within the cochlea that were first described by (Kemp, 1978), and later attributed to OHCs (Mountain and Hubbard, 1989). The emissions can be either spontaneous or evoked, the latter of which can be further categorised depending on the stimulation used to evoke them. Distortion product otoacoustic emissions (DPOAEs) are routinely evoked and recorded to assess the function of OHCs *in vivo*, as described in section 1.6.3.

1.1.6 **Stereocilia**

Protruding from the apical surface (the cuticular plate) of all cochlear hair cells are specialised microvilli known as stereocilia. These actin-rich structures are arranged in a staircase-like fashion, in three rows of ascending height (Figure 1.3).

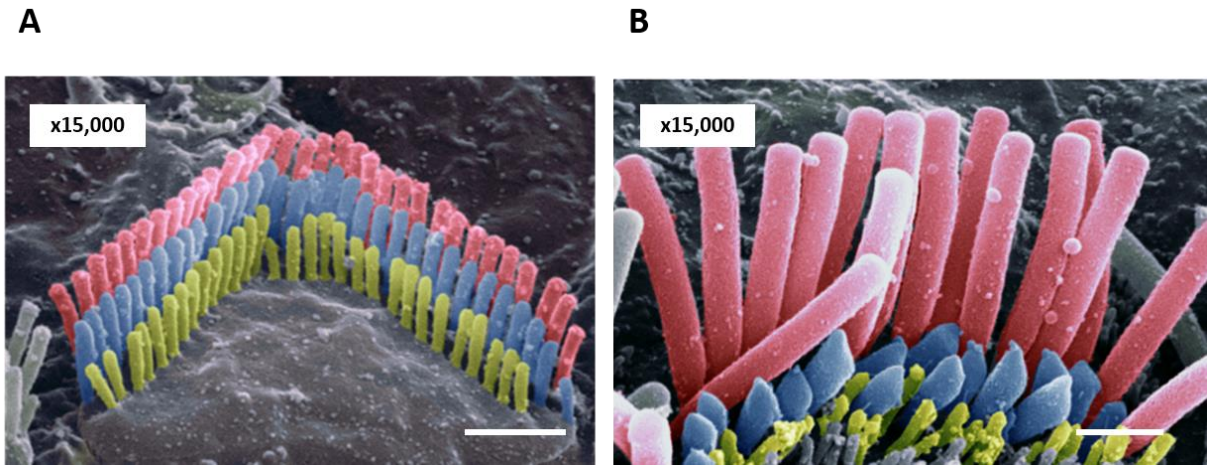

Figure 1.3: Representative pseudo-coloured scanning electron micrograph (SEM) images of stereocilia on top of an (A) OHC and (B) IHC from a wild type mouse at postnatal day 16 (P16). Each hair bundle exhibits three rows of stereocilia arranged in ascending height from the shortest (yellow) to the tallest (red) row. At the tips of the two shorter rows (yellow and blue) reside the mechano-electrical transduction (MET) channels. Connecting stereocilia in a shorter row to one in a taller row are tip links, not visible here, but assumed to be present due to the 'prolate' appearance of the stereocilia tips in the shorter rows, particularly evident in the IHC. Magnification is indicated on each individual micrograph. Scale – 1 µm.

Each stereocilium narrows towards its base in the cuticular plate. This highly organised arrangement is frequently referred to as the hair bundle. Stereocilia vary in length depending on their location along the cochlear spiral – those at the apex are longer, and those at the base are shorter (Lim, 1980). Each stereocilium is tethered to another in an adjacent row via fine filaments called tip links. These are composed of cadherin 23 (CDH23) and protocadherin 15 (PCDH15) dimers (Siemens et al., 2004, Kazmierczak et al., 2007) that originate from the tip of the shorter stereocilia and the side of the taller stereocilia respectively. Mutations in *CDH23* or *PCDH15*, the genes that encode the tip link proteins, result in hearing loss due to reduced functioning of the MET channel machinery (Alagramam et al., 2011). Due to tension in the tip link, their presence is indicated by a prolate (tapered) tip shape in the shorter stereocilium (Pickles et al., 1984). Residing on the two shorter rows of the stereocilia, and thought to be connected to the tip links, are the mechano-electrical transduction (MET) channels

(Denk et al., 1995). Seminal research on the MET channel in bullfrogs demonstrated a mechanical gating of a transduction channel is critical for hearing function (Corey and Hudspeth, 1983). Furthermore, although the MET channel is non-selective for cations, it does exhibit a selection bias for Ca^{2+} ions (Lumpkin et al., 1997).

Table 1.1 details a number of genes critical for stereocilia function, along with accompanying mouse models (Barr-Gillespie, 2015).

Table 1.1: Selected key genes for hair bundles. Adapted from Barr-Gillespie (2015).

Gene symbol	Gene name	Deafness mutant	Hair bundle phenotype	Protein localisation
ACTB	Actin beta	*Actb* knockout	Progressive degeneration of hair bundles	Stereocilia shafts
ACTG1	Actin gamma 1	DFNA20/26, *Actg1* knockout	Progressive degeneration of hair bundles	Stereocilia shafts
ATP2B2	ATPase, Ca^{2+} transporting, plasma membrane 2	*Atp2b2* knockout	Progressive degeneration of hair bundles	Shafts (excluded from taper); concentration toward tips
CAPZ	Capping protein (A1, A2, and B genes)	n/a	unknown	Stereocilia tips
CDH23	Cadherin 23	USH1D, DFNB12	Disorganised hair bundles	Tip links; transient lateral links; kinocilial links
DFNB31	Whirlin	USH2D, DFNB31	Short stereocilia	Tips; ankle links
EPS8	Epidermal growth factor receptor pathway substrate 8	*Eps8* knockout	Short stereocilia	Stereocilia tips
EPS8L2	EPS8-like 2	*EPS8l2* knockout	Progressive degeneration of hair bundles	Stereocilia tips
ESPN	Espin	DFNB36	Short and thin stereocilia; degeneration in the cochlea	Short ESPN splice forms throughout stereocilia shafts; long isoform (ESPN-1) at tips
FSCN2	Fascin 2	$Fscn2^{R109H}$	Progressive degeneration of hair bundles	Stereocilia shafts
MYO1C	Myosin IC	$Myo1c^{Y61G}$	Slowed adaptation	Toward stereocilia tips
MYO1H	Myosin IH	n/a	Unknown	Toward stereocilia tips
MYO3A	Myosin IIIA	DFNB30	Progressive hearing loss	Thimble-like pattern at tips
MYO3B	Myosin IIIB	n/a	Unknown	Thimble-like pattern at tips

MYO6	Myosin VI	DFNA22, DFNB37	Fusion and elongation of stereocilia; apical membrane uplifting	Shafts and taper region
MYO7A	Myosin VIIA	USH1B, DFNA11, DFNB2	Disorganized hair bundles	Tip links; transient lateral links; kinocilial links
MYO15A	Myosin XVA	DFNB3	Short stereocilia	Stereocilia tips
PCDH15	Protocadherin 15	USH1F, DFNB23	Disorganized hair bundles	Tip links; transient lateral links; kinocilial links
PLS1	Plastin 1	*Pls1* knockout	Progressive degeneration of hair bundles	Stereocilia shafts
PTPRQ	Protein tyrosine phosphatase receptor Q	DFNB84	Fusion and elongation of stereocilia	Ankle region, stereociliary shafts
RDX	Radixin	DFNB24, Rdx knockout	Progressive degeneration of hair bundles	Concentrated near base of stereocilia; activated RDX only found above the taper region
USH1C	Harmonin	USH1C, DFNB18	Disorganized hair bundles	Tip link upper insertion; tips in early development
USH1G	Sans	USH1G	Disorganized hair bundles	Tip link upper insertion; tips in early development

1.1.7 **Stereocilia mechano-electrical transduction and maintenance**

In order to maintain the structure of stereocilia, the actin turnover at their tips is dynamic with constant polymerisation and depolymerisation taking place. Actin monomers are packaged into filaments at the tip of the stereocilia, and are translocated towards the hair cell body by myosin motor proteins to regulate their length, with complete renewal of the stereocilia core every 48 hours (Schneider et al., 2002, Schwander et al., 2010).

Furthermore, it has been suggested that MET current is also required for maintenance of the stereocilia themselves, and that this may indeed be linked to filamentous (F) -actin polymerisation (Caberlotto et al., 2011a). This relationship between stereocilia maintenance and MET current has been demonstrated in IHCs (Corns et al., 2018), and also in the two shorter, transducing stereocilia rows on which the MET channels reside (Velez-Ortega et al., 2017). More recently it was also shown that, through examination of the distribution of marker proteins and stereocilia length, mechano-

electrical transduction is likely involved in the specification and maintenance of stereocilia row identity and height (Krey et al., 2020).

Additionally, it is thought that MET current is not only required for maintenance of stereocilia, but also regulates the differentiation, and spontaneous activity, of spiral ganglion neurons (SGNs) in the developing cochlea (Sun et al., 2018).

1.1.8 Molecular identity of the MET channel

Proper functioning of the MET channels is critical for transduction of sound-induced vibrations into electrical signals. While the composition of the MET channel has been widely researched, the molecular identity of the MET channel has proved elusive for a number of years. It is speculated to consist of several proteins interacting as one unit, leading to usage of the term 'MET channel complex' (Figure 1.4). In order to be considered as a MET channel complex candidate, a molecule must exhibit properties shared by current candidates. These include localisation to the tips of stereocilia in the hair cell membrane, similar interacting partners and intrinsic properties (Effertz et al., 2015).

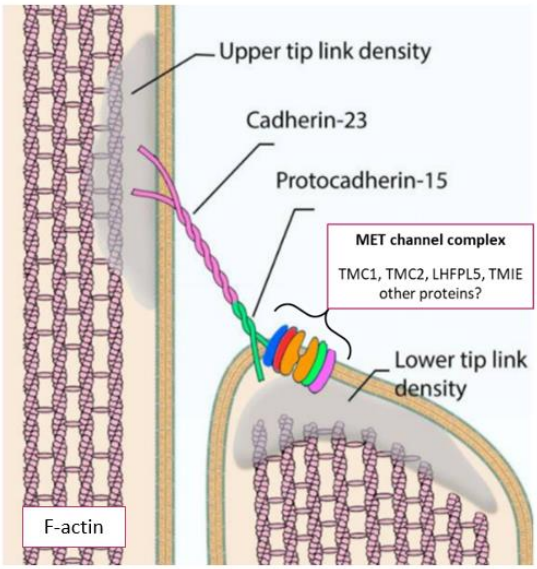

Figure 1.4: Schematic diagram of stereocilia MET channel complex proteins. While a number of proteins have been identified as part of the MET channel complex, additional proteins are thought to be involved. TMC1 – transmembrane channel like 1; TMC2 – transmembrane channel like 2; LHFPL5 – Lipoma HMGIC fusion partner-like 5; TMIE – transmembrane inner ear. Adapted from Kurima et al. (2015).

Mounting evidence indicates that TMC1 (transmembrane channel like 1) is the crucial protein that constitutes the MET channel (Fettiplace, 2016). Dominant mutations in the *TMC1* gene cause progressive deafness in both mice and humans (Kurima et al., 2002). Both fluorophore-tagged Tmc1 and its paralogue Tmc2 are localised to the stereocilia tips during the early postnatal period, which is also when hair cell mechano-electrical transduction is first detected (Kawashima et al., 2011). Moreover, both proteins are only detected with the two 'transducing' shorter rows of stereocilia where the MET channels are present (Kurima et al., 2015). Interestingly, *TMC2* is expressed roughly two days before *TMC1* in IHCs, and expression of either gene alone is sufficient for mechano-electrical transduction (Pan et al., 2013). Critically, deletion of both *TMC* genes results in hearing loss, loss of hair cell mechanosensitivity and an overt vestibular phenotype (Kawashima et al., 2011). Furthermore, an interaction between the Tmc proteins and PCDH15, the lower component of the tip link thought to be attached to the MET channel, has been identified (Maeda et al., 2014). These data suggest that both proteins may interact to form a critical component of the MET channel.

Other proteins that localise to the stereocilia tips have been discussed as potential MET channel complex candidates. The tetraspan protein LHFPL5 (Lipoma HMGIC fusion partner-like 5, formerly formally known as TMHS (tetraspan membrane protein of hair cell stereocilia)) and TMIE (transmembrane inner ear), a protein with two transmembrane domains, are known to interact with each other. Furthermore, both interact with the tip link component PCDH15, and mouse mutants for both genes exhibit hearing loss, leading to the conclusion that the two proteins are components of the MET channel (Mitchem et al., 2002, Longo-Guess et al., 2005, Xiong et al., 2012, Zhao et al., 2014).

1.1.9 Ribbon synapses and innervation of the cochlea

Afferent neurons transmit the signal from the depolarised IHC to the auditory cortex in the ascending auditory pathway. IHC depolarisation triggers release of the neurotransmitter glutamate from vesicles that are tethered to a specialised organelle known as the ribbon synapse, an electron-dense structure anchored to the plasma membrane found only in inner ear and retinal cells (Nouvian et al., 2006), and

pinealocytes in the brain (McNulty and Fox, 1992). Glutamate is released from these vesicles in the presynaptic density into the synaptic cleft at the base of the hair cells. It travels across the synaptic cleft and binds to glutamate receptors on the post-synaptic density of a type I SGN.

Conversely, OHCs are innervated by efferent neurons that originate from the superior olivary complex (SOC) in the central auditory pathway and descend towards the OHCs. These efferent fibres can be classified into medial (MOC) and lateral (LOC) (Warr, 1992). The MOC efferents are the most well-studied, and effects attributed to them include the control of the dynamic range of hearing improvement of signal detection in background noise, and protection from acoustic injury (Guinan, 1996, Elgoyhen, 2020).

All cochlear hair cells are innervated by SGNs, which reside within the bony modiolus and are excited by the signal transmitted from the hair cells, and deliver the signal to the cochlear nucleus in the brainstem. The two types of afferent neurons display morphological differences, which enable them to perform distinct roles in signal transmission. Each IHC is innervated by multiple type I SGNs, which constitute 95% of SGNs (Perkins and Morest, 1975). Type I SGNs have larger diameters than type II SGNs, and are myelinated. Conversely, the unmyelinated type II SGNs represent 5% of all SGNs. They extend long projections and contact several OHCs simultaneously. Similar to hair cells along the basilar membrane, the SGN network exhibits tonotopic organisation. Up to 30 afferents innervate a single IHC, which in part explains how the cochlea can respond to sound pressure levels that vary over a large range.

Interestingly, a recent study utilising RNA-Sequencing techniques demonstrated that type I SGNs are molecularly diverse, and can be discerned into three main subclasses. Furthermore, diversification and promotion of spontaneous activity of type I SGNs is dependent on the correct functioning of the mechano-electrical transduction machinery, even prior to the onset of hearing. (Sun et al., 2018)

1.1.10 **Sound transduction**

The conversion of mechanical vibrations into electrical signals, known as sound transduction, takes place in the cochlear hair cells. In a resting hair cell, approximately 15% of the MET channels are already open, and its potential is approximately -60 mV (Hudspeth, 1989). When sound wave-induced vibrational energy arrives at the oval window from the ossicles, it is transmitted to the basilar membrane and travels along its length, starting from the base. Displacement of the tectorial membrane relative to the basilar membrane deflects the OHC stereocilia they are in contact with. Conversely, the stereocilia of IHCs are indirectly deflected by the motion of the endolymph in which they are immersed.

This deflection towards the tallest stereocilia in the hair bundle causes the tip links connecting stereocilia in adjacent rows to stretch. While under tension, the tip links pull open the 'mechanically-gated' MET channels they are tethered to on the two shorter 'transducing' rows of stereocilia.

Subsequently, K^+ ions from the surrounding endolymph passively enter the cell body through the now open MET channels, causing rapid depolarisation of the cell. This is followed by an influx of Ca^{2+} ions through voltage-gated calcium channels in the cell body membrane. This results in release of glutamate (Klinke, 1986) from vesicles tethered to the ribbon synapse from the presynaptic density into the synaptic cleft at the base of the hair cell. Once glutamate binds to α-amino-3-hydroxy-5-methylisoxazole-4- proprionic acid (AMPA) receptors at the post-synaptic density of afferent type I SGNs (Matsubara et al., 1996), an action potential is generated and the subsequent electrical signal travels up the auditory nerve to the auditory cortex in the brain, where it is processed. Repolarisation of the hair cell is achieved when the channels close and the stereocilia return to their resting position. (Figure 1.5)

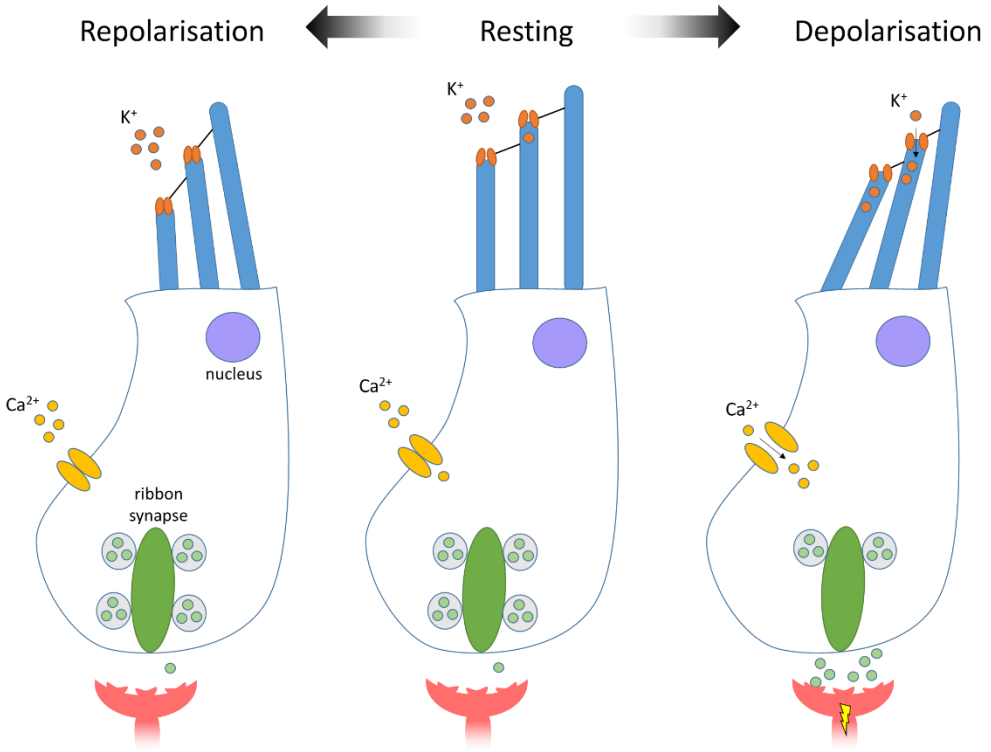

Figure 1.5: Depolarised IHCs convert mechanical vibrations into electrical signals. When the cell is in its resting state, the MET channels (orange) are partially open and the Ca^{2+} channels (yellow) are closed. The vesicles (grey) containing the neurotransmitter glutamate are tethered to the ribbon synapse (green). When the stereocilia (blue) deflect towards the tallest row, the tip links stretch to open the MET channel and K^+ from the surrounding endolymph enters the cell, which is now in depolarised. This results in the voltage-gated Ca^{2+} channels opening, and allows Ca^{2+} to enter the cell soma. Subsequently, the vesicles move to the edge of the cell and its vesicles release glutamate across the synapse (red), where they bind to receptors on the afferent nerve (red) and initiate the transmission of the electrical signal down the auditory nerve. Repolarisation occurs when the channels have closed and the stereocilia return to their normal position. Ca^{2+} - calcium ion; K^+ - potassium ion.

1.2 Central auditory system

The central auditory system is responsible for transmitting the electrical signal generated in the organ of Corti to the auditory cortex in the brain, where it is deciphered. A degree of processing, however, occurs even before the signal reaches the auditory cortex – for example, localisation of sound in space is achieved in the superior olivary complex (located in the caudal pons) through comparing sound intensity and timing of input from both ears in a process known as binaural processing (van der Heijden et al., 2013).

The axons of the SGNs coupled to the IHCs are packaged together as the auditory nerve, which carries the signal through the interior of the modiolus to the cochlear nucleus located in the brainstem. From here, the signal is transmitted to the superior olivary complex. Briefly, auditory fibres from the superior olivary complex travel via the inferior colliculus in the midbrain, medial geniculate nucleus in the thalamus, and finally converge on the auditory cortex in the temporal lobe (Figure 1.6). The tonotopic organization observed along the basilar membrane is maintained throughout these structures. (Staecker and Thompson, 2013, Barha et al., 2016, Hall, 2012)

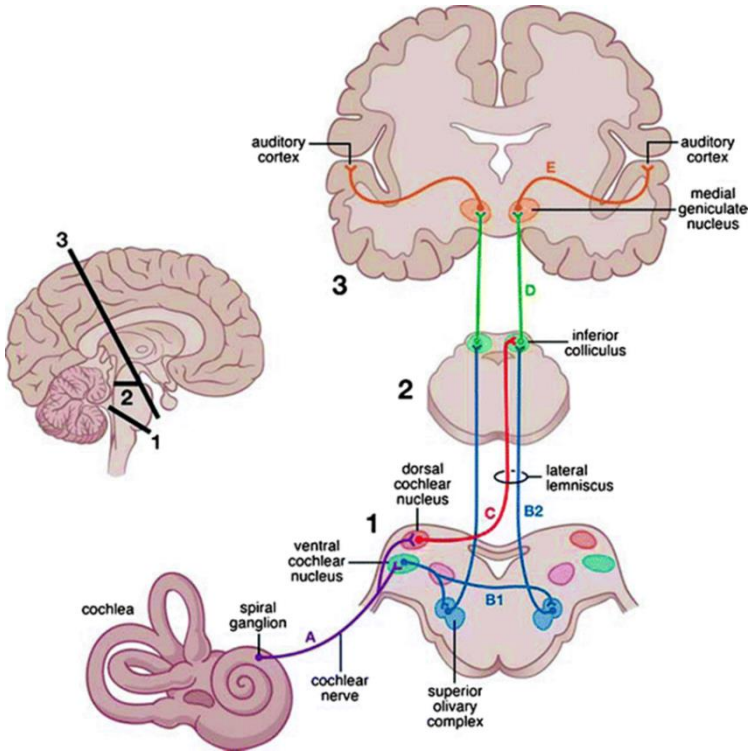

Figure 1.6: Schematic diagram of the bilateral ascending auditory pathway from the cochlea to the auditory cortex including auditory structures within the brainstem (1), midbrain (2), and cortex (3). A cross section of the human brain, indicating the three regions of the auditory pathway is also depicted on the left. The auditory pathway is highly conserved between mammals. The unilateral auditory pathway includes the cochlear nerve (A), ventral cochlear nucleus to contralateral and ipsilateral superior olivary complex (B1), superior olivary complex to inferior colliculus (B2), dorsal cochlear nucleus to contralateral inferior colliculus (C), inferior colliculus to medial geniculate nucleus (D), and medial geniculate nucleus to auditory cortex (E). Adapted from Hall, 2012.

1.3 Development of the inner ear

Development of the inner ear begins with the thickening of the pre-placodal region of the ectoderm into the otic placode around embryonic day 8 (E8) in the mouse (Morsli et al., 1998) (approximately 19-21 days in the developing human embryo), induced in part by fibroblast growth factor (FGF)

signalling (Ohyama et al., 2007). Invagination of the otic placode gives rise to the otic vesicle at E9.5, and the resulting cochlear duct grows from the ventral portion (Li et al., 1978). From here, the cochlear duct continues to elongate and coil.

Various mechanisms are involved in the patterning of the developing cochlea. The transcription factor SRY-related HMG box (Sox) 2 is an early marker of developing inner ear prosensory domains. It plays diverse roles in sensory cell development and is itself regulated by Notch signalling (Dabdoub et al., 2008). Furthermore, bone morphogenetic protein (BMP) signalling is established along a gradient, which contributes to the patterning of both sensory and non-sensory regions of the cochlea (Ohyama et al., 2010).

While these pathways and others contribute to patterning of the various cochlear regions, they are not overtly responsible for the differentiation of hair cells and supporting cells, which are known to arise from a common progenitor from experiments using chicken embryos (Fekete et al., 1998). It is the transcription factor, Atonal homolog 1 (Atoh1, also known as Math1), that is crucial in specifying the formation of the hair cells (Bermingham et al., 1999, Woods et al., 2004), and furthermore demonstrates a mutually antagonistic relationship with Sox2 (Dabdoub et al., 2008). The last cells to exit the cell cycle at the base of the cochlea are the first cells to differentiate into hair cells (Groves et al., 2013).

1.3.1 **Hair bundle development**

Development of the avian hair bundle is well documented by (Tilney et al., 1992)). In the mouse, development of the mechano-electrical transduction machinery begins at approximately E14 (McGrath et al., 2017). At this time point, a lawn of microvilli covers the apical surface, or cuticular plate, of the hair cell (Figure 1.7). A single kinocilium, a true cilium unlike stereocilia, appears amongst the microvilli and migrates to the periphery of the cuticular plate. This stage is crucial in the development of planar cell polarity and establishes the orientation of the resulting hair bundle. Following this, microvilli surrounding the kinocilium elongate into stereocilia of graded heights,

leading to the recognisable 'staircase-like' structure of three rows (Tilney et al., 1992). The developing stereocilia can be observed as early as P0 (Anniko, 1983), and the kinocilium disappears shortly after birth (Lim and Anniko, 1985). Mechano-electrical transduction currents can be detected from birth, and reach mature levels around one week later (Lelli et al., 2009). OHCs reach functional maturity at approximately P8 (Marcotti and Kros, 1999), and IHCs mature by P12 (Kros et al., 1998), which signifies the onset of hearing in mice. In addition to bundle formation, functional maturity also involves changes to the repertoire of ion channels and currents that hair cells possess. Synaptogenesis generally occurs in the postnatal cochlea, and is thought to last for at least 14 days (Anniko, 1983, Michanski et al., 2019).

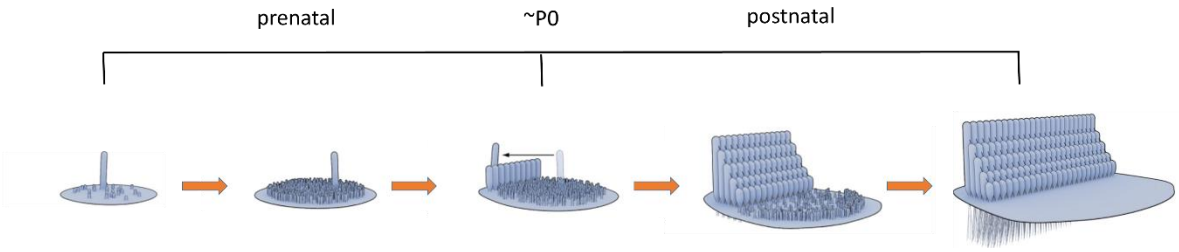

Figure 1.7: Schematic diagram of sequential stages of avian hair bundle development. While avian hair cells have four rows of stereocilia instead of three (like human and mouse), developmental stages are similar. At the onset, the apical hair cell surface contains microvilli and one kinocilium. The microvilli grow in length, before the kinocilium moves to the lateral edge of the hair cell. Some microvilli elongate to form stereocilia of graded heights. Note that mammalian hair bundles are arranged in a distinct 'W' or 'U' shape that is not shown here. P – postnatal day. Adapted from Schwander et al., 2010.

1.4 Vestibular system

The vestibular system of the inner ear is responsible for detecting and modulating motion and position of the body in space. It is important in postural reflexes, the automatic movements that combat the effects of gravity during movement. The vestibular labyrinth is continuous with the cochlear labyrinth (Figure 1.1). It consists of five end organs – three semi-circular canals that are perpendicular to one another, and two otolith organs, the saccule and the utricle (Brosel et al., 2016). The semi-circular canals respond to rotational accelerations, whereas the otolith organs detect linear acceleration (Angelaki and Cullen, 2008).

The hair cells of the vestibular system are located within the two otolith organs and the three ampullae, which are situated at the base of the three semi-circular canals. Vestibular hair cells are similar to cochlear hair cells in that they are surrounded by supporting cells and convert sensory vibrations into electrical signals via the opening of MET channels followed by depolarisation and release of glutamate. The vestibular hair bundles are positioned in various orientations, meaning the vestibular system is receptive to a shift of orientation in any direction. Furthermore, there are two types of vestibular hair cells, which exhibit numerous morphological, electrophysiological and functional differences to each other (Burns and Stone, 2017).

1.5 Hearing loss

Deafness is a broad term to describe a wide range of heterogeneous diseases associated with partial or full loss of hearing. The charity Royal National Institute for Deaf People (RNID, previously Action on Hearing Loss) estimated that in 2018, over 12 million people in the UK lived with either conductive or sensorineural hearing loss (1 in 6 people), and it is likely this number will increase to 15.6 million by 2035. This increase in sufferers is reflective of an ageing population in the UK, as people aged 50 and over with hearing loss accounts for 40% of all national cases. (RNID)

Hearing loss in humans can range from mild to profound, as determined by a pure-tone audiogram (Table 1.2). This categorisation is accompanied by common symptoms and recommended courses of treatment (if any). Hearing loss can occur alongside other co-morbidities (syndromic), or in isolation as the only symptom (non-syndromic).

Table 1.2: Classification of hearing loss. Adapted from World Health Organisation and Zahnert (2011).

Grade of hearing loss	Mean hearing loss in pure-tone audiogram (dB)	Clinical findings	Recommendations
None	<25	No or very slight hearing problems. Able to hear whispers	Counselling, follow-up examination; if conductive hearing loss is present, evaluate indication for surgery
Mild	26-40	Able to hear and repeat words spoken in normal voice at 1 meter	Counselling, hearing aids may be advisable; if conductive hearing loss or combined hearing loss is present, surgical treatment may be indicated

Moderate	41-60	Able to hear and repeat words spoken in raised voice at 1 meter	Hearing aids recommended; if conductive hearing loss or combined hearing loss is present, surgical treatment may be indicated
Severe	61-80	Able to hear some words when shouted into better ear.	Hearing aids needed; if an external hearing aid is not possible, consider an implanted hearing aid or cochlear implant; lip-reading and signing for supportive treatment
Profound	>81	Unable to hear and understand even a shouted voice.	Failure of a hearing-aid trial is now usually considered an indication for a cochlear or brainstem implant; lip-reading and signing can be taught in addition

Hearing loss represents a significant global social and economic problem. Although hearing is not a critical human sense, hearing loss in any form can be debilitating due to gradual loss of ability to communicate. This can lead to feelings of frustration and subsequently social isolation (Weinstein and Ventry, 1982). Furthermore, early-onset forms of hearing loss are associated with almost all areas of child development: speech and language acquisition, psychosocial and psychoeducational development, to name a few (Tharpe and Gustafson, 2015). These developmental difficulties can lead to a range of more chronic issues later in life.

Additionally, hearing loss inflicts a substantial burden on health services and the economy. A 2014 report estimated that in the previous year, £24.8bn in potential economic output was lost in the UK, and this cost will rise to £38.6bn by 2031 if this is not addressed. These figures are due to lower employment rates for those with hearing loss than across the rest of the population (Commision on Hearing Loss, 2014). Despite this substantial financial burden, only £1.11 is spent on research into hearing loss for every person affected, which compares with £11.35 spent on vision research for every person with sight loss (RNID, 2014).

Depending on its origin, hearing loss can be categorised as either conductive or sensorineural.

1.5.1 **Conductive hearing loss**

Conductive hearing loss arises from damage to the outer or middle ear, which prevents or reduces sound-induced vibrations from reaching the inner ear. Causes include overgrowth of the ossicles, malformation of the auditory canal or tympanic membrane, build-up of earwax and otitis media (OM), or inflammation of the middle ear (Dougherty and Kesser, 2015) which can occur with or without effusion (accumulation of liquid in the middle ear). OM is the leading causes of deafness in children, and it is estimated that by the age of three, over 75% of children will have suffered from at least one episode of acute OM (Klein, 1994).

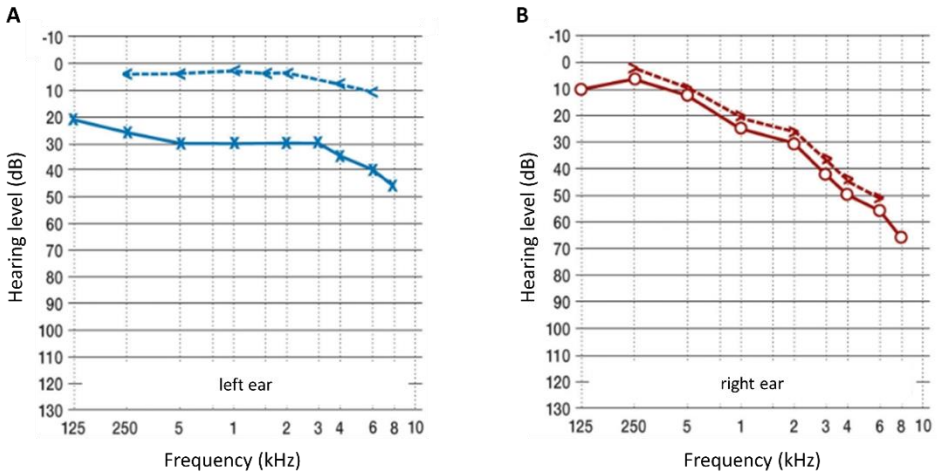

Figure 1.8: Representative audiograms for a patient with conductive hearing loss in the left ear (A) and sensorineural hearing loss in the right ear (B). An audiogram is a graphical display of an individual's hearing ability, showing low to high frequencies (kHz) on the x-axis, and low to high intensity (dB) on the y-axis. While various symbols may be used on audiograms, most clinicians use a standard set of symbols and colours. X and O are used to plot a patient's air conduction hearing thresholds for the left and right ear, respectively, whereas > and < are used to plot the patient's bone conduction hearing thresholds for the left and right ear, respectively. Moreover, left ear thresholds are marked in blue, and right ear thresholds in red. **(A)** In cases of conductive hearing loss, air conduction thresholds are elevated, but bone conduction thresholds are within normal limits (-10 to +15 dB) as the sound energy bypasses the outer and middle ear and goes directly to the inner ear. **(B)** In cases of sensorineural hearing loss, both air and bone conduction thresholds show the same degree of elevation. Adapted from Zahnert, 2011.

Following an initial occurrence of OM with effusion, subsequent episodes are common – with a recurrence rate as high as 40% (Tos, 1984). Management of OM with effusion can involve the insertion of a grommet into the tympanic membrane to drain the middle ear fluid, but this is a temporary treatment (Venekamp et al., 2018). Differences in audiograms between patients with conductive (Figure 1.8A) and sensorineural (Figure 1.8B) hearing loss can be observed. In this example, the

conductive hearing loss does not vary between frequencies, whereas the sensorineural hearing loss is more prominent at higher frequencies.

1.5.2 Sensorineural hearing loss

Sensorineural hearing loss arises from damage to the cochlea, the internal auditory canal (which contains the seventh and eighth cranial nerves), or the otic capsule (Wang et al., 2019a). Sensorineural hearing loss most commonly results from degeneration of the cochlear hair cells (Chien et al., 2015).

Approximately half of the 12 million hearing loss cases in the UK have a genetic basis. Around 70% of these cases are non-syndromic (Brown et al., 2008), meaning patients do not present with any other related symptoms. Different forms of hearing loss are often characterised by the nature of the causal mutation, with autosomal dominant and recessive mutations causing DFNA and DFNB conditions respectively. Autosomal recessive mutations account for 80% of genetics cases (Shearer, 1999). X-linked hearing loss, caused by mutation of a gene on the X chromosome, is rarer, with patients experiencing other symptoms such as syndactyly (as part of STAR syndrome) or neurologic symptoms (as part of X-linked Adrenoleukodystrophy) (Corvino et al., 2018). The gene most often mutated in congenital sensorineural hearing loss is *connexin 26* (Chan and Chang, 2014), which encodes the gap junction beta 2 (GJB2) transmembrane protein and was first reported by Kelsell et al (1997). GJB2 is thought to be critical in the clearing and recycling of K^+ from the organ of Corti to the endolymph of the scala media, thus helping to maintain the endocochlear potential (Kikuchi et al., 2000).

1.5.3 Hair cell regeneration

Although hair cells in some vertebrates such as birds (Bermingham-McDonogh and Rubel, 2003) and zebrafish (Lush and Piotrowski, 2014) can be regenerated from supporting cells that re-enter the cell cycle, adult mammalian cochlear hair cells cannot – meaning that their loss is permanent and irreversible (Groves, 2010). However, it is known that in the mouse early postnatal cochlea, supporting cells can transform into hair cells via transdifferentiation (Franco and Malgrange, 2017), whereby terminally differentiated cells return to their naïve state and differentiate along another pathway.

Although this ability is progressively lost after the first postnatal week, spontaneous regeneration of cochlear hair cells has been documented in both *in vivo* mouse models (Cox et al., 2014) and explant cultures (Bramhall et al., 2014). In contrast, select mammalian vestibular hair cells are thought to have a limited capacity to regenerate from supporting cells when damaged is induced by ototoxins (Forge et al., 1993, Kawamoto et al., 2009, Li et al., 2016), and indeed are able to achieve mitotic regeneration in newborn mice (Burns et al., 2012). In order to prevent hearing loss, there is, therefore, a need to intervene before irreversible damage is acquired, or alternatively to investigate the possibility of 'oto-regenerative' medicine to instead treat hearing loss.

Current treatments options for sensorineural neural hearing loss are somewhat limited, and have variable success. Hearing aids are worn on the external ear (pinna) and work by amplifying incoming sounds. Conversely, cochlear implants are surgically inserted into the cochlea, whereby generated electrical signals bypass the hair cells and directly stimulate the auditory nerve. Cochlear implants can be used once a patient with severe or profound sensorineural hearing loss does not benefit from the use of hearing aids (Roche and Hansen, 2015).

1.5.4 **Age-related hearing loss (AHL)**

The term presbycusis describes aged-related hearing loss (ahl), and is the most common form of sensorineural hearing loss (Reis and Escada, 2016). It is characterised by a gradual loss of hearing sensitivity with age, with a classic symptom of experiencing difficulty understanding speech in noisy environments (Gates and Mills, 2005). Presbycusis can be categorised into four groups: sensory (atrophy of the organ of Corti), neural (loss of auditory neurons), strial (degeneration of the stria vascularis) and possibly mechanical (stiffening of the basilar membrane) (Schuknecht, 1964). Sensory presbycusis is characterised by degeneration of cochlear hair cells in a base-to-apex manner, which translates into initially high frequency hearing loss that progressively affects mid to lower frequencies (Tawfik et al., 2019). Similarly, 'presbystasis' refers to aged-related vestibular dysfunction. Due to

numerous other potential causes of vertigo in the elderly, however, diagnosis of true presbystasis can be challenging (Ciorba et al., 2015).

Genome-wide association studies (GWAS) have been instrumental in identifying new deafness candidate genes. The UK Biobank study (Sudlow et al., 2015) is a large-scale, open-access resource that collects phenotypic and genotypic data from UK adults aged between 40 and 69 years with the aim to facilitate research into aged-related disease. A recent study has utilised the self-reported hearing data from 250,000 participants from the Biobank to identify novel loci associated with aged-related hearing loss (Wells et al., 2019), and confirmed protein localisation within the cochlea for several putative novel deafness genes. Studies like these are crucial in identifying new deafness gene candidates, and subsequently, help to elucidate the genetic mechanisms involved in hearing.

1.5.5 Hearing loss and cognitive decline

Mid-life progressive hearing loss is thought to be the largest 'potentially' modifiable risk factor for developing dementia. This exceeds smoking, high blood pressure, lack of exercise and social isolation (Livingston et al., 2017). Furthermore, both age-related hearing loss and dementia are multifactorial and heterogeneous conditions, which may hamper identification of the link between them. As such, there are varying hypotheses as to why there appears to be a correlation. The popular 'cognitive load' hypothesis suggests that an individual with hearing loss will devote higher cognitive resources to perceiving and decoding sound, at the expense of other cognitive processes (Wayne and Johnsrude, 2015). Conversely, the 'common cause' hypothesis argues that hearing loss and cognitive decline arise from a common neurodegenerative process in the ageing brain (Stahl, 2017). Others include the cascade and harbinger hypotheses (Uchida et al., 2019).

1.5.6 Tinnitus

Tinnitus refers to the perception of sound in the absence of an external stimulus. The condition is extremely common, affecting 1 in 8 people in the UK (RNID, 2014), often worsens with age, and heterogeneous: cases can be acute or chronic, constant or intermittent, and occur isolated or

alongside another ailment, such as stress (Baguley et al., 2013). There is a myriad of risk factors associated with tinnitus, including neurological, cardiovascular and psychological factors. There is also a strong correlation between tinnitus and hearing loss, and the prevalence of tinnitus increases with hearing loss (Chung et al., 1984).

Although the exact cause of tinnitus is unknown, it is often postulated that the condition arises from the central auditory system. An unnecessary increase in the spontaneous firing rate of neurons in auditory structures (Roberts et al., 2010) due to for example ototoxins or noise insult, is one explanation given.

1.5.7 Noise exposure and other environmental factors

A major environmental cause of hearing loss is noise exposure, and unlike genetic cases, noise-induced hearing loss (NIHL) is preventable. The degree of NIHL increases with the intensity, measured in decibels (dB), of the sound. Exposure can be chronic, often experienced in cases of occupation NIHL (e.g. operating heavy machinery), or arise from one sudden, exceptionally loud noise (e.g. an explosion/blast).

Noise exposure can result in two types of damage depending on the intensity and duration of the insult. They are known as temporary threshold shifts (TTS) in which hearing loss is transient, or permanent threshold shifts (PTS) where hearing loss is irreversible. TTS is hypothesised to be caused by the uncoupling of OHCs to the tectorial membrane, possibly due to temporary buckling of the supporting cells (Nordmann et al., 2000). However, hearing often recovers within 24-48 hours, although its long-term effects are poorly understood (Le et al., 2017). In cases of PTS, hair cell death and nerve fibre degeneration are observed (Nordmann et al., 2000). Furthermore, cochlear synaptopathy, also known as hidden hearing loss, is a condition that arises due to noise exposure but without experiencing PTS. Loss of afferent ribbon synapses at the base of IHCs is thought to be the cause (Shi et al., 2016). As a result, patients with hidden hearing loss often have difficulty in understanding speech in noisy environments.

Besides genetic predisposition and noise exposure, other causes of hearing loss include ototoxic damage, viral infections and physical injury to the ear. Furthermore, genetic predisposition and noise exposure can result in increased susceptibility to NIHL.

1.6 Mouse models of human disease

Due to a combination of limitations such as variation between individuals and ethical concerns, human patients cannot always be used for the study of disease. A robust model system therefore needs to be practical and easy to access, have a means to reduce variability, and crucially mimic the manner in which human tissues behave and interact *in vivo*. Cell lines provide an unlimited supply of material but only allow examination of a homogenous system within a limited environment (Kaur and Dufour, 2012), and do not permit the study of an entire organism's physiology and interactions across organ systems. Computer modelling programs enable users to eliminate difficulties associated with the use of living cells and tissue, but naturally, programs are unable to replicate the unpredictability of a living, breathing organism. Therefore, in order for a model system to represent the complexity of the entire human body and its associated diseases as well as possible, an animal model is often the primary choice.

Mus musculus, the laboratory mouse, is arguably the definitive model organism for biomedical research. Its popularity over other models is in part due to its genetic similarity with humans – both genomes are thought to contain ~20,000-25,000 protein-coding genes, and approximately 99% of mouse genes have a human homologue (Waterston et al., 2002). Despite the obvious difference in body size, there are remarkable similarities between mouse and human physiology in body systems such as nervous, cardiovascular, endocrine, immune and musculoskeletal (Rosenthal and Brown, 2007). Additionally, the mouse is a highly practical species to work with – it is relatively cheap to maintain, breeds regularly and prolifically, has a short lifespan (usually between 12 and 18 months) and, importantly, its genome can be readily manipulated. It is also easy to generate genetically identical individuals for controlled studies. The short reproductive cycle of mice allows inbred and

outbred strains to be produced as required, and now in the modern age of biotechnology, mice with specific mutations and phenotypes allow the creation of mouse models that are prone to develop genetic diseases of interest such as diabetes, cancer, neurological disorders, asthma and deafness. Currently, advanced techniques such as CRISPR/Cas9 are used to target specific regions of the mouse genome with great efficiency and precision, with hopes to design molecular therapies for human patients (Sander and Joung, 2014).

1.6.1 **Genetic manipulation in mice**

Before the now conventional use of targeted mutagenesis, selective breeding of mice with spontaneous or randomly introduced mutations to generate an experimental cohort was routine. This technique formed the basis of the 'forward', or 'classical' genetics approach to identify genes of interest. This has since been superseded by reverse genetics, whereby a targeted mutation is induced in an organism to examine a possible incurred phenotype. Although forward genetics approaches are time consuming and expensive, they offer an unbiased approach to studying the link between a mutation and a phenotype (Gurumurthy et al., 2016).

Due to the ease of their genetic manipulation, a variety of mouse models with various mutations can be generated. This includes the generation of knockout, knockin or knockdown models and conditional models, in which the spatial and temporal expression of a gene of interest can be controlled.

Embryonic DNA injection uses homologous recombination to mutagenize the mouse genome. It is still regularly used since its inception in the early 1980s. The most common method involves modifying embryonic stem cells that have been removed from a preimplantation embryo, and injecting them into a host preimplantation embryo which may result in a chimera (Adams and van der Weyden, 2008). Using embryos from mice with different coat colours is a useful way to tell if the modified cells have been successfully introduced, as chimeric mice will have a bicolour coat.

The use of the CRISPR/Cas9 system, however, is now routinely employed to edit the mouse genome with great precision. In brief, this method was adapted from a defence mechanism in the immune system of prokaryote species, in which a section of invading DNA is copied into the host genome. The locus of clustered regularly interspaced short palindromic repeats (CRISPR) serves as a memory bank to be used against future attacking pathogens. When this occurs, corresponding CRISPR RNA (crRNA) is transcribed and will bind to the foreign DNA, which is always upstream of a protospacer adjacent motif (PAM) sequence. A CRISPR-associated (Cas) protein Cas9, directed by the crRNA, then cleaves the DNA at the targeted point. crRNA and trans-activating tracrRNA are both essential for proper cleavage of the DNA. The subsequent genomic repair, through either non-homologous end joining (NHEJ) or homology-directed repair (HDR) can then be exploited for genome editing (Wijshake et al., 2014). This technology is efficient in targeting the gene of interest, as well as being relatively inexpensive and fast to design and implement (Doudna and Charpentier, 2014). More recently, advanced CRISPR techniques such as base editing (Komor et al., 2016) and prime editing (Anzalone et al., 2019) have been utilised to manipulate the genome with greater efficacy and specificity than previous techniques, and without the requirement for double stranded breaks or donor templates.

Base editing technology works by inducing desired point mutations, and the two major classes are cytosine and adenine base editors (CBEs and ABEs). However, base-editing is generally limited to the four transition mutations (as opposed to transversion mutations), and undesired by-stander mutations can be generated (Kantor et al., 2020). Conversely, while prime editing technology is generally considered to be less efficient than base editing, it has the capacity to introduce a greater variety of mutations including point mutations, and small insertions and deletions, with high precision. Its efficiency is determined by the design of prime editing guide RNA (pegRNA), which both specifies the target site and encodes the desired edit (Anzalone et al., 2019). CRISPR/Cas9 technology shows great potential in the generation of mouse models that are characterised by specific mutations found in human patients, which could eventually lead to therapies tailored to individual patients with distinct disease phenotypes.

1.6.2 **The mouse as a model for hearing loss**

Historically rats, cats and guinea pigs were popular models used for hearing research. However, *Mus musculus* surpassed all other models for the study of the auditory and vestibular systems in 2005 (Ohlemiller et al., 2016). The mouse's rise in popularity in deafness research reflects the genetic and molecular advances in gene editing in the mouse, and the near absolute eradication of genetic variance using inbreeding.

Although mouse and human inner ears are structurally and functionally very similar, it is important to note that the range of frequencies that can be detected by each species is different (though there is some overlap (Figure 1.9). The mouse can detect sounds ranging from 2 kHz up to 100 kHz, with an optimal sensitivity range of between 15 kHz and 20 kHz (Ehret, 1974, Turner et al., 2005). Conversely, the human frequency range is often given as between 20 Hz and 20 kHz, with the optimal sensitivity range between 2 kHz and 4 kHz (Heffner and Heffner, 2007). Other laboratory animals possess a more comparable hearing range, demonstrating how the auditory systems of different species have adapted to be more sensitive at given frequencies (Figure 1.9).

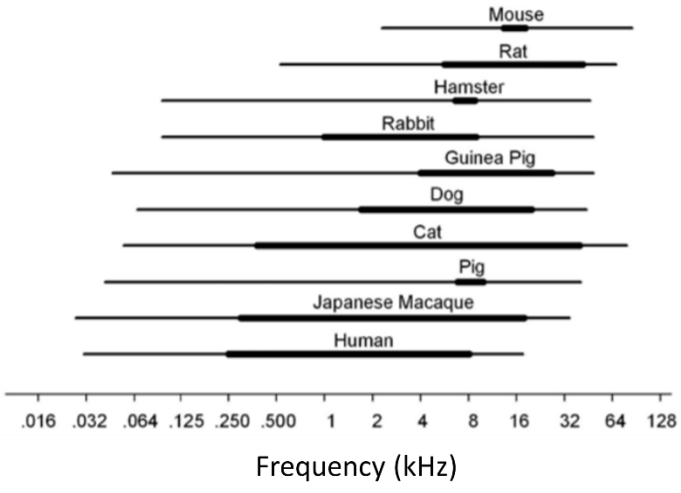

Figure 1.9: The hearing range of laboratory animals compared with that of humans. Thin lines indicate the range of frequencies that can be detected at 60 dB SPL; thick lines indicate the range that can be detected at 10 dB SPL (i.e. the most sensitive frequency range). Adapted from Heffner and Heffner (2007).

Within the field of mouse genetics, it is widely recognised that genetic background can heavily influence phenotype. Therefore, ideally experiments should always be conducted on a range of genetic backgrounds to minimise the risk of incorrectly interpreting a phenotype (Crawley et al., 1997). Of the most common strains used in deafness research, many vary widely in onset and severity of hearing loss (Zheng et al., 1999, Johnson et al., 2006).

Many common strains that exhibit age-related hearing loss are homozygous for a mutation in the *Cdh23* gene, which is a partial loss-of-function allele at the *ahl* locus. A G-to-A substitution at nucleotide 753 ($Cdh23^{753A}$) results in in-frame skipping of exon 7 (Noben-Trauth et al., 2003). Wild type *Cdh23* encodes the cadherin 23 protein, a component of the tip link connecting adjacent rows of stereocilia (Siemens et al., 2004). Additionally, mutant alleles of *Cdh23* (for example, those harboured by the *waltzer* mouse model), cause Usher Syndrome type 1D in humans (Di Palma et al., 2001), a genetic disease characterised by combined blindness and deafness.

The CBA sub-strains of laboratory mice are considered the best-characterised strains with 'normal' hearing, due to their wild type *Cdh23* allele (Ohlemiller et al., 2016). Although the C57BL/6N and J sub-strains (generated at the National Institutes of Health and the Jackson Laboratory, respectively) are popular choices for modelling disease, both sub-strains harbour the $Cdh23^{ahl}$ allele (Kane et al., 2012, Noben-Trauth et al., 2003), making them unattractive models in which to study late-onset phenotypes. However, the allele has been repaired using CRIPSR/Cas9 technology in C57BL/6N mice (Mianné et al., 2016), and also in C57BL/6J mice (unpublished data), at the MRC Harwell Institute.

1.6.3 **Auditory and vestibular phenotyping of mouse models**

Numerous phenotyping tools are available to identify and characterise hearing or vestibular dysfunction in the mouse. The click box is a crude test often used to initially determine the presence or absence of hearing, in which a high-frequency stimulus of roughly 90 dB SPL is emitted from a box held above the animal. The presence of the Preyer reflex, recognised by the flicking back of the pinna and occasionally a startle reflex, indicates some hearing capacity (Hardisty-Hughes et al., 2010).

To more thoroughly investigate hearing capacity, the Auditory Brainstem Response (ABR) test is used. Often regarded as the gold standard of auditory phenotyping, the ABR is an auditory evoked potential used to measure the activity of the auditory nerve in response to a sound stimulus. Briefly, an anaesthetised mouse is exposed to a stimulus of a given frequency (in kHz) and of decreasing intensity (in dB SPL). Electrodes inserted sub-dermally record the elicited electrical response in the SGN and cranial nerve, and is displayed as a waveform or trace. An auditory threshold is defined as the lowest sound intensity stimuli that elicits a recognisable trace, e.g. resembling traces produced from higher sound intensity stimuli. The individual peaks observed in the waveform correspond to the excitation of different origins along the ascending auditory pathway. Although the exact origins are unknown, distinct cell populations are thought to give rise to certain peaks (Figure 1.10) (Melcher and Kiang, 1996, Henry, 1979). Additionally, in some waveforms, the summating potential is observed before the first peak and is thought to be generated from the hair cells (Johnstone and Sellick, 1972). It is also thought that the 'assigned' wave numbers may correspond to different regions of the auditory pathway, depending on the species.

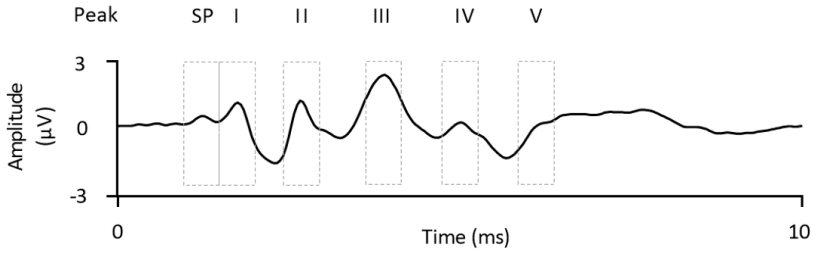

Figure 1.10: An ABR waveform from a wild type mouse displaying the summating potential (SP) and the first five peaks, in response to a 60 dB SPL stimulus. These peaks are thought to originate as a result of electrical activity in distinct regions along the auditory pathways. The various peaks are thought to arise from the following cell populations: PI: spiral ganglion neurons, PII: cochlear nucleus, PIII: superior olivary nucleus, PIV: medial superior olive principle cells and the inferior colliculus, PV: inferior colliculus. The hair cells are thought to give rise to the SP. ms – milliseconds.

To assess the function of OHCs specifically, otoacoustic emissions can be recorded as they are generated by OHCs only. DPOAEs are commonly measured by projecting two sounds of different frequencies directly into the auditory canal, and recording the OHC response.

Discovering an overt vestibular phenotype is considerably easier. Obvious behavioural abnormalities such as head bobbing or tilting, or circling are indicative of a severe vestibular phenotype, and these can be observed in the home cage (Hardisty-Hughes et al., 2010). The identification of a more subtle phenotype can be achieved through performing the swim test, due to the removal of the ground, which would normally provide tactile information (Sawada et al., 1994). A mouse with vestibular dysfunction will likely display abnormal behaviour when placed in water, such as circling, immobile floating or tumbling due to an inability to keep afloat.

1.7 Forward and reverse genetics screens

As previously mentioned, the purpose of a genetic screen is to identify a link between a change in phenotype with a change in genotype (Kile and Hilton, 2005). Reserve genetics screens, popularised in the 1980s, involve the disruption of a known gene and identification of the resulting phenotype (Hardy et al., 2010). A large and ongoing example of a mammalian reverse genetics screen is the International Mouse Phenotyping Consortium (IMPC), which aims to 'identify the function of every protein-coding gene in the mouse genome' by systematically generating and phenotyping a knockout mouse line for each gene. As of June 2019, 5861 knockout mouse models had been generated, with 69,982 phenotypes identified (Cacheiro et al., 2019). Conversely, the more classic, unbiased, forward screens work by identifying a mutation responsible from a known phenotype (Moresco et al., 2013). In particular, mutagenesis-driven screens have been instrumental in the discovery of disease-causing genes, and have been very successful in identifying numerous models of hearing loss (Bowl and Dawson, 2015).

1.7.1 Use of ENU in mutagenesis-driven screens

N-ethyl-*N*-nitrosourea (ENU) is an alkylating agent used to induce random point mutations in the DNA of mouse spermatogonial stem cells. A/T bases are primarily affected at a rate of 87%, and C/G bases at 13%. In subsequent protein products, this results in primarily missense mutations (64%), followed by alteration of splice sites (26%) and nonsense mutations (10%) (Justice et al., 1999). ENU

mutagenesis has been a useful tool in generating mutants in forward genetics screens since the 1970s (Russell et al., 1979), and more recently was employed to generate mouse mutants for the Harwell Ageing Screen (Potter et al., 2016).

1.7.2 Harwell Ageing Screen

The Harwell Ageing Screen, data from which was first published in 2016, was a phenotype-driven forward genetics screen that aimed to identify novel gene function by phenotyping progeny of mutagenised mouse cohorts (Potter et al., 2016). The primary purpose of the screen was to identify novel genes associated with age-related phenotypes and diseases by inducing point mutations in C57BL/6J mice using ENU. To generate large cohorts of mice homozygous for the ENU mutation, a rigorous breeding strategy was employed. Briefly, male C57BL/6J mice (G_0) dosed with ENU via intraperitoneal injection were mated to wild type sighted-C3H (C3H.Pde6b+) females. The male offspring heterozygous for ENU-induced mutations (G_1) were outcrossed to wild type sighted-C3H females. The female offspring from this cross (G_2) were then mated to their G_1 fathers to produce the phenotyping cohort (G_3) which includes mice wild type, heterozygous and homozygous for the ENU-induced mutations present in the G_1 males. As C57BL/6J mice carry the *Cdh23*^{ahl} gene allele (Noben-Trauth et al., 2003), G_2 females were genotyped for this and only offspring carrying the wild type *Cdh23* allele (inherited from sighted-C3H mice) were used for auditory phenotyping, thus eliminating the potential effect of the *ahl* allele interacting with any phenotype resulting from the ENU-induced mutations. G_3 cohorts then entered a high-throughput phenotyping pipeline, which examined numerous characteristics throughout lifespan (Table 1.3). These included tests observing metabolic function, neurobehaviour, and vision and auditory function. Tissues were taken from mice at the end of the pipeline for further analysis. Auditory phenotyping was conducted at 14 and 39 weeks of age using click box and ABR.

Of the 105 mutant lines identified from the screen, 27 were detected after 6 months, indicating a late-onset phenotype had been identified (the primary purpose of the screen). Of the 26 hearing loss

mutants identified, 17 mutants exhibited an early-onset phenotype. Causative mutations were identified by chromosomal mapping, following by linkage analysis and genome sequencing.

Table 1.3: Overview of Harwell Ageing Screen phenotyping pipeline. For tests where a single sex was initially phenotyped, the other sex was screened when outliers were suspected (indicated by brackets). ECG – electrocardiogram; SHIRPA – SmithKline Beecham, Harwell, Imperial College and Royal London Hospital phenotype assessment; MRI – magnetic resonance imaging; DEXA – dual energy X-ray analysis; IPGTT – intraperitoneal glucose tolerance test. Adapted from Potter et al, (2016).

Test	**Phenotypic Area**	**Group**	**Age (weeks)**
ECG	Cardiac	All	12
SHIRPA	Neurological	Females (males)	13, 66
Grip strength	Musculoskeletal/neurological	All	13, 66
Slit lamp/opthalmoscope	Vision	All	15, 49, 65, (73)
Optokinetic drum	Vision/neurological	All	15, 49, 65, (73)
Click box	Hearing	Non *ahl*	14, 26, 39, 50
ABR	Hearing	Non *ahl*	14, 39
Echo-MRI	Growth/body composition	Males (females)	16, 27, 51, 71
DEXA	Musculoskeletal/body composition	Females (males)	16, 51
X-ray	Musculoskeletal	Females (males)	16, 51, 74
Pupillometry	Vision/neurobehaviour	All	18, 68
Sleep tracking	Neurobehaviour	Females (males)	18, 68
Clinical chemistry	Pathology	Females (males)	28, 53, 80
Fasted bleed	Diabetes/metabolism	Males (females)	17, 28, 52, 80
Fasted insulin	Diabetes/metabolism	Males (females)	33, 57, 72
IPGTT	Diabetes/metabolism	Males (females)	33, 57, 72

1.7.3 **MPC-169**

One of the 150 pedigrees generated and phenotyped, Muta-Ped-C3PDE-169 (MPC-169), contained eight mice of 69 tested that exhibited a severe auditory phenotype at all frequencies tested when first phenotyped at 14 weeks of age (Figure 1.11).

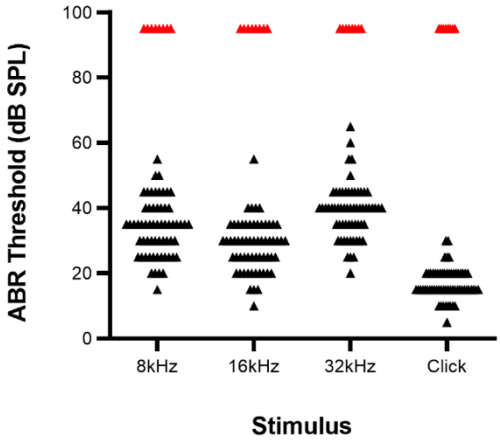

Figure 1.11: Affected mice in the MPC-169 pedigree exhibit early-onset, severe hearing loss. ABR phenotyping of pedigree MPC-169 at 14 weeks of age identified 8 mice with elevated hearing thresholds (red triangles) compared to their normal hearing colony mates (n = 61, black triangles). All affected mice failed to respond to the highest intensity stimulus (90 dB SPL) at the three frequencies tested, or the click stimulus, and so their thresholds are shown as 95 dB SPL. MPC – Muta-Ped-C3PDE; dB SPL – decibels sound pressure level; kHz – kilohertz. Phenotyping conducted by Dr Joanne Dorning, Carlos Aguilar and Dr Prashanthini, Shanthakumar, MRC Harwell Institute (unpublished data).

Linkage and mapping studies identified a critical interval on chromosome 5 (Figure 1.12A). Subsequent whole genome sequencing detected a G-to-A substitution at position 12 in the *Clarin2 (Clrn2)* gene (Figure 1.12B), whereby the fourth codon (TGG, encoding a tryptophan (Trp, W) residue in the wild-type sequence) was changed for a premature stop codon (TGA). This nonsense mutation results in a suspected severely truncated mutant peptide (W4STOP), essentially generating a null protein (if translated at all).

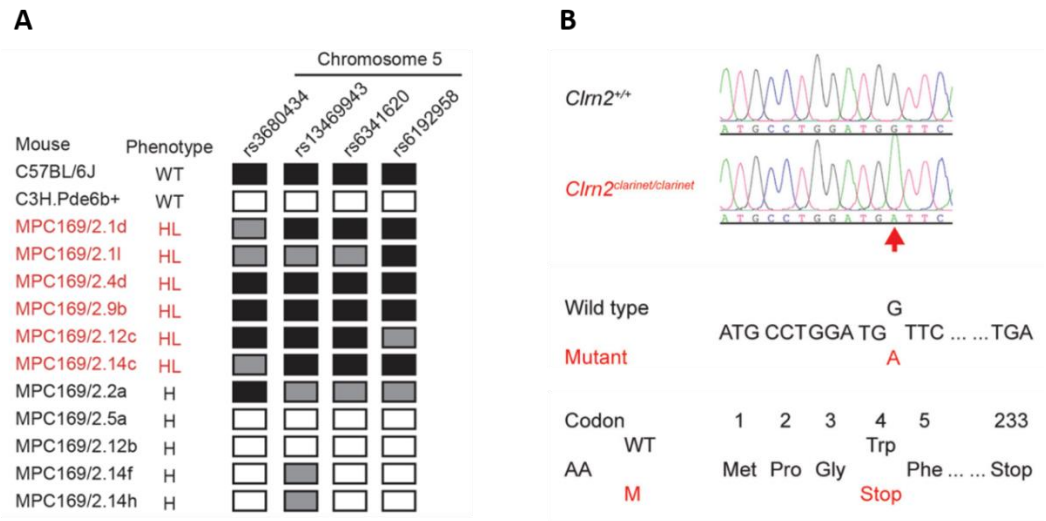

Figure 1.12: **SNP mapping and whole genome sequencing of mouse pedigree MPC169. (A)** DNA from 6 hearing loss (HL) mice and 5 hearing (H) littermate controls were analysed by whole genome SNP mapping. The first column indicates the mouse identification numbers and the second column their respective observed phenotypes. The genotype of each mouse is either homozygous for C57BL/6J (black) or C3H (white) or heterozygous (grey) background strains for each SNP marker. The analysis defined a ~12.25 megabase (Mb) critical interval on chromosome 5 between markers rs6341620 and rs6192958 (Chr5:37258904-49503837). **(B)** Confirmation of the whole genome sequencing identified an ENU-induced coding lesion in exon 1 (ENSMUSE00000385096) of the Clrn2 gene (ENSMUSG00000049530) transcript (ENSMUST00000053250, Ensembl). The lesion consists of a nucleotide transition (c.12G>A) at codon 4, which alters the wild type sequence TGG, encoding a Tryptophan (Trp), to the mutant sequence TGA, encoding a premature stop codon (p.Trp4Stop). Electropherograms show the sequence surrounding Clrn2 nucleotide 12 (indicated by an arrow) in wild type ($Clrn2^{+/+}$) and homozygous (M) ($Clrn2^{clarinet/clarinet}$) clarinet mice. Adapted from Dunbar et al., 2019.

Preliminary tests on progeny of the MPC-169 cohort were undertaken by Dr Philomena Mburu at MRC Harwell Institute. ABR phenotyping at P14 confirmed a very early-onset hearing loss (Figure 1.13A) that is heritable in a recessive manner. Furthermore, to establish the early temporal expression of *Clrn2* in the mouse inner ear, RNA from wild type whole cochleae aged E17.5 – P28 were extracted and processed for qRT-PCR studies (Figure 1.13B). The abundance of *Clrn2* transcripts remained constant between E17.5 and P12, with a sudden ~three-fold increase observed between P12 and P16.

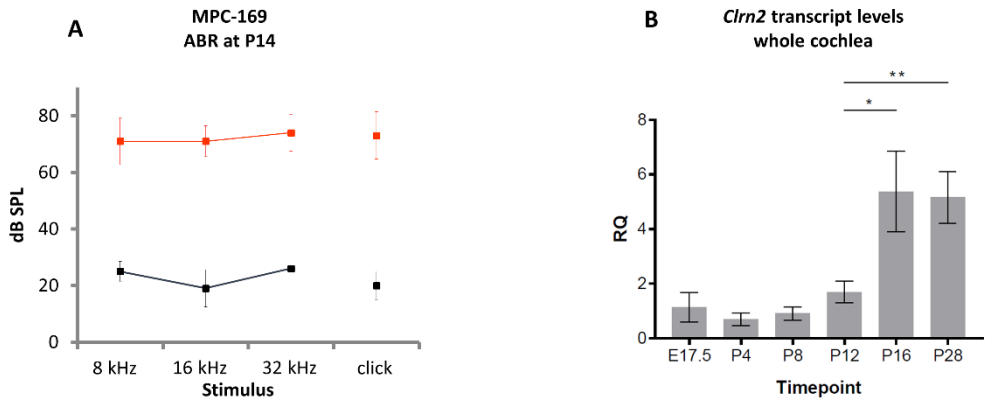

Figure 1.13: Preliminary analysis of MPC-169 and *Clrn2* inner ear transcripts. (A) Averaged ABR recordings from MPC-169 progeny show affected (red squares) mice display elevated thresholds at P14, in comparison to unaffected (black squares) mice, at all frequencies tested. Data shown are mean ± s.d. **(B)** qRT–PCR studies in C57BL/6J wild type mouse whole cochleae at various time points to determine the level of *Clrn2* transcripts, with values calculated relative to expression level at P4. RQ – relative quantification (arbitrary units). For each time point, the data shown are mean ± s.d. of 5 biological replicates. *p < 0.05, **p < 0.01, one-way ANOVA. Both studies were performed by Dr Philomena Mburu at MRC Harwell Institute.

1.8 *Clrn2*

Clrn2 is one of three members of the *Clrn* mammalian gene family (Table 1.4). It has three coding exons amounting to 699 base pairs (bp), with 944 bp including its untranslated regions (UTR) at the N and C termini. The encoded protein, clarin-2, comprises 232 amino acids and has a mass of approximately 25.5 kilodaltons (kDa). The clarins belong to a superfamily of transmembrane (or tetraspan) proteins, which also includes connexins and claudins. Additionally, they are closely related to the TARP (transmembrane AMPA receptor regulatory protein) stargazin (Adato et al., 2002), coded for by the *Cacng2* gene. Stargazer mouse mutants display distinctive head-tossing, seizures and ataxic gait (Noebels et al., 1990).

1.8.1 Usher Syndrome

Usher Syndrome (USH) is a rare autosomal recessive disorder characterised by combined sensorineural deafness and retinitis pigmentosa (RP) (Bonnet and El-Amraoui, 2012). Numerous mutations in proteins involved in stereocilia function have been found to cause USH in various mouse models (Boeda et al., 2002, Mburu et al., 2003, Caberlotto et al., 2011a, Grati et al., 2012, Caberlotto et al., 2011b). While mouse models of USH recapitulate the auditory phenotypes seen in humans, these models fail to faithfully reproduce the vision phenotypes exhibited alongside (Géléoc and El-

Amraoui, 2020). The three USH types are distinguished by phenotypic presentation. Type 3 (USH3) is the least severe form and is characterised by progressive hearing loss, sporadic vestibular dysfunction and variable RP (Mathur and Yang, 2015). In 2002, *Clrn1* was discovered as the causative gene in USH3A (Adato et al., 2002). Since then, *Clrn1* knockout mice have been generated and found to exhibit elevated ABR thresholds at 2-3 weeks, with profound deafness occurring by 4 weeks. *Clrn1* knockouts also exhibit: vestibular dysfunction (circling behaviour); loss of OHC function (absent DPOAEs); and disorganised hair cell bundles (Geng et al., 2009). Additionally, *Clrn1* has been found to be critical for MET channel function and localisation of synaptic components in zebrafish (Ogun and Zallocchi, 2014), as well as regulation of actin filaments at the cellular level (Tian et al., 2009).

Table 1.4: Characteristics of the genes and encoded proteins in the *Clrn* family in the mouse. It is interesting to note that although *Clrn1* has 4 exons, exon 2 is routinely spliced out. Of the four isoforms, *Clrn1-201* is the predominant functional isoform in the sensorineural epithelial cells of the cochlea and retina (Zallocchi et al., 2009), and as such is the isoform included in this table. bp – base pairs; kDa – kilodaltons.

Gene	ENSEMBL ID	Chromosome	mRNA Exons	Transcript length (bp)	Amino acids	Approx. protein weight (kDa)
Clrn1	ENSMUST00000051408.7	3	3	699	232	25.8
Clrn2	ENSMUST00000053250.4	5	3	699	232	25.5
Clrn3	ENSMUST00000053716.7	7	3	681	226	25.6

The glycoprotein clarin-2 is classed as a tetraspan/tetraspanin protein due to its four alpha-helical transmembrane domains (Figure 1.14). While both the N and C terminus are located within the cell, the protein has two extracellular loops. Additionally, the C terminus houses a class II PDZ binding motif, a region critical for protein-protein interactions. Protein homology between human (*Homo sapiens*) clarin-2 and its mouse (*Mus musculus*) orthologue is significant, with both proteins consisting of 232 amino acids and sharing 94% of their peptide sequence (ENSEMBL).

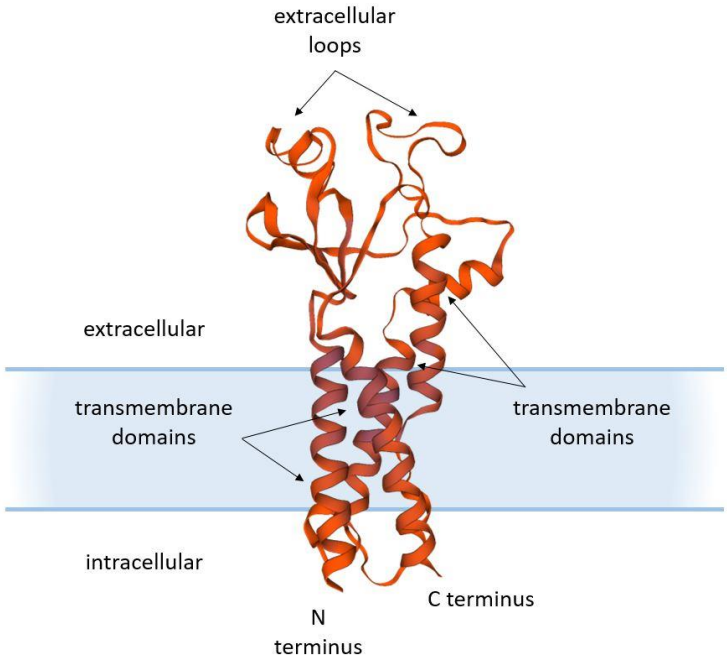

Figure 1.14: Predicted structure of wild type mouse clarin-2 protein. Note the four transmembrane domains displayed as helices. Predicted with the mouse clarin-2 protein sequence (ENSEMBL) using SWISS-MODEL software from the Swiss Institute of Bioinformatics.

At the beginning of my doctoral studies, a PubMed search for *Clrn2* or its encoded protein clarin-2 returned no hits and it had not been, therefore, associated with any disease – auditory or otherwise. This, combined with the preliminary data from the Harwell Ageing Screen implicating *Clrn2* as a deafness-associated gene, makes it an attractive target for studies into the molecular genetics of mammalian deafness and providing insight on the mechanisms involved in hearing.

1.9 PhD hypothesis and research aims

The hypothesis for my PhD project is that *Clrn2* is critical for mammalian hearing. To study this hypothesis, the following aims research aims were established:

- Confirm *Clrn2* as a novel deafness gene
- Fully characterise the auditory phenotype of a *Clrn2* mouse mutant
- Elaborate on the pathobiology associated with *Clrn2*-associated hearing loss

- Identify the expression and localisation of *Clrn2/*clarin-2 in the mouse ear
- Identify and investigate the requirement of *Clrn2/*clarin-2 at different stages of development and maturation of the auditory system.

My investigations will provide insight into the requirement of *Clrn2* for mammalian hearing, and should elaborate on the mechanisms that are critical for the proper function of the auditory system.

Chapter 2: Materials and Methods

2.1 Mice

2.1.1 Husbandry

All animals were housed and maintained in the Mary Lyon Centre, MRC Harwell Institute, under specific opportunistic pathogen-free conditions, in individually ventilated cages adhering to environmental conditions as outlined in the Home Office Code of Practice. All animal studies were licenced by the Home Office under the Animals (Scientific Procedures) Act 1986 Amendment Regulations 2012 (SI 4 2012/3039), UK, and additionally approved by the Institutional Ethical Review Committee. Regulated procedures were performed under Project Licence 17/0006 (and its predecessor, 30/3015). Mice were euthanised by cervical dislocation, a Home Office Schedule 1 method.

2.1.2 Generation of mouse cohorts

2.1.2.1 *Clrn2*^{clarinet}

The *Clrn2*^{w4stop} (*clarinet*) mutant was originally identified as pedigree MPC-169 from the MRC Harwell Institute Ageing Screen, wherein recessive G_3 pedigrees were generated from N-ethyl-N-nitrosourea (ENU)-mutagenised C57BL/6J male mice (Potter et al., 2016).

Briefly, linkage mapping and whole-genome sequencing (Figure 1.12) was undertaken, which identified a lesion within the *Clrn2* gene, causing a Trp4* nonsense mutation in the encoded protein. Carriers were back-crossed to C57BL/6J for 10 generations, and the resulting *clarinet* mice were maintained on this background.

2.1.2.2 Additional *Clrn2* mutants

The *Clrn2*^{del629} and *Clrn2*^{fl} mice were generated by the Molecular and Cellular Biology team at MRC Harwell Institute, using CRISPR/Cas9 methods. Both cohorts were maintained on a C57BL/6N background.

Following Cas9-induced cleavage, DNA is repaired through either non-homologous end joining (NHEJ) or homology directed repair (HDR), the latter of which is far less common. We made use of this imperfect system by exploiting the NHEJ approach to generate the *Clrn2*^{del629} mouse (where *Clrn2*'s second exon is deleted), and the HDR approach to generate the *Clrn2*^{fl} mouse (where a long single-stranded DNA (lssDNA) donor encompassing *loxP* sites flanking *Clrn2*'s second exon is integrated into the gene) (Figure 2.1). For further details on this lssDNA donor approach, see (Codner et al., 2018). Briefly, four single guide RNAs (sgRNAs) (Table 2.1) and a single lssDNA (Table 2.2) donor were co-injected with *Cas9* mRNA into one-cell embryos using a pronuclear injection technique.

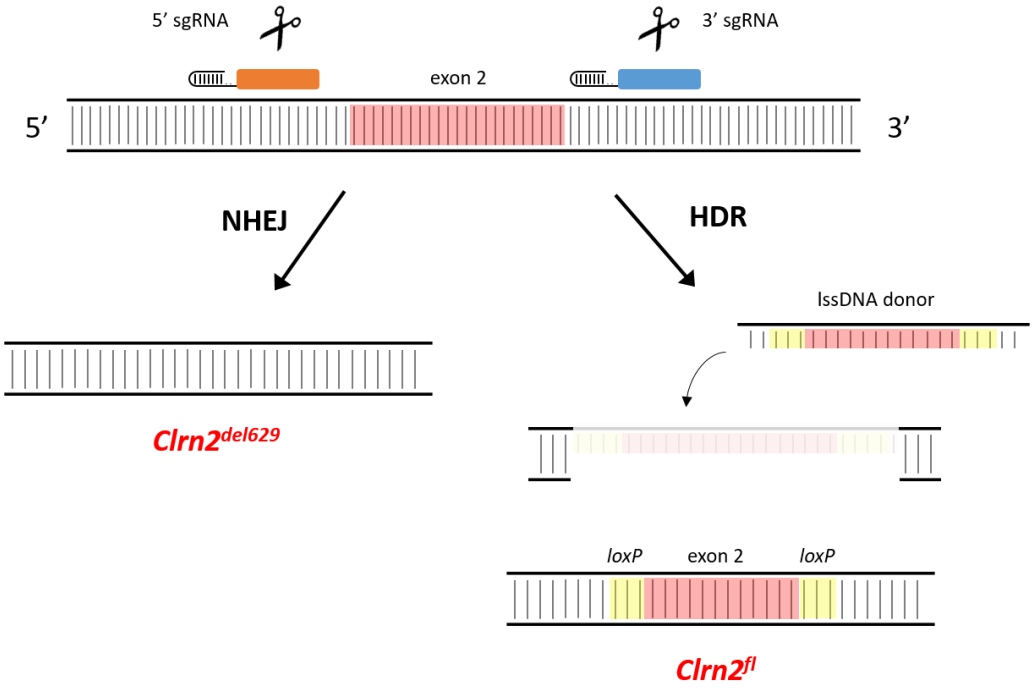

Figure 2.1: Generation of additional *Clrn2* mutants using CRISPR/Cas9 technology and a long single-stranded (lssDNA) donor approach. The Cas9 enzyme induces a double stranded break at the sites targeted by the sgRNA (in this case, either side of *Clrn2*'s second exon). The break is repaired by either non-homologous end joining (NHEJ) or homology directed repair (HDR). In the latter event, a lssDNA donor is integrated into the genome. For details on the sgRNAs and composition of the lssDNA donor, see Table 2.1 and Table 2.2, respectively.

Table 2.1: sgRNAs used in the generation of the *Clrn2*^{fl} mouse. Two sgRNAs were used at each site to increase the chance of cutting. sgRNA – single guide RNA; PAM – protospacer adjacent motif. sgRNAs were designed and generated by the Molecular and Cellular Biology team at MRC Harwell Institute.

Name	Protospacer sequence	PAM sequence
5' Clrn2_1	ACTCTGCCAAGCCAATGCCT	TGG
5' Clrn2_2	AGCCAATGCCTTGGGCTTAT	GGG
3' Clrn2_1	AGGGCACTTTTATTGCAGTC	TGG
3' Clrn2_2	AGACTCAAAAGGAAGCTAAA	GGG

Table 2.2: lssDNA donor sequence (1,049 nucleotides) used in the generation of the additional *Clrn2* mutants. lssDNA – long single-stranded DNA. The lssDNA donor was designed and generated by the Molecular and Cellular Biology team at MRC Harwell Institute.

Feature	Location/Qualifiers
5' homology arm	1..150
5' *loxP*	151..213
Critical region	214..837
Exon 2 (ENSMUSE00000401986)	514..693
3' *loxP*	838..899
3' homology arm	900..1049

Microinjection buffer (MIB; 10 mM Tris–HCl, 0.1 mM EDTA, 100 mM NaCl, pH7.5) was prepared and filtered through a 2 nm filter and autoclaved. Cas9 mRNA, sgRNAs and single-stranded oligodeoxynucleotides (ssODNs) were diluted and mixed in MIB to the working concentrations of 100 ng/µl, 50 ng/µl each and 50 ng/µl, respectively. Injected embryos were re-implanted in CD1 pseudo-pregnant females. Host females were allowed to litter and rear F_0 progeny.

The founders for each line were genotyped, and further genotyping of their progeny confirmed either the deletion of exon 2 (*Clrn2*^{del629}) or integration of the lssDNA donor, resulting in *loxP* sites flanking

exon 2 (*Clrn2*^{fl}). Copy counting by droplet digital (dd) PCR was performed, and no evidence of random donor insertions into the genome was found in either line. Both mutants were maintained on a C57BL/6N background. For further details, see 5.2.3.

2.1.3 **Genotyping**

Pinna biopsies were taken from mice at P14, or tail biopsies were taken at the time of death for younger mice. Tissue was stored at -20°C until required. All genotyping was performed by the GEMS (Genotyping and Mutation detection Screens) core facility at MRC Harwell Institute.

2.1.3.1 *Clrn2*^{clarinet} *cohort*

The Idaho Technology LightScanner system was used to genotype *clarinet* samples for the SNP (G>A) mutation. Following DNA extraction from samples, PCR to amplify regions of interest was performed in the presence of the binding dye LCGreen. Following heating on the LightScanner, florescence emitted by bound LCGreen was monitored. Fluorescence decreases over time until all DNA is melted and all LCGreen is unbound.

The 'unlabelled probe' genotyping technique was used to distinguish samples where scanning may not be sensitive enough. A 3' block oligonucleotide probe (LunaProbe) was designed to sit directly over the SNP, and asymmetric PCR was performed (using unequal primer concentrations to preferentially amplify one strand over the other) which created two products: the full PCR product, and the probe bound to the opposite strand. During the subsequent melting step, the probe melted at a lower temperature. The mutant allele produced the most fluorescence, enabling resolution between wild type, heterozygous and homozygous samples (Figure 2.2).

To genotype *clarinet* mice, the following primer/probe sets were used at 20 ng/µl each in the PCR reaction:

- Clarin2-W4STOP_LS_F: *AAAGATGTCCACTTGCCCAA* (0.1 µl)
- Clarin2-W4STOP_LS_R: *TGAGAAACTGAGTAGAGATGCCA* (0.5 µl)
- Clarin2-W4STOP_LS_PrF: *GGATGATTCAAAAAGGTGTGGTACGG* (0.5 µl)

Each 10 µl PCR reaction contained the three primer/probe sets, 2 µl of template DNA at a 1:10 dilution, 5 µl HotShot master mix, 1 µl of LCGreen and 0.9 µl of ddH_2O. Assays were run on the 7500/7900 Fast Real-Time PCR system (Applied Biosystems) according to following steps:

1. Initial denaturation
    a. 95˚C for 2 min
2. Denaturation and annealing/extension (55 cycles):
    a. 95 ˚C for 30 sec
    b. 60 ˚C for 30 sec
    c. 72 ˚C for 30 sec
3. Hybridisation
    a. 95 ˚C for 30 sec
    b. 25 ˚C for 30 sec
    c. 15 ˚C for 30 sec

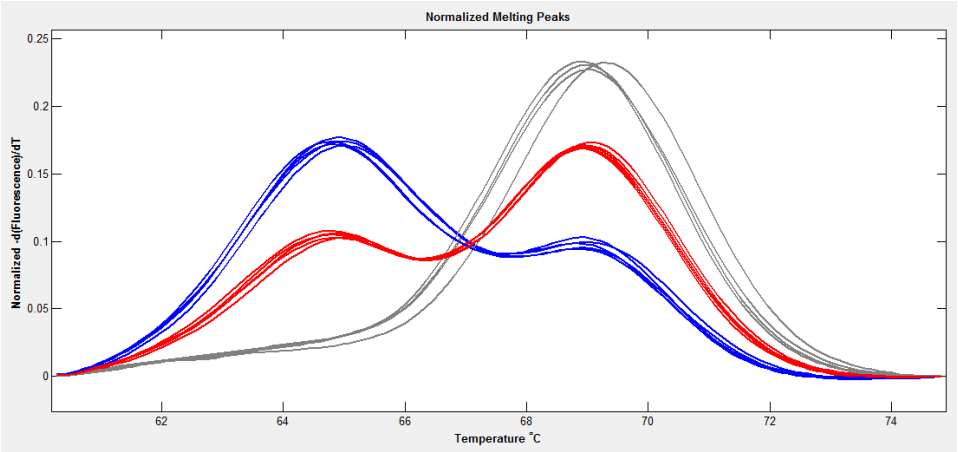

Figure 2.2: Examples of normalised melting peaks for homozygous (grey), heterozygous (red) and wild type (blue) *clarinet* samples, using the LightScanner unlabelled probe genotyping technique. The homozygous mutant sample emits increased fluorescence compared to the wild type. The heterozygous samples are identified by two peaks (one per temperature), produced by the presence of both alleles. Figure provided by the GEMS core facility, MRC Harwell Institute.

2.1.3.2 *Clrn2del629 cohort*

Clrn2^{del629} tissue was genotyped by the GEMS core facility at MRC Harwell Institute, by qPCR copy counting, using both a wild type and mutant assay against a known reference assay: *Dot1l*. This is the standard reference assay employed by the GEMS core facility, used for a number of reasons: the *Dot1l* gene is unaffected by differences in individual samples, and because there are always two copies of *Dot1l*, in the majority of cases (including genotyping of *Clrn2* cohorts) this assay works well as a reference assay. For autosomal genes such as *Clrn2*, the three possible genotypes were distinguished by different copy counts according to the results of the assays (Table 2.3).

Table 2.3: Expected genotyping ratios when using wild type and mutant assays in conjunction.

Clrn2^{fl} **genotype**	**Wild type Assay**	**Mutant Assay**
Wild type	2	0
Heterozygous	1	1
Homozygous mutant	0	2

The wild type assay uses a probe and primers binding to the wild type region (Table 2.4), which is deleted in the mutant. The mutant assay uses a probe and primers that only amplify in the presence of the 629 nucleotide deletion (Table 2.5).

Table 2.4: Oligonucleotide sequences used in the *Clrn2*^{del629} wild type genotyping assay.

Oligo	**5' label**	**Sequence 5' → 3'**	**3' label**	**Oligo Type**
Clrn2-CR-LOA-WT1_F	n/a	GCTCTGGTCAGCATGGGTT	n/a	Wild type Forward
Clrn2-CR-LOA-WT1_PROBE	FAM	TTGCTATTCTCAACATCATTCAGGTCCC	BHQ1	Wild type Probe
Clrn2-CR-LOA-WT1_R	n/a	GGGCCATTGACTGCTCTGTA	n/a	Wild type Reverse

Table 2.5: Oligonucleotide sequences used in the *Clrn2*^{del629} mutant genotyping assay.

Oligo	5' label	Sequence 5' → 3'	3' label	Oligo Type
Clrn2-DEL629-MUT1_F	n/a	AACCCTTCCTGCCACATTCATAT	n/a	Mutant Forward
Clrn2-DEL629-MUT1_PROBE	FAM	TGCCAAGCCATACATAAGGGCAC	BHQ1	Mutant Probe
Clrn2-DEL629-MUT1_R	n/a	GGCAGCTGGCAAGGTTTAC	n/a	Mutant Reverse

DNA was extracted from tissue using the Taqman Sample-to-SNP Kit (Applied Biosystems), and the qPCR run in a 1:10 dilution from the crude preparation. The kit utilises the activity of Taq polymerase, which hybridises to the complementary target sequence, and the FAM reporter dye, which only emits a fluorescent signal when separated from the quencher by Taq polymerase; i.e., when the amplified target sequence is complementary to the probe. This reaction allows allelic discrimination between genotypes.

A x1 qPCR master master mix totalling 10 µl contained 2.5 µl DNA (in the 1:10 dilution), 5 µl Applied Biosystems GTX Taqman master mix, 0.225 µl of 20 µM Dot1l forward and reverse each, 0.2 µl of 5 µM *Dol1l* probe, 0.3 µl FAM assay (5 µM probe and 15 µM each primer) and 1.55 µl ddH_2O. Each sample was run in technical duplicate. The qPCR cycling conditions (run on an Applied Biosystems 7500/7900 Fast Real-Time PCR system or a ThermoFisher QuantStudio 7) were as follows:

1. Initial denaturation
    a. 95˚C for 20 sec
2. Denaturation and annealing/extension (40 cycles):
    a. 95 ˚C for 3 sec
    b. 60 ˚C for 30 sec

Results were analysed using CopyCaller v2.0 (Applied Biosystems) (Figure 2.3), or an in-house equivalent based on this software.

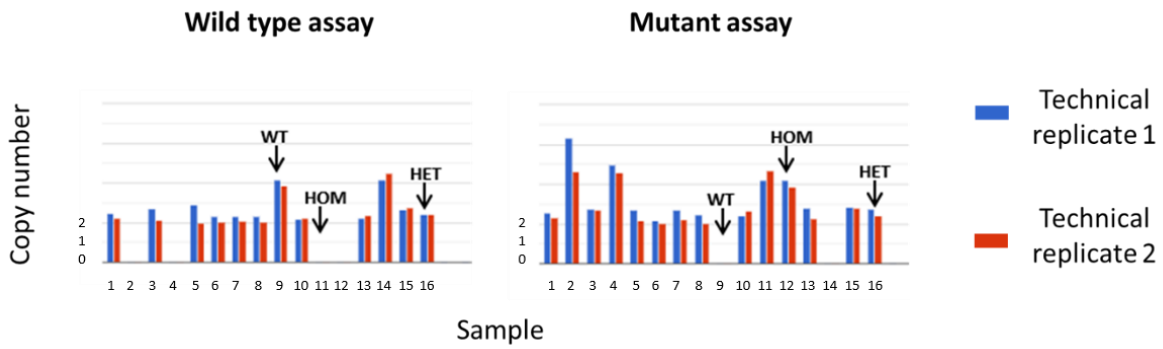

Figure 2.3: Example of copy number counting assay results for the genotyping of *Clrn2*^{del629} samples. For the wild type assay, wild type and homozygous mutant samples are distinguished by a copy count of 2 and 0, respectively. The opposite is true for the mutant assay. Heterozygous samples are distinguished by a copy count of 1. Examples are indicated by arrows. WT – wild type; HET – heterozygous; HOM – homozygous.

Compound heterozygous mutants were genotyped for both the *Clrn2*^{w4stop} (*clarinet*) and *Clrn2*^{del629} alleles.

2.1.3.3 *Clrn2*^{fl}*;Myo15*^{cre} *cohort*

Samples from the *Clrn2*^{fl}*;Myo15*^{cre} cohort were genotyped for both the *Clrn2*^{fl} and *Myco15*^{cre} alleles. To assess the *Clrn2*^{fl} allele, samples were genotyped using qPCR copy counting, with both a wild type and mutant assay against the known *Dot1l* reference assay. The same master mix solution and PCR cycling parameters were used as for the *Clrn2*^{del629} genotyping.

The wild type assay (Table 2.6) assesses binding to the wild type sequence that is deleted in exon 2. The mutant assay (Table 2.7) recognises and verifies the presence of the 5' *loxP* site.

Table 2.6: Oligonucleotide sequences used in the *Clrn2*^{fl} wild type genotyping assay.

Oligo	5' label	Sequence 5' → 3'	3' label	Oligo Type
Clrn2-FLOX-3'-WT1_F	n/a	GCTGGGCTCCCAAGTGTTAG	n/a	Wild type forward
Clrn2-FLOX-3'-WT1_PROBE	FAM	AGGGCACTTTTATTGCAGTCTGGAAGA	BHQ1	Wild type probe
Clrn2-FLOX-3'-WT1_R	n/a	TGGCAGCTGGCAAGGTTT	n/a	Wild type reverse

Table 2.7: Oligonucleotide sequences used in the *Clrn2*^{fl} mutant genotyping assay.

Oligo	5' label	Sequence 5' → 3'	3' label	Oligo Type
CLRN2-FLOX-EM2-MUT1_F	n/a	AACCCTTCCTGCCACATTCATA	n/a	Mutant forward
CLRN2-FLOX-EM2-MUT1_PROBE	FAM	CGTCGAGGCGATCGCATAACTTCG	BHQ1	Mutant probe
CLRN2-FLOX-EM2-MUT1_R	n/a	GTGCCTCACAGTTGACATTACAG	n/a	Mutant reverse

A similar approach using wild type and mutant assays was also used to genotype the *Myo15*^{cre} allele, again alongside the *Dot1l* reference assay. In this instance, universal probe and primers were designed for the *Myo15* sequence. The wild type assay (Table 2.8) assesses binding to the wild type sequence that is deleted in exon 2. The mutant primer bridges the junction designed for the mutant allele (Table 2.9).

Table 2.9Error! Reference source not found.Table 2.8: Oligonucleotide sequences used in the *Myo15*^{cre} wild type genotyping assay.

Oligo	5' label	Sequence 5' → 3'	3' label	Oligo Type
Myo15-CRE-Univ-F	n/a	TCCAAGCAGTGTCTCCAAGTC	n/a	Universal forward
Myo15-CRE-Univ-Probe	FAM	CCTGAACCTGTGACACCTGCCC	BHQ1	Universal probe
Myo15-CRE-MUT-R	n/a	CCTCTTCTTCTTGGGCACCATG	n/a	Mutant reverse

Table 2.9: Oligonucleotide sequences used in the *Myo15*^{cre} mutant genotyping assay.

Oligo	5' label	Sequence 5' → 3'	3' label	Oligo Type
Myo15-CRE-Univ-F	n/a	TCCAAGCAGTGTCTCCAAGTC	n/a	Universal forward
Myo15-CRE-Univ-Probe	FAM	CCTGAACCTGTGACACCTGCCC	BHQ1	Universal probe
Myo15-CRE-MUT-R	n/a	CCTCTTCTTCTTGGGCACCATG	n/a	Mutant reverse

Following genotyping of the two alleles, further genotyping was required to verify recombination between the *loxP* sites. Again, samples were genotyped using qPCR copy counting with both a wild type and mutant assay against *Dot1l*. The wild type assay uses probe, and forward and reverse primers, that bind to the wild type critical region (Table 2.10). The mutant assay is designed to only amplify if Cre recombination has occurred (Table 2.11).

Table 2.10: Oligonucleotide sequences used to verify Cre recombination at *loxP* sites in the wild type assay.

Oligo	5' label	Sequence 5' → 3'	3' label	Oligo Type
CLRN2-CR-LOA-WT1_F	n/a	GCTCTGGTCAGCATGGGTT	n/a	Wild type Forward
CLRN2-CR-LOA-WT1_PROBE	FAM	TTGCTATTCTCAACATCATTCAGGTCCC	BHQ1	Wild type Probe
CLRN2-CR-LOA-WT1_R	n/a	GGGCCATTGACTGCTCTGTA	n/a	Wild type Reverse

Table 2.11: Oligonucleotide sequences used to verify Cre recombination at *loxP* sites in the mutant assay.

Oligo	5' label	Sequence 5' → 3'	3' label	Oligo Type
CRISPRFLOX-POSTCRE_F	n/a	TCGAGGCGATCGCATAACT	n/a	Mutant Forward
CRISPRFLOX-POSTCRE_PROBE	FAM	TTATACGAAGTTATCGCCGGCGGG	BHQ1	Mutant Probe
CRISPRFLOX-POSTCRE_R	n/a	ACTGATGGCGAGCTCAGA	n/a	Mutant Reverse

The same qPCR master mix was used (page 46, again in a X1 dilution), along with the same cycling conditions. Again, each sample was run in technical duplicate and the results were analysed using CopyCaller (or equivalent) software.

2.2 Auditory phenotyping

2.2.1 Click box

Prior to ABR, a preliminary 'click box' test was performed on each mouse. A ~20 kHz tone stimulus at 90 dB SPL was emitted from a click box, held 30 cm above the mouse. A mouse with normal hearing should exhibit a Preyer reflex (an ear flick with or without a startle response), whereas this reflex may be diminished or absent in a hearing-impaired mouse. Responses were graded as follows: 2 – normal response; 1 – reduced response; 0 – no response.

2.2.2 Auditory Brainstem Response (ABR)

Mice were anaesthetised via intraperitoneal injection with a mixture of ketamine hydrochloride (100 mg/kg) and xylazine (10 mg/kg) and placed in a heated chamber (Datesand Ltd.) to maintain body temperature at 37˚C. Once the appropriate level of anaesthesia was reached (indicated by a reflex induced by pinching the feet, but not when applying pressure to the sides of the abdomen), mice were placed on a heated mat (to maintain normal body temperature) inside a sound-attenuated chamber (ETS-Lindgren SD enclosure). Recording electrodes (Grass Telefactor F-E2-12) were placed sub-dermally over the vertex (active), into the right mastoid (reference), and left mastoid (ground). To prevent eyes drying out, 'artificial tears' (Viscotears®, Novartis) were applied to the surface of each eye.

Acoustic stimuli were delivered to the right ear at a distance of 10 mm via a free field transducer (ES1 Tucker Davis Technology (TDT), Alachua, FL), controlled by TDT SigGen/BioSig software, using TDT system III hardware. The transducer output was calibrated using a ¼ inch measuring microphone (7016 ACO-Pacific, Belmont, CA) and SigCal software (TDT). The normalised output was periodically checked using a Brüel and Kjær PULSE system with a type 4939 ¼ inch measuring microphone attached to a high frequency 3110 processing module. For calibration, the microphone capsule was placed inside a pistonphone calibrator (Aco-Pacific type 511e), which produced a 1 kHz tone at 94 dB SPL, which was analysed again using the Brüel and Kjær PULSE hardware and software. ABR responses were collected,

amplified and averaged using TDT system III hardware and BioSig software (Tucker Davis Technology (TDT), Alachua, FL). Tone-burst stimuli totalled 7 millisecond (ms) duration including rise/fall gating using a 1 ms Cos2 filter. Stimuli were first played at 90dB SPL followed by decreasing steps of 5-10 dB SPL (as is standard practice within the laboratory) until a threshold was determined visually by the absence of replicable response peaks. Stimuli consisted of 0.1 ms broadband clicks of alternating polarity presented at a rate of 21/sec for a total of 300 averages and tone-burst stimuli at 8 kHz, 16 kHz and 32 kHz, presented at a rate of 42.5/sec for a maximum of 1000 repetitions. All ABRs were performed blind to genotype to ensure thresholds were obtained in an unbiased manner.

Mice were injected subcutaneously with 0.1 ml atipamezole (Antisedan^{TM}, 5mg/ml) to aid recovery unless they were aged P16, in which case the procedure was terminal and mice were culled by cervical dislocation. Mice were observed until fully recovered and returned to the home cage. All traces were re-scored by another user to ensure accuracy of the threshold called.

2.2.3 **Distortion Product Otoacoustic Emissions**

TDT system 3 hardware and BioSig (Tucker Davis Technology) software was used to examine DPOAEs. An ER10B+ low noise probe microphone (Etymotic Research) was used to measure the DPOAE near the tympanic membrane. Tone stimuli were presented via separate MF1 (Tucker Davis Technology) speakers, with f1 and f2 at a ratio of f2/f1 = 1.2 (L1=65dB SPL, L2=55dB SPL). DPOAE frequencies, calculated using the f2/f1 ratio of 1.2, were recorded from 6 to 32 kHz at 2 kHz intervals.

Mice were anaesthetised via intraperitoneal injection with a mixture of ketamine hydrochloride (100 mg/kg), xylazine (10 mg/kg) and acepromazine (2.5 mg/kg) and placed in a heated chamber (Datesand Ltd.). Once surgical anaesthesia was reached, indicated by the absence of both a pedal reflex and response to pressure applied to the abdomen, the pinna was removed to gain sufficient access to the auditory canal. A pipette tip containing the DPOAE probe assembly was carefully placed into the outer ear, and the mouse was placed on a heated mat inside a sound-attenuated chamber (ETS-Lindgren). In-ear calibration was performed before each test. The f1 and f2 tones were presented continuously

and a fast-Fourier transform was performed on the averaged response of 356 epochs (each ~21ms). The level of the 2f1-f2 DPOAE response was recorded and the noise floor calculated by averaging the ten frequency bins either side of the 2f1-f2 frequency. Mice were culled via cervical dislocation following the procedure.

2.3 Vestibular phenotyping

Various tests were carried out to assess vestibular phenotype. All tests were carried out according to protocols established by (Hardisty-Hughes et al., 2010).

2.3.1 Behavioural studies

The platform and contact righting tests were carried out by Dr Pranav Patni and Professor Aziz El-Amraoui at the Institut Pasteur in Paris, France.

2.3.1.1 *Platform test*

In the platform test, animals were placed on a small platform (7 × 7 cm, at a height of 29 cm) and the amount time spent on the platform was recorded over a period of 2 min.

2.3.1.2 *Contact righting test*

The contact righting test consisted of placing a mouse in a closed transparent tube and assessing its ability to successfully regain a standing position upon a 180° rotation of the tube (score 1) or fail (score 0).

2.3.2 Swim test

Swim tests were carried out at both MRC Harwell Institute and the Institute Pasteur in Paris, France (here by Dr Pranav Patni and Professor Aziz El-Amraoui).

Mice were transported to the phenotyping room and allowed to acclimatise in the home cage for 15 min. Meanwhile, a generic baby bath was filled with Millipore water at 22-26°C and a depth of at least 15 cm. The water temperature was continuously monitored and modified as necessary. The mouse was carefully lowered into the water and observed for a maximum of 1 min to obtain a swim test score, then removed from the water and gently dried before being returned to the home cage. Mice

were immediately rescued from the water if they displayed any signs of distress. Mice were scored on their swimming ability based on the criteria in Table 2.12.

Table 2.12: Score and corresponding behaviour of mice undergoing the swim test. Adapted from Hardisty-Hughes et al., 2010.

Score	Behaviour
0	Swims normally. Mouse body is elongated and the tail propels in a flagella-like motion
1	Irregular swimming. Includes: swimming in a circle, swimming on side (left/right preference should be noted), swimming in an unbalanced manner (tail is raised and beats in an unstable manner)
2	Immobile floating. May follow or precede brief disorientation
3	Underwater tumbling. Mouse is unable to maintain a balanced body position and continuously tumbles

2.4 Electroretinogram recordings

Electroretinogram (ERG) experiments were performed by Dr Pranav Patni and Professor Aziz El-Amraoui at the Institut Pasteur in Paris, France.

Prior to measuring ERGs, mice were kept in the dark to adapt to darkness overnight (Michel et al., 2017). Mice were anesthetised with a mixture of ketamine (80 mg/kg, Axience) and xylazine (8 mg/kg, Axience), and placed on a warming pad to maintain body temperature. Their pupils were dilated with tropicamide (Mydriaticum; Théa, Clermont-Ferrand) and phenylephrine (Neosynephrine; Europhta, Monaco). The cornea was locally anesthetised with oxybuprocaine chlorhydrate (Théa, Clermont-Ferrand). Both upper and lower eyelids were retracted to keep the eyes open and bulging. Retinal responses were recorded with a gold-loop electrode brought into contact with the cornea through a layer of lubrithal (Dechra), with needle electrodes placed in the cheeks and back used as reference and ground electrodes respectively (Yang et al., 2009). The light stimuli were provided by an LED in a Ganzfeld stimulator (SIEM Bio-médicale). Responses were amplified and filtered (1 Hz-low and 300 Hz-high cut-off filters) with a one-channel DC-/AC amplifier. One level of stimulus intensity (8 cd.s/m^2) was used for scotopic ERG recordings. Each of the responses obtained was averaged over five flash stimulations. Photopic cone ERGs were recorded in a rod-suppressing background light of 20 cd.s/m^2, after a 5-minute adaptation period. An 8 cd.s/m^2 level of stimulus intensity was used for the light-

adapted ERGs. Each cone photopic ERG response presented was averaged over ten consecutive flashes.

2.5 Electrophysiological studies

Electrophysiological experiments were carried out by Dr Laura Corns, Dr Stuart Johnson, Anna Underhill, Adam Carlton and Professor Walter Marcotti at the University of Sheffield. Animals used for electrophysiological studies were licensed by the Home Office under the Animals (Scientific Procedures) Act 1986 and were approved by the University of Sheffield Ethical Review Committee. All recordings were performed at room temperature (RT).

Recordings were made from apical-coil OHCs and IHCs of *clarinet* and control mice aged P6-22, with a number of basal-coil OHCs also investigated at P7-8. Apical-coil OHCs from *Clrn2*$^{fl/fl}$*;Myo15*$^{cre/+}$ and control mice were studied in acutely dissected cochlea at P7 and P10.

Cochleae were harvested and dissected in normal extracellular solution (in mM): 135 NaCl, 5.8 KCl, 1.3 $CaCl_2$, 0.9 $MgCl_2$, 0.7 NaH_2PO_4, 5.6 D-glucose, 10 HEPES-NaOH. Sodium pyruvate (2 mM), MEM amino acids solution (50X, without l-Glutamine) and MEM vitamins solution (100X) were added from concentrates (Fisher Scientific). The pH was adjusted to 7.5 (308 mosmol/kg). The dissected cochleae were transferred to a microscope chamber, immobilised with a nylon mesh (Corns et al., 2016) and continuously perfused with a peristaltic pump using the above extracellular solution. The organs of Corti were viewed using an upright microscope (Leica DMLMF; Nikon) with Nomarski optics (x60 or x63 objectives).

2.5.1 Mechano-electrical transduction current recordings

MET currents were elicited by stimulating the hair bundles of OHCs and IHCs using a fluid jet from a pipette (tip diameter 8–10 µm) driven by a piezoelectric disc (Corns et al., 2014). The pipette tip of the fluid jet was positioned near to the bundles to elicit a maximal MET current. Mechanical stimuli were

applied as 50 Hz sinusoids (filtered at 0.25 kHz, 8-pole Bessel) with driving voltages of ± 40 V. MET currents were recorded with a patch pipette solution containing (in mM): 106 Cs-glutamate, 20 CsCl, 3 $MgCl_2$, 1 EGTA-CsOH, 5 Na_2ATP, 0.3 Na_2GTP, 5 HEPES-CsOH, 10 sodium phosphocreatine (pH 7.3). Membrane potentials were corrected for the liquid junction potential (LJP) of −11 mV, measured between electrode and bath solutions.

2.5.2 Patch clamp recordings

Patch clamp recordings were performed using an Optopatch (Cairn Research Ltd) amplifier. Patch pipettes were made from soda glass capillaries with a typical resistance in the extracellular solution of 2–3 MΩ. In order to reduce the electrode capacitance, patch electrodes were coated with surf wax (Mr Zoggs SexWax). Basolateral membrane recordings were performed using an intracellular solution containing (in mM): 131 KCl, 3 $MgCl_2$, 1 EGTA-KOH, 5 Na_2ATP, 5 HEPES-KOH, 10 Na_2-phosphocreatine (pH 7.3; osmolality ~296 mmol/kg). Data acquisition was controlled by pClamp software using Digidata 1440A boards (Molecular Devices). Recordings were low-pass filtered at 2.5 kHz (8-pole Bessel), sampled at 5 kHz and stored on computer for off-line analysis (Origin: OriginLab). Membrane potentials in voltage clamp were corrected for the voltage drop across the uncompensated residual series resistance and for a LJP of −4 mV measured between electrode and bath solutions.

2.6 Scanning electron microscopy

Mice were culled and inner ears were dissected and fixed in 2.5% glutaraldehyde (TAAB Laboratories Equipment Ltd.) in 0.1M phosphate buffer (PB) (Sigma-Aldrich) overnight at 4˚C. After 3x 15 min washes in PB, ears older than P12 were decalcified in 4.5% ethylenediaminetetraacetic acid (EDTA) in PB for a predetermined amount of time depending on the age of the tissue, usually between 6 and 12 hrs at 4˚C. After further washing to remove EDTA, ears were stored in PB until sub-dissection using a stereo microscope (Zeiss) to expose the organ of Corti. Ears were then 'OTO-processed' at RT in a Leica EM TP automated tissue processor (Leica Microsystems). This consisted of a one hour incubation of 1% osmium tetroxide (OsO_4) (TAAB Laboratories Equipment Ltd.) in 0.1M sodium cacodylate (Sigma-

Aldrich), a 30 minute incubation of 1% thiocarbohydrazide (Sigma-Aldrich) in ddH_2O, and another one hour incubation of OsO_4. Each step was separated by 7x 5 minute ddH_2O washes.

This was followed with dehydrations in ethanol (Fisher Scientific) of increasing concentrations of 25%, 40%, 60%, 80%, 95% and x2 100% for 45 min each at 4˚C, and storage in acetone (VWR Chemicals), also at 4˚C. Ears were then critical point dried using a critical point drier (CPD 300, Leica Microsystems) using liquid CO_2. Ears were mounted on G301F 12.5 mm specimen stubs using Agar 12 mm adhesive carbon tabs and silver paint (all Agar Scientific), then sputter coated (Q150R S, Quorum Technologies) with two coats of platinum. Samples were imaged using a JSM 6010LV Scanning Electron Microscope (JEOL).

Overview micrographs of the sensory epithelium were taken at magnifications ranging between x1,500 and x2,500 magnification. For closer examination of stereocilia architecture, micrographs of several hair cells were taken at magnifications ranging between x5,000 and x8,500. Micrographs of individual OHCs and IHCs were taken x15,000 magnification. Hair cell morphology along the sensory epithelium was assessed by taking representative images of apical, mid and basal turns of the cochlea. It should be noted that there are numerous factors to consider when comparing SEM micrographs, such as distance of sample from microscope, height of sample, angle of sample in relation to microscope. Although dimensions of stereocilia can be estimated through calculations using the formulae in Figure 2.4, a true measure cannot be obtained.

Measurements of individual stereocilia were taken by Carlos Aguilar, MRC Harwell Institute. A minimum of three ears (one ear per mouse) were analysed for each genotype per time point. Duplicate images of the middle turn (180° to 360°) of the cochlea were taken, with a 5° tilt between them to account for uncertainty due to plane rotation. OHC and IHC bundles were imaged at x15,000 and x8,000 magnification respectively, both at a constant working distance of 20 µm. Three different bundles were analysed per animal, with up to nine different measurements taken per bundle: three measurements from the tallest row stereocilia, three from the middle row and three from the shortest

row (if present). IHC and OHC measurements were obtained using ImageJ software (NIH) and corrected using a pseudo-eucentric tilting approach (adapted from (Bariani et al., 2005)). A single measure, x_1 (the length of the tallest row of one stereocilium), was taken on a first micrograph and measured again (x_2) on the corresponding 5°-tilted duplicate micrograph. Perpendicular countermeasures (y_1 and y_2) to x_1 and x_2 were also taken in every instance. Later, countermeasures were fed into the first equation (ζ) (Figure 2.4A), to estimate uncertainty. Every pair of tilted-coupled measures (x_1 and x_2) was then fed into the second equation (ξ) (Figure 2.4B), along with the calculated uncertainty estimate (ζ), thus obtaining a close approximation of the true measure of the stereocilia heights.

A

$$\zeta = \frac{(\Delta y)\cos\triangle\varphi + (2y_1\,(y_1 - \Delta y)\,/d)\sin\Delta\varphi}{(1 + y_1\,(y_1 - \Delta y)\,d^2\sin\Delta\varphi) + (\Delta y/d)\cos(2\Delta\varphi)}$$

B

$$\xi = \frac{2d - 2\zeta\cos\Delta\varphi}{d/x_1 + d/x_2}$$

Figure 2.4: Equations used to measure stereocilia heights from scanning electron micrographs. ζ = uncertainty estimate; $y_{1,2}$ = perpendicular countermeasures to measures $x_{1,2}$; Δy = arithmetic difference of countermeasures y_1 and y_2; Δϕ = tilting angle (5°); d = working distance (20 µM); $x_{1,2}$ = tilted paired-measures of structure of interest; ξ = estimate of true size of structure of interest (µm).

2.7 Immunohistochemistry

2.7.1 Immunolabelling of whole-mounts

2.7.1.1 *clarin-2 labelling*

P5 and P8 wild type C57BL/6J mice were culled, and their inner ears dissected and fixed in 4% paraformaldehyde (PFA) in phosphate buffered saline (PBS) overnight at 4°C. After 3x 15 min washes in PBS, ears were sub-dissected in PBS using a stereo microscope (Zeiss) to expose the organ of Corti. Samples were then permeabilised using 0.1% Triton X-100 in PBS for 10 min at RT, then blocked for 1 hour at RT. Samples were incubated with primary antibodies diluted in block overnight at 4°C or RT.

To enable detection, samples were incubated with fluorophore-conjugated secondary antibodies, and Alexa Fluor® phalloidin 488 (Thermo Fisher Scientific, 1:200) to stain stereocilia, for 2 hours at RT, then stained with DAPI (Thermo Fisher Scientific, 1:2500) for 5 min at RT to detect nuclei. 3x 15 min PBS with 0.1% Tween (PBST) washes followed each antibody step. Samples were mounted onto slides in SlowFade® Gold (Life Technologies) and visualised using a Zeiss LSM 700 (inverted) or 710 (upright) fluorescence confocal microscope. Primary antibodies used and their dilutions are as follows: 'bespoke-made' Rb61 rabbit anti-clarin-2 (Covalab, 1:50 and 1:100), rabbit anti-clarin-2 (Abcam (ab122790), 1:50). Secondary antibody: donkey anti-rabbit 568 (Thermo Fisher Scientific, 1:200). Block: 5% donkey serum in PBST or 1% bovine serum albumin (BSA) (New England BioLabs) in PBST.

A summary of antibodies and conditions used for clarin-2 labelling can be found in Table 2.13.

Table 2.13: Summary of antibodies and conditions employed in clarin-2 immunofluorescence experiments on cochlear tissues.

Anti-clarin-2 Primary antibody	Primary antibody species origin	Primary antibody dilutions	Age of tissue (postnatal day)	Type of tissue	Secondary antibodies
Bespoke-made (Covalab)	Rabbit	1:50, 1:100	8	Whole mount	donkey anti-rabbit 568
Abcam (ab122790)	Rabbit	1:50	5, 8	Whole mount	donkey anti-rabbit 568
Atlas (HPA042407)	Rabbit	1:1000	30	Vibratome-cut section	donkey anti-rabbit 488, 568

2.7.1.2 *Ribbon synapse labelling*

Mice were culled, and inner ears were dissected and fixed in 4% PFA in PBS for 1 hour at room temperature (RT). After 3x 5 min washes in PBS, ears were sub-dissected to expose the sensory epithelium then permeabilised using 0.1% Triton X-100 in PBS for 10 min at RT. Samples were blocked in 5% donkey serum (Sigma) for 1 hour at RT and immuno-labelled with primary antibodies diluted in block overnight at 37°C. To enable detection, samples were incubated with fluorophore-conjugated secondary antibodies for 1 hour at 37°C, then stained with DAPI (1:2500, Thermo Fisher Scientific) for

5 min at RT. 3x 15 min PBST washes followed each antibody step. Samples were mounted onto slides in SlowFade® Gold (Life Technologies) and visualised using a Zeiss LSM 700 or 710 fluorescence confocal microscope with the x63 objective. Primary antibodies used and their dilutions were as follows: rabbit anti-Ribeye (Synaptic Systems; 1:200); mouse anti-GluR2 (Millipore; 1:200). Secondary antibodies: Alexa Fluor® donkey anti-rabbit 568 (Invitrogen; 1:200); Alexa Fluor® donkey anti-mouse 488 (Invitrogen; 1:500).

2.7.2 Immunolabelling of vibratome sections

P30 +/- 1 day wild type mice were culled, and ears dissected and fixed in 4% PFA overnight at 4°C, or for 1 hour at RT. After 3x 15 min washes in PBS, ears were decalcified in 10% EDTA in PBS for 1 day at 4°C. After another 3x 15 min PBS washes, ears were submerged in 4% agarose (Sigma-Aldrich) in PBS and mounted in a BEEM capsule (Agar Scientific). Mid-modiolar sections of 200 µm each were cut on a VT1000S vibratome (Leica). Samples were immediately incubated with primary antibody diluted in block overnight at 4˚C. The following day, sections were washed in PBS as before and incubated with secondary antibody and Texas Red-X Phalloidin (Invitrogen), to stain stereocilia, in blocking solution for 2 hours at RT. After washing, sections were stained with DAPI (1:2500) for 5 min at RT before 3x 5 min washes in PBS. Sections were transferred to a PBS-filled fluorodish (Thermo Fisher Scientific) and imaged free-floating using a Zeiss LSM 700 or 710 fluorescence confocal microscope, with the x20 objective. Primary antibody: rabbit anti-Clrn2 (Atlas Antibodies (HPA042407), 1:1000). Secondary antibodies: donkey anti-rabbit 488 and 568 (Thermo Fisher Scientific, 1:1000). Block: 4% Triton-X, 8% goat serum, 1 g BSA, 50 ml X1 PHEM buffer (X4 stock solution was made with 60 mM PIPES (Melford Biolaboratories), 25 mM HEPES (Biobasic UK), 10 mM EGTA (VWR Chemicals) and 4 mM $MgSO_4 \cdot 7H_20$ (Sigma-Aldrich) in 500 ml ddH_2O).

2.8 Histology

To assess gross morphology of cochleae, mice were culled, heads were removed, skinned and bisected sagittally. Half-heads were then fixed in 10% neutral buffered formaldehyde (Surgipath), generally overnight at RT. Subsequent steps were performed by the Histology team at MRC Harwell Institute.

Samples were decalcified for 3 days in Kristenson decalcifying solution (DFB) (Pioneer Research Chemicals Ltd.). Samples were then dehydrated in increasing concentrations of ethanol, cleared using xylene and saturated with molten paraffin wax under vacuum, all in either a Shandon Pathcentre™ or Excelsior™ AS Tissue Processor (both Thermo Fisher Scientific). Samples were embedded in block of paraffin wax, and after solidifying, 5 µm sagittal sections were cut in the mid-modiolar plane using the Finesse™ ME+ microtome (Thermo Fisher Scientific) and collected onto charged slides. Sections were stained with haematoxylin and eosin (H&E) and imaged using a Zeiss light microscope.

2.9 RT-PCR

To allow analysis of the *Clrn2* ^{del629} allele, whole cochlear ducts were collected from P21 (+/− 1 day) *Clrn2* $^{+/+}$, *Clrn2* $^{+/del629}$ and *Clrn2* $^{del629/del629}$ littermate mice (2 animals (4 ducts in total) per genotype), and stored in RNA *later* Stabilising Solution (Invitrogen) at −20°C until processed. Total RNA was extracted using TRIzol Reagent (Invitrogen) and used as template for cDNA generation using the High Capacity cDNA Reverse Transcription kit (Applied Biosystems). Subsequent PCR amplification was undertaken utilising *Clrn2*-specific primers: *Clrn2-Exon 1 Forward (CTCATTAGTATGCCTGGATGG)*/*Clrn2-Exon 3 Reverse (TTAGTCTTGATTTCTGGAAGGG),* and then electrophoresed on a 2% agarose gel. β-actin was used as an internal control. PCR products were excised and purified using the GENECLEAN II kit (MP Biomedical) and subjected to Sanger sequencing (Oxford Source Bioscience). Data were analysed using the SeqMan Pro (DNASTAR) software.

2.10 **Statistical analyses**

All statistical analyses were carried out using GraphPad Prism. Before statistical testing, distribution of data was assessed to determine whether a parametric or nonparametric statistical test should subsequently be used. A one-way ANOVA or two-way ANOVA, to assess one or two factors respectively, was performed to compare data between more than two groups. A threshold of $p<0.05$ was used to determine if differences were statistically significant. On graphs, statistical significance is represented as follows: * = $p<0.05$, ** = $p<0.01$, *** = $p<0.001$ unless otherwise stated.

Unless stated, all results are shown as mean ± standard error of the mean (s.e.m).

Chapter 3: Characterisation of the *clarinet* mouse model

3.1 Introduction

The Harwell Ageing Screen employed a forward genetics approach to identify novel genes associated with disease phenotypes. Briefly, the chemical mutagen *n*-ethyl-*n*-nitrosourea (ENU) was used to randomly induce mutations in the spermatogonial stem cells of male mice. Once these mice regained fertility they were used to father recessive G_3 pedigrees, which were recurrently phenotyped throughout their lives to identify phenodeviants. A subset of mice from the MPC-169 cohort were found to have elevated ABR thresholds at 3 months of age (Figure 1.11), pertaining to profound hearing loss. Genome-wide single nucleotide polymorphism (SNP) mapping studies of affected (deaf) and unaffected (hearing) G_3 mice were undertaken, revealing a ~12 megabase (Mb) critical interval on chromosome 5. Subsequent whole genome sequencing of an affected mouse (Figure 1.12) identified a homozygous mutation within the critical interval consisting of a non-synonymous G-to-A transition at nucleotide 12 of the *Clrn2* gene (ENSMUST00000053250). The *Clrn2* mutation leads to a p.Trp4* (tryptophan-to-stop) nonsense mutation in the encoded clarin-2 protein, resulting in a severely truncated protein (W4STOP).

The mouse line, renamed *clarinet,* underwent preliminary phenotyping conducted by Dr Philomena Mburu at the MRC Harwell Institute (Figure 1.13A). Due to the breeding strategy used in the Harwell Ageing Screen, mice in these studies had a mixed genetic background (C3H.Pde6b+ / C57BL/6J). In order to minimise biological variation due to background effects, *clarinet* mice were backcrossed to C57BL/6J for ten generations. Once congenic on C57BL/6J, these mice were used to investigate the *clarinet* mutation.

To confirm that the $Clrn2^{clainet}$ allele is responsible for causing the hearing loss phenotype, a second allele was generated using CRISPR/Cas9-mediated genome editing in zygotes. Briefly, two guide RNAs

were designed to direct Cas9 to specifically cleave the DNA strands either side of the region that encodes the second exon of *Clrn2*. Then through the innate process of non-homologous end joining (NHEJ), the DNA repair machinery joins the two cleaved ends resulting in deletion of the intervening sequence – in this case the sequence encompassing the second exon of *Clrn2*.

The resulting *Clrn2*^{del629} mutant was crossed with the *Clrn2*^{clarinet} mutant, and complementation testing was performed to confirm *Clrn2* is the gene responsible for the phenotype observed in the MPC-169 mutant (3.2.2). Following this, the *clarinet* mouse underwent auditory phenotyping (3.2.4). Histological and ultrastructural analyses of the cochlea were undertaken to evaluate gross morphology and hair cell architecture, respectively (3.2.6 and **Error! Reference source not found.**). V estibular phenotyping and electroretinography (ERG) studies were undertaken by Prof Aziz El-Amraoui and colleagues at the Institut Pasteur to determine whether, like its paralogue *Clrn1, Clrn2* is an Usher gene (3.2.8 and 3.2.9). Immunolabelling of the synaptic components in cochleae was undertaken to assess synaptic function (3.2.10).

Electrophysiology studies were conducted by Prof Walter Marcotti and his team at the University of Sheffield to assess electrophysiological properties of *clarinet* hair cells (3.2.11).

Together, these investigations demonstrate a critical role for *Clrn2* in the mammalian auditory system, and have additionally elaborated upon the genetic mechanisms involved in the maintenance of hair cell stereocilia.

3.2 Results

3.2.1 Generation of a second *Clrn2* (*Clrn2*^{del629}) allele

ENU mutagenesis causes many random mutations throughout the genome. Indeed, it is likely that multiple ENU-induced mutations may be present within a mapped critical region. As such, it is common to confirm that the correct lesion has been identified as causing the observed recessive

phenotype through complementation testing. This is particularly important when the candidate lesion is identified in a novel gene (i.e. a gene that has not previously been associated with the phenotype).

This is done by generating 'compound heterozygotes', which are mice that carry two different mutations for the same gene; one in each copy of the gene. If the phenotype matches that of a homozygous mutant (which carries two copies of a gene each with the same mutation) then it can be assumed that the homozygous gene mutation is responsible for the phenotype observed. As the *clarinet* mutation (referred to in this section as *Clrn2*^{w4stop} for clarity) was generated through a mutagenesis screen, a complementation test was needed to confirm that this *Clrn2* lesion is the genetic cause of the hearing loss exhibited by these mice, and that it is not caused by an as-yet-unidentified second ENU-induced lesion within the candidate interval. Unfortunately, a *Clrn2* knockout mouse was not available from any of the mutant mouse repositories and so we embarked on designing and generating one at Harwell.

The wild type, full-length *Clrn2* transcript of 699 bp (excluding UTRs) consists of three coding exons, which are all in the same frame. The first, second and third exons encode the four transmembrane domains present in the encoded protein, which comprises 232 amino acids. Using CRISPR/Cas9 genome editing, the Molecular and Cellular Biology team at MRC Harwell Institute deleted *Clrn2*'s

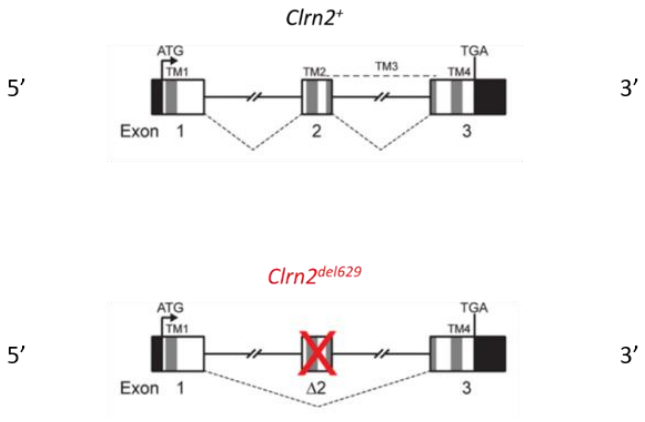

Figure 3.1: Schematic representation of mouse wild type (*Clrn2*$^{+}$) and *Clrn2*^{del629} mutant allele, generated through CRISPR/Cas9 genome editing. The *del629* mutation results in the deletion of *Clrn2*'s second of three exons (illustrated by a red cross). The wild type *Clrn2* gene spans approximately 10.4 kb of genomic DNA on chromosome 5. The start (ATG) and stop (TGA) codons, and untranslated regions, are represented in black. Genomic regions encoding the four transmembrane (TM) domains are shown in grey. 5' and 3' ends are indicated.

second exon via the NHEJ mechanism. This likely generated a splice mutant in which exon 1 reads straight into exon 3 (Figure 3.1).

In order to confirm the *Clrn2*^{del629} mutation results in this deletion of the second exon, transcripts from wild type, heterozygous and homozygous mice from the *Clrn2*^{del629} cohort were investigated. Briefly, cochlear ducts from P21 animals were harvested, RNA was extracted from which cDNA was generated, which was then amplified. Oligonucleotide primers were designed to exon 1 (forward primer) and exon 3 (reverse primer) (see 2.9 for details), the primer combination determined to produce the strongest signal when run on a gel during optimisation stages (data not shown). The amplification products for samples from animals of the three genotypes were then run out, adjacently, on a gel and imaged. Excised bands were then purified and sent for Sanger sequencing to confirm the *Clrn2* RNA transcripts present in cochlear ducts from each genotype.

Gel imaging of the RT-PCR products showed transcript expression in *Clrn2*$^{+/+}$ cochlear ducts as expected, with PCR products consisting of 699 bp (the size of the full-length wild type fragment) (Figure 3.2A). The homozygous *Clrn2*$^{del629/del629}$ product produced a band of 519 bp; the size expected following the removal of exon 2, leaving only exons 1 and 3 to be transcribed. The heterozygous *Clrn2*$^{del629/+}$ product demonstrated transcription of both wild type and homozygous transcripts (Figure 3.2A).

Sanger sequencing of excised purified products revealed that wild type *Clrn2* transcript, as expected, was expressed as normal with boundaries for exon 1: exon 2 and exon 2: exon 3 observed in the resulting chromatogram (Figure 3.2B). Sequencing of the homozygous band confirmed the absence of exon 2, leaving exon 1 and exon 3 spliced together in-frame (Figure 3.2C).

These analyses have confirmed the deletion of exon 2 in *Clrn2*$^{del629/del629}$ mice. As *Clrn2*'s second exon encodes the protein's second and part of its third transmembrane domain, it can be postulated that the novel isoform encoded by the *Clrn2*^{del629} mutant allele lacks these key domains. Despite this, portions of the proteins, such as the first and fourth transmembrane domains, would potentially remain unchanged.

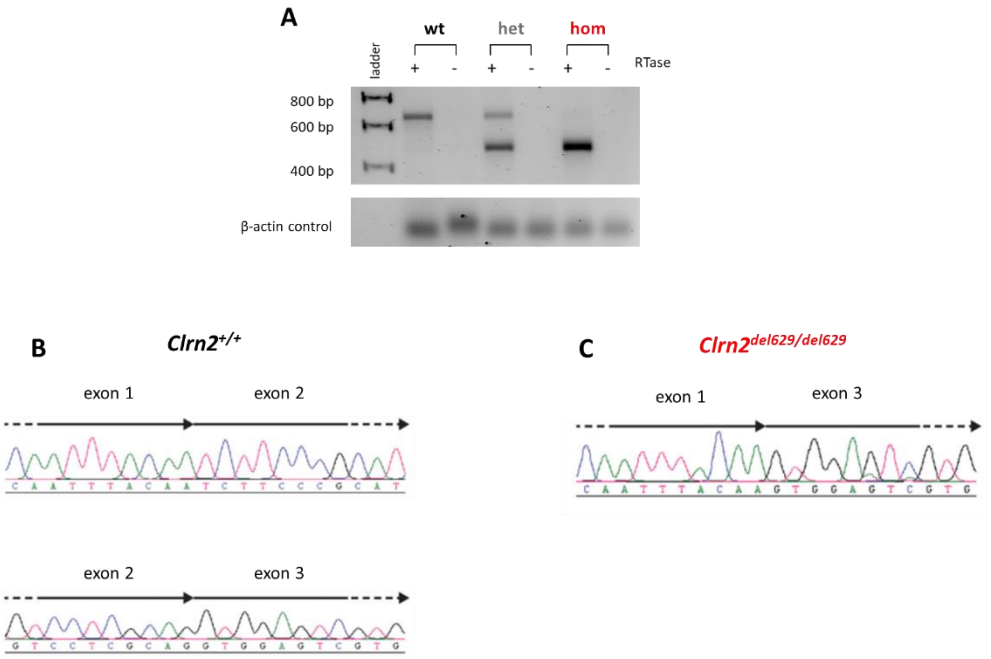

Figure 3.2: RT-PCR analysis and sequencing of P21 *Clrn2*^{del629} cochlear ducts. (A) RT-PCR products of samples pooled by genotype electrophoresed on a 2% agarose gel alongside controls processed without reverse transcriptase (RTase) for each genotype. Wild type and homozygous ducts express full length (699 base pairs (bp)) and partial (minus exon 2; 519 bp) *Clrn2* transcripts, respectively. **(B)** Sanger sequencing confirmed the presence of wild type cDNA product, with the expected exon 1: exon 2 and exon 2: exon 3 boundaries observed. **(C)** Deletion of *Clrn2*'s second exon results in the splicing of exon 1 straight into exon 3. A – adenine (green), C – cytosine (blue), G – guanine (black), T – thymine (pink).

3.2.2 **Complementation test**

Now that there was a second, likely loss-of-function, *Clrn2* mouse mutant available, I was able to undertake a complementation test. This was achieved by intercrossing *Clrn2*$^{w4stop/+}$ mice with *Clrn2*$^{del629/+}$ mice and phenotyping the offspring, which included compound heterozygous (*Clrn2*$^{w4stop/del629}$) mice.

Mice from the *Clrn2*$^{w4stop/del629}$ cohort underwent auditory phenotyping at P21. ABR thresholds of compound heterozygotes were significantly higher than those exhibited by wild type and mice

heterozygous for each allele, at all frequencies tested (Figure 3.3A) (mean click threshold 91 ± 3 dB SPL, compared to 20 ± 3 dB SPL for wild type (*Clrn2*$^{+/+}$) controls).

Clrn2$^{w4stop/del629}$ mice also underwent terminal DPOAE testing at P28 to assess OHC function. This revealed the compound heterozygotes had a decreased response compared to two control groups (Figure 3.3B), which was more pronounced at the lower and mid frequencies tested. At all frequencies, the response from compound heterozygote mice resides within or just above the noise floor. Responses were significantly different between experimental mice and both control groups at 8 and 16 kHz (frequencies of 2 x f1-f2), but only between experimental mice and wild type mice at 32 kHz. These results indicate that by P28, compound heterozygote mice have a loss of OHC function.

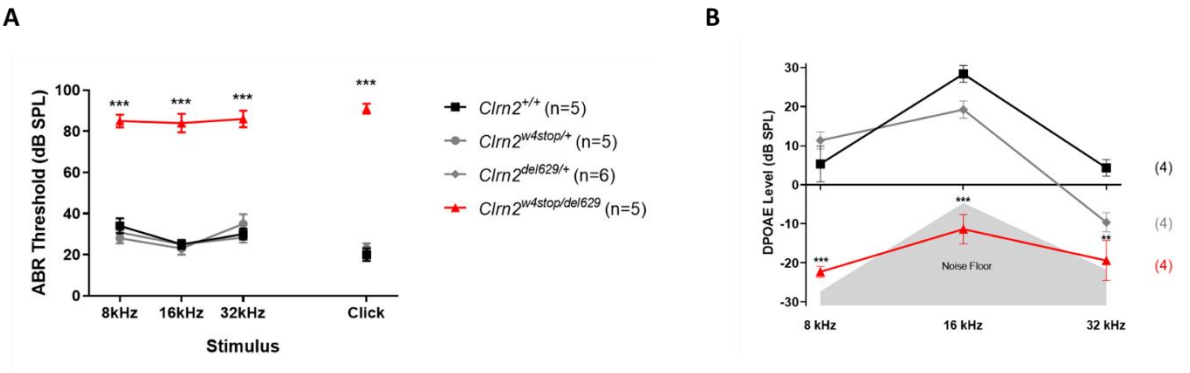

Figure 3.3: ***Clrn2*$^{w4stop/del629}$ mice exhibit profound auditory dysfunction. (A)** Averaged auditory brainstem response (ABR) thresholds of *Clrn2*$^{+/+}$ (black squares), *Clrn2*$^{w4stop/+}$ (grey circles), *Clrn2*$^{del629/+}$ (grey diamonds) and *Clrn2*$^{w4stop/del629}$ (red triangles) at P21 ± 1 day. Compound heterozygote mice show a severe hearing loss across all frequencies, compared to all control groups. **(B) *Clrn2*$^{w4stop/del629}$ mice produce decreased DPOAE responses.** Averaged Distortion Product Otoacoustic Emission (DPOAE) responses at P28 ± 1 day from compound heterozygote mice (red triangles) are reduced compared to wild type (black squares) and heterozygous (grey diamonds) controls, generally lying within the noise floor (shaded grey region). n numbers for mice of each genotype are displayed alongside the key. Data shown are mean ± s.e.m., **p<0.01, ***p<0.001, one-way ANOVA.

Following the terminal DPOAE at P28, cochleae were harvested and prepared for scanning electron microscopy (SEM) to assess inner ear structure. While the gross structure of the sensory epithelium was similar to *Clrn2*$^{del629/+}$ controls, the number of OHC stereocilia rows differed, interestingly, between compound heterozygous samples (Figure 3.4A). Of the three images (obtained from two separate animals), two images showed bundles exhibiting three rows and one image showed bundles exhibiting two (indicated by red arrowheads). IHCs, however, appeared unaffected (Figure 3.4B). Failure of the second (*Clrn2*^{del629}) allele to rescue the phenotype confirms the original hypothesis that the *clarinet* allele (*Clrn2*^{w4stop}) is indeed the mutation underlying the recessive hearing loss phenotype identified in pedigree MPC-169. Furthermore, the ultrastructural analyses of the cochlear sensory epithelia appears to indicate a subtle abnormality in the architecture of the auditory hair bundle of compound heterozygote mice, which warrants further investigation.

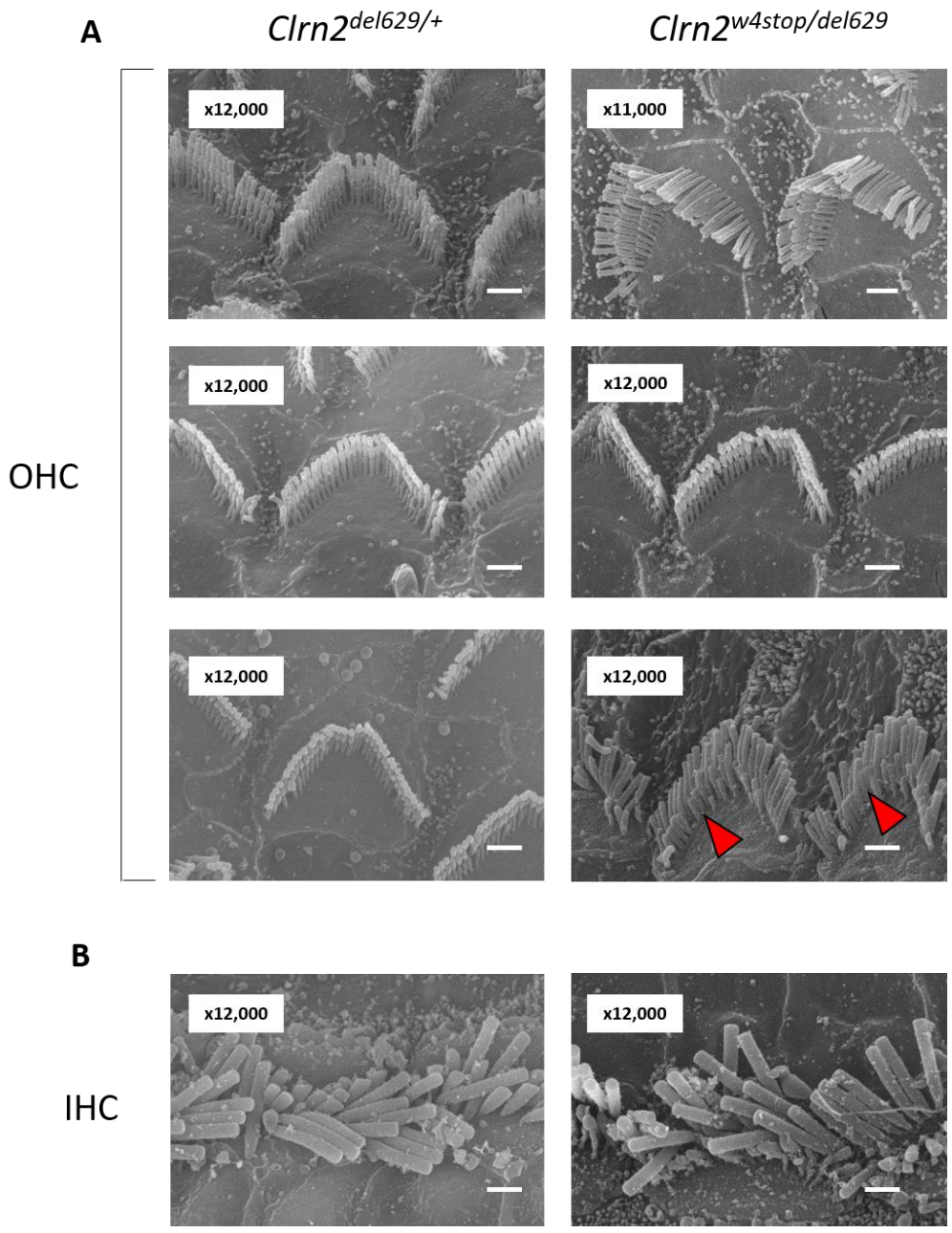

Figure 3.4: Scanning electron micrographs from control *Clrn2*$^{del629/+}$ and compound heterozygous *Clrn2*$^{w4stop/del629}$ cochleae at P28. (A) While control OHCs (n = 3, 3 animals) exhibit normal hair bundle architecture, compound heterozygote OHCs (n = 3, 2 animals) exhibit either two (indicated by red arrowheads) or three rows of stereocilia. (B) IHCs from compound heterozygotes (n = 1) resemble those of controls (n = 3, 3 animals). Magnification is indicated on each individual micrograph. Scale –1 µm.

Detailed auditory and ultrastructural characterisation of the *Clrn2*^{del629} mutant is described in 5.2.1 and 5.2.2.

3.2.3 *clarinet* viability and body weight

The *clarinet* model, generated through ENU-induced spontaneous mutation, is the first known *Clrn2* mouse mutant. Therefore, in order to ascertain whether the *Clrn2*^{clarinet} mutation affects viability, the number of wild type, heterozygous and homozygous animals were counted at weaning (where ear biopsies were also taken for genotyping). Across ten litters sampled, the three genotypes were present in line with standard Mendelian ratios (1:2:1 for wild type, heterozygotes and homozygotes respectively) (X^2 = 0.019, 2 degrees of freedom; p=0.99), with an average number of 5.3 pups per litter (Figure 3.5). These counts indicate that the *Clrn2*^{clarinet} mutation is not embryonic nor neonatal lethal.

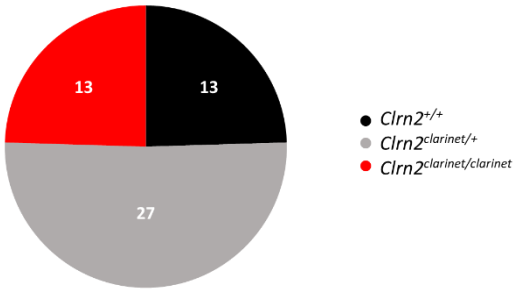

Figure 3.5: The *Clrn2*^{clarinet} mutation does not affect viability. Expected Mendelian Ratios (1:2:1) are exhibited across 10 clarinet litters (53 pups total), with counts conducted at weaning age. n numbers for each genotype are indicated in the corresponding section on the pie chart.

Additionally, in order to determine whether the *Clrn2*^{clarinet} mutation affects postnatal growth, body weights were measured at P16, P21, P28 and P42. This showed that body weights were similar across genotypes at P16 in both female and male mutant mice (Figure 3.6). The significantly lower mean body weight of the wild type females might be due to variable body weight between individuals during morphological development at this juvenile time point.

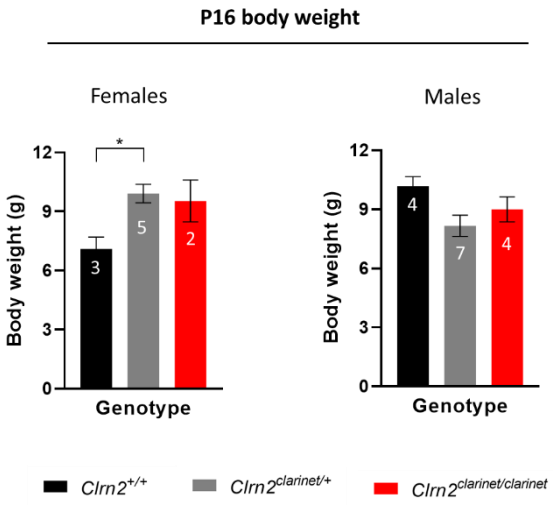

Figure 3.6: Averaged body weights at P16 suggest that the *Clrn2*^{clarinet} mutation does not affect body weight at this time point, in either males or females. In fact, the only significant difference detected was between wild type and heterozygous females. n numbers for each group are indicated on the corresponding bar. Data shown are mean ± s.e.m. *p=0.03, one-way ANOVA.

Moreover, body weights recorded at P21, P28 and P42 showed that both female and male *clarinet* mutant mice gained weight with a similar trajectory to their wild type and heterozygous littermates (Figure 3.7). It should be noted that due to splitting the females and males for this analysis, n numbers in some groups were too small for reliable statistical testing.

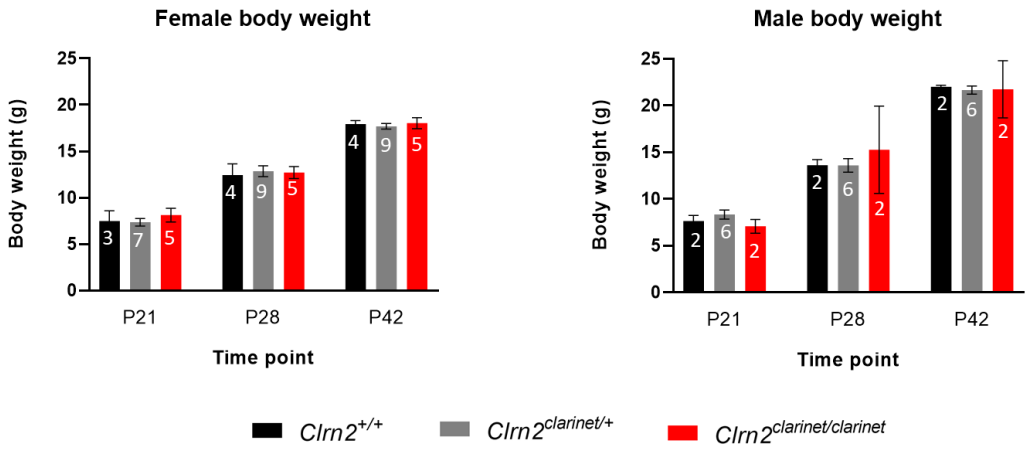

Figure 3.7: Genotype-averaged body weights suggest that the *Clrn2*^{clarinet} mutation does not significantly affect body weight gain during development, in either males or females. n numbers for each group are indicated on the corresponding bar. Data shown are mean ± s.e.m.

Taken together, these body weight data indicate that the *clarinet* mutation does not affect the ability of homozygous mutant mice to thrive.

3.2.4 *clarinet* ABR time course

To establish the onset and progression of auditory dysfunction in *clarinet* mice, ABR measures were recorded at several time points. Phenotyping was first performed at P16, a few days after the onset of hearing in mice (~P12, (Kros et al., 1998)) to establish the onset of hearing loss. Due to the low body weight (translating to poorer predicted recovery rates) of P16 mice undergoing this procedure, the P16 ABR was terminal and tissue was collected for ultrastructural analysis immediately after death. The remaining ABRs were recorded using a second cohort of mice and were conducted partially longitudinally at P21, P28 and P42. In addition to a click stimulus, ABR hearing thresholds were determined in response to 8 kHz, 16 kHz, 32 kHz frequency stimuli to assess hearing function along the cochlear spiral (apical to basal regions, respectively). Briefly, stimuli were presented first at 90 dB SPL and subsequently at decreasing intensities, with 5 dB SPL intervals, until a recognisable ABR waveform could not be distinguished. Mice that did not produce detectable waveforms at 90 dB SPL were assigned a threshold of 95 dB SPL.

ABR recordings undertaken at P16 demonstrate that even just after the onset of hearing, *Clrn2*$^{clarinet/clarinet}$ homozygous mutants display elevated hearing thresholds (e.g. with a mean click threshold of 64 ± 15 dB SPL) at all frequencies tested, in comparison to their *Clrn2*$^{+/+}$ wild type and *Clrn2*$^{clarinet/+}$ heterozygous littermate controls (e.g. with a mean click threshold of 29 ± 6 dB SPL and 25 ± 8 dB SPL, respectively) (Figure 3.8A).

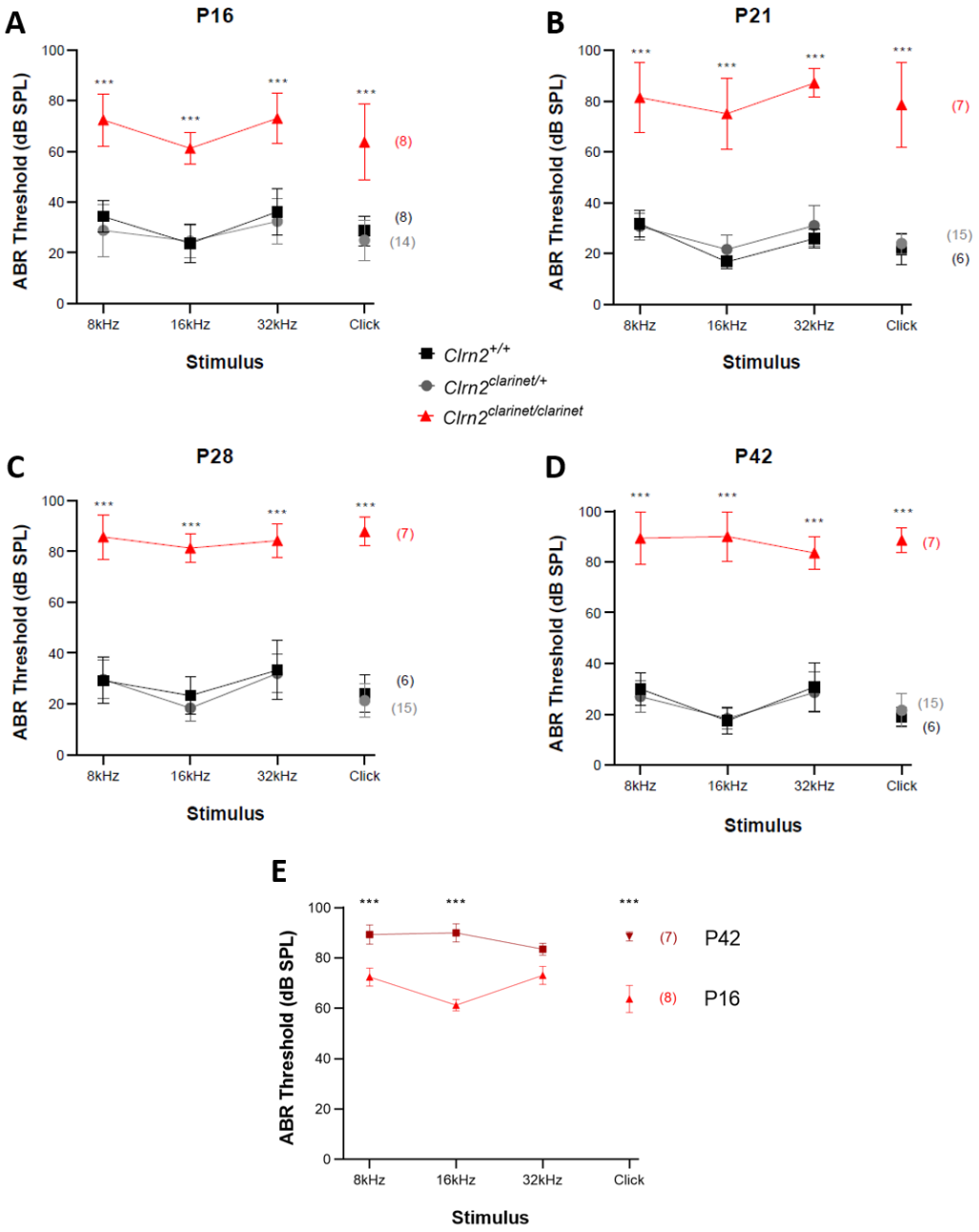

Figure 3.8: **Averaged ABR thresholds in *clarinet* mice demonstrate an early-onset, progressive hearing loss at all frequencies tested.** While *Clrn2*$^{+/+}$ and *Clrn2*$^{clarinet/+}$ thresholds are within the expected range, *Clrn2*$^{clarinet/clarinet}$ thresholds are initially elevated at P16 **(A)** and progress to profound by P42 **(D)**. n numbers for each genotype are indicated to the right of each graph. **(E)** *Clrn2*$^{clarinet/clarinet}$ mice display progressive hearing loss from P16 (lighter red) to P42 (darker red). Data shown are mean ± s.e.m., **p<0.01, ***p<0.001, two-way ANOVA.

Hearing thresholds were closely monitored over the next weeks to assess for any progression in hearing impairment, with recordings taken at P21 (Figure 3.8B), P28 (Figure 3.8C) and P42 (Figure 3.8D). Hearing thresholds of *Clrn2*$^{clarinet/clarinet}$ mice increased over this time course at all frequencies tested, demonstrating a progressive nature of hearing loss. By P42 (Figure 3.8D), the hearing loss was profound (e.g. with a mean click threshold of 84 ± 6 dB SPL) compared to that of controls, which remained constant over the time course. As the hearing thresholds of *Clrn2*$^{clarinet/+}$ heterozygous mice mimic those of wild types across all ages and frequencies, it can be deduced that one wild type copy of the *Clrn2* gene is sufficient for auditory function. Additionally, separating data measured from male and female *clarinet* mice at P42 confirms there is no significant sexual dimorphism in relation to auditory function (Figure 3.9, p>0.3 across all frequencies). As such, sex was not considered a variable during further characterisation of the *clarinet* model.

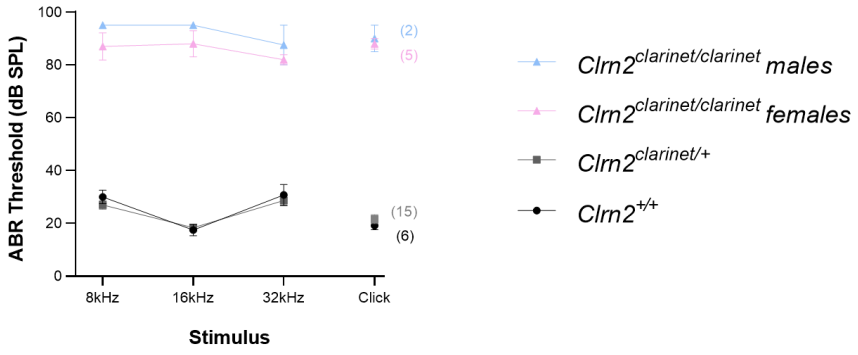

Figure 3.9: **Averaged ABR thresholds for P21 *clarinet* mice with mutants separated by sex.** n numbers for genotypes are indicated in the key. Data shown are mean ± s.e.m., unpaired t-test.

Representative ABR waveforms from mice of each genotype demonstrate how the hearing thresholds were estimated in response to the click stimulus at P21 (Figure 3.10). In these examples, thresholds were called at 25 dB SPL for both *Clrn2*$^{+/+}$ and *Clrn2*$^{clarinet/+}$ mice (black arrows), whereas an ABR threshold could not be detected at or below 90 dB SPL in the *Clrn2*$^{clarinet/clarinet}$ mouse (waveforms for ≤70 dB SPL are shown).

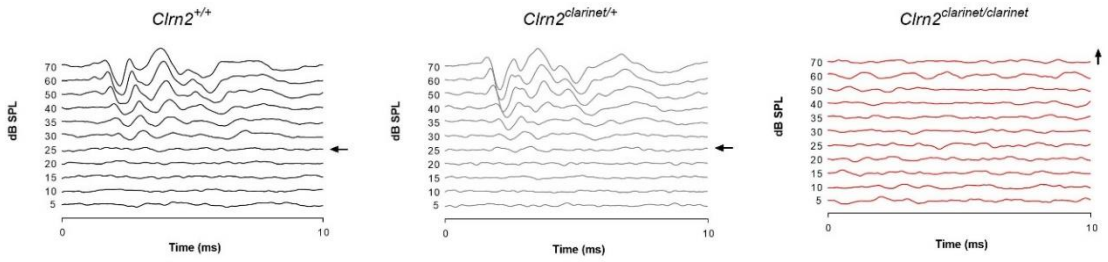

Figure 3.10: **Representative ABR waveforms recorded in response to a click stimulus for P21 wild type, heterozygous and homozygous *clarinet* mice.** Black arrows indicate the intensity stimulus at which the threshold was called (25 dB SPL for both wild type and heterozygous animals). The threshold called for the clarinet mutant was above 70 dB SPL (the upper intensity limit for these graphs), and as such is represented by an upturned arrow (for any mouse that did not produce a recognisable ABR trace at 90 dB SPL, the threshold was called at 95 dB SPL). ms – milliseconds.

3.2.5 *clarinet* distortion product otoacoustic emission testing

To assess OHC-specific function, *clarinet* mice underwent terminal DPOAE testing at P42. This demonstrates that *Clrn2*$^{clarinet/clarinet}$ mice emit reduced otoacoustic emissions when compared with their wild type and heterozygous littermate controls (Figure 3.11). This confirms that at least part of the auditory dysfunction in *clarinet* mice is caused by the dysfunction of OHCs. The difference between mutants and controls is not as obvious compared to that previously observed between the compound heterozygous mice (*Clrn2*$^{w4stop/del629}$) and their controls (Figure 3.3B).

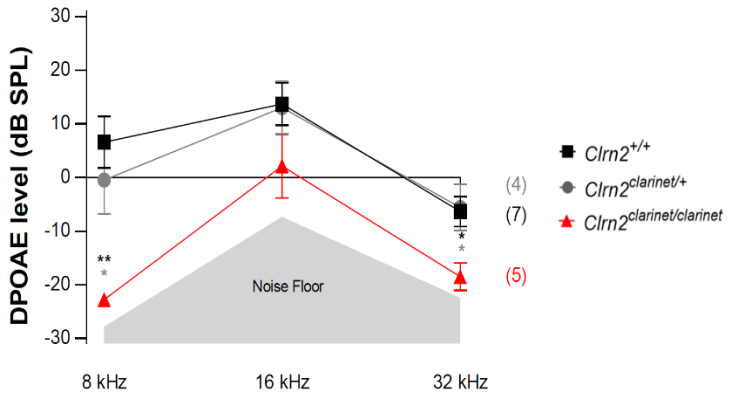

Figure 3.11: *Clrn2*$^{clarinet/clarinet}$ mice fail to produce normal DPOAE responses. While above the noise floor, homozygous mutants at P42 produce decreased DPOAE responses in comparison to controls, who respond within the expected range. n number for each genotype is indicated next to the graph. Data shown are mean ± s.d. *p<0.05, **p<0.01, one-way ANOVA.

However, a direct comparison cannot be made between the two mutants due to the difference in ages that DPOAE recordings were obtained; *Clrn2*^{clarinet} *mutants* were approximately 2 weeks older than compound heterozygotes.

Extensive auditory phenotyping of *clarinet* mice including a partially longitudinal ABR time course and DPOAE testing indicates that the *Clrn2*^{clarinet} mutation causes early-onset, severe and progressive hearing loss in mice. Exact p values for all statistical tests performed on auditory phenotyping data can be found in Table 3.1.

Table 3.1: Exact p values for ABR and DPOAE phenotyping of *clarinet* animals.

				Stimulus			
Figure	**Comparison**	**Test**	**Age**	**8 kHz**	**16 kHz**	**32 kHz**	**Click**
3.3A	*Clrn2*$^{clarinet/del629}$ vs *Clrn2*$^{+/+}$	ABR	P21	1.48×10^{-8}	5.02×10^{-10}	2.14×10^{-8}	2.92×10^{-12}
3.8A	*Clrn2*$^{clarinet/clarinet}$ vs *Clrn2*$^{+/+}$	ABR	P16	3.65×10^{-8}	3.13×10^{-11}	4.45×10^{-8}	4.32×10^{-7}
3.8B	*Clrn2*$^{clarinet/clarinet}$ vs *Clrn2*$^{+/+}$	ABR	P21	2.70×10^{-11}	1.17×10^{-12}	3.90×10^{-14}	2.50×10^{-11}
3.8C	*Clrn2*$^{clarinet/clarinet}$ vs *Clrn2*$^{+/+}$	ABR	P18	9.67×10^{-12}	3.60×10^{-14}	1.44×10^{-10}	3.90×10^{-14}
3.8D	*Clrn2*$^{clarinet/clarinet}$ vs *Clrn2*$^{+/+}$	ABR	P42	3.96×10^{-13}	3.30×10^{-14}	2.45×10^{-11}	3.30×10^{-14}
3.11	*Clrn2*$^{clarinet/clarinet}$ vs *Clrn2*$^{+/+}$	DPOAE	P28	1.12×10^{-3}	2.27×10^{-1}	3.40×10^{-2}	-

3.2.6 **Gross cochlear morphology**

To first investigate the possibility of any gross abnormalities within the cochlea that could be involved with the hearing loss exhibited, histological assessment was carried out on *clarinet* cochlear sections.

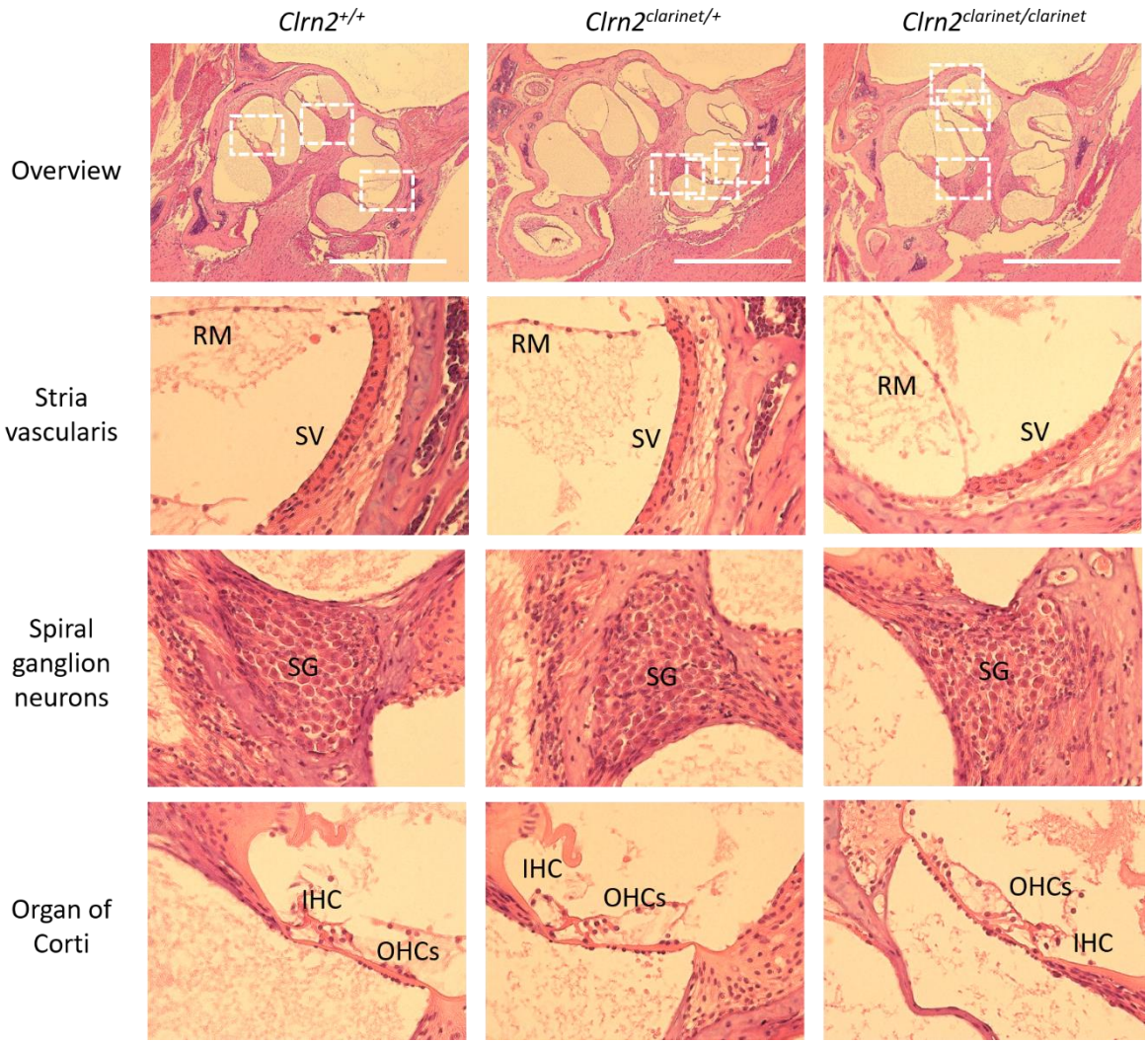

Figure 3.12: **Histological assessment of P20 *Clrn2*$^{clarinet/clarinet}$ mid-modiolar cochlear sections indicates normal gross morphology.** There appear to be no overt detectable differences between the homozygous mice (n=1) and the *Clrn2*$^{+/+}$ (n=1) and *Clrn2*$^{clarinet/+}$ (n=3) control groups (overview, x10 magnification top panel). The second, third and fourth panel rows include higher-magnification images (x40) of each overview. RM – Reissner's membrane; SV – stria vascularis; SG – spiral ganglion; IHC – inner hair cell; OHCs – outer hair cells. Scale – approx. 1 mm.

Paraffin-embedded mid-modiolar P20 sections were stained with H&E and examined under a light microscope. *Clrn2*$^{clarinet/clarinet}$ mice cochleae appeared morphologically normal, with no obvious

cochlear defects, when compared with both wild type and heterozygous aged-matched controls (Figure 3.12). The spiral ganglion neurons, the stria vascularis and the organ of Corti of *Clrn2*$^{clarinet/clarinet}$ homozygous mutants were indistinguishable from both control groups at all turns of the cochlea. This histological assessment suggests that any cause of hearing loss was not detectable through gross observation.

3.2.7 Changes in *clarinet* hair bundle structure over time

Considering the previously reported disordered architecture of auditory hair bundles in *Clrn1* mutants (Geller et al., 2009, Geng et al., 2009, Geng et al., 2012, Dulon et al., 2018) and the possible subtle bundle phenotype observed in the *Clrn2* compound heterozygotes (Figure 3.4), scanning electron microscopy was employed to investigate *clarinet* hair cell stereocilia bundle development and maturation. Briefly, fixed cochleae were sub-dissected to reveal the sensory epithelium before undergoing osmium tetroxide and thiocarbohydrazide treatment, which further fixed the sample and increased its electrical conductivity. Samples were then dried and sputter coated before imaging under a vacuum using a scanning electron microscope.

To closely analyse the hair bundle structure of the *clarinet* mutant, P16 *clarinet* cochleae were first examined due to the elevated ABR thresholds exhibited by mutants at this early time point. Overview images of the *clarinet* cochlear sensory epithelium at this time point showed patterning comparable to that of both wild type and heterozygous controls (Figure 3.13, top panel), with three uniform rows of OHCs and one row of IHCs below. No loss of hair cells, or damage to hair cells or supporting cells was noted at any region along the basilar membrane. This, combined with ABR recordings showing hearing loss constant across all frequencies, suggested that the *Clrn2*^{clarinet} mutation does not preferentially affect any particular region in the cochlea. As such, representative images only, taken along various points along the sensory epithelium, are included in Figure 3.13.

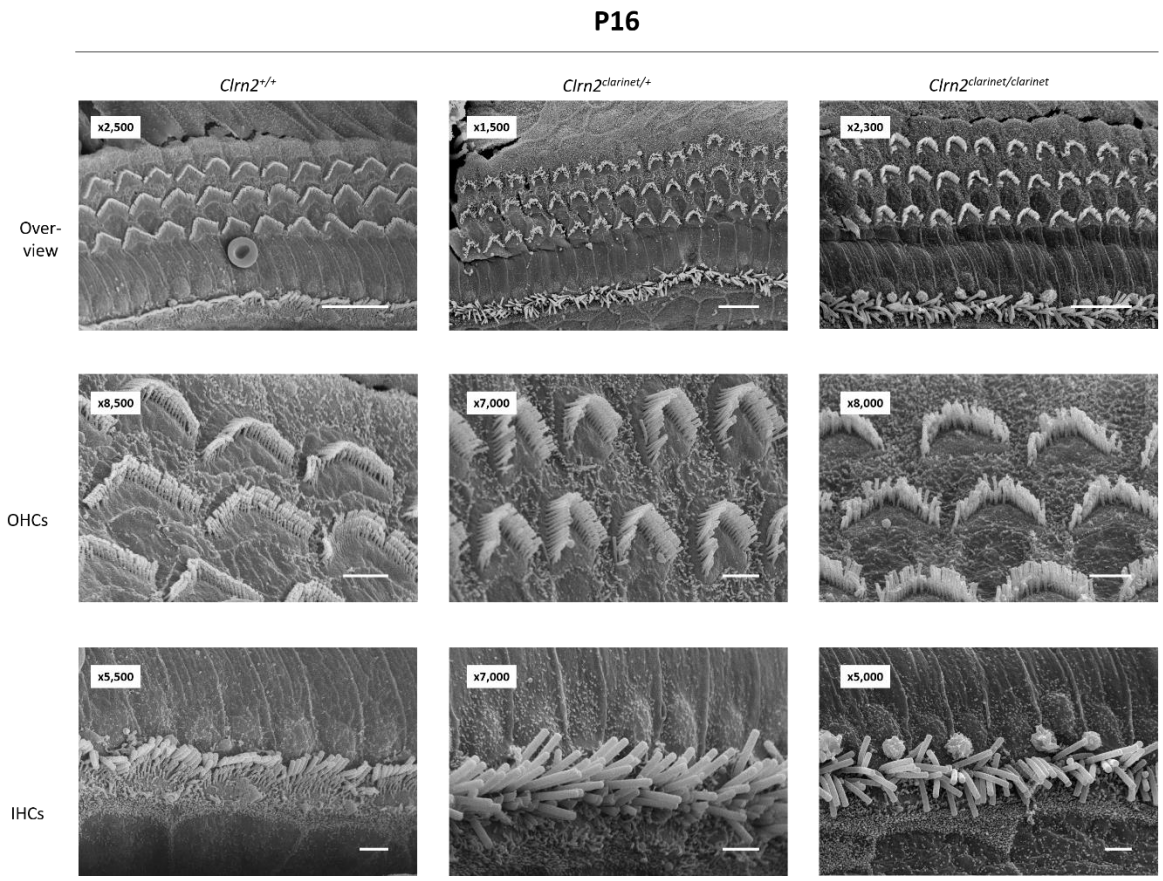

Figure 3.13: **Representative scanning electron micrographs of cochlear hair cells indicate no gross patterning issues in the sensory epithelium of P16 *Clrn2*$^{clarinet/clarinet}$ mice in comparison to *Clrn2*$^{+/+}$ and *Clrn2*$^{clarinet/+}$ controls.** The top panel (scale – 10 µm) shows an overview of the three rows of OHCs and one row of IHCs. The middle panel (scale – 2 µm) shows a selection of OHC bundles, which in the homozygous mutant appears to only exhibit two rows of stereocilia. The bottom panel (scale – 2 µm) shows rows of IHC bundles, which appear normal in the mutant. Magnification is indicated on each individual micrograph. OHCs – outer hair cells; IHCs – inner hair cells.

In order to examine the hair bundles of both OHCs and IHCs in more detail, further scanning electron micrographs were taken at higher magnification of hair bundles of individual cells. Micrographs were subsequently pseudo-coloured to help distinguish between stereocilia in adjacent rows. Indeed, this close inspection confirmed that at P16, almost all third row stereocilia (yellow) were absent in the *clarinet* mutant (top panel), and additionally the second (blue) row appeared to be less uniform in height (evident on stereocilia on the left hand side of the bundle) in comparison to the wild type counterpart (Figure 3.14).

Again, while the gross morphology of mutant IHC bundles was similar to the control, the second (blue) row stereocilia tips appeared less prolate than in the wild type. As previously discussed, a prolate (tapered) stereocilia tip is indicative of a tip link that connects two stereocilia in adjacent rows together. Therefore, it can be reasoned that the tip link in *clarinet* IHCs is either damaged or absent.

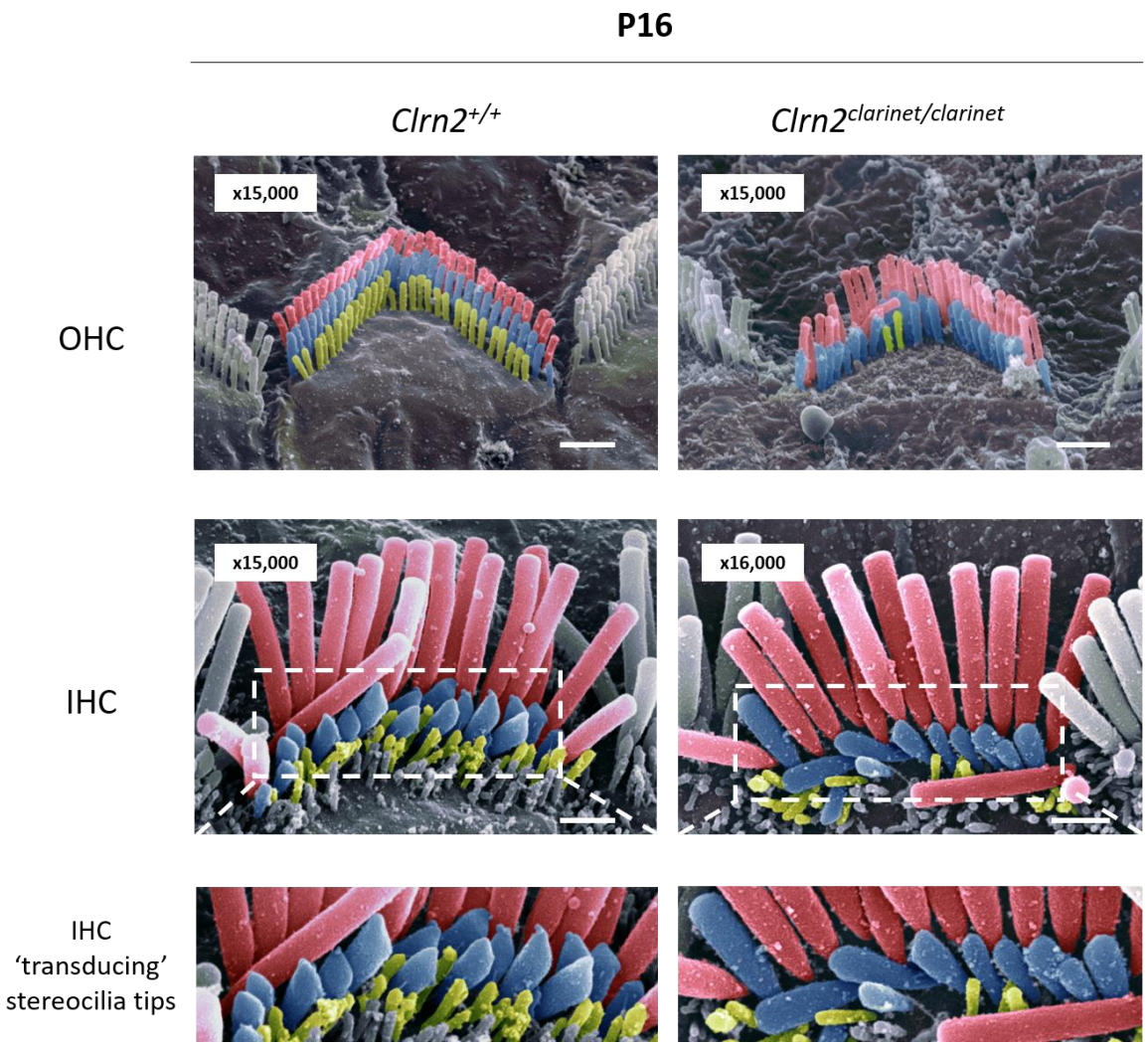

Figure 3.14: **Pseudo-coloured scanning electron micrographs of individual OHC and IHC mid-cochlear bundles show *Clrn2*$^{clarinet/clarinet}$ stereocilia morphology is to wild type controls at P16.** However, on closer inspection of OHC bundles (top panel), the shortest row of stereocilia (yellow) is almost completely absent. IHC bundles (middle panel) of mutants closely resemble those in controls apart from the lack of tapering of second row stereocilia (blue) tips, shown more closely in the zoomed-in bottom panels. The tallest row stereocilia (red) appear normal in both OHCs and IHCs. For wild type, heterozygous (not shown) and mutant individual mice, n = 1, 4 and 3, respectively). Multiple micrographs were taken per cochlea, per animal. Images taken and pseudo-coloured by Dr Andrew Parker, MRC Harwell Institute. Magnification is indicated on each individual micrograph. Scale – 1 µm.

This close examination of hair bundles at P16 revealed a curious phenotype, whereby at P16 the shortest row of stereocilia is absent. However, this 'snapshot' of *clarinet* hair bundle morphology did not shed light on the cause of this absence, and furthermore raises the question: did the third row begin to develop and subsequently regress or resorb due to the *clarinet* mutation, or did it never develop? To answer this question, cochleae from P8 *clarinet* mice were processed for scanning electron microscopy and imaged at high magnification, as before. As mentioned previously, mechanotransduction currents in the developing mouse cochlea reach mature levels approximately one week after birth (Lelli et al., 2009), with OHCs reaching functional maturity at approximately P8 (Marcotti and Kros, 1999).

Examination of *clarinet* OHC bundles at P8 revealed that the third row stereocilia (yellow) are indeed present, although appear much shorter than their wild type counterparts (Figure 3.15, top panel), and far less uniform in height. This is also true for the second row (blue), whose height is varied.

The P8 *clarinet* IHC bundle (Figure 3.15, middle panel) closely resembled the appearance of the P16 bundle, with a distinct lack of prolate second row (blue) stereocilia tips (bottom panel). The third row (yellow) also appeared fewer in number. Despite these architectural differences, the general shape of both the OHC and IHC bundle was constant with that of the controls, and the top row stereocilia (red) appeared normal.

The SEM imaging of *Clrn2*$^{clarinet/clarinet}$ P8 and P16 OHC bundles demonstrated a drop in height between P8 and P16 for the shortest row of stereocilia, and possibly the second row; in other words, the two 'transducing' rows of stereocilia are affected by the *clarinet* mutation. As the third row stereocilia are present at P8, this suggests that while development begins normally, the stereocilia begin to resorb and are almost entirely absent by P16.

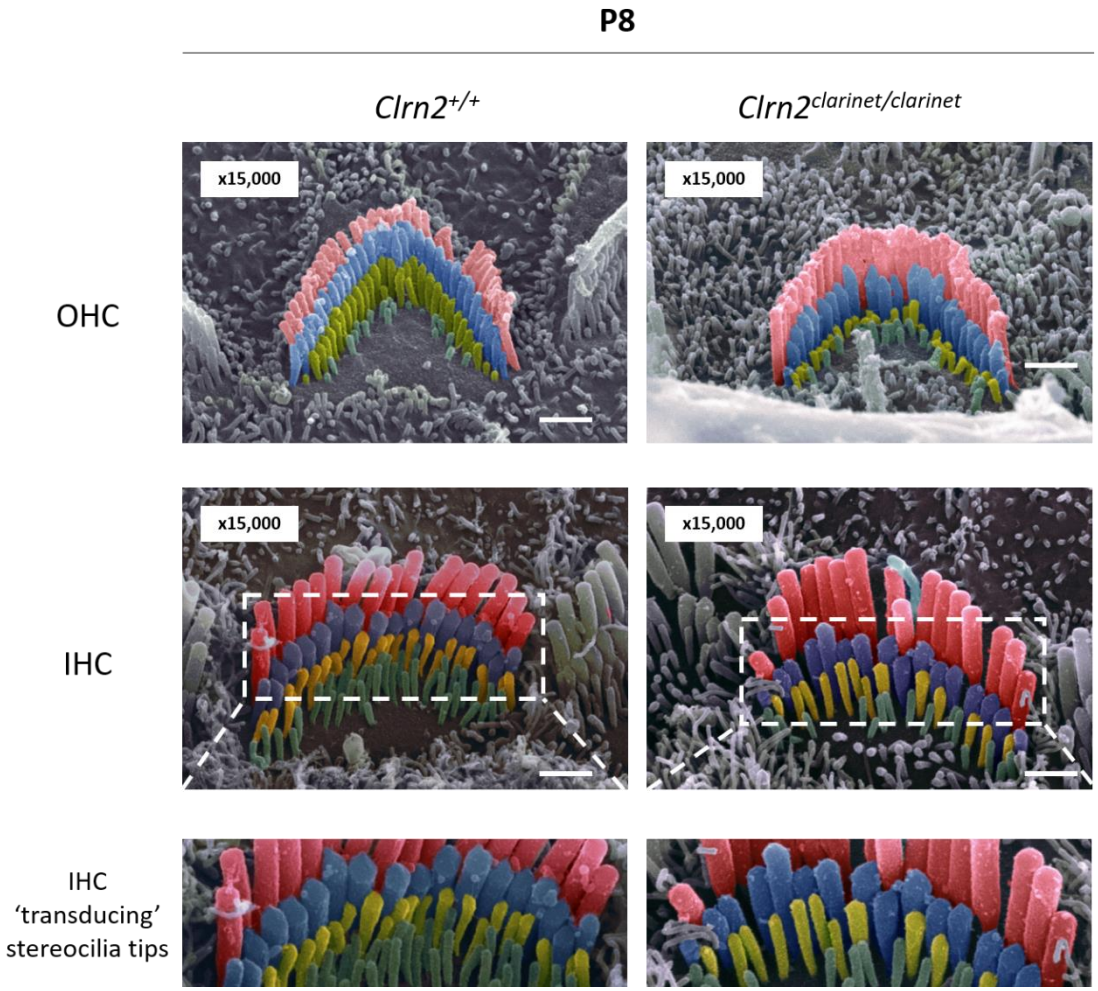

Figure 3.15: **Pseudo-coloured scanning electron micrographs of individual OHC and IHC mid-cochlear bundles show *Clrn2*$^{clarinet/clarinet}$ stereocilia architecture is comparable, at a gross morphological level, to wild type controls at P8.** On closer inspection of OHC bundles (top panel), the shortest row of stereocilia (yellow) is much shorter than in the wild type, and the second row (blue) appears to be less uniform in height. IHC bundles (middle panel) of mutants closely resemble those in controls apart from the lack of tapering of second row stereocilia (blue) tips. Note that the kinocilium (light blue) can be seen in the mutant IHC bundle. Fourth row stereocilia/microvilli (green) reside at the bottom of the bundle. For wild type, heterozygous (not shown) and mutant individual mice, n = 1, 1 and 3, respectively). Multiple micrographs were taken per cochlea, per animal. Images taken and pseudo-coloured by Dr Andrew Parker, MRC Harwell Institute. Magnification is indicated on each individual micrograph. Scale– 1 µm.

In order to quantify this change in height, stereocilia lengths taken from the middle region of the cochlea were measured by Carlos Aguilar, MRC Harwell Institute. The heights of individual stereocilia were measured using micrographs, for both OHCs and IHCs, and at both P8 and P16. Briefly, at least nine stereocilia per bundle, and at least two bundles were measured. Images were taken from at least three animals per genotype. In order to account for uncertainly due to plane rotation, duplicate images were taken with a 5˚ tilt between them and measurements were input into equations to give a more accurate estimate of the true stereocilia height. Further details of the equations are included in 2.6. Numerous differences in heights differences were observed in OHC stereocilia rows (Figure 3.16A). At P8, the average heights of stereocilia in all three OHC rows are significantly shorter in *Clrn2*$^{clarinet/clarinet}$ mice relative to *Clrn2*$^{+/+}$ control littermates (tallest −13%, middle −25%, shortest −52%). By P16 in OHC bundles, the average height of stereocilia in all three rows continue to be shorter in *Clrn2*$^{clarinet/clarinet}$ mice relative to the controls (tallest −9%, middle −25%, shortest −87%), with many shortest row stereocilia now absent. However, in both P8 and P16 IHC bundles, there were no significant differences in the average heights of stereocilia between *clarinet* and wild type control mice in any row (Figure 3.16B).

Overall, these ultrastructural analyses of *clarinet* hair cells have demonstrated a distinct hair bundle phenotype: in OHCs, the third row stereocilia, while appearing to initially develop normally during neonatal stages, begin to resorb before almost completely disappearing by P16. The second row may be progressing similarly or more slowly, given the shorter and more varied stereocilia heights. The same two rows in IHCs are fewer in number and less prolate, indicating the absence of a tip link. These data suggest that the *Clrn2*^{clarinet} mutation affects the two 'transducing' rows of stereocilia.

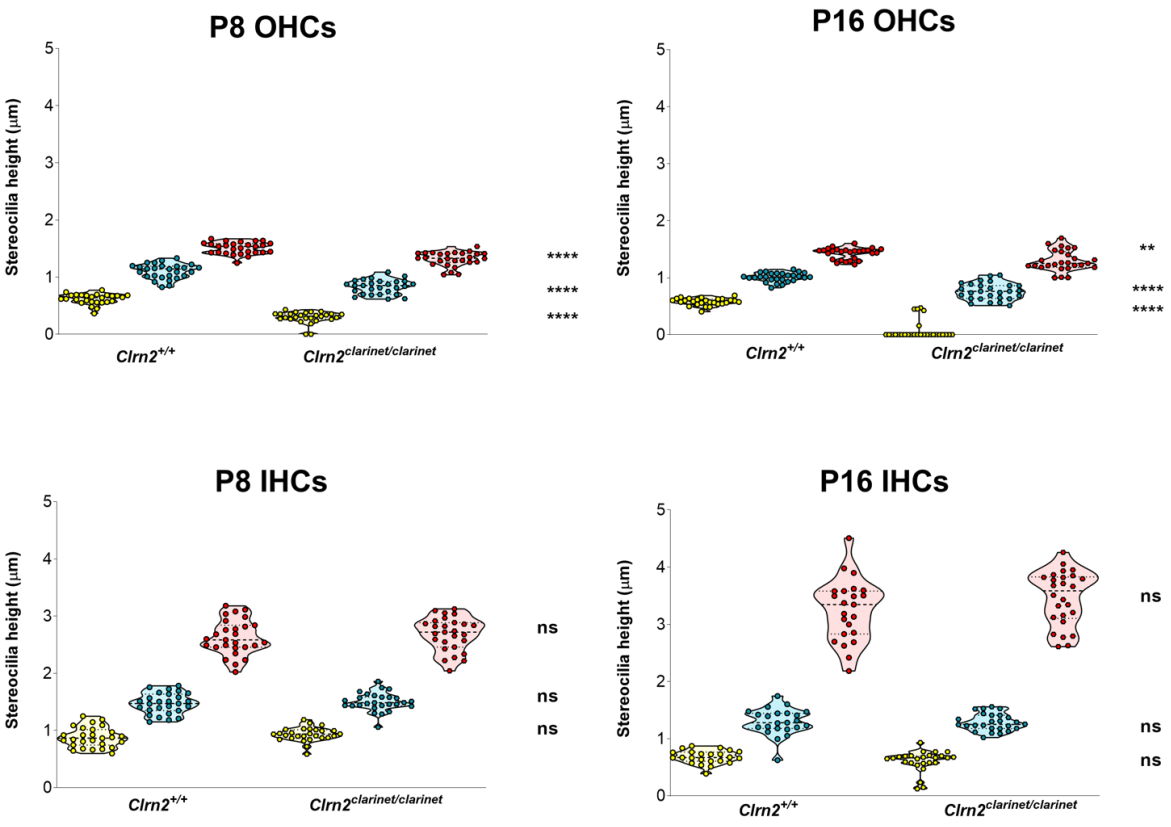

Figure 3.16: **Distribution of individual measures across genotypes shows shorter *clarinet* OHC, but not IHC stererocilia at both P8 and P16. (A)** OHC stereocilia measurements at P8 and P16 show a significant difference in height of *Clrn2*$^{clarinet/clarinet}$ stereocilia compared to wild type controls. For the shortest row at P8: *Clrn2*$^{+/+}$: 0.6188 ± 0.0944 p.µm (n = 27); *Clrn2*$^{clarinet/clarinet}$: 0.2948 ± 0.1029 p.µm (n = 27) (p<0.0001, Mann–Whitney ranks comparison), and at P16: *Clrn2*$^{+/+}$: 0.579 ± 0.06179 p.µm (n = 27); *Clrn2*$^{clarinet/clarinet}$: 0.07282 ± 0.1626 p.µm (n = 27) (p<0.0001, Mann–Whitney ranks comparison). **(B)** IHC stereocilia measurements at either time point showed a difference between mutants and wild types. For the shortest row at P8: *Clrn2*$^{+/+}$: 0.8808 ± 0.1753 p.µm (n = 27); *Clrn2*$^{clarinet/clarinet}$: 0.9313 ± 0.1217 p.µm (n = 27) (P = 0.2244, unpaired t-test); and at P16: *Clrn2*$^{+/+}$: 0.6784 ± 0.1171 p.µm (n = 23); *Clrn2*$^{clarinet/clarinet}$: 0.6063 ± 0.1855 p.µm (n = 26) (p=0.2436, Mann–Whitney ranks comparison). **p< 0.01; ****p< 0.0001; NS p>0.05. p.µm – projected height in µm; OHC – outer hair cell; IHC – inner hair cell; n.s. – not significant.

3.2.8 **Longitudinal vestibular phenotyping**

As previously discussed in the introduction, *Clrn2*'s paralogue, *Clrn1*, is the causative gene for USH3A. As USH (as a whole) is characterised by combined blind-deafness and vestibular dysfunction, several phenotyping tests were employed to investigate vision and balance in *clarinet* mice to assess the possibility of *Clrn2* as an USH gene.

While any overt vestibular phenotype in mice can be easily detected by head bobbing or tilting, or circling within the home cage, the swim test can be useful in identifying a more subtle vestibular deficit. As part of the USH3A phenotype, *Clrn1* knockout mice exhibit vestibular defects. Swim testing of younger adults (P21-P90) indicates some mutants are less stable in water, and additionally some mutants display head bobbing by 6 months that becomes more apparent with age (Geng et al., 2009). Therefore, vestibular function was investigated in adult *clarinet* mice through various behavioural phenotyping tests.

In swim tests carried out at P28 (one month) and P60 (two months) by Dr Pranav Patni and Prof Aziz El-Amraoui at the Institut Pasteur, *clarinet* mice exhibited normal swimming behaviour, indistinguishable from aged-matched heterozygous controls were all mice tested scored 0 (Figure 3.17). Heterozygous mice were deemed appropriate to use as controls in all experiments conducted at the Institut Pasteur, given the normal hearing thresholds of *Clrn2*$^{clarinet/+}$ mice.

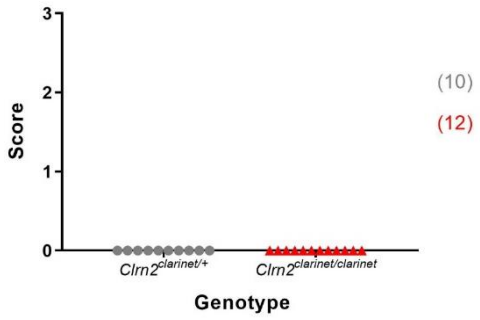

Figure 3.17: **Swim testing at P28 and P60 indicates the *clarinet* mutation does not cause early-onset vestibular function.** Due to their similarity, data for both time points was combined and displayed as one. Scoring was recorded according to criteria published in Haridisty-Hughes et al (2010). Overall n numbers for each genotype are indicated to the right of the graph. For *Clrn2*$^{clarinet/+}$ animals: P28, n = 3, and P60, n = 7, and for *Clrn2*$^{clarinet/clarinet}$ animals: P28, n = 5, and P60, n = 7. Carried out by Dr Pranav Patni, Institut Pasteur.

Further tests investigating overt vestibular function were carried out at the Institut Pasteur and included the platform, contact-righting and trunk-curl tests. At both P28 and P60 and across all tests, mutant mouse behaviour was indistinguishable from that of heterozygous controls (data not shown).

Swim testing carried out at MRC Harwell Institute revealed a vestibular phenotype in all *Clrn2*$^{clarinet/clarinet}$ mice from 6 months (the earliest time point tested) (Figure 3.18), in which mutant mice either swam in a circular motion or on one side (scoring a 1 on the scale, where 3 is the most severe response) or initially froze when placed into the water (scoring a 2). Interestingly, some mutant mice scored 0 (indicating normal swimming) in later swim tests, which could indicate their initial response at 6 months was confounded by being placed into a novel environment. These results suggest the *Clrn2*^{clarinet} mutation causes a variable mild-to-moderate vestibular phenotype, though greater n numbers are required to confirm this.

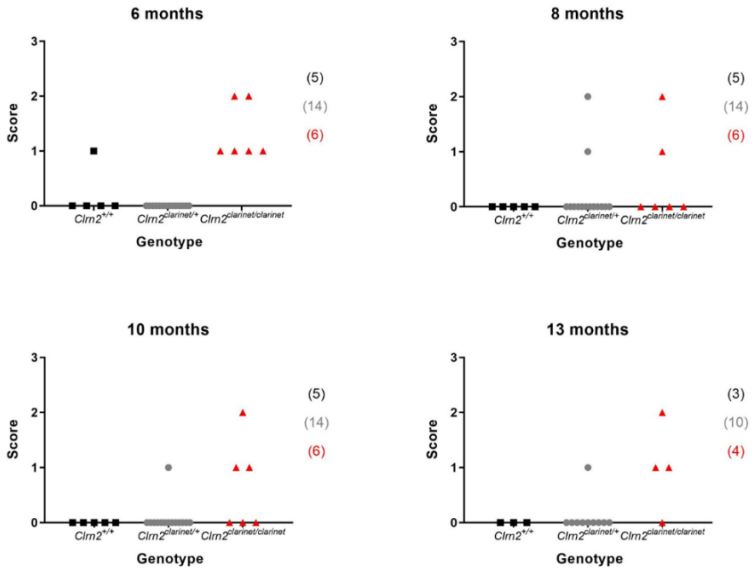

Figure 3.18: **Longitudinal swim testing of *clarinet* mice at MRC Harwell Institute indicates vestibular dysfunction.** Mutant mice were tested alongside aged-matched control littermates from 6 months at two or three month intervals up to 13 months. Scoring was recorded according to criteria published in Haridisty-Hughes et al., 2010. n numbers for each time point are indicated to the right of the graph.

Combined, these data could indicate that the *Clrn2*^{clarinet} mutation causes late-onset vestibular dysfunction, which is only detectable from 6 months of age.

3.2.9 **Electroretinogram response**

Depending on the type, USH patients exhibit varying levels of visual impairment due to onset of retinitis pigmentosa (RP). The visual impairment exhibited in USH3A, caused by mutations in *Clrn1*, is varied, and as mentioned previously, mouse models fail to recapitulate the visual deficits exhibited by patients (Géléoc and El-Amraoui, 2020).

The electroretinogram (ERG) is a non-invasive phenotyping test used to assess electrical activity of cells in the retina in response to a light stimulus. ERG responses are characterised by an initial negative deflection (known as the a-wave), which is followed by a positive peak (known as the b-wave). The amplitudes of the waves vary according to the intensity of the light stimulus. Conducting the test under scotopic or photopic conditions assesses the rod and cone functions respectively. ERGs were performed on *clarinet* mice at both 3 and 6-7 months at the Institut Pasteur. Responses from *Clrn2*$^{clarinet/clarinet}$ mice were similar to those of *Clrn2*$^{clarinet/+}$ heterozygous controls, with unaffected time-to-peak values for both a- and b-waves (Figure 3.19). Additionally, the lack of change in ERG amplitude responses (data not shown) indicates normal photoreceptor kinetics, and standard sensitivity of photoreceptor cells in the *clarinet* retina.

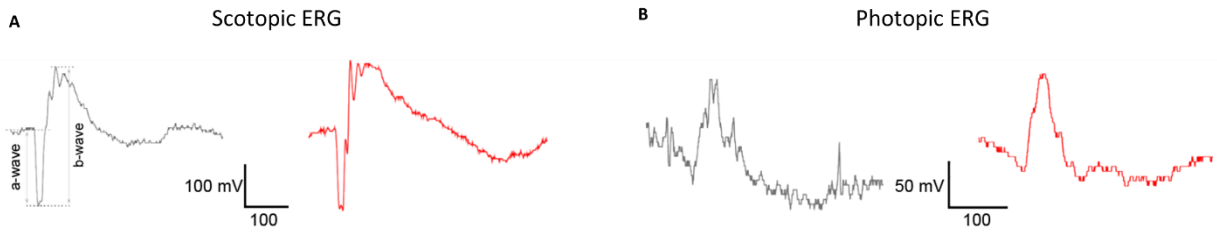

Figure 3.19: Electroretinogram (ERG) responses from representative control *Clrn2*$^{clarinet/+}$ (grey) and mutant *Clrn2*$^{clarinet/clarinet}$ (red) mice. Each trace represents an ERG response from the eye of age-matched *Clrn2*$^{clarinet/+}$ and *Clrn2*$^{clarinet/clarinet}$ mice, demonstrating no significant difference in a- or b-wave amplitudes under either scotopic **(A)** or photopic **(B)** conditions. Carried out by Dr Pranav Patni, Institut Pasteur.

3.2.10 **Synaptic labelling**

To further investigate the role of clarin-2 within the hair cell, and given that *Clrn1* is thought to have a function in maturing IHC ribbon synapses (Zallocchi et al., 2012, Ogun and Zallocchi, 2014), immunolabelling of synaptic densities in *clarinet* mice was performed. Localisation of the pre- and post-synaptic densities were investigated in the apical region of P21 mice using Ribeye (a component of the pre-synaptic ribbon) and GluR2 (a subunit of the post-synaptic glutamate receptor on afferent SGNs) markers, respectively. P21 was chosen as *clarinet* mice already exhibit significant hearing loss at this time point. Labelling of densities was indistinguishable between *Clrn2*$^{clarinet/clarinet}$ ears and both wild type and heterozygous littermate controls (Figure 3.20A), and this observation was reinforced by counting the number of matched and unmatched puncta per 5 hair cells, which indicated no significant differences across genotypes (Figure 3.20B).

These results suggest that unlike its paralogue, clarin-2 is not required for maturation and coordination of IHC ribbon synapses in the cochlea.

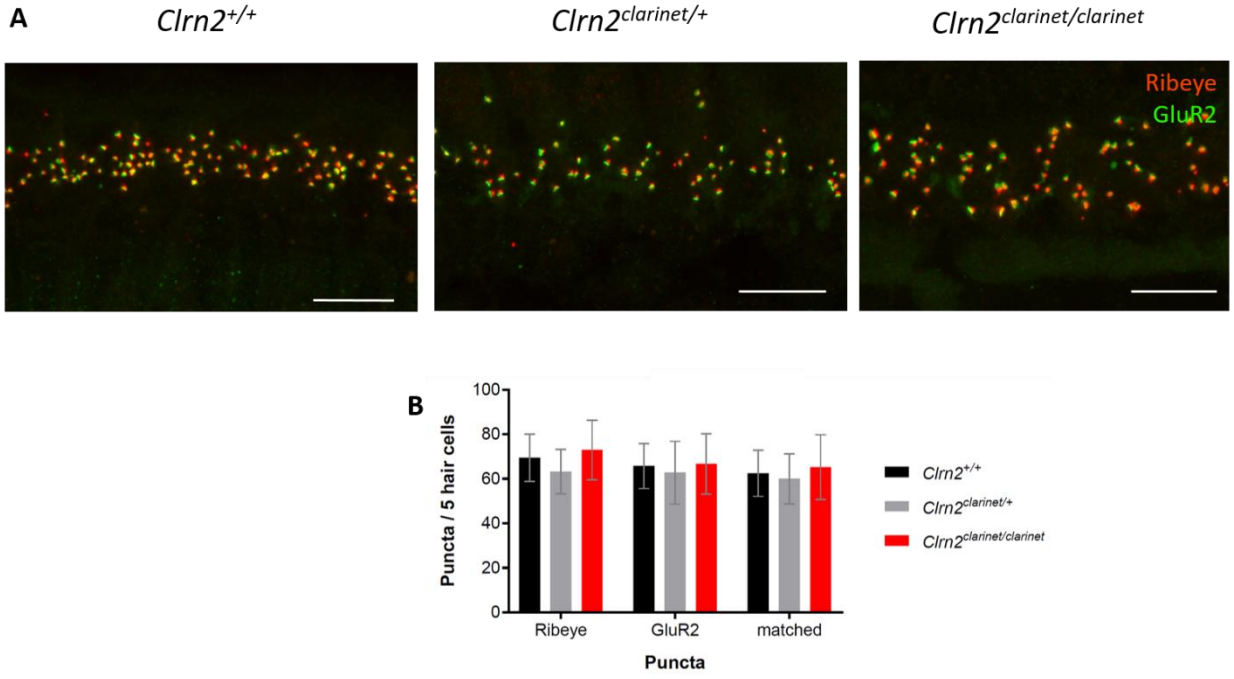

Figure 3.20: P21 *clarinet* mice display the correct number and localisation of pre- and post-synaptic densities in their IHCs. **(A)** Cochlear wholemounts labelled with a pre-synaptic ribbon marker Ribeye (red) and the post-synaptic density marker GluR2 (green) are indistinguishable from their wild type and heterozygous littermate controls (n=4 per genotype), which is quantified by puncta counts per 5 IHCs **(B)**. All images and counts were taken from the apical region of the cochlea. The dotted outlines in the wild type sample indicates the approximate position of 3 IHCs, with the ribbon synapses located at the bottom of the cells. Data shown are mean ± s.e.m, one-way ANOVA. Scale – 10 µm.

3.2.11 **Electrophysiological properties of cochlear hair cells**

Ultrastructural analysis of the architecture of developing (P8) *clarinet* hair cells revealed an interesting phenotype – the resorption of the third row OHC stereocilia (the shortest transducing row) (Figure 3.15). By P16, the third row OHC stereocilia is completely missing and IHC stereocilia are less prolate, indicating absence of the tip link (Figure 3.14). These findings could infer the possible loss or dysfunction of the mechano-electrical transduction channels that reside on the two shortest transducing stereocilia rows.

Therefore, in order to examine the mechano-electrical transduction properties of *clarinet* cochlear hair cells in detail, various electrophysiological analyses were performed by Dr Laura Corns, Dr Stuart Johnson and Prof Walter Marcotti at the University of Sheffield. Similarly to data collected at the Institut Pasteur, heterozygous *Clrn2*$^{clarinet/+}$ mice were used as controls to reduce the overall numbers of mice required for experiments.

Electrophysiological investigations carried out on *clarinet* mice examined the acquisition of mechano-electrical transduction of developing (P6-P8) IHCs and OHCs, and potassium currents in mature (P15-16 and P22) IHCs and OHCs.

1.1.1.1 *Analysis of developing mechano-electrical transduction channels*

Cochlear hair cell MET channels currents were measured in P6-8 apical coil hair cells by displacement of hair bundles in the excitatory and inhibitory direction. This was achieved using a piezo-driven fluid jet, as described in Corns et al. (2014) and Corns et al (2016).

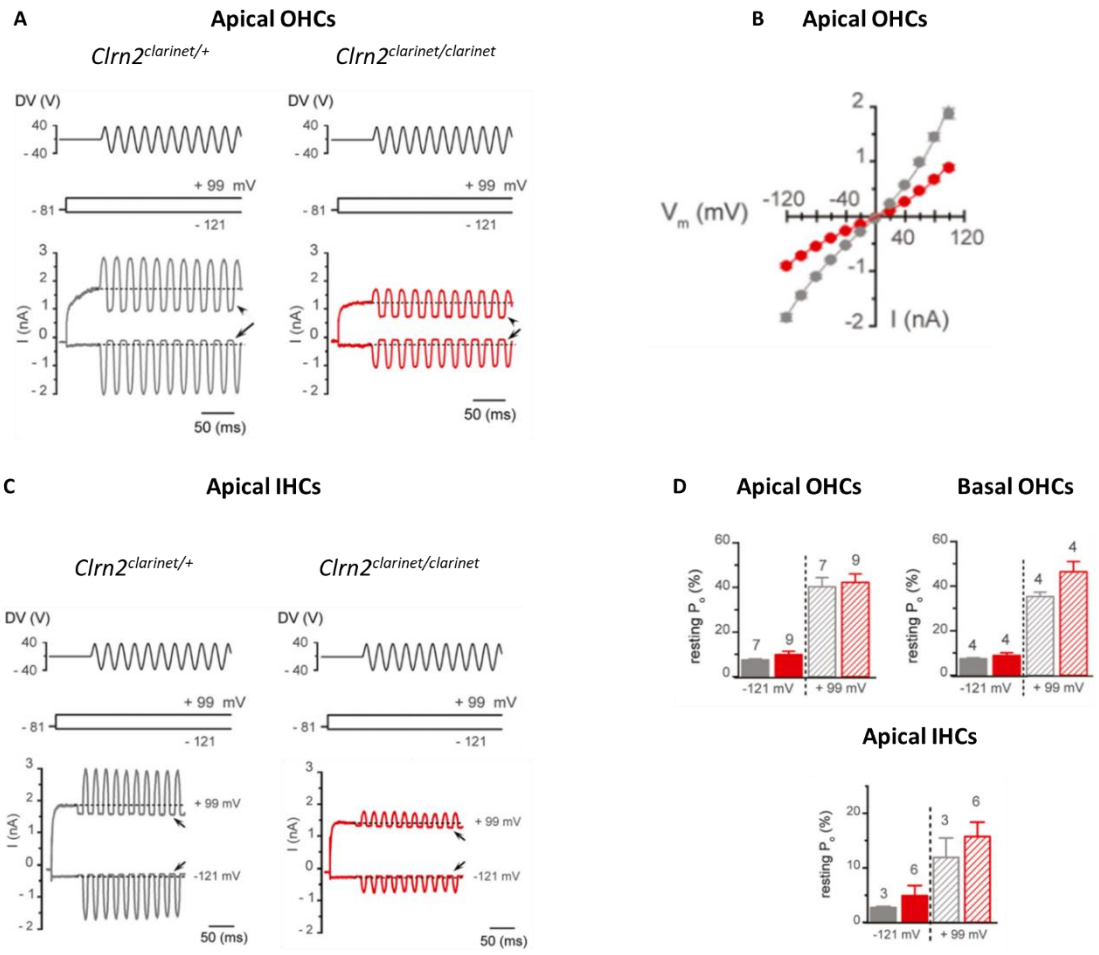

Figure 3.21: MET channel currents in immature *clarinet* hair bundles. (A) Currents are reduced in *clarinet* apical OHCs (P6) compared to aged-matched heterozygous controls. Currents were recorded by applying sinusoidal force stimuli of 50 Hz to the hair bundles at −121 mV and +99 mV. The driver voltage (DV) signal of ± 40 V to the fluid jet is shown above the traces, and the holding potential was −81 mV. Extracellular Ca^{2+} concentration was 1.3 mM. Arrows and arrowheads indicate the closure of the MET currents (i.e. resting MET current) elicited during inhibitory bundle displacements at hyperpolarized and depolarized membrane potentials, respectively. Dashed lines indicate the holding current. **(B)** The average peak-to-peak current–voltage curves recorded from *Clrn2*$^{clarinet/+}$ (grey, P6, n = 7) and *Clrn2*$^{clarinet/clarinet}$ (red, P6-7, n = 9) apical-coil OHCs were significantly different. **(C)** MET channel current is also reduced in P8 apical IHCs compared to P7 controls. **(D)** The open resting probability (P_0) of the MET current at the membrane potentials of −121 mV and +99 mV remains similar between the two genotypes across various hair cell populations, as indicated. n numbers for each group are shown above the individual columns. Data are mean ± s.e.m. Conducted by Dr Laura Corns, Dr Stuart Johnson and Prof Walter Marcotti at the University of Sheffield. V_m – resting membrane potential ; mV – millivolts; V – volts; ms – milliseconds; nA – nanoampere.

At hyperpolarised membrane potentials of -121 mV (millivolts), hair bundles were displaced in the excitatory direction (where stereocilia deflect toward the tallest row) to elicit an inward MET channel current. While both *Clrn2*$^{+/+}$ and *Clrn2*$^{clarinet/clarinet}$ MET channels produced a response, the maximal MET current in P6 OHCs was reduced in homozygous mice in comparison to aged-matched heterozygotes (Figure 3.21A). The difference in maximal MET current in 1.3 mM Ca^{2+} was significant between *Clrn2*$^{clarinet/+}$ (−1,842 ± 66 pA at −121 mV, *n* = 7) and *Clrn2*$^{clarinet/clarinet}$ (−902 ± 39 pA, *n* = 9) OHCs (Figure 3.21B). Additionally, a reduction in MET channel response was also observed in P8 *clarinet*

apical IHCs in comparison to P7 controls (Figure 3.21C). Despite these differences, open resting probability (P_0) in OHCs (apical and basal) and apical IHCs were comparable to controls at both positive and negative membrane potentials (Figure 3.21D).

1.1.1.2 *Potassium currents in mature hair cells*

Mouse cochlear OHCs begin to display adult-like characteristics from around P8 in conjunction with the expression of the negatively-activated K^+ current $I_{K,n}$, (Marcotti and Kros, 1999), which is carried by the KCNQ4 channel (Kubisch et al., 1999). Therefore, to investigate the maturation status of *clarinet* OHCs, potassium currents in P22 *clarinet* apical OHCs were elicited by applying a series of depolarising voltage steps from -144 mV in 10 mV increments, from a holding potential of -84 mV.

Clrn2$^{clarinet/clarinet}$ OHCs were found to exhibit the same complement of potassium currents as *Clrn2*$^{clarinet/+}$ controls (Figure 3.22A-C). The size of the total outward K^+ current at 0 mV, which includes both the $I_{K,n}$ and the classical delayed rectified outward K^+ current I_K (Marcotti and Kros, 1999), was similar between heterozygote controls (2.9 ± 0.6 nA, n = 5) and *clarinet* mutants (3.2 ± 0.5 nA, n = 6). The size of the $I_{K,n}$ current was also comparable between the two groups. These data suggest that *Clrn2* is not involved in the acquisition of the adult-like basolateral membrane properties of OHCs.

Potassium currents in mature *clarinet* IHCs were also investigated. The onset of adult-like characteristics in IHCs occurs approximately four days later than OHCs, at around P12 (Kros et al., 1998, Marcotti, 2012). IHC functional maturation is achieved by the down-regulation of immature-type currents and inward rectifier currents, and expression of $I_{K,n}$ and the fast-activating large-conductance Ca^{2+}-activated K^+ current (Marcotti et al., 2003).

To assess potassium currents in IHCs, the currents were first elicited by applying depolarising voltage steps in 10 mV nominal increments from –124 mV up to + 30 mV, starting from the holding potential of −84 mV. In P22 IHCs, the total outward K^+ current at 0 mV was similar between control *Clrn2*$^{clarinet/+}$ (11.6 ± 1.6 nA, n = 4) and mutant *Clrn2*$^{clarinet/clarinet}$ (10.7 ± 1.0 nA, n = 5) mice. However, closer inspection of the time-course of current activation showed some differences. These were assessed in

greater detail by delivering a voltage protocol that allowed evaluation of both $I_{K,n}$ and $I_{K,f}$ currents (Figure 3.22D-F). IHCs were held at −64 mV and subjected to depolarising voltages in 10 mV increments from −144 mV to more positive values. While controls expressed both $I_{K,n}$ and $I_{K,f}$ currents, *clarinet* mutant IHCs did not and instead expressed I_{K1} (Figure 3.22G and H), which is in fact characteristic of an immature, pre-hearing IHC (Marcotti et al., 1999). The physiological consequence of this was that mature mutant IHCs did not acquire the fast-graded voltage response to stimulation that is normally present in adult IHCs. Additionally, in some cases, adult mutant IHCs retained the ability to fire an initial Ca^{2+}-dependant action potential (Figure 3.22I), a characteristic that is generally exhibited by immature cells (Kros et al., 1998, Marcotti et al., 2003). In mutants, immature-type currents were not down-regulated and as such, their functional differentiation into mature cells was not achieved. Results from recording potassium currents from mature apical *clarinet* hair cells demonstrated that OHCs but not IHCs were allowed to functionally mature, and additionally mature IHCs retain some characteristics of pre-hearing developing cells.

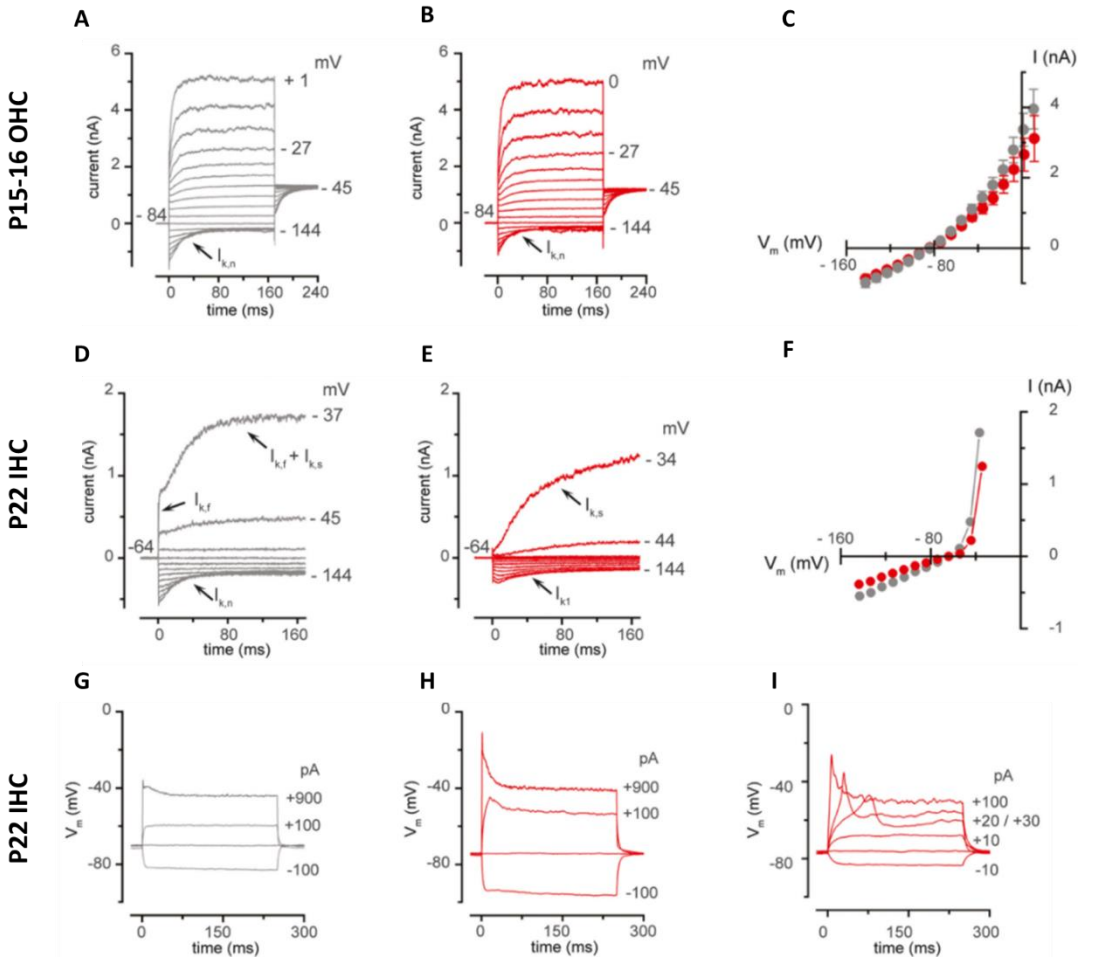

Figure 3.22: Potassium currents recorded in adult *clarinet* (red) mice indicate the correct functional maturation of OHCs, but not IHCs, when compared to heterozygous controls (grey). (A, B) potassium currents were recorded from P15 *Clrn2*$^{clarinet/+}$ and P16 *Clrn2*$^{clarinet/clarinet}$ apical OHCs. The size of the $I_{K,n}$, current was measured in isolation as the deactivating tail currents (difference between instantaneous and steady-state inward currents) for voltage steps from the holding potential to −124 mV, was 545 ± 115 pA (n = 5) in *Clrn2*$^{clarinet/+}$ and 595 ± 67 pA (n = 7) in *Clrn2*$^{clarinet/clarinet}$ OHCs. **(C)** average peak current-voltage relation for the total K^+ current recorded from *Clrn2*$^{clarinet/+}$ (P15-16, n = 7) and *Clrn2*$^{clarinet/clarinet}$ (P15-16, n = 5) OHCs. **(D, E)** potassium currents recorded from P22 mature *Clrn2*$^{clarinet/+}$ and *Clrn2*$^{clarinet/clarinet}$ apical-coil IHCs, using the same voltage protocol described above, with a holding potential of −64 mV. **(F)** average peak current-voltage relation for the total K^+ current recorded from the IHCs shown in **(D)** and **(E)**. **(G, H, I)** voltage responses from P22 *Clrn2*$^{clarinet/+}$ and *Clrn2*$^{clarinet/clarinet}$ IHCs. Note that Ca^{2+}-dependent action potentials (characteristic of pre-hearing cells) could be induced in mature IHCs **(I)**. Data are mean ± s.e.m. Conducted by Dr Laura Corns, Dr Stuart Johnson and Prof Walter Marcotti at the University of Sheffield.

Overall, the electrophysiological investigations have revealed critical information about *Clrn2*'s role in both developing and mature hair cells. In both immature OHCs and IHCs, MET channel function is reduced. This may be due to the resorption of the second transducing row of stereocilia, or alternatively this lack of current might have caused the stereocilia resorption; either way, the *clarinet* mutation appears to affect the transducing stereocilia and their MET channels. Potassium current recordings from adult mice demonstrated that while OHCs of *clarinet* animals develop normally, IHCs

do not, and instead remain in an immature, pre-hearing state. This could indicate that proper IHC, but not OHC, development requires a normal MET current.

3.2.12 **Ultrastructural analyses of adult *clarinet* auditory hair bundles**

Finally, to assess whether the bundle defect observed at P8 and P16 is limited to the third (shortest) row only in mature mice, an older time point was investigated to asses any progressive loss of stereocilia in other rows. *clarinet* cochleae were imaged at P28, at least two weeks after the onset of hearing at approximately P12. By P28, *Clrn2*$^{clarinet/clarinet}$ mice have profound hearing loss compared to their wild type and heterozygous littermates (Figure 3.23). Scanning electron micrographs of individual hair cells reiterated the abnormal morphology of the hair bundle in comparison to both controls. Again, the shortest row of OHC stereocilia (yellow) was missing with heights of middle row stereocilia (blue) varied, and the IHC shortest and middle row stereocilia were fewer in number and did not appear prolate. As before, the tallest row (red) was comparable to controls.

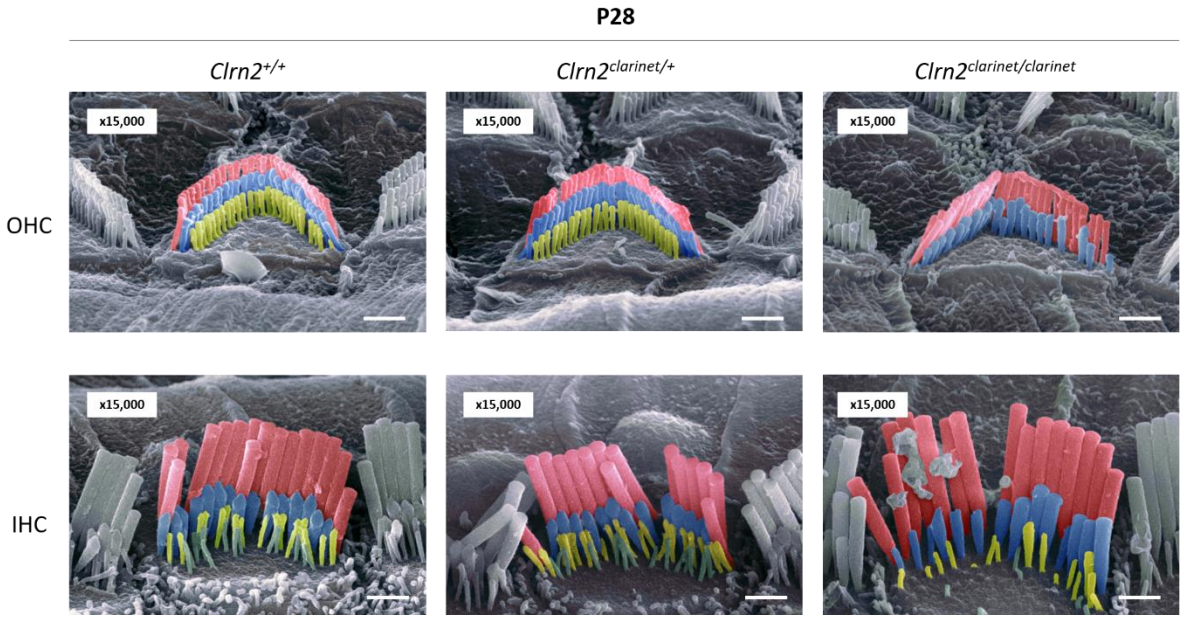

Figure 3.23: Pseudo-coloured scanning electron micrographs of individual OHC and IHC mid-cochlear bundles show *Clrn2*$^{clarinet/clarinet}$ stereocilia morphology is distinguishable from wild type and heterozygous controls at P28. Images taken and pseudo-coloured by Dr Andrew Parker, MRC Harwell Institute. Magnification is indicated on each individual micrograph. Scale – 1 µm.

These ultrastructural analyses undertaken at P28 demonstrate that the phenotype exhibited by developing *clarinet* mutants is retained into adulthood, and furthermore the second (blue) stereocilia row appears to be affected.

3.3 Discussion

These studies involving the characterisation of the ENU-induced *clarinet* mouse model have uncovered *Clrn2* as a novel hearing loss gene, and have begun to shed light on the requirement of clarin-2 in the mammalian inner ear.

The *Clrn2*^{clarinet} mutation was generated as part of the Harwell Ageing screen and following preliminary phenotyping, was found to elicit increased ABR thresholds. After genome mapping and whole genome sequencing, a nonsense-causing (Trp4*) mutation in the *Clrn2* gene was identified, and the mouse model was made congenic on the C57BL/6J background by 10 generations of backcrossing.

Complementation testing, auditory phenotyping and scanning electron microscopy imaging of compound heterozygote mice confirmed that *Clrn2* is the causative gene for this phenotype.

Extensive auditory phenotyping revealed an early-onset hearing loss, which causes a progressive and severe hearing loss affecting all frequencies tested. This is likely due to the resorption of shorter row stereocilia in mutant hair bundles, as revealed by ultrastructural analysis of the cochleae of *clarinet* and *Clrn2*$^{w4stop/del629}$ mice.

While USH genes have structural and functional roles in hair bundles, vestibular and visual phenotyping suggest that unlike its paralogue *Clrn1*, *Clrn2* is not an USH gene. While gross cochlear morphology was normal, including patterning and number of hair cell bundles, *Clrn2*^{clarinet} mice exhibit several hair bundle abnormalities: the third stereocilia row of OHCs, while developing normally initially, begins to regress and almost completely resorbs by P16, with the second row possibly regressing in a similar fashion. IHC second and third row stereocilia are fewer in number and less prolate than controls, indicating the absence of the tip link. The MET channels, found on these two

shorter 'transducing' rows of stereocilia, were found to be dysfunctional in both IHCs and OHCs, and while OHCs express normal potassium currents, IHCs do not, indicating failure to mature. Finally, again unlike in *Clrn1* mutants, *clarinet* synaptic formation appeared normal.

These findings suggest that the *Clrn2*^{clarinet} mutation affects the transducing stereocilia, and/or the MET channels, which leads to hearing loss. This is the first time *Clrn2* has been associated with deafness, and in fact any disease. The severe phenotype caused by the *Clrn2*^{clarinet} mutation is perhaps to be expected, due to the nonsense mutation at the fourth amino acid resulting in a severely truncated protein, if indeed a peptide is produced. It can therefore, essentially, be described as a loss-of-function mutation. In fact, the *del629* mutation is also likely to be a loss-of-function mutation, due to failure to complement. As mentioned previously, detailed characterisation of the *Clrn2*^{del629} mutant is covered in 5.2.1 and 5.2.2.

This leads to several questions. Firstly, what is the spatial and temporal localisation of clarin-2 in the cochlea? Furthermore, as qRT-PCR data generated from the original cohort show a large increase in *Clrn2* expression (Figure 1.13B) after the onset of hearing, after the hair bundle phenotype has been established, does *Clrn2* have a role in maintenance of the hair cell as well as a role in the initial patterning of the hair bundle? Additionally, how would the *Clrn2*^{del629} mutation affect hearing in homozygotes?

To answer these questions, extensive immunolabelling was employed to assess localisation of clarin-2 in the cochlea. Additionally, a new mouse mutant with a floxed *Clrn2* allele was generated (*Clrn2*^{fl}) and phenotyped, alongside mice homozygous for the *Clrn2*^{del629} mutation. These investigations are detailed in Chapters 4 and 5, respectively.

Chapter 4: Spatial and temporal expression and localisation of *Clrn2*/clarin-2

Introduction

The results presented in Chapter 3 identify the *Clrn2* gene as essential for mammalian hearing. Specifically, a subtle stereocilia abnormality is observed in maturing *Clrn2* mutant inner and outer hair cells, which appears to be associated with defective MET channel activity in the postnatal period. These data indicate the *clarinet* mutation causes an early-onset hair cell phenotype.

However, qRT-PCR data using whole cochlea RNA extracted from wild type mice indicates a 3-fold increase in *Clrn2* expression in the cochlea between P12 and P16, that is maintained at P28 (Figure 1.13B); in other words, *Clrn2* expression increases significantly from postnatal to juvenile time stages, which may suggest an additional role for *Clrn2* in the functionally mature adult cochlea.

As such, preliminary immunolabelling experiments were carried out at P20 to assess the localisation of the clarin-2 protein. A 'bespoke-made' anti-clarin-2 antibody, raised in rabbit (Rb61 anti-clarin-2, Covalab) was generated by Dr Philomena Mburu at MRC Harwell Institute. Initial immunolabelling studies using this antibody on P20 wild type whole mount cochleae appeared to demonstrate sporadic, punctate clarin-2 localisation within the stereocilia of both inner and outer hair cells (Figure 4.1).

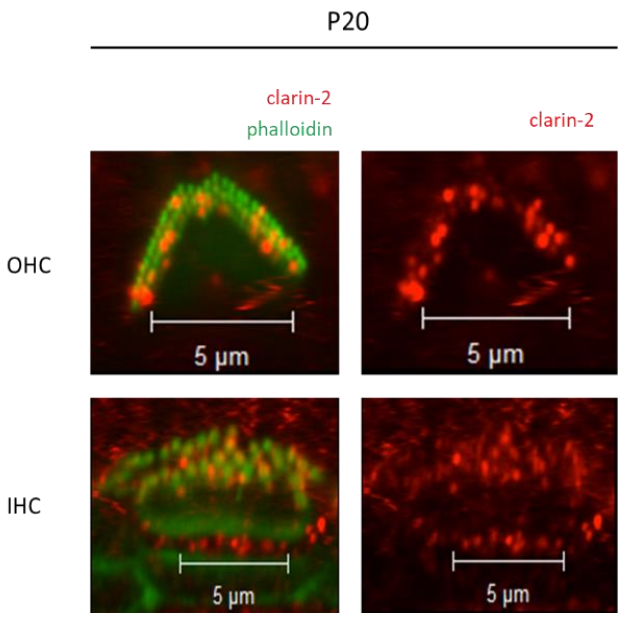

Figure 4.1: Preliminary immunolabelling of P20 wild type whole mount tissues appears to show clarin-2 localisation in the stereocilia of IHCs and OHCs. The anti-clarin-2 antibody was generated in-house and was raised in rabbit (Covalab). F-actin is labelled with a phalloidin antibody (AF-568). The clarin-2 antibody was used at a concentration of 1:50. Magnification at x63 with zoom.

To verify that these promising results were accurate and reliable, subsequent localisation experiments were conducted. This included using several different anti-clarin-2 antibodies, both the bespoke-made and commercially-available, on cochlear tissue processed using various methods, such as whole mount and vibratome sections. Given that the hearing loss in *Clrn2* mutants affects all frequencies, and that the hair bundle structural abnormalities are observed across all regions of the sensory epithelium, the tonotopic region of the spiral imaged in these clarin-2 localisation experiments was deemed not critical and as such several regions of the cochlear spiral are depicted in the following images.

4.2 Results

4.2.1 Visualisation of single-cell RNA-seq data

Although the qRT-PCR data (Figure 1.13B) suggests *Clrn2* is expressed in the neonate cochlea, this experiment used whole cochlear ducts and as such, further exploration into the expression of *Clrn2* transcripts in specific cochlear cell types could not be determined. Therefore, I investigated cochlear single-cell RNA sequencing (scRNA-seq) datasets that are publically accessible through the gene

Expression Analysis Resource (gEAR) database (https://umgear.org/). This resource allows researchers to mine and visualise data.

The first dataset explored was from Kolla et al. (2020), in which the authors investigated transcript expression in the mouse cochlear epithelium. Briefly, cells from both female and male CD1 mice were obtained from the cochlear epithelium. Following quality control, gene expression was captured with a Chromium Controller (10X Genomics) and sequenced with NextSeq (Illumina). Groups were annotated based on cluster-specific gene markers. The top five and six IHC and OHC marker genes at P1 were *Ccer2, Pcp4, Cib2, Pvalb* and *Acbd7*, and *Cgrp*, *Serpina1c*, *Veph1*, *Cacng2*, *Strip2* and *Msln1,* respectively. The top five IHC and OHC marker genes at P7 were *Pvalb, Calb2, Otof, Rprm* and *Cabp2*, and *Ocm, Pcp4, Ighm, Cib2* and *Calb1*, respectively.

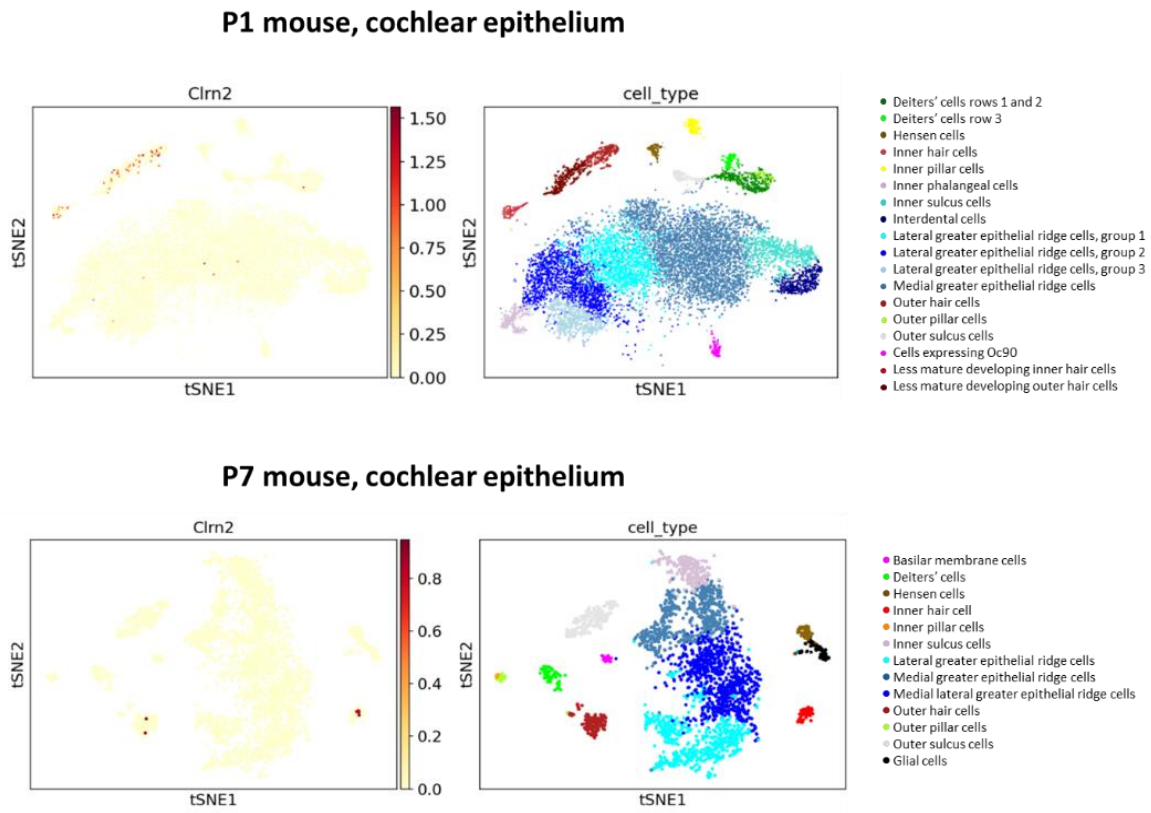

Figure 4.2: Visualisation of single cell RNA-seq data for *Clrn2* in mouse cochlear epithelium from Kolla et al., 2020. Both panels show tSNE plots of *Clrn2* expression in the cochlear epithelium at P1 (top panel) and P7 (bottom panel). Data was visualised using the gene Expression Analysis Resource (gEAR) from the University of Maryland (https://umgear.org). Figure adapted from Vona et al., 2021. tSNE – t-distributed stochastic neighbour embedding.

These data demonstrate that *Clrn2* transcripts are present in both inner and outer hair cells at P1 and P7 (Figure 4.2). According to Kolla et al, this was based on 14,043 cells obtained from between 20 and 32 P1 pups, and 3413 cells obtained from between 15 and 24 P7 pups. At these stages, *Clrn2* expression appears to be exclusively restricted to hair cells within the sensory epithelia. Further scRNA-seq data from the Kelley lab suggests *Clrn2* transcripts are not present at E14 or E16 (data not shown). These data were based on 5253 cells obtained from between a total 20 and 24 pups from two litters of E14 timed-pregnant females, and 7961 cells obtained from between a total of 20 and 24 pups from two litters of E16 pregnant-timed females.

The second dataset analysed was from Kubota et al. (2021), in which the authors examined expression in mouse cochlear cell groups. In this dataset from the Heller lab, single cells from cochlear ducts of P2 Fgfr3-tdTomato/Sox2-GFP and Lfng-GFP mice were collected. Following quality control, samples were tagmented with the Nextra XT system (Illumina), and subsequent sequencing was performed with NextSeq 500 (Illumina). Groups were annotated based on cluster-specific gene markers. The top five hair cell marker genes were *Ccer2, Lhfpl5, Pou4f3, Slc52a3* and *Calb1*.

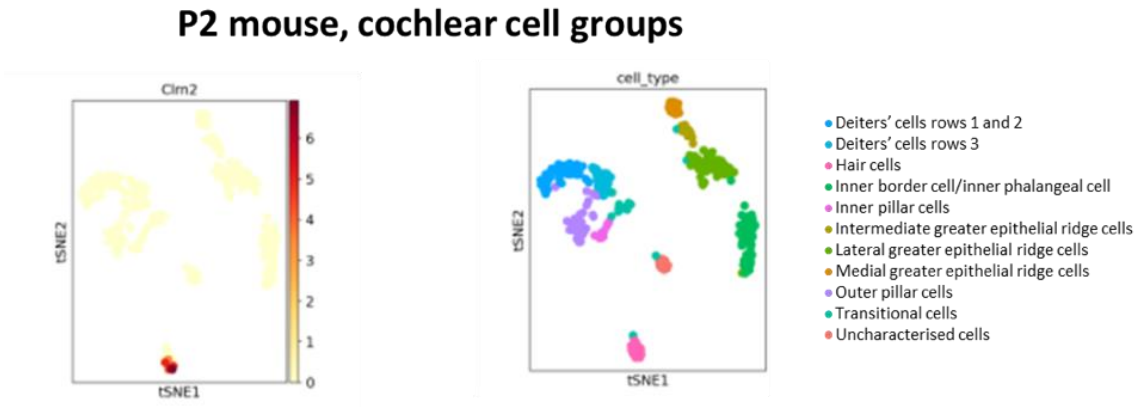

Figure 4.3: Visualisation of single cell RNA-seq data for *Clrn2* in P2 mouse cochlear cell groups from Kubota et al., 2021. Data were visualised on the gene Expression Analysis Resource (gEAR) from the University of Maryland (https://umgear.org). tSNE – t-distributed stochastic neighbour embedding.

Analysis of this scRNA-seq dataset indicates consistency with the Kolla et al scRNA-seq dataset, showing that *Clrn2* transcripts are exclusively present in hair cells and not in any other sensory epithelial cells at this early P2 postnatal stage (Figure 4.3).

Further *in silico* analyses of *Clrn2* expression available on the gEAR database suggest that *Clrn2* is readily detected in older P15 single-cell and adult-sorted hair cells (Liu et al., 2014, Liu et al., 2018, Ranum et al., 2019) (data not shown).

Taken together, these two datasets, along with the phenotyping of *clarinet* mice detailed in Chapter 3, indicate that *Clrn2* is an essential hair cell gene that is required to be expressed in hair cells from the perinatal period onwards. While these results imply one should see hair cell-restricted expression of *Clrn2,* immunolabelling studies, using cochlear tissue from similarly aged mice to those used for the scRNA-seq studies described above, are required to confirm this and to determine the subcellular localisation of the encoded clarin-2 protein.

4.2.2 **Immunolabelling of whole mounts**

Firstly, immunolabelling of mouse whole mount using the bespoke-made Rb61 anti-clarin-2 antibody on mouse whole mount cochlear tissue was conducted in an attempt to replicate the staining in Figure 4.1. For these studies wild type mouse P8 cochleae were utilised. There are several reasons for using tissues at this age: the Kolla et al. scRNA-seq dataset shows *Clrn2* transcripts to be present in hair cells at P7; the qRT-PCR results indicate constant expression levels of *Clrn2* transcript between P4 and P8 (Figure 1.13B); and, mice lacking clarin-2 already exhibit morphological and electrophysiological hair cell phenotypes by P8 (Figure 3.15 and Figure 3.21, respectively). Taken together, these findings suggest that clarin-2 protein should be present in hair cells at P8.

As the anti-clarin-2 primary antibody dilution used in the preliminary experiments was 1:50, the validation studies were undertaken using primary antibody dilutions of 1:50 and 1:100 (Figure 4.4, top and bottom panels respectively). A phalloidin conjugate was used to stain the F-actin present in hair cell stereocilia. The anti-clarin-2 antibody appears to non-specifically stain all tissue weakly (at both

concentrations) (Figure 4.4, third panels), and the staining is stronger at the 1:50 dilution. Higher-magnification imaging of hair cell stereocilia did not reveal specific staining of these structures (data not shown).

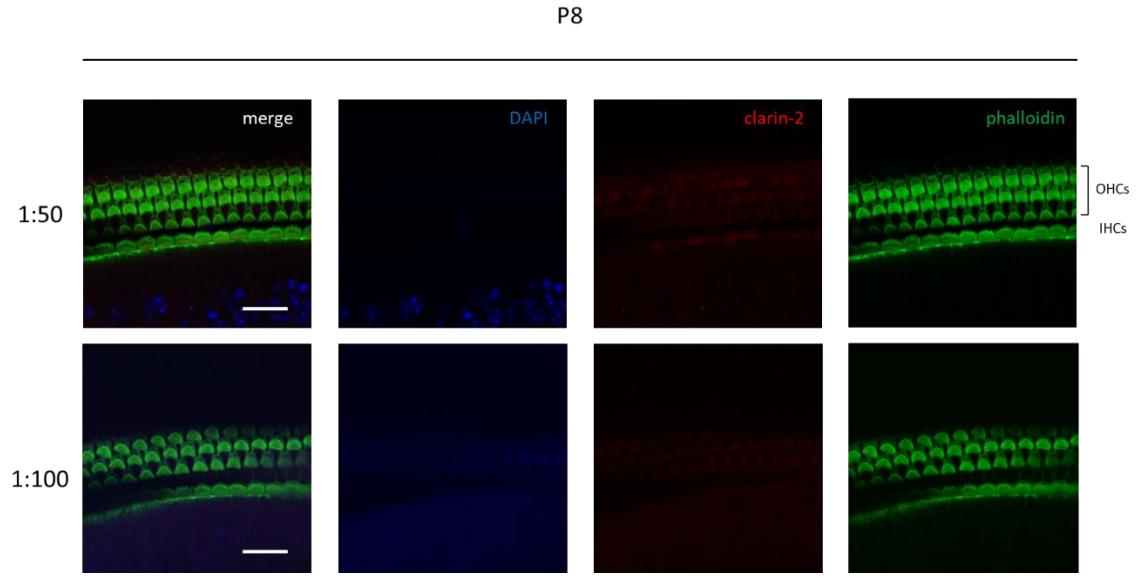

Figure 4.4: Immunolabelling of P8 wild type C57BL/6J sensory epithelium with Rb61 anti-clarin-2 (red) shows non-specific staining of inner and outer hair cells at both 1:50 (top panel) and 1:100 dilutions (bottom panel). Tissue was also stained with phalloidin to detect F-actin (green), and DAPI (blue) to detect nuclei. Note that these are not maximum intensity projections. x63 magnification, scale – 20 µm.

Absence of specific labelling, even when using high concentrations of primary antibody, could be due to two main reasons: the primary antibody lacks specificity/avidity for clarin-2; or, the amount of clarin-2 present in the hair cell is very small, and as such below levels of detection. In addition, the generalised background labelling could be due to the antibody cross-reacting with other non-specific proteins. In order to determine if the problem lies with the bespoke-made antibody, the experiment was repeated using a commercially-available antibody from Abcam (ab122790). However, at both P5 and P8, incubation with the Abcam anti-clarin-2 antibody resulted in non-specific staining of sensory epithelium in the cochlear duct (Figure 4.5). Staining did not dramatically differ between P5 (top panel) and P8 (bottom panel) tissue.

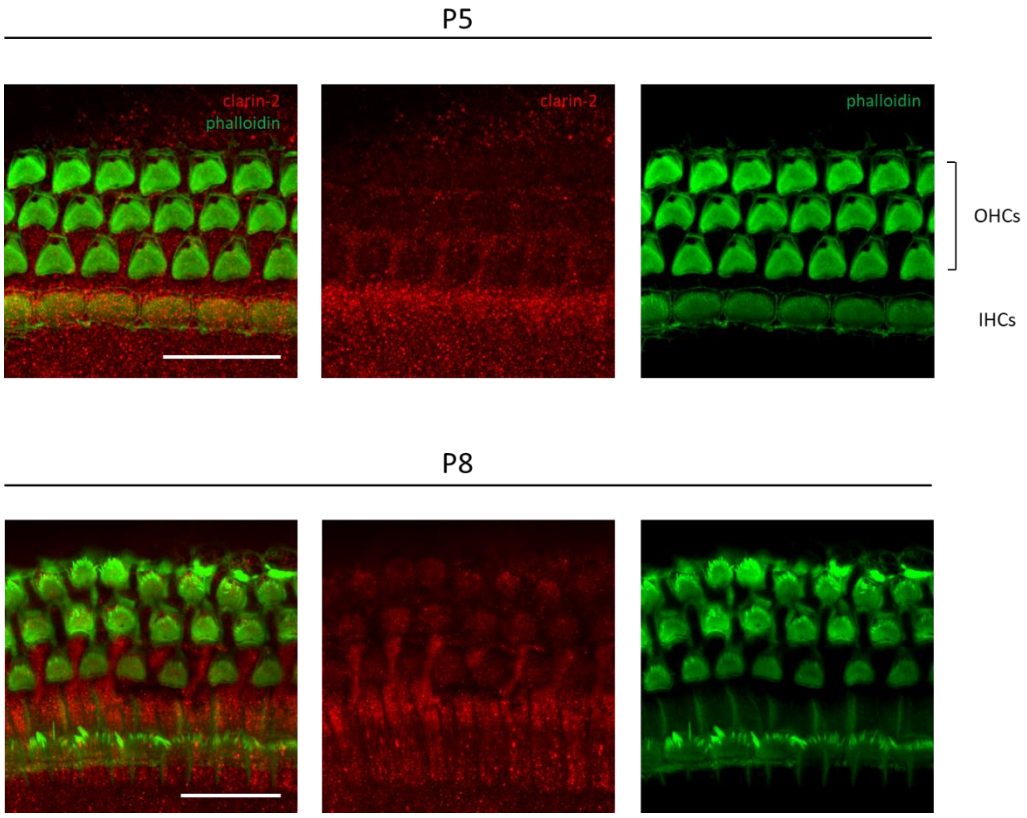

Figure 4.5: Immunolabelling of postnatal wild type whole mount tissue with Abcam anti-clarin-2 antibody shows non-specific staining of sensory epithelium. Tissue was also stained with phalloidin to detect F-actin in the stereocilia. All images are maximum intensity projections. x63 magnification, with added zoom of 2.7 (P5 images) and 2.2 (P8 images). Scale – 20 µm

4.2.3 Immunolabelling of vibratome-cut cochlear sections

Whole mount immunolabelling of postnatal animals with two different clarin-2 antibodies (the bespoke-made Rb61 and the commercially available Abcam (ab122790)) were, despite numerous attempts, unsuccessful. However at this time, colleagues working to identify genes associated with aged-related hearing loss within the UK Biobank cohort, reported successful immunolabelling of clarin-2 employing vibratome-cut cochlear sections prepared from a P30 wild type mouse and using a commercially-available anti-clarin-2 antibody (Atlas (HPA042407)). From their immunolabelling result, they conclude that clarin-2 is localised to IHCs and OHCs (Figure 4.6) (Wells et al., 2019).

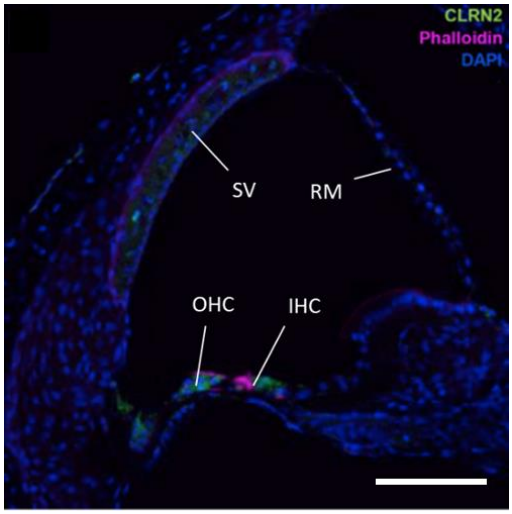

Figure 4.6: Immunofluorescence image of P30 mouse organ of Corti, showing clarin-2 localisation in hair cell bodies. The vibratome sections (200 µm thick) also stained with phalloidin (magenta) to detected acting, and DAPI (blue) to detect nuclei. Magnification x20 magnification 100 µm, scale - . SV – stria vascularis; RM – Reissner's membrane. Adapted from Wells et al., 2019.

Using this protocol, initial immunolabelling of P30 C57BL/6J vibratome-cut cochlear tissue appeared successful, with clarin-2 staining appearing in the organ of Corti and more specifically around the hair cells (data not shown). Further immunolabelled sections appear to show weak anti-clarin-2 staining in the stereocilia of both inner and outer hair cells, and additional stronger staining in cells lateral to the OHCs – possibly Boettcher, Hensen, or Claudius cells (Figure 4.7, top and middle panels). However, a no primary negative control (incubated with block only, without the anti-clarin-2 antibody) showed strong non-specific staining of inner and outer hair cell stereocilia (Figure 4.7, bottom panel).

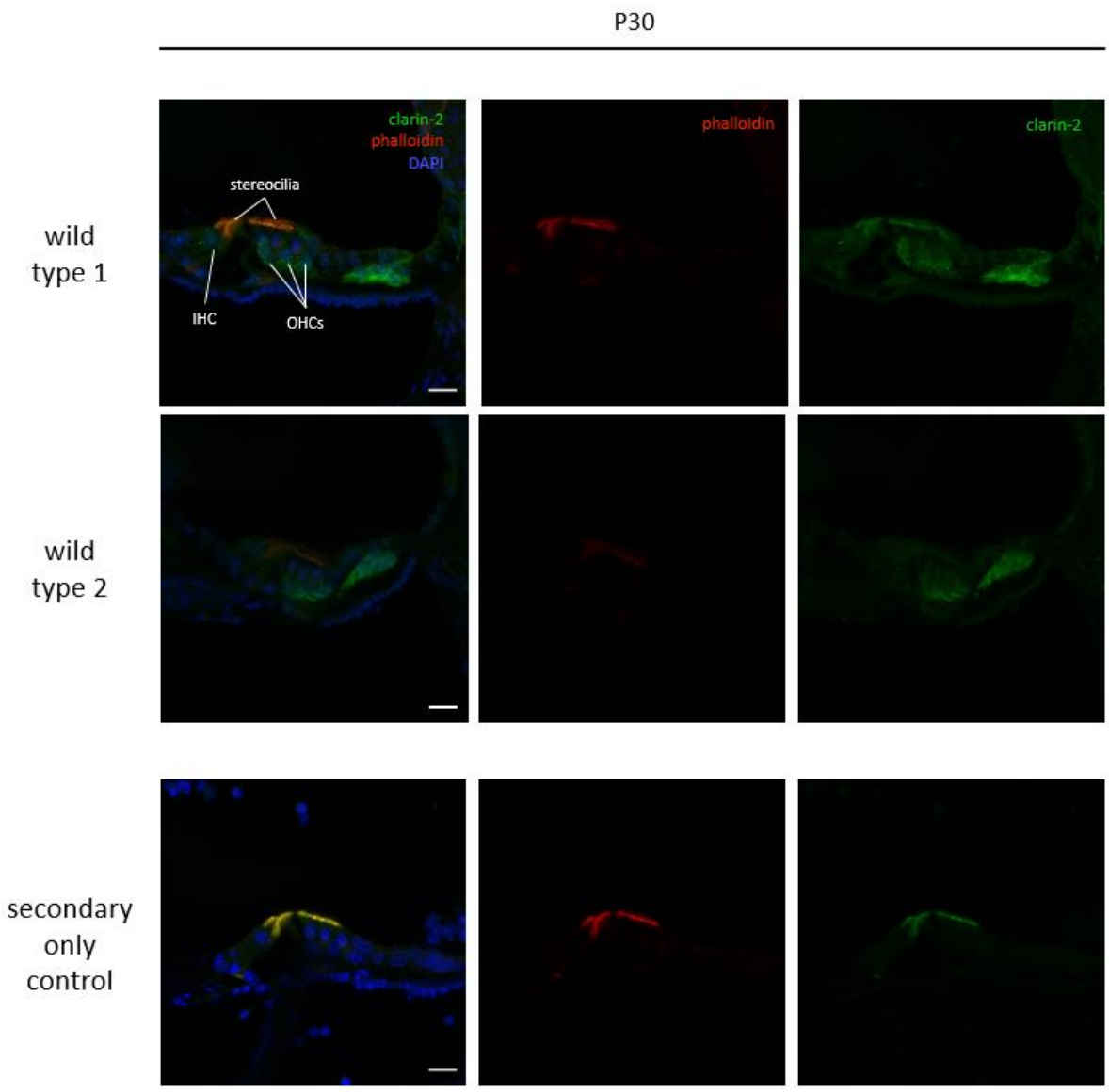

Figure 4.7: Atlas anti-clarin-2 antibody staining (green) on vibratome sections from wild type P30 cochlea appears to target tissue non-specifically (top and middle panels), but a secondary only control sample demonstrates specific staining of the inner and outer hair cell stereocilia (bottom panel). Staining in wild type 1 (top panel) stains stereocilia and cell bodies of all hair cells, as well as cells to the right of the OHCs, which could be Boettcher, Hensen, or Claudius cells. Similar non-specific staining is seen in wild type 2 (middle panel), with more staining at the base of the cell body. Tissue was also stained with Texas Red to detect phalloidin/F-actin (red), and DAPI (blue) to detect nuclei. Staining for wild type 2 (middle panels) is weak for all antibodies, but present. Maximum intensity projections taken with x20 magnification with a x1.5 zoom. Scale – 20 µm.

In another attempt to obtain a true signal using the Atlas anti-clarin-2 antibody, the experiment was repeated using age-matched wild type mice, but with the configuration of primary and secondary antibodies switched for each experiment (Figure 4.8A and B). When this was done, no anti-clarin-2 signal was detected in either configuration, under either experimental or control conditions.

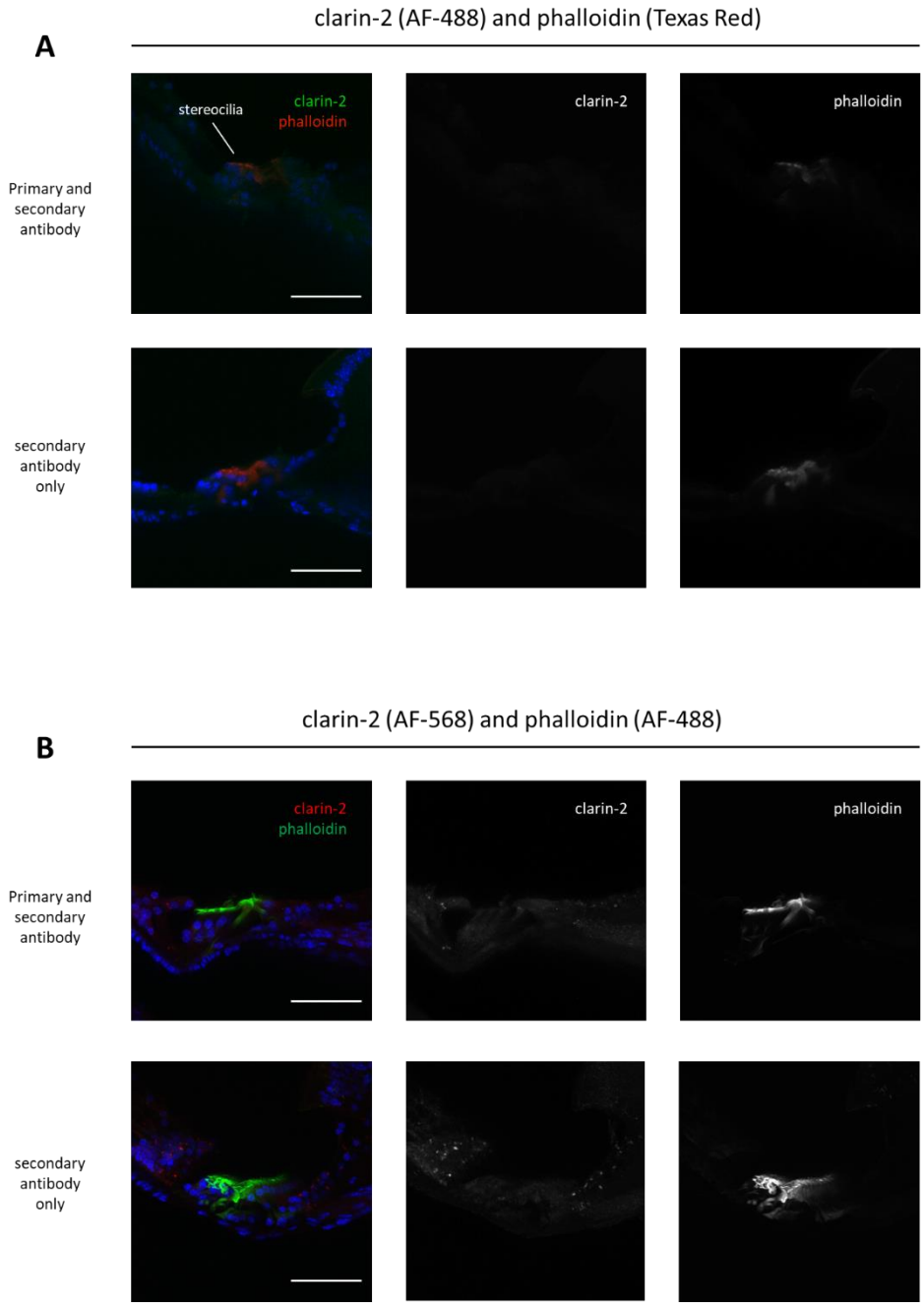

Figure 4.8: Different configurations of primary and secondary antibodies, and phalloidin markers, does not improve Atlas anti-clarin-2 signal. Neither the first configuration **(A)**, clarin-2 with AF-488 (green) and phalloidin with Texas Red (red)) nor the second configuration **(B)**, clarin-2 with AF-568 (red) and phalloidin with AF-488 (green)) demonstrated clarin-2 staining. Immunolabelling of tissue and imaging was performed by Dr Sherylanne Newton, MRC Harwell Institute. Maximum intensity projections taken with x20 magnification. AF – AlexaFluor. Scale – 50 µm.

4.3 Discussion

In order to ascertain the temporal and spatial localisation of clarin-2 protein in the mouse cochlea, various immunolabelling experiments were carried out and these are summarised in this chapter. Despite using several different anti-clarin-2 antibodies (both bespoke-made and commercially available), used at various concentrations, on tissue processed in several ways, and combinations of reagents, ultimately the cellular/subcellular localisation of clarin-2 could not be determined using traditional immunofluorescence techniques (Table 2.13).

While immunolabelling can be an efficient method to determine the localisation pattern of proteins, there is a multitude of factors that could explain why it was not successful in this instance. Firstly, the available cochlear epithelium scRNA-seq data suggest that *Clrn2* transcripts are specifically found in hair cells (Figure 4.2 and Figure 4.3). However, compared with other known hair cell-specific genes (for example *Myo7a*, *Myo15* and *Strc*), the abundance of *Clrn2* transcripts is much lower, which might suggest that the level of translated clarin-2 protein is also very low. As such, it could be the case that the level of clarin-2 protein within hair cells is below detectable levels when using these particular anti-clarin-2 antibodies. While increasing the concentration of primary antibody can help to overcome this, there comes a point where background (non-specific) staining masks any specific signal.

Secondly, it could be theorised that clarin-2 protein is degraded during the dissection and processing of the cochlear tissue. This is unlikely, as the protocol has worked well for immunolabelling studies involving other hair cell proteins. However, if this is the case, this could be alleviated by more gentle handling (particularly during the sub-dissection of the cochlea in whole mount tissue), use of protein inhibitors to reduce protein degradation, or by attempting another processing method such as cryosectioning – although these, of course, come with their own obstacles. Additionally, protein can degrade if not fixed appropriately; however, the methods of fixation used here (4% paraformaldehyde (PFA) in PBS overnight at 4˚C, with gentle agitation) are standard for fixing cochlear tissue for immunolabelling experiments, and in all experiments appropriate care was taken to ensure proper

fixation and subsequent washing of the tissue. Any future attempts using these anti-clarin-2 antibodies could be undertaken with different fixation methods, and other modifications to the protocol, such as including an antigen retrieval step – which was not used in my experiments due to the delicate nature of whole mount cochlear tissue. If antigen retrieval is attempted in future experiments, extra care (for example, more gentle handling) would need to be taken to ensure the integrity of the tissue. Other more sensitive approaches could also be investigated, such as using an ABC detection kit.

Finally, clarin-2 may simply not be present in hair cells, or indeed the organ of Corti, at the time points explored. However, this is unlikely for three reasons: the qRT-PCR data from wild type C57BL/6J (Figure 1.13B) mice demonstrates expression of *Clrn2* transcripts that increase three-fold from P12 to P16 which remains constant through to P28 (the latest time point tested); the scRNA-seq data also suggest that *Clrn2* transcripts are present in hair cells over the time points tested; and *clarinet* mice exhibit a hair cell phenotype. While none of these experiments provide conclusive evidence that clarin-2 will be present in hair cells over the ages tested, together they are highly indicative.

Ultimately, it is likely the case that the anti-clarin-2 antibodies tested do not have sufficient affinity for clarin-2 under the conditions used, and perhaps additional antibodies should be tested (including antibodies from LifeSpan Biosciences (LS-C396116), Abbexa (abx303441) and Proteintech (23994-1-AP)). However, mouse clarin-2 is a relatively small 232-amino acid protein that has four-transmembrane domains and two extracellular loops, and as such the opportunity for immunogenic regions is very limited (Figure 4.9A). The two commercially available antibodies used in these experiments are reportedly raised against the same region of the clarin-2 protein: the second extracellular loop. Similarly, the bespoke-made antibody was raised using a peptide that includes the second extracellular loop and the remaining C-terminal sequence (Figure 4.9B).

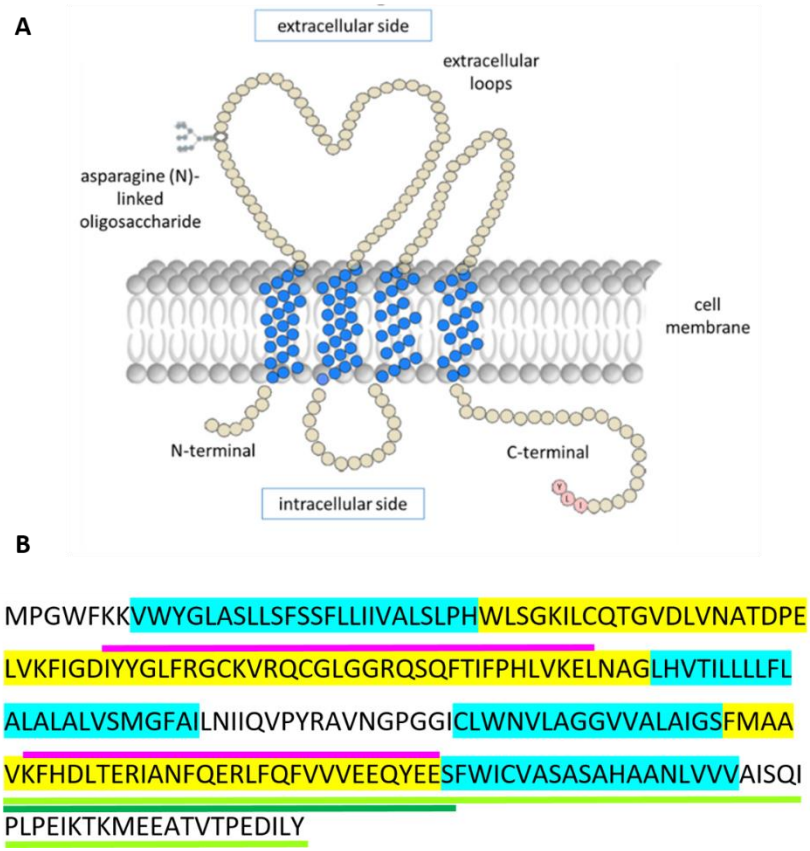

Figure 4.9: Mouse clarin-2 protein. (A) Predicted topology of clarin-2. Four transmembrane domains are indicated in blue. There are two extracellular loops and one extracellular oligosaccharide. Both the N and C terminals are intracellular. **(B) clarin-2 protein sequence with predicted structural features. Blue and yellow highlighted residues indicate transmembrane domains and non-transmembrane domains, respectively.** Pink regions indicate predicted extracellular loops. Commercial antibodies target the same region within the second extracellular loop (dark green region), and the 'bespoke-made' antibody target the same region plus residues to the N terminus of the protein (light green region).

Given the lack of specific staining (without background staining) of any tissue, it is unlikely that the anti-clarin-2 antibodies are cross-reacting with other members of the clarin protein family; namely clarin-1, which is known to localise to stereocilia and synaptic terminals at various postnatal time points (Zallocchi et al., 2009). However, this cannot be ruled out given the moderate conservation between the orthologues, which share 36% of their peptide sequence and score 56% for 'positive' residues (which are structurally similar) (Figure 4.10).

While increasing the concentration of the anti-clarin-2 primary antibody may boost its signal, it can also increase background signal – which can result in the antibody detecting any tissue present (which is likely the case in Figure 4.5). For these reasons, generating an anti-clarin-2 antibody is difficult and other methods to visualise clarin-2 localisation should be explored.

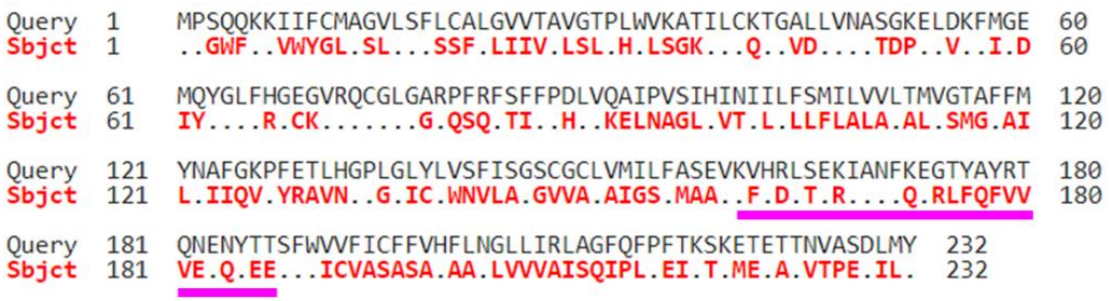

Figure 4.10: clarin-1 and clarin-2 peptide sequence alignment. Sequences are 36% identical, and scored 56% for positives (for residues with similar chemical structure, charge and so on). Query – clarin-1-201; Sbjct (red) – clarin-2-201. Dots represent identical residues; note that this sequence alignment does not illustrate positives. Numbers indicate residue number (both proteins comprise 232 residues. The pink region indicates clarin-2's (predicted) second extracellular loop. Of the 28 composite residues of this loop, 11 residues (39%) are shared with clarin-1's respective residues. Assessed using the Basic Local Alignment Search Tool (BLAST) (https://blast.ncbi.nlm.nih.gov/).

As to why I could not replicate the labelling reported by (Wells et al., 2019), it should be noted that their immunolabelling study does not report the use of appropriate controls, such as: including a secondary antibody-only control; labelling with primary antibody that has been pre-absorbed with the immunising peptide; or, labelling of cochlear tissue that does not express clarin-2 (such as *Clrn2*$^{clarinet/clarinet}$ homozygous tissue). As such, it is therefore difficult to fully interpret their results.

As mentioned, other approaches can be exploited to indirectly address the question of which cochlear cells are required to express clarin-2 for hearing. The use of conditional knockouts is an example of this, and this is explored in Chapter 5.

Chapter 5: Separating the prenatal and postnatal requirement of *Clrn2*

5.1 Introduction

As discussed in Chapter 3, *Clrn2* was confirmed as a novel hearing gene in mice. Investigation of the *clarinet* mouse model (characterised by a W4STOP truncation) has revealed an early-onset, progressive hearing loss. Through electrophysiological experiments and ultrastructural analyses, *Clrn2* was shown to be required for both MET current and stereocilia maintenance, once the bundle architecture has been established. The work undertaken in Chapter 4 unfortunately demonstrated the unreliable nature of typical immunological and molecular methods used to investigate protein localisation. However, qRT-PCR studies undertaken using whole cochlear RNA extracted from wild type mice revealed a three-fold increase in *Clrn2* transcript levels between P12 and P16, with expression remaining high until at least P28 (the latest time point investigated) (Figure 1.13B). This suggests that clarin-2 not only has a role in the functional maturation of the hair cell bundle, but that it is also important after the onset of hearing (~P12), an age when the bundle architecture has already been established.

Before my studies in *Clrn2* began, there were no reports of *CLRN2* mutations causing hearing loss in humans. Colleagues at University College London and King's College London were, however, able to investigate *CLRN2* as part of the UK Biobank study. The UK Biobank is an open source GWAS database with over 500,000 participants, aged between 40 and 69 when recruited into the study between 2006 and 2010 (Sudlow et al., 2015). Phenotypic and genotypic characteristics collected from participants include data from questionnaires, physical measurements, sample assays, imaging and genome-wide genotyping.

To investigate self-reported hearing difficulty within the Biobank cohort, participants completed questionnaires on their hearing. Analysis into age-related hearing impairment using data from the UK

Biobank was carried out by Dr Helena Wells, Prof Frances Williams and Dr Sally Dawson at King's College London Department of Twin Research and Genetic Epidemiology, and the University College London Ear Institute. One GWAS was undertaken using self-reported hearing difficulty, and a second was based on self-reported hearing aid use. Of the 44 independent genome-wide significant loci identified, 34 were novel associations with hearing difficulty (Wells et al., 2019).

To directly assess a link between adult hearing difficulty and the *CLRN2* gene, an association was tested between all 484 genotyped and imputed SNPs within 100 kb of the gene. Within this specific region, 36 SNPs were associated with hearing impairment, which included five highly associated SNPs that are located in or very close to the gene (Figure 5.1). The 'rs35414371' SNP with the highest association (p = 1.60E-11) is located only 2 kb downstream of the *CLRN2* gene (Figure 5.1, purple diamond). The second most associated SNP, 'rs13147559' (p = 1.70E-11), lies within exon 2 of the *CLRN2* gene. This SNP (c.337C > G) represents a missense variant (Leucine to Valine) in the encoded second transmembrane domain. *In silico* studies show that the Leucine residue at position 113 is evolutionarily conserved across species. Furthermore, two prediction tools, PolyPhen-2 and MutationAssessor, suggest that substitution with a Valine residue at this position might be detrimental to clarin-2 protein function, returning scores of 'possibly damaging' and 'medium' respectively (data not shown).

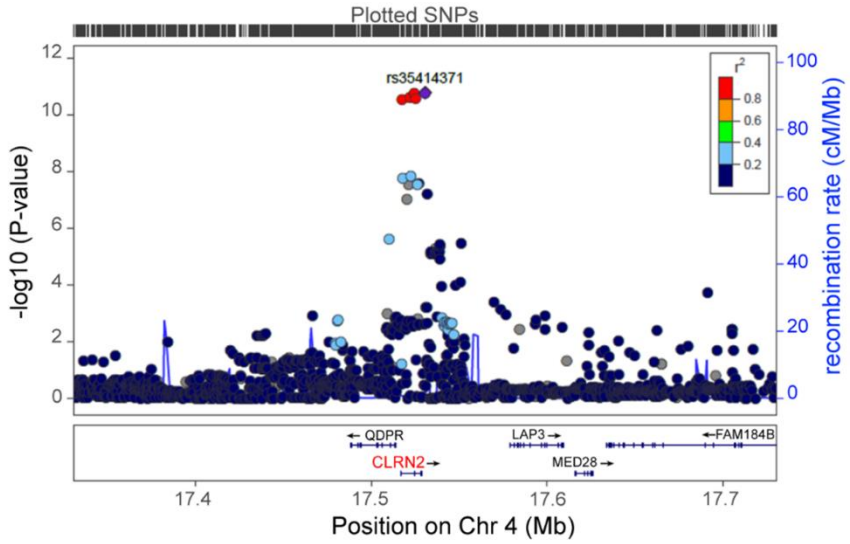

Figure 5.1: Regional plot of P-values for single nucleotide polymorphism (SNP) association with hearing difficulty around the *CLRN2* gene locus on chromosome 4. The genes within the region are indicated and the direction of their transcription is shown by black arrows. Colouring is based on linkage disequilibrium (LD) across the region with the most associated SNP, rs35414371, shown in purple. Data generated by Dr Helena Wells, Prof Frances Williams and Dr Sally Dawson. Data reproduced from Dunbar et al., 2019. Mb – megabases.

These data collected and analysed by colleagues suggest that the *CLRN2* gene is associated with age-related hearing function in humans. This finding supports the previously stated supposition that clarin-2 may have an important 'maintenance' function in the mammalian auditory system.

In order to distinguish the cellular requirement of clarin-2 for hearing, and to determine if clarin-2 has a maintenance role after the onset of hearing, a *Clrn2* conditional knockout model was needed to allow the spatial and temporal expression of clarin-2 to be controlled.

The Cre/*loxP* system is a common approach used to control gene expression, and thereby can be utilised to investigate spatial and temporal requirement of a given gene. In this technology, harnessed from bacterial systems, offspring receive a target gene flanked by *loxP* (floxed allele) sites from one parent and Cre recombinase under the control of a tissue-specific promoter from the other. The target gene is knocked out in cells/tissues where the recombinase is expressed, resulting in cell/tissue-specific knockouts (Lakso et al., 1992, Orban et al., 1992, Paigen, 2003).

CreER(T) (estrogen receptor) variant Cre driver lines allow inducible Cre activation, which occurs only after administration of tamoxifen (Metzger and Chambon, 2001). This allows for the controlled

temporal deletion of floxed target genes in cells/tissues expressing the CreER(T) recombinase. For a more detailed description on this system, see the review by Kim et al (2018). Unfortunately, a conditional *Clrn2* knockout mouse was not available from any of the mutant mouse repositories.

The *Clrn2* gene is relatively simple, consisting of 3 exons that are all in-frame. While all being in-frame, there are no reports suggesting additional splice isoforms other than the full-length transcript (exons 1-2-3 spliced together). As such, when designing a conditional knockout allele for *Clrn2,* options were limited to floxing exon 2. However, before utilising such a conditional knockout model, it was deemed important to investigate and understand the phenotype of mice constitutively missing this exon. The generation and phenotyping of this mouse (*Clrn2*^{del529}) is described in this chapter.

5.2 Results

5.2.1 *Clrn2*^{del629} auditory phenotype

As covered in Chapter 3, transcript analysis of RNA extracted from cochlear ducts collected from *Clrn2*^{del629} mice identified that the deletion of exon 2 resulted in exons 1 and 3 being spliced together (Figure 3.2). Exons 1 and 3 are in-frame to each other and as such could lead to the production of a smaller protein, lacking two of the four transmembrane domains that are encoded by exon 2. To assess the effect of this deletion mutation on auditory function, *Clrn2*$^{del629/del629}$ mice were bred and subject to auditory phenotyping. If the deletion of exon 2 is a null allele, the *Clrn2*$^{del629/del629}$ mice should phenocopy *clarinet* mutant animals. However, if the deletion generates a hypomorphic allele (i.e. retains some function), mice homozygous for this deletion allele may exhibit a hearing loss that is not as severe as that seen in *clarinet* mutants.

As with the *clarinet* mutant, the number of wild type, heterozygous and homozygous animals, born from *Clrn2*$^{del629/+}$ heterozygous intercross matings, were counted at weaning to determine if the *del629* mutation affects viability. Across six litters sampled, the three genotypes were present in line with the expected standard Mendelian ratios (1:2:1 for wild type, heterozygotes and homozygotes respectively), with an average number of 5.2 pups per litter (Figure 5.2). These counts indicate that, like the *Clrn2*^{clarinet} mutation, the *Clrn2*^{del629} mutation is neither embryonic, nor neonatal, lethal.

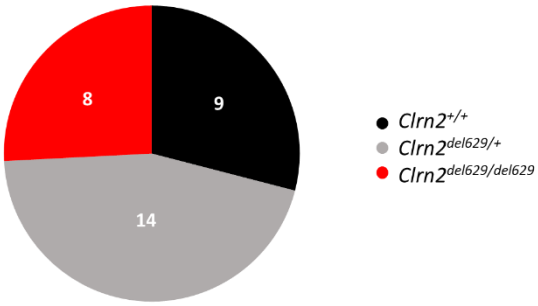

Figure 5.2: The *Clrn2*^{del629} mutation does not affect survival. Expected Mendelian Ratios (1:2:1) are exhibited across six *Clrn2*^{del629} litters (31 pups total), with counts conducted at weaning age. n numbers for each genotype are indicated in the corresponding section on the pie chart.

Furthermore, in order to determine whether the *Clrn2*^{del629} mutation affects the postnatal growth of mutant animals, body weights recorded before the ABR procedure at P21 were compared across genotypes. Body weights at P21, of both female and male mutant mice (Figure 5.3), were not overtly different from their sex-matched littermates. This suggests that the *Clrn2*^{del629} mutation does not affect the ability of null mice to thrive during this pre-weaning period.

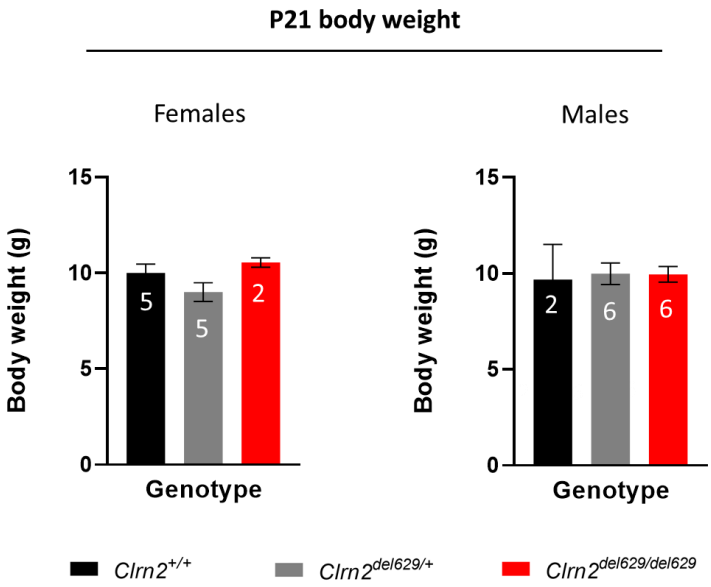

Figure 5.3: Averaged body weights at P21 suggest that the *Clrn2*^{del629} mutation does not affect the pre-weaning growth of male or female mutant mice. n numbers for each group are indicated on the corresponding bar. Data shown are mean ± s.e.m.

Clrn2^{del629} mice underwent ABR testing at P21. This age was chosen for several reasons: the auditory system has largely matured by this point, the expression of wild type *Clrn2* is increased, and (most importantly) to match with a time point at which *clarinet* mice underwent ABR testing.

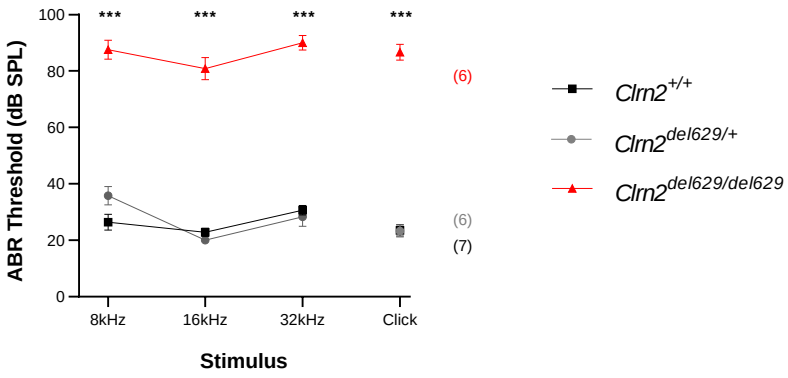

Figure 5.4: Averaged ABR thresholds are elevated in P21 *Clrn2*^{del629} mice at all frequencies tested. n numbers for each genotype are indicated to the right of the graph. Data shown are mean ± s.e.m., ***p<0.001, one-way ANOVA.

While P21 (± 1 day) heterozygous mice (grey) exhibit thresholds (mean click threshold of 23 ± 5 dB SPL) comparable to that of wild type littermates (black) (mean click threshold of 24 ± 6 dB SPL), aged-matched homozygous *Clrn2*$^{del629/del629}$ mice (red) demonstrate profound hearing loss at all frequencies tested (Figure 5.4), with a mean click threshold of 87 ± 7 dB SPL, whereas demonstrating the recessive nature of the mutation. Interestingly, the mean thresholds of *Clrn2*^{del629} homozygotes appear to be marginally higher than those of age-matched *Clrn2*^{clarinet} homozygotes (Figure 5.5) (mean click threshold of 79 ± 17 dB SPL), at all frequencies tested, though these differences are not statistically significant.

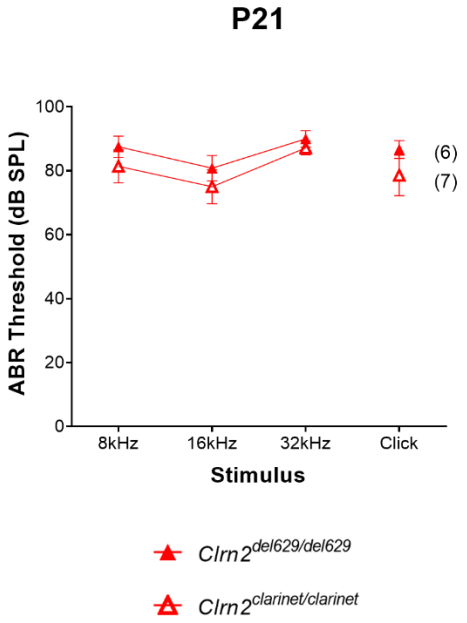

Figure 5.5: Isolated averaged ABR thresholds of *Clrn2* mutants at P21 indicates that *Clrn2*$^{del629/del629}$ (solid triangle) hearing loss is slightly more severe than the *Clrn2*$^{clarinet/clarinet}$ (open triangle) phenotype. n numbers for each group are indicated to the right of the graph. Data shown are average ± s.e.m.

To further assess auditory function, *Clrn2*^{del629} mice underwent terminal DPOAE testing at P28. This revealed an OHC-specific functional deficit in *Clrn2*$^{del629/del629}$ animals, with homozygotes eliciting significantly reduced emissions at the lower frequencies (8 kHz) in comparison to wild type and heterozygous age-matched littermates (Figure 5.6). While the mean responses at the mid (16 kHz) and

higher (32 kHz) frequencies were reduced compared to controls, these differences were not statistically significant.

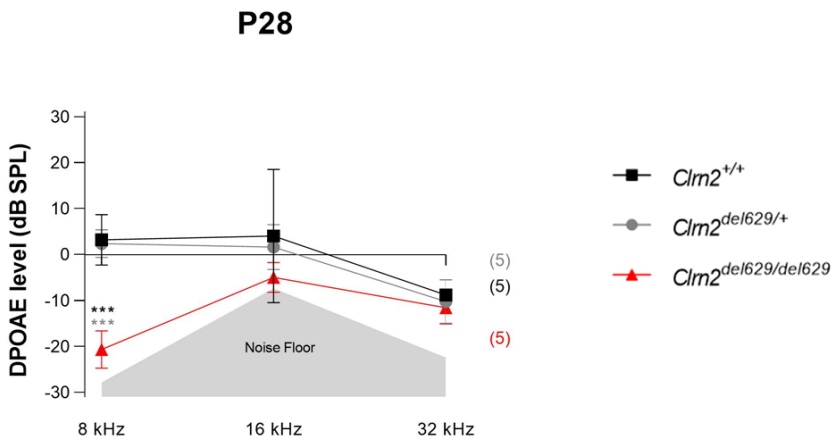

Figure 5.6: Averaged DPOAE responses in P28 *Clrn2^{del629} mice* are reduced at lower frequencies. n numbers for each group are indicated to the right of the graph. Data shown are mean ± s.d. ***p<0.001, one-way ANOVA.

DPOAE recordings are grossly similar between the *Clrn2^{del629}* and *Clrn2^{clarinet}* mutants, apart from the response to the 32 kHz stimulus, which is lower in *clarinet* animals (Figure 3.11). Furthermore, recordings from *del629* control groups are relatively low when compared to those elicited from controls from the *clarinet* cohort. Slight variability cannot be eliminated between individuals, and reasons for differences could include depth of anaesthesia (which is itself influenced by numerous factors) and positioning of the probe in the ear canal.

The auditory phenotyping undertaken in *Clrn2^{del629}* mice demonstrates a severe, early-onset hearing deficit that largely phenocopies that of the *Clrn2^{clarinet}* mutant.

5.2.2 Ultrastructural analysis of the *Clrn2*^{del629} mutant

To investigate *Clrn2*^{del629} hair bundle architecture, inner ears from P28 animals were collected and processed for scanning electron microscopy. Gross patterning of the sensory epithelium was normal, with three rows of OHCs and one row of IHCs extending along its length (data not shown).

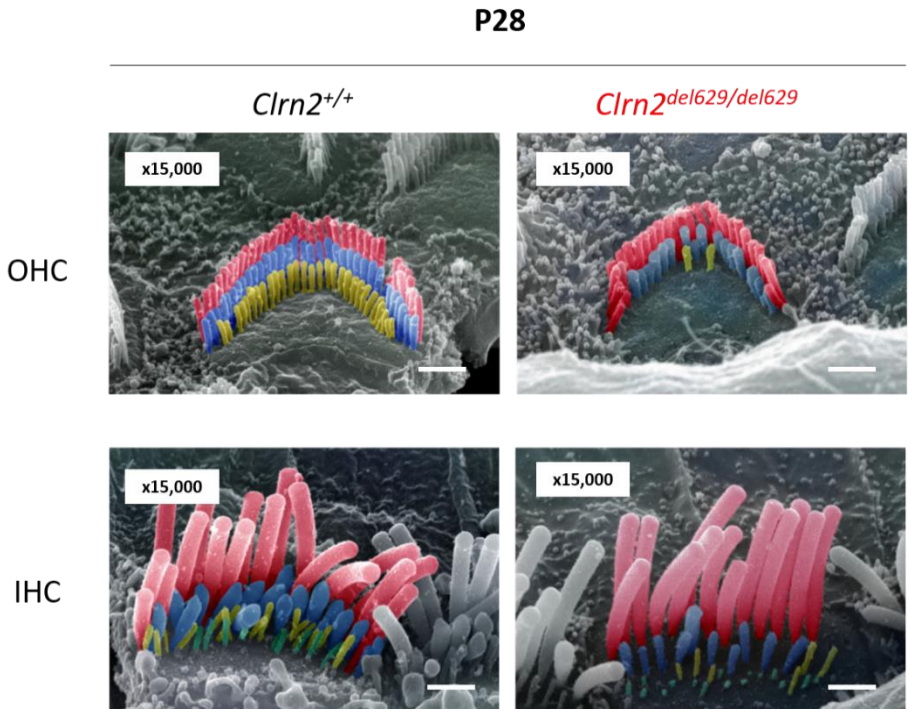

Figure 5.7: Ultrastructural analysis demonstrates abnormal hair bundle architecture in *Clrn2*^{del629} homozygous mice. Representative pseudo-coloured scanning electron micrographs illustrate the three rows of tallest (red), middle (blue) and short (yellow) of stereocilia in P28 (± 1 day) OHC and IHC wild type (left panels) and homozygous (right panels) bundles. For control (wild type and heterozygous) and mutant individual mice, n = 2 and 2, respectively). Magnification is indicated on each individual micrograph. Scale – 1 µm.

Close examination of the hair bundle, however, revealed identical pathologies to those seen in the *clarinet* mutant, demonstrably the almost complete absence of the third row stereocilia in OHC bundles (Figure 5.7, top panel). Again, reminiscent of *clarinet,* second and third row stereocilia of IHC bundles are fewer in number and less prolate compared to controls (Figure 5.7, bottom panel). This close investigation of the *Clrn2*^{del629} hair bundles has demonstrated a phenotype strikingly similar to that of *clarinet* mice, and may lead to the severe auditory phenotype exhibited.

Taken together, the molecular, auditory and ultrastructural investigations of the *Clrn2*^{del629} mouse demonstrate that deletion of the second exon of the *Clrn2* gene causes an early-onset and severe hearing loss affecting all frequencies tested. Furthermore, as their auditory and hair bundle phenotypes are comparable to those present in *clarinet* mutant mice, it is likely that the *Clrn2*^{del629} mutation represents a complete loss-of-function allele, and as such is suitable to adapt for use as a conditional allele.

5.2.3 Design and generation of a conditional *Clrn2* knockout mouse

Based on the phenotype of the *Clrn2*^{del629} mutant, an allele allowing the controlled deletion of the second exon of the *Clrn2* gene would permit investigation into the cellular requirement of *Clrn2*/clarin-2 in the inner ear. Furthermore, if coupled with an appropriate inducible Cre recombinase, a *Clrn2* floxed exon 2 allele would also enable studies to distinguish between developmental- and maintenance-specific roles of *Clrn2* in the mammalian cochlea.

Therefore, a conditional *Clrn2* allele (*Clrn2*^{fl}) was designed, with a view to introduce *loxP* sites either side of exon 2 using CRISPR/Cas9 technology combined with a long single-stranded DNA (lssDNA) donor.

This genome editing project was conducted by the Molecular and Cellular Biology team at the MRC Harwell Institute. Briefly, sgRNAs (the custom guide RNAs which target the gene of interest) and a lssDNA (the donor template for homologous recombination) were co-injected along with Cas9 mRNA into single-cell embryos. Details of the sgRNA and lssDNA sequences used to insert *loxP* sites into the *Clrn2* gene are included in 2.1.2.2, and methods for this approach are described in detail in (Codner et al., 2018).

While non-homologous end joining (NHEJ) is the most common core mechanism of DNA repair following DNA cleavage as part of this process, homology-directed repair (HDR) is required in order for foreign DNA to be incorporated into the genome in a targeted region. Through HDR, an lssDNA

donor oligonucleotide comprising 5' and 3' homology arms and two *loxP* sites flanking *Clrn2*'s second exon were inserted into the gene (Figure 5.8).

Once a founder carrying the *Clrn2*^{fl} allele had been used to establish a colony, progeny could be bred with specific Cre driver lines to tightly control the expression of *Clrn2* for a given tissue or time point. When crossed with such a line, the *loxP* sites flanking exon 2 of *Clrn2* are identified and cleaved by the Cre recombinase present.

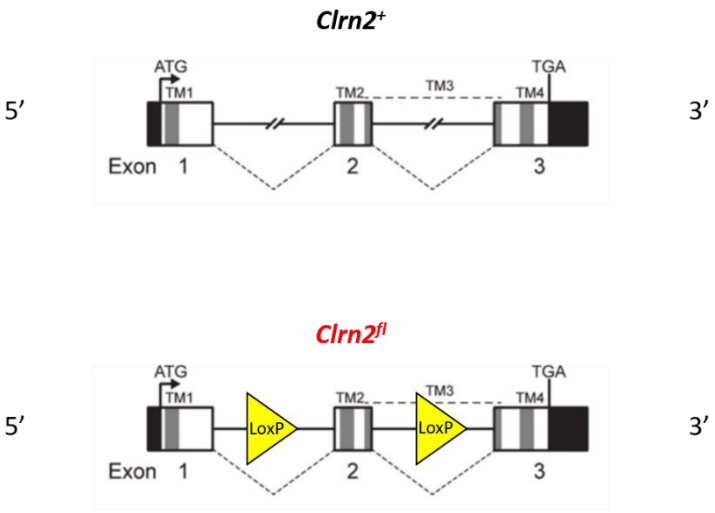

Figure 5.8: Schematic representation of mouse wild type (*Clrn2*$^{+}$) and *Clrn2*^{fl} mutant alleles, generated through CRISPR/Cas9 genome editing. When crossed with a Cre driver line, the *loxP* sites (yellow triangles) flanking the second exon of *Clrn2* are recognised by Cre recombinase, which mediates site-specific deletion of the DNA sequence between the *loxP* sites. This deletion of exon 2 results in a non-functional protein, as demonstrated by the *Clrn2*^{del629} mutant. The start (ATG) and stop (TGA) codons, and untranslated regions, are represented in black. Genomic regions encoding the four transmembrane (TM) domains are shown in grey. 5' and 3' ends are indicated.

The *Clrn2*^{del629} mouse carries a germline deletion of exon 2 of the *Clrn2* gene (i.e. deleted in every cell of the body), meaning therefore that no cell is able to produce functional clarin-2. However, the *Clrn2*^{fl} mouse carries a floxed *Clrn2* allele in every cell of the body, and therefore all cells that would normally express functional clarin-2 still do. It is only after Cre-mediated recombination that exon 2 is deleted and functional clarin-2 will be lost, which only occurs in those cells that express Cre.

5.2.4 Hair cell-specific deletion of *Clrn2* causes hearing loss

The cochlear sensory epithelium scRNA-seq data and the stereocilia bundle phenotype identified in *clarinet* mice together suggest that clarin-2 is critical for hair cell function and hearing. To investigate the requirement of *Clrn2* in immature auditory hair cells, the *Clrn2*^{fl} mouse was crossed to the *Myo15*^{cre} mouse, in which *Cre* expression is under the control of the *Myo15* promoter (Figure 5.9). The *Myo15*^{cre} mouse was obtained with permission from Professor Christine Petit, Institute Pasteur.

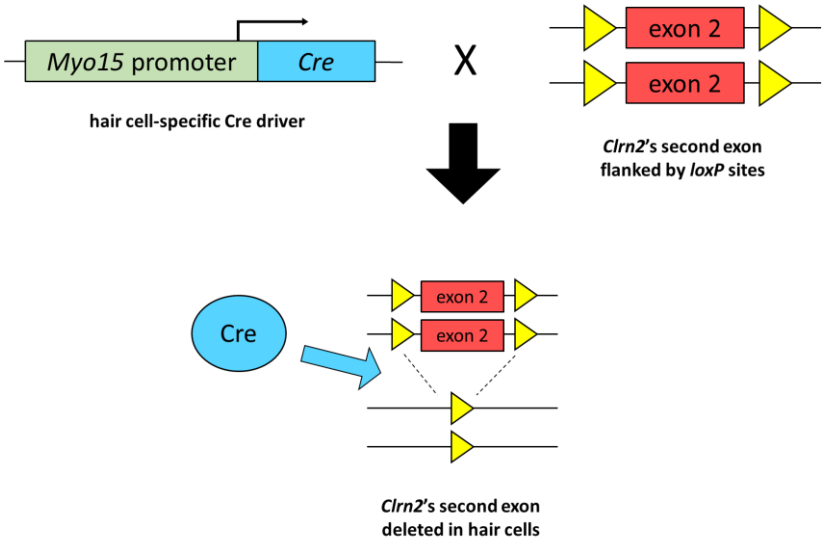

Figure 5.9: Schematic representation of a breeding strategy for generating a conditional *Clrn2* mutant. In the case of the *Clrn2*^{fl}*;Myo15*^{cre} mutant, one parent harbours a hair cell-specific (Myo15) driven *Cre* gene and the other harbours *loxP* sites (yellow) flanking *Clrn2*'s second exon (red). Expression of Cre recombinase (blue circle) mediates site-specific deletion between the loxP sites and ablation of *Clrn2*'s second exon. Adapted from Kim et al., 2018.

In *Myo15*^{cre} animals, Cre recombinase is specifically and robustly expressed in both inner and outer auditory hair cells from approximately P3 onwards in the cochlea (Caberlotto et al., 2011b). Therefore, the *Clrn2*^{fl}*;Myo15*^{cre} mouse will express *Clrn2* as normal during embryonic development, but cease to express functional *Clrn2* in hair cells during the early postnatal period. Auditory phenotyping and ultrastructural analyses of this conditional knockout mouse would therefore shed light on the temporal and spatial requirement of *Clrn2* in the early post-natal cochlea, and more specifically in the hair cells.

In order to obtain the *Clrn2*$^{fl/fl}$*;Myo15*$^{cre/+}$ experimental mice (only one copy of *Cre* is required to elicit Cre-mediated recombination) as well as the five control genotype groups, female mice heterozygous for the floxed allele (*Clrn2*$^{fl/+}$*;Myo15*$^{+/+}$*)* were crossed to male mice also heterozygous for the floxed allele, and heterozygous for the Cre (*Clrn2*$^{fl/+}$*;Myo15*$^{cre/+}$*)*.

ABRs were first recorded at P21, in accordance with phenotyping carried out in other *Clrn2* mutants at the same age. As mentioned, the breeding strategy above yielded six genotype groups, all of which were phenotyped.

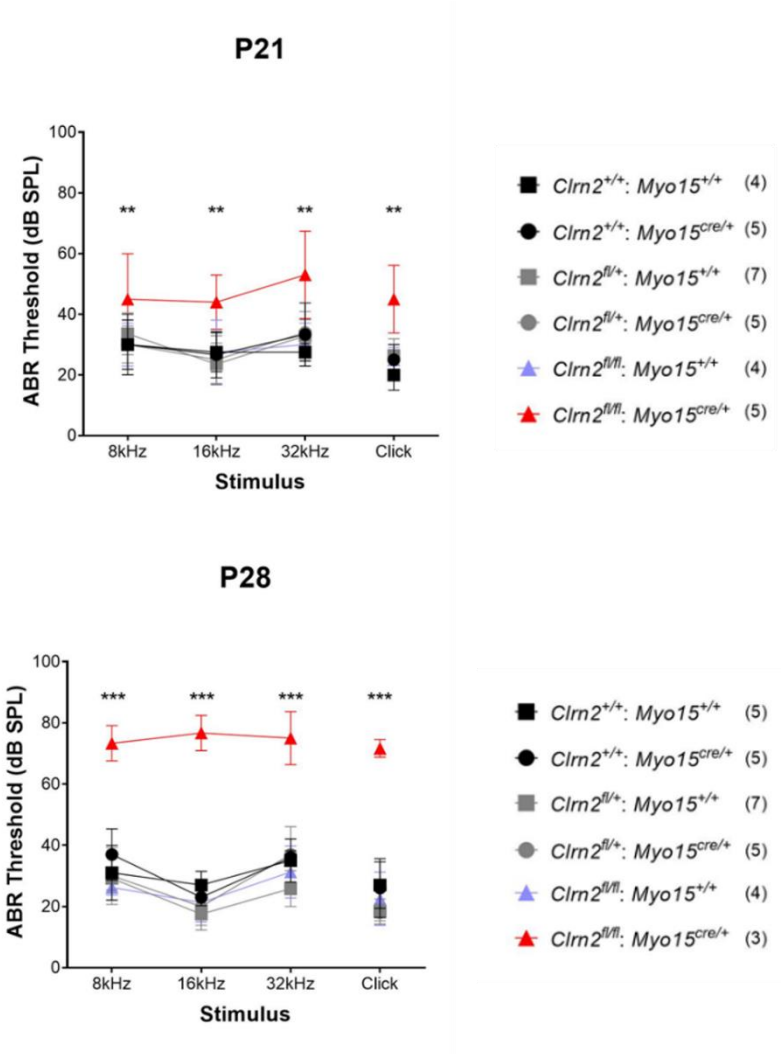

Figure 5.10: Averaged ABR thresholds are elevated in *Clrn2*$^{fl/fl}$*;Myo15*$^{cre/+}$ mice at all frequencies tested. While age-matched littermate controls exhibit normal hearing, *Clrn2*$^{fl/fl}$*;Myo15*$^{cre/+}$ mice (red) exhibit slightly elevated thresholds at P21 (± 1 day) which have progressed to approximately 75 dB SPL by P28 (± 1 day). n numbers for each genotype are indicated to the right of each graph. Data shown are average ± s.e.m. *p<0.03, **p<0.0001, two way ANOVA.

At P21, *Clrn2*$^{fl/fl}$*;Myo15*$^{cre/+}$ mice display elevated thresholds (Figure 5.10, red triangles) (mean click threshold 44 ± 11 dB SPL) when compared to all control groups (for example, mean click threshold 23 ± 3 dB SPL for *Clrn2*$^{fl/fl}$*;Myo15*$^{+/+}$ mice). However, the degree of hearing loss is not as severe as that previously seen in the aged-matched *Clrn2*$^{clarinet/clarinet}$ and *Clrn2*$^{del629/del629}$ mutants (mean click thresholds of 79 ± 17 dB SPL and 87 ± 7 dB (Figure 5.5), respectively. By P28, the hearing loss exhibited by *Clrn2*$^{fl/fl}$*;Myo15*$^{cre/+}$ animals has progressed (mean click threshold 72 ± 3 dB SPL) to similar levels exhibited by age-matched *clarinet* mutants (Figure 5.11). Statistical differences are observed between P28 mutants at 8 kHz and the click stimulus, but this may be due to low n numbers of *Clrn2*$^{fl/fl}$*;Myo15*$^{cre/+}$ mice available at this time point.

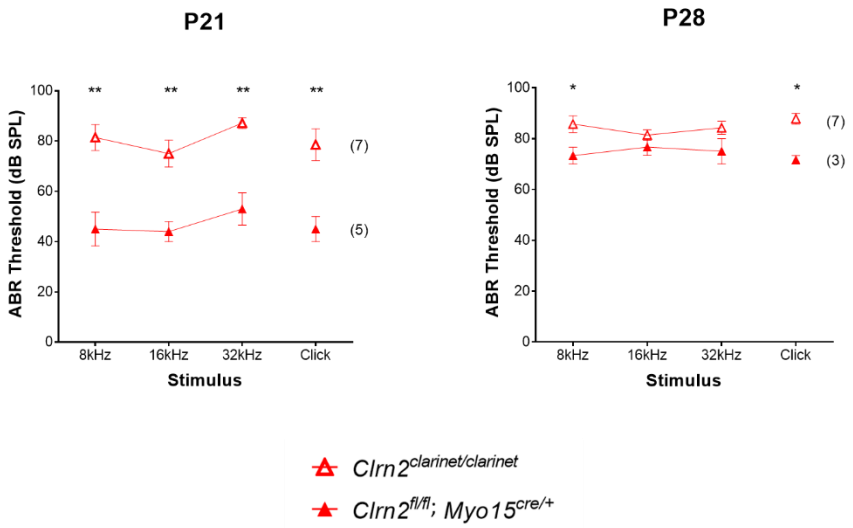

Figure 5.11: Isolated averaged ABR thresholds of *Clrn2* mutants at P21 and P28 indicates that *Clrn2*$^{fl/fl}$*;Myo15*$^{cre/+}$ (solid triangle) hearing loss progresses more slowly than the *Clrn2*$^{clarinet/clarinet}$ (open triangle) phenotype. n numbers for each group are indicated to the right of each graph. Data shown are average ± s.e.m. **p<0.005, *p<0.05, two way ANOVA.

Taken together, these data demonstrate that while hearing loss is present at P21 in the *Clrn2*$^{fl/fl}$*;Myo15*$^{cre/+}$ conditional knockout mice, it is not as severe as the hearing loss exhibited by the age-matched *Clrn2* constitutive (global) knockout mutants (*clarinet* and *del629*). However, by P28 (just

7 days later) the hearing thresholds of the *Clrn2*$^{fl/fl}$;*Myo15*$^{cre/+}$ mice are similar to those of age-matched *clarinet* mutants.

5.2.5 Ultrastructural analyses of *Clrn2*$^{fl/fl}$;*Myo15*$^{cre/+}$ mice

Longitudinal ABR testing of the *Clrn2*$^{fl/fl}$;*Myo15*$^{cre/+}$ mice indicates an early-onset progressive hearing loss phenotype. To investigate whether this could be attributable to abnormal hair bundle organisation, cochlear ducts from P42 control and experimental mice were collected and processed for scanning electron microscopy.

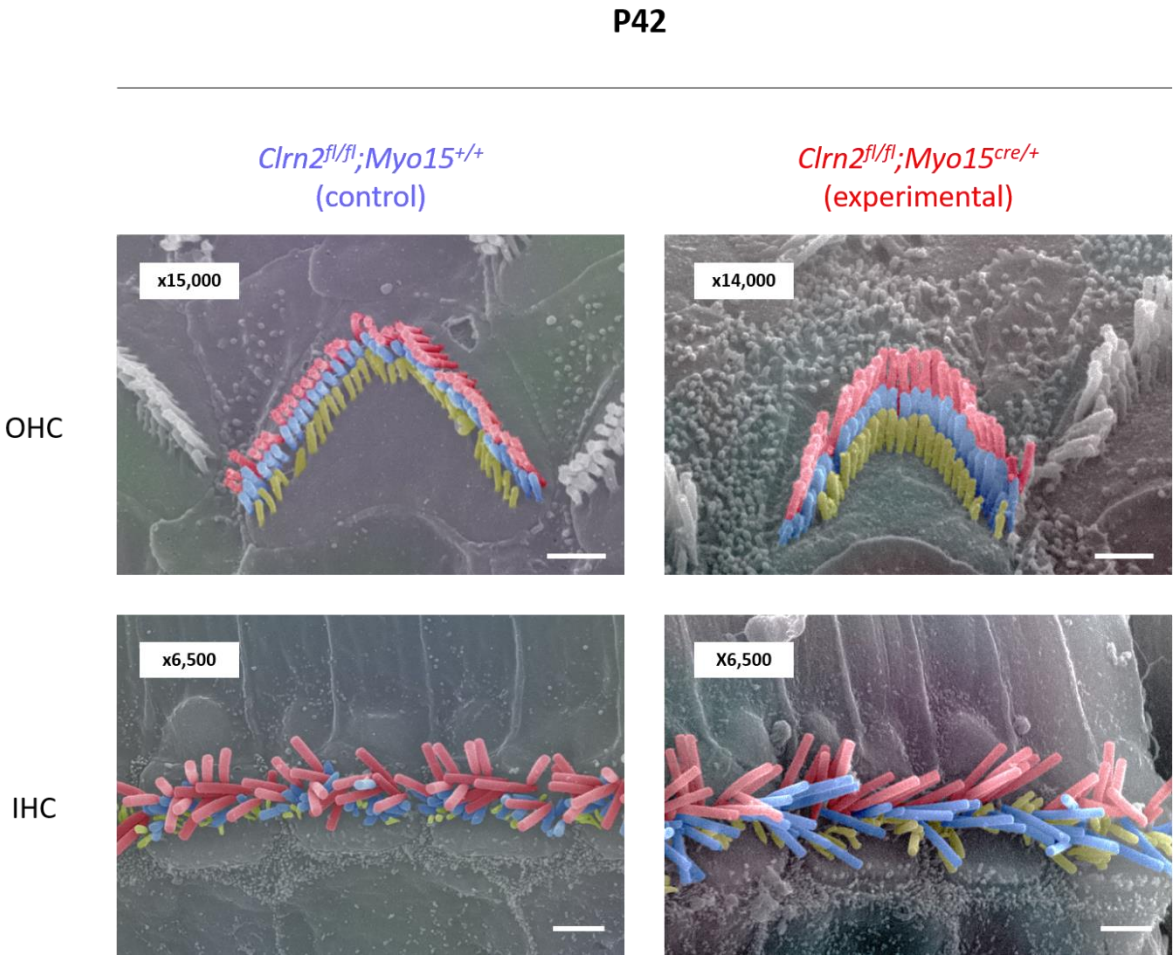

Figure 5.12: SEM ultrastructural analysis of *Clrn2*$^{fl/fl}$;*Myo15*$^{cre/+}$ hair bundles at P42 demonstrate normal OHC stereocilia that resemble those of the *Clrn2*$^{fl/fl}$;*Myo15*$^{+/+}$ controls (top panels). For control and experimental individuals, n = 11 and 5, respectively. Magnification is indicated on each individual micrograph. Top row scale – 1 µm; bottom row scale – 2 µm.

Similar to *clarinet* and *del629* mutant mice, the gross patterning and polarity of the sensory epithelium in *Clrn2*$^{fl/fl}$*;Myo15*$^{cre/+}$ mice is unaffected. However, unlike age-matched *clarinet* and *del629* mutant mice, the OHC bundles of the conditional knockout mice have three rows of stereocilia arranged in the typical staircase pattern and are indistinguishable from *Clrn2*$^{fl/fl}$*;Myo15*$^{+/+}$ controls (Figure 5.12, top panel). In addition, the IHC bundles also appear to be unaffected (Figure 5.12, bottom panel). However, it is important to note that partial loss of IHC stereocilia is much more difficult to ascertain compared with loss of OHC stereocilia, as IHC bundles are not as structurally well-defined as OHC bundles.

5.2.6 Electrophysiological properties of *Clrn2*-deficient immature hair cells

Close inspection of *Clrn2*$^{fl/fl}$*;Myo15*$^{cre/+}$ hair bundles has demonstrated that lack of clarin-2 in hair cells from approximately P3 does not lead to the progressive resorption of third row stereocilia. This is in contrast to the phenotype observed in both the *clarinet* and *del629* mutants.

Therefore, in order to investigate whether MET channel function is affected, preliminary electrophysiological recordings were obtained from juvenile *Clrn2*$^{fl/fl}$*;Myo15*$^{cre/+}$ mutant OHCs by collaborators Adam Carlton, Anna Underhill and Professor Walter Marcotti at the University of Sheffield. Data was collected between P7 and P10 due to the increasing difficulty and reliability of measuring at older ages, as the OHC stereocilia begin to attach to the tectorial membrane. Additionally, data was collected only for OHCs, due to challenges in recording MET currents from IHCs.

In MET currents measured in apical OHCs at P7 (just before OHCs reach functional maturity at P8), *Clrn2*$^{fl/fl}$*;Myo15*$^{cre/+}$ recordings (red) appear very similar to the currents measured in the control (black) (Figure 5.13A). This is in stark contrast to recordings from *clarinet* apical OHCs at P6, which are distinctly reduced compared to controls (Figure 3.21A). However, a few days later, *Clrn2*$^{fl/fl}$*;Myo15*$^{cre/+}$ MET current has reduced in the mutant (Figure 5.13B). However, the open probability of the MET channel remains unchanged in the mutant (data not shown), and it should be noted that these are representative recordings from single animals.

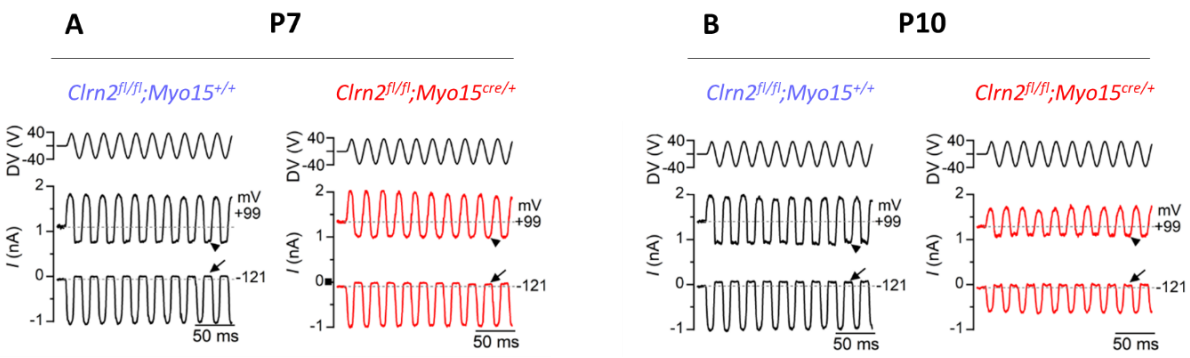

Figure 5.13: MET channel current is comparable between control and *Clrn2$^{fl/fl}$;Myo15$^{cre/+}$* mice. (A) Representative saturating MET currents recorded from P7 apical-coil OHCs of control (left, black) *Clrn2$^{fl/fl}$;Myo15$^{+/+}$* and experimental (right, red) *Clrn2$^{fl/fl}$;Myo15$^{cre/+}$* mice. Currents were recorded by applying sinusoidal force stimuli of 50 Hz to the hair bundles between −121 mV and +99 mV in 20 mV increment. For clarity, only the MET current at −121 mV and +99 mV are shown. The driver voltage (DV) signal of ± 40 V to the fluid jet is shown above the traces (positive deflections of the DV are excitatory). The holding potential was −81 mV. Extracellular Ca^{2+} concentration was 1.3 mM. The arrows and arrowheads indicate the closure of the MET currents (i.e. resting MET current) elicited during inhibitory bundle displacements at hyperpolarized and depolarized membrane potentials, respectively. Dashed lines indicate the holding current, which is the current at the holding membrane potential. **(B)** Representative saturating MET currents as described in **(A)**, but instead obtained from P10 OHCs. For control and experimental individuals at each time point, n = 18 and 13, respectively. Performed by Adam Carlton, Anna Underhill and Professor Walter Marcotti at the University of Sheffield.

The difference in MET current between P7 and P10 is small; this may indicate that lack of clarin-2 in hair cells is only just beginning to take effect. These results indicate clarin-2 may have an indirect, auxiliary role at the MET channel complex, and the phenotype observed in the P10 mutant may be due to slow turnover of clarin-2 within the hair bundles. Furthermore, as the scanning electron micrographs show normal hair bundle architecture and tapered stereocilia (indicating the presence of a tip link) (Figure 5.12), this implies the MET channel complex is present but dysfunctional in the absence of postnatal *Clrn2*. While MET currents were not recorded at older time points for aforementioned reasons, it is expected that OHC current will continue to decrease into adulthood. It is important to note that these results are preliminary, and further investigations into the electrophysiological properties of the *Clrn2$^{fl/fl}$;Myo15$^{cre/+}$* hair bundles are ongoing.

5.2.7 Temporal deletion of *Clrn2*

Investigations using the *Clrn2$^{fl/fl}$;Myo15$^{cre/+}$* mouse have shed light onto the role of *Clrn2* within postnatal auditory hair cells. However, only the spatial expression of the gene in hair cells could be

controlled under the *Myo15* promoter within the Cre driver line. Furthermore, given the UK Biobank population was comprised of individuals aged between 40 and 69 years of age at recruitment (from 2006), clarin-2 has been associated with age-related hearing difficulty. Therefore, in order to differentiate between the requirement of *Clrn2* in different tissues, and more specifically investigate the function of clarin-2 once the bundles have been established and therefore after the onset of hearing, it was decided to cross the *Clrn2*^{fl} mouse with an inducible Cre driver. This would permit the controlled expression of *Clrn2* with administration of tamoxifen (as described earlier in this chapter), which would allow us to dissociate the pre- and post-hearing roles that clarin-2 may have.

The B6.Cg-Tg(UBC-cre.EsR1)1Ejb/J mouse, also known as the UBC-CreER^{T2} mouse, is a ubiquitous Cre driver, meaning that upon tamoxifen dosing Cre recombination results in the deletion of sequences flanked by *loxP* sites in all tissues. Crossing this mouse with the *Clrn2*^{fl} mouse would allow global deletion of *Clrn2,* following tamoxifen administration.

Based on data from previous experiments within the lab, a dosing and phenotyping regime was devised. Firstly, auditory phenotyping (including the standard click box and ABR procedures) would be carried out at P21 to establish baseline hearing function. Following this, tamoxifen would be administered via the common oral gavage method between P35 and P42 (5-6 weeks of age). To allow full recombination following dosing, mice would then undergo auditory phenotyping 2-3 weeks later at P56 (8 weeks) and finally DPOAE testing at P63 (9 weeks). Immediately following this terminal procedure, cochleae from mice would be harvested for SEM processing to evaluate the effect of the global knockout of *Clrn2* on hair bundles after the onset of hearing.

Due to the coronavirus pandemic, this investigation had to be postponed and as such could not be completed within the timeframe of my doctoral studies.

5.3 Discussion

In this chapter, the role of *Clrn2* in auditory hair cells has been further explored through the use of two novel mutants.

Data from the UK Biobank suggests that the *CLRN2* gene is associated with age-related human loss, given the age range (40 – 69 years) of the participants. The second most highly associated SNP results in a Leucine to Valine substitution in exon 2, which as previously mentioned is predicted to have a 'damaging' or 'medium' effect on protein function, according to the PolyPhen-2 and MutationAssesor prediction tools, respectively (data not shown).

Furthermore, the molecular, auditory and ultrastructural investigations into the *Clrn2*^{del629} mouse have demonstrated that the deletion of *Clrn2*'s second exon results in a spliced isoform of *Clrn2*. The resultant phenotype largely reflects that exhibited by *Clrn2*^{clarinet} mice, whose 'null' allele encodes a severely truncated mutant protein (W4STOP). However, the hearing loss exhibited by *Clrn2*^{del629} mutants is marginally worse than that displayed by *Clrn2*^{clarinet} mutants. This is intriguing, as the *Clrn2*^{del629} encoded protein is predicted to more closely resemble wild type clarin-2 (though modelling the proteins is required to confirm this). There could be several reasons for this slight discrepancy in phenotype, though it should be noted that this difference is not significant at any of the frequencies tested.

When crossed with the Myo15 Cre driver line, *Clrn2*^{fl} mice exhibit moderate hearing loss at P21 which progresses to profound within a week. However, this phenotype is slower to progress than that of the *clarinet* mutant (which produces a severely truncated clarin-2 protein) or the *Clrn2*^{del629} mutant (whose second and third transmembrane domains are compromised). Furthermore, ultrastructural analyses of *Clrn2*$^{fl/fl}$*;Myo15*$^{cre/+}$ hair bundles revealed a full complement of stereocilia, comparable to wild type hair bundles. This is accompanied by the slow decrease of MET channel current in the OHCs of juvenile mice, between P7 and P10. Therefore, as *Clrn2* expression ceases in hair cells at approximately P3 due to the Cre activity, this indicates that hair bundle architecture is established before P3 or shortly after

(as residual clarin-2 protein may still be present before degradation). This suggests that *Clrn2* is either required before P3, or is expressed elsewhere in the cochlea besides the hair cells; however, the scRNA-seq data obtained from the gEAR database argues against the latter.

As described earlier, data from the *Clrn2^{fl};UBC-CreER^{T2}* mice will allow controlled deletion of *Clrn2*'s second exon, which we will exploit to induce global deletion of exon 2 in adulthood (between P35 and P42) as opposed to hair cell-specific postnatal deletion, as achieved with the *Clrn2^{fl};Myo15^{cre}*mouse). This will provide insight into *Clrn2*'s role in mature tissue, and will complement the UK Biobank data, which implicates *CLRN2* in aged-related hearing loss.

In addition to these human data, investigation into *Clrn2* mutant mice confirms *Clrn2* is required in postnatal hair cells, and additionally plays a role in the maintenance of the hair bundle into adulthood. These data, therefore, suggest that *Clrn2* has multiple roles within the mammalian auditory system.

Chapter 6: Discussion

6.1 Introduction

The hypothesis for my PhD project was that the *Clrn2* gene is critical for mammalian hearing. Before my studies, *Clrn2* had not been implicated as a deafness gene, and indeed had never been associated with any disease, or been the focus of a published scientific paper.

As such, the research aims were to confirm *Clrn2* as a novel deafness gene, and to characterise various *Clrn2* mouse mutants to investigate the requirement and role of the encoded clarin-2 protein. This was achieved mainly through comprehensive auditory phenotyping, and functional characterisation, of $Clrn2^{clarinet}$, $Clrn2^{del629}$ and $Clrn2^{fl};Myo15^{cre}$ mice.

6.1.1 *Clrn2* is required for mammalian hearing

The *clarinet* mutant was identified as part of the Harwell Ageing Screen, after a subset of mice from pedigree MPC-169 were found to display elevated ABR thresholds at 14 weeks of age. Genome mapping and sequencing identified a nonsense mutation in the *Clrn2* gene that leads to a Trp4Stop change in the encoded clarin-2 protein. The allele was then backcrossed to C57BL/6J for ten generations, and used in a complementation test with a second *Clrn2* allele ($Clrn2^{del629}$). Failure of these two loss-of-function alleles to complement one another confirms that *Clrn2* is essential for hearing function in mice. In order to understand the onset and severity of hearing loss caused by the absence of *Clrn2*, intercross *clarinet* mice were subject to comprehensive auditory and behavioural phenotyping. $Clrn2^{clarinet}$ mutants display elevated hearing thresholds, across all frequencies tested, from P16 and exhibit a progressive hearing loss phenotype that worsens to profound by P42 (Figure 3.8). Ultrastructural analyses of mutant cochleae reveals that although organ of Corti gross structure is normal, and although mutants develop the characteristic staircase hair bundle structure initially, the shortest stereocilia row begins to regress and is almost completely absent by P16; the second row begins to lose its uniform height as well (Figure 3.14). This is accompanied by dysfunctional MET

channels from an early age (Figure 3.21), as well as reduced potassium currents in IHCs which indicates their failure to mature (Figure 3.22). These results suggest that while clarin-2 protein is not required for the initial patterning of the hair bundle, it is critical for hair bundle maintenance and MET channel function in the early postnatal period, which is before the acquisition of hearing (~P12).

At the beginning of my studies, there were no reports regarding the function of *Clrn2*/clarin-2. However, its paralogue, *Clrn1* had been identified as the causative gene in Usher Syndrome type 3A (USH3A) (Adato et al., 2002). Usher syndrome is the most common genetic condition that affects hearing and vision, and sometimes balance. Clinically, there are three types of Usher syndrome (USH1, USH2 and USH3), with hearing loss arising due to abnormal development of cochlear hair cells, loss of vision due to progressive degeneration of retinal cells, and varying degrees of balance problems caused by abnormal development of the vestibular hair cells. Usher syndrome is inherited as a recessive disorder, caused by mutations in one of ~10 different genes, the encoded proteins of which are reported to function as part of a so-called USH interactome (Figure 6.1) (Mathur and Yang, 2015, Fuster-García et al., 2021). As such, it was postulated that *Clrn2* may be an Usher gene. However, *clarinet* mice were indistinguishable from their control littermates in numerous behavioural vestibular tests, and furthermore did not exhibit any vision defects as part of the ERG testing; though, as

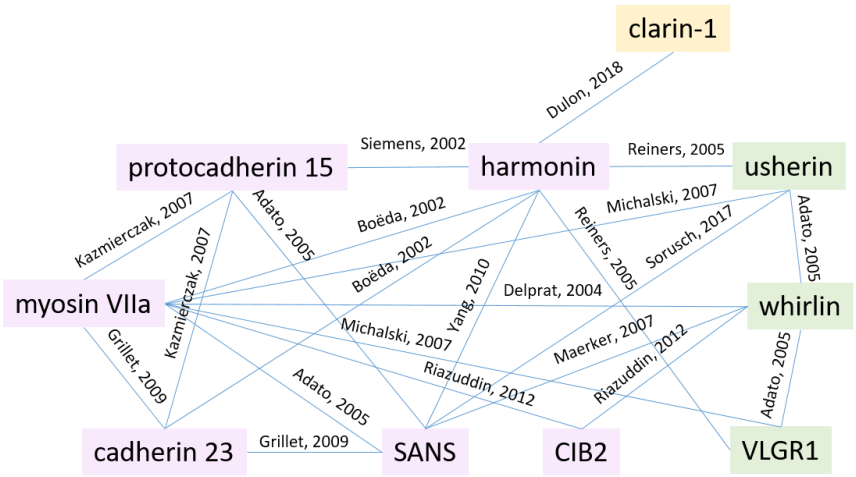

Figure 6.1: Biochemically known interactions between proteins in the USH interactome. Reference numbers for papers included in the original review are indicated along each line (see original paper for these references). At the time of publication, clarin-1 had not been confirmed as an USH gene. Adapted from Mathur and Yang, 2015 and Fuster-García et al., 2021.

mentioned previously, mouse models of USH fail to recapitulate the human condition (Géléoc and El-Amraoui, 2020).

Furthermore, while *Clrn1* mutants demonstrate dysfunctional IHC ribbon synapses, *clarinet* P21 IHC synapses appear to be unaffected (Figure 3.20).

clarinet mutants appear to exhibit a late-onset vestibular phenotype as demonstrated by the swim tests undertaken from 6 months onward (Figure 3.18), though not at earlier time points (up to 2 months) (Figure 3.17). Interestingly, *Clrn1* knockout mice exhibit variable and progressive vestibular dysfunction (Geng et al., 2009). My results may indicate that *Clrn2* is required for vestibular hair bundle function into adulthood, but further studies are required to investigate this. Indeed, measurement of vestibular sensory-evoked potentials (VsEPs), produced in response to transient linear acceleration of the head (Jones et al., 2011) is required to fully assess any vestibular deficit, but this platform is currently not available at MRC Harwell Institute. There are several utricular scRNA-seq datasets available on the gEAR portal. Interestingly, *Clrn2* appears to not be highly expressed in the early postnatal utricle, but does show expression in older (P100) utricular hair cells (type I and II) (McInturff et al., 2018).

6.1.2 **Constitutive deletion of *Clrn2*'s second exon**

The CRISPR/Cas9-generated C*lrn2*^{del629} mouse lacks exon 2 of the *Clrn2* gene. Its auditory phenotype is slightly more severe than that exhibited by the *Clrn2*^{clarinet} mutant (see 5.3). There could be several reasons for this discrepancy in phenotype. A possible explanation is that other proteins compensate for the near complete lack of clarin-2 in the *clarinet* mutant, but not in the case of the *Clrn2*^{del629} mutant which is predicted to retain some of its key domains. Candidates for compensation could be the other members of the clarin protein family, namely clarin-1, as its role in the hair cell is already established; as such, *Clrn1* expression should be examined in *Clrn2* mutant cochleae in future investigations.

Another potential reason for the difference in phenotypes could be a more active inhibition of the mutant *Clrn2*^{del629} protein. The altered structure of this protein, with only two of its four key

transmembrane domains intact, may be localising as normal but disrupting the mechano-electrical transduction complex it is thought to be part of, or interact with. This could inadvertently prevent other critical interacting or related proteins from fulfilling their crucial roles. Finally, the difference may be attributable to 'strain effect': the *Clrn2*^{clarinet} and *Clrn2*^{del629} mice were maintained on a C57BL/6J and on C57BL/6N backgrounds, respectively. As discussed in the introduction (1.6.2), both these strains (as well as many others) carry the *Cdh23*^{ahl} allele (Noben-Trauth et al., 2003) at the *ahl* locus on chromosome 10 (Johnson et al., 1997), which results in age-related hearing loss beginning at the high frequencies from 3-4 months of age (Zheng et al., 1999). It is also worth noting that other mutations have arisen between the two C57BL6 sub-strains which may contribute to any difference in phenotype, hearing or otherwise (such as behavioural (Bryant et al., 2008, Kane et al., 2012)).

6.1.3 **Sub-cellular localisation of *Clrn2*/clarin-2**

Data presented in Chapter 4 suggested a role for clarin-2 in the auditory bundle. Additionally, preliminary qRT-PCR *Clrn2* transcript data and scRNA-seq data presented in Chapter 5 also supported this. However, despite numerous attempts to visualise clarin-2 in the cochlea, using various anti-clarin-2 antibodies under various conditions, I was unable to confirm clarin-2's localisation using immunohistochemistry techniques. Collaborators at the Institut Pasteur attempting to detect over-expressed clarin-2 in HeLa cells, using a transient transfection approach employing plasmids for full-length clarin-2, were also unable to do so (Dunbar et al., 2019).

Possible reasons for the failure to determine clarin-2's subcellular localisation have been described at the end of Chapter 5. Briefly, the polyclonal anti-clarin-2 antibodies used may be cross-reacting with other members of the clarin protein family – indeed, all the commercial antibodies target clarin-2's second extracellular loop, and there is considerable homology between clarin-1 and clarin-2 residues at this location (Figure 4.10) (this is discussed in more detail in 4.3). Secondly, as *Clrn2* transcripts are expressed at low levels in hair cells (as demonstrated by data from the gEAR resource), it can be inferred that clarin-2 protein is also scarce; though importantly, this is not always the case (Vogel and

Marcotte, 2012). Additionally, despite careful handling and treatment of samples and reagents, protein and tissue may have been degraded or damaged, respectively, during the immunofluorescence process; however, gross hair bundle structure (as indicated by phalloidin staining of whole mounts in Figure 4.4 and Figure 4.5) did not appear to be disrupted or abnormal, which indicates stereocilia were not damaged during processing. Finally, despite strong evidence against this, clarin-2 may not actually localise to hair cells, but may be expressed elsewhere in the cochlea, such as in other cell types in the organ or Corti or the stria vascularis.

Despite the lack of success using traditional immunofluorescence techniques, alternative intuitive methods have indirectly suggested localisation of *Clrn2*/clarin-2 to the cochlear hair bundle. Using an injectoporation approach (as described in (Xiong et al., 2014)), colleagues at the Institut Pasteur were able to detect GFP-tagged clarin-2, which had been injected into P2 cochlear cultures, in the stereocilia of hair cells (Dunbar et al., 2019). Furthermore, using RT-PCR, *Clrn2* transcripts were detected in both IHCs and OHCs, isolated from P15 wild type cochleae (Dunbar et al., 2019). While these experiments suggest that clarin-2 localises to stereocilia when expressed in hair cells, they do not prove that *Clrn2* is hair cell-specific – indeed, clarin-2 may be expressed in other cochlear cell types. Although the Human Tissue Atlas suggests that clarin-2 protein is expressed in a number of human adult tissues such as testis, kidney, digestive tract and brain, this database does not show expression in cochlear tissue (https://www.proteinatlas.org/ENSG00000249581-CLRN2/tissue). *CLRN2* gene expression is observed in similar tissues according to human RNAseq data available on GeneCards (https://www.genecards.org/cgi-bin/carddisp.pl?gene=CLRN2#expression).

The above techniques demonstrate how alternative methods can be used to determine the localisation of proteins that cannot otherwise be verified using primary antibodies in immunolabelling assays. Besides using RT-PCR-based techniques in isolated cell types, other methods could also be used to detect *Clrn2* transcripts, and importantly allow visualisation in tissues – namely, *in situ* hybridisation. Anticipating this might be necessary in the context of *Clrn2*, I began to prepare for this

by attempting to generate a riboprobe against *Clrn2* messenger RNA (mRNA), with the aim to apply the technique on cochlear cryosections. Once a riboprobe was generated, it was sent to Professor Andy Groves and Dr Melissa McGovern at the Baylor College of Medicine (Texas) to test. However, preliminary experiments were inconclusive and unpromising, with no staining in the organ of Corti detected at P15 (data not shown). Further optimisation of the process may yield more success in future experiments – this could involve attempting the labelling on whole mount or vibratome-cut tissue, adjusting the incubation time of the riboprobe with the tissue, and modifying the fixation composition and time.

Another indirect method could be used to determine whether clarin-2 is expressed in hair cells: exploitation of conditional *Clrn2* knockout mice (see 6.1.4).

6.1.4 **Postnatal hair cell-specific *Clrn2* mutation and possible roles for clarin-2**

As alluded to above, floxed *Clrn2* mice can be crossed with Cre driver lines to control the spatial and temporal expression of *Clrn2*. Indeed, this approach was used in Chapter 5, whereby *Clrn2*^{fl}*;Myo15*^{cre} mice underwent auditory phenotyping. In these mice, *Clrn2* is knocked out from approximately P3 in IHCs and OHCs only (due to the Myo15 Cre driver), and is assumed to remain present in all other cochlear cell types (Caberlotto et al., 2011b). The severe auditory phenotype observed at P28 demonstrates that *Clrn2*/clarin-2 is required to be expressed in IHCs and OHCs for hearing function, and that loss in hair cells alone is sufficient to cause a hearing loss that is as severe as when *Clrn2*/clarin-2 is not present in any cells.

As demonstrated in Chapter 5, the auditory phenotype exhibited by *Clrn2*^{fl}*;Myo15*^{cre} mice is slower to progress than that of both the *clarinet* and the *Clrn2*^{del629} mice (possibly because residual functional protein has not been degraded by the time the mice were phenotyped, after the Cre driver is switched on) – although it is important to note that hearing loss is still considerable in this mutant, and thresholds are comparable to the other *Clrn2* null mutants by P28. This indirectly implies that clarin-2 is indeed expressed in auditory hair cells. To examine Cre-mediated clarin-2 protein turnover in

Clrn2^{fl}*;Myo15*^{cre} mice, multiple western blots on homogenised cochlear ducts at short intervals could be performed to assess protein levels over time – though this is subject to a working and reliable anti-clarin-2 antibody. The pulse chase method could alternatively be employed to assess the stability of the protein at the cellular level. The other two mutants, *Clrn2*^{fl}*;Myo15*^{cre} mice retain their three rows of stereocilia into adulthood, at least until P42. This could suggest that clarin-2 is, in fact, not required to maintain hair bundle architecture, and as such is likely to have more than one function within the hair cells. Given the difference in the hair bundle phenotype shown by *Clrn2*$^{clarinet/clarinet}$ and *Clrn2*$^{fl/fl}$*;Myo15*^{cre} mice, it suggests that the consequence of losing clarin-2 may be dependent on the maturation state of the hair cell/stereocilia bundle at the time of clarin-2 loss. Further experiments would need to be conducted to explore the nature of potential roles at various time points, but such roles could include maintenance of critical structures within the hair bundle (such as the upper tip link density, the MET channel complex or tip link itself), or interacting with, or chaperoning, other critical proteins (discussed at the end of this section).

The maturation state of hair cells is thought to be linked to the expression of the two Tmc proteins; as discussed in 1.1.8, both proteins are candidates for the pore-forming unit of the MET channel complex. In postnatal cochleae, expression of *Tmc1 and Tmc2* mRNA increases 20-fold and 40-fold respectively, and a switch from primarily *Tmc2* to *Tmc1* expression is complete by P8 (Kawashima et al., 2011). As this is approximately when OHCs reach functional maturity (Marcotti and Kros, 1999), this time period is critical for the maturing hair bundle; interestingly, this coincides with reduction of MET channel current in *Clrn2*^{fl}*;Myo15*^{cre} animals (between P7 and P10) (Figure 5.13). This is also when *clarinet* hair bundles show deviation from controls (Figure 3.15). Therefore, it could be hypothesised that stereocilia respond differently to clarin-2 (or lack thereof) depending on their maturation state, which is linked to the switch from *Tmc2* to *Tmc1* and the functional maturity of the OHC MET channel complex (as mentioned, approximately P8; IHCs reach maturity around P12, at the onset of hearing (Kros et al., 1998)).

Finally, as *Clrn2* is only knocked out in hair cells from around P3 due to the Myo15 Cre driver, these results indicate that *Clrn2* is required before P3, or is expressed elsewhere besides the hair cells entirely. Of course, the *Clrn2*^{fl} mouse can be crossed with other Cre drivers to further investigate its expression pattern, and help distinguish its developmental role from its adult role in hearing. Specific experiments are described later in this chapter.

To speculate on possible functions for clarin-2 (both in developing and adult tissue), it is useful to refer to its paralogues. According to data on the gEAR database (https://umgear.org/), *Clrn3* is not expressed in the mouse auditory system and therefore it is not speculated to have a function related to mammalian hearing. Conversely, as discussed previously, *Clrn1* is a known deafness gene, and is in fact the causative gene in USH3A (Adato et al., 2002). Clarin-1 is suspected to have a role in IHC synaptic organisation (Zallocchi et al., 2012, Ogun and Zallocchi, 2014), which was one of the reasons I performed synaptic labelling on *Clrn2*$^{clarinet/clarinet}$ cochlear ducts. Although my mutant data at P21 did not reveal any overt defects and was comparable to the controls (Figure 3.20), further experiments could be carried out to detect a more subtle phenotype. Additionally, the experiment could be repeated at a range of other time points (Zallocchi et al (2012) conducted their experiments in *Clrn1* knockout mice at P14 and earlier), or could alternately be carried out on cochlear ducts from noise-challenged control and mutant mice to assess whether a 'stressed' system reveals any dysfunction at the synapse (see section 6.5.3 for further details).

As mentioned previously, clarin-1 is also suggested to have a function in the hair bundle (Geng et al., 2012). My data have shown that global mutation of *Clrn2* results in a subtle bundle defect that is associated with profound, progressive hearing loss at all frequencies test. *Clrn1* mutants exhibit disorganised hair bundles, which is thought to be related to compromised MET channel function (Geng et al., 2012) – but the gradient staircase-like architecture of the bundle is not disrupted; this is not the case for global *Clrn2* mutants (*clarinet* and *del629*). An interesting future experiment could involve generating double mutants (*Clrn1*$^{-/-}$; *Clrn2*$^{-/-}$) and respective heterozygotes to investigate whether

there is any compensation in the absence of either functional family member; subsequent experiments could involve performing longitudinal ABRs to assess hearing, and imaging the cochlear sensory epithelium to determine how hair bundles may be disrupted.

Clarin-2 (along with clarin-1) is a tetraspan protein (membrane proteins characterised by four transmembrane domains); the function of other tetraspans thought to be present in the hair bundle could shed light on the role of clarin-2. Very interestingly, LHFP5 (a known component of the MET channel complex) is a tetraspan thought to interact with PCDH15 (the lower component of the tip link), and is speculated to play a role in tip link assembly (Xiong et al., 2012, Mahendrasingam et al., 2017). Therefore, it could be useful to assess for an interaction between clarin-2 and both LHFP5 and PCDH15; alternatively, localisation of the latter two proteins in *Clrn2* mutants could be examined.

More broadly, tetraspans have many dynamic functions at the membrane in a multitude of tissues; such roles include cell activation, adhesion, motility and stability (Maecker et al., 1997). Indeed, tetraspans are known for their numerous and diverse interactions with other proteins (Levy and Shoham, 2005). It could be postulated, therefore, that clarin-2 may be involved in one or more of these roles – perhaps tethering of proteins to the hair cell membrane, chaperoning of other proteins to the tip of the stereocilia, or even generating a favourable microenvironment within the membrane itself. Future research, as discussed in more detail in 6.5.2, could focus on identification of clarin-2's interaction network, and subsequent elucidation of specific interactions.

6.2 Other *Clrn2* mutants

6.2.1 *Clrn2* IMPC mutant mouse phenotype

Although before my doctoral studies *Clrn2* had never been the focus of a scientific paper, *Clrn2* knockout mice (*Clrn2*$^{em1(IMPC)J}$) have since been generated as part of the International Mouse Phenotyping Consortium (IMPC) and have undergone phenotyping at the Jackson Laboratory. The *Clrn2* mutation, engineered using the CRISPR/Cas9 system, results in the deletion of 226 bp, which should cause the 'deletion of exon 1, amino acid change after residue 3, and early termination 11

amino acids later' (IMPC). A severe auditory phenotype at 14 weeks in both male (n = 4) and female (n = 4) homozygotes was observed at all frequencies tested (Figure 6.2). Homozygotes exhibited decreased prepulse inhibition (an operational measure of sensorimotor gating (Brody et al., 2004)) and startle reflexes compared with controls. Unsurprisingly, homozygotes did not exhibit startle reflexes ($p = 1.12\times10^{-48}$ and 9.51×10^{-25} for males and females, respectively). However, mutants also exhibited a number of metabolic differences, including decreased heart rate, lean body mass and bone density and mineral content, and increased total body fat; interestingly, only males were affected for these conditions. Altered body composition in the *Clrn2* mutants could indicate a role for clarin-2 in metabolic function – however, while in-depth metabolic phenotypes were not assessed in either *clarinet* or *del629* mice, homozygotes did not weigh significantly less than controls. Therefore, further body composition analyses should be used to investigate whether lean muscle mass and fat mass, or bone density, are affected (an Echo MRI Analyzer and DEXA scanning, respectively, could be used to assess this).

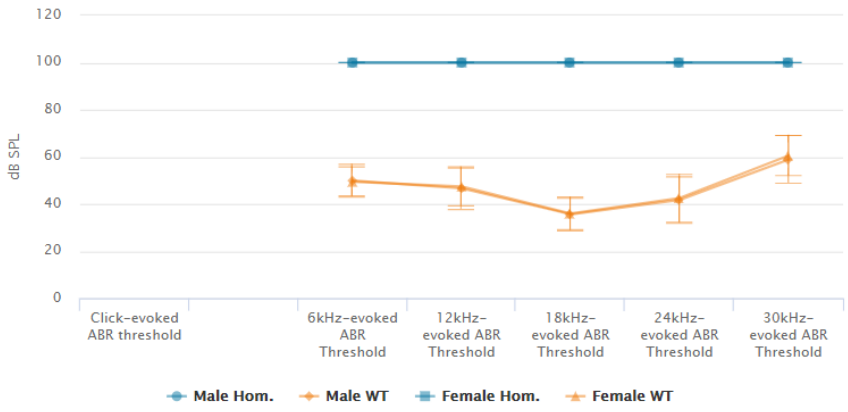

Figure 6.2: Evoked ABR thresholds in *Clrn2*$^{em1(IMPC)J}$ mice at 14 weeks. 727 mice were phenotyped, including 8 mice homozygous for the mutation (4 of each sex). All homozygous mice failed to exhibit an ABR waveform for all frequency stimuli up to 95 dB SPL, and are therefore recorded as having an ABR threshold of 100 db SPL. This is in comparison to controls (356 males and 363 females) that displayed thresholds of between 35 db SPL and 65 db SPL. Phenotyping was performed at the Jackson Laboratory. Adapted from the IMPC website (https://www.mousephenotype.org/data/genes/MGI:3646230). WT – wild type; Hom – homozygous.

This IMPC hearing phenotype matches those of the *Clrn2*^{clarinet} and *Clrn2*^{del629} mutant mice detailed in this thesis – indeed, the allele is similar to that of the *clarinet* mutant. Furthermore, the other

phenotypes observed demonstrate how data collected as part of the IMPC could be used in the future to address the potential pleiotropic effects of *Clrn2* mutations.

6.2.2 *clrn2* in zebrafish

At the start of my project *Clrn2*/clarin-2 had not been studied in any species, and my studies have involved the characterisation and investigation of three *Clrn2* mouse models. However, in a recent study, our collaborators have investigated the function of *clrn2* in zebrafish (*Danio rerio*) (Vona et al., 2021).

While their inner ear structure is less comparable than mice to that of humans due to their smaller size, there are several benefits to using zebrafish. The general structure of the hair bundle is conserved between mammals and zebrafish (Pickett and Raible, 2019), and additionally while mouse and human cochleae are coiled, the zebrafish hearing apparatus is not coiled or encapsulated, allowing easier access (Leitner, 2014). As well as possessing inner hair sensory epithelia, zebrafish also harbour clusters of hair cells in lateral line organs known as neuromasts, whose primary function is to detect directional water flow. Their superficial location enables ease of manipulation and study (Pickett and Raible, 2019). Along with their relative ease and speed of breeding, and transparency during larvae development, these attributes make the zebrafish an attractive model in which to study hearing loss.

Using qRT-PCR, Vona et al demonstrate that *clrn2* mRNA is first detected at 18 hours post fertilisation (hpf) in whole mount embryos/larvae, which is equivalent to E9 in mice. Furthermore, whole mount *in situ* hybridisation experiments using an anti-sense *clrn2* probe revealed strong expression in the otic vesicle in 3 and 5 days post fertilisation (dpf) zebrafish embryos.

As part of their investigations, Vona et al used CRISPR technology to generate zebrafish mutants known as ‘crispants’, disrupting the *clrn2* gene. To assess for a startle response, crispants were subject to acoustic-evoked behavioural response testing (similar to a click box test in mice). This demonstrated that 6 dpf mutants display reduced responses after sound stimulation compared to controls, indicating

hearing loss in the crispants. In addition to this, F-actin staining of 5 dpf crispant hair cells with showed disruption of the bundle architecture, along with fewer hair cells compared to wild type controls.

These results somewhat echo those of *clarinet* mutant mice. While direct comparisons cannot be drawn between the two species, it is not unexpected that *clrn2* is required for hearing in zebrafish due to modest conservation between the orthologous genes, which share approximately 50% of their sequence (ENSEMBL). Furthermore, *Clrn1* knockout zebrafish exhibit weakened or absent startle responses (Gopal et al., 2015), which suggests conservation of function of the clarin protein family, rather than just clarin-2.

6.3 *Clrn2* mutants phenocopy other mutants with disrupted hair bundles

The work performed as part of this project has demonstrated that lack of functional clarin-2 results in a severe, early-onset and progressive hearing loss. Close inspection of the hair bundle at the morphological and electrophysiological level suggests this may be due to the progressive resorption of 'transducing' stereocilia and disruption to MET channel activity. Alternatively, the resorption of transducing stereocilia may be due to the lack of MET channel currents, which is reported to be crucial for maintenance of IHCs (Corns et al., 2018).

Interestingly, similar phenotypes have been observed in other mouse mutants who exhibit abnormal shortening of transducing stereocilia. The human condition USH1G is caused by mutations in the *Sans* gene (Weil et al., 2003), and the *Ush1g*$^{-/-}$ mutant *jackson shaker* is characterised as having hearing loss and disorganised hair bundles (Kikkawa et al., 2003), but not shortening of 'transducing' stereocilia (unlike the constitutive *Clrn2* mutants (*Clrn2*^{clarinet} and *Clrn2*^{del629}). Furthermore, *Ush1g*$^{fl/fl}$*Myo15*$^{cre/+}$ mice were generated to investigate the postnatal hair cell-specific requirement of sans (Caberlotto et al., 2011b), and a severe and early-onset auditory defect was detected at all frequencies tested, along with circling behaviour and behavioural tests indicating overt vestibular dysfunction from P21. Additionally, although hair bundles in these mutants appeared similar to controls at P8, IHC displays a decrease in MET currents (though OHCs were unaffected), and

furthermore by P22 a reduction in the middle and shortest rows of transducing stereocilia was pronounced, demonstrating a similar mechanism of regression over time that is observed in the clarinet mutant. Given the sans protein localises to the tips of these two rows only, Caberlotto et al concluded that sans is therefore involved either the maintenance or renewal of the tip link. This phenotype is strikingly similar to that of the *Clrn2*^{clarinet} mice, whereby the shortest row of OHC stereocilia regresses and is missing by P22, by which point, the IHC stereocilia appear fewer in number and are less prolate. It is interesting to note that the constitutive *Clrn2* mutants phenocopy the hair cell-specific sans mutant, but not the constitutive sans mutant – this may suggest a difference in the temporal requirement of the two proteins.

At the upper tip link density, sans is suspected to interact with Myo7a (Grati and Kachar, 2011) (Figure 6.3) which is the causative gene in human USH1B (Weil et al., 1995), and originally known as the mouse shaker-1 gene (Gibson et al., 1995). Several mutations in the gene are associated with deafness and vestibular dysfunction in the shaker-1 mouse model (Hasson et al., 1997). Investigating three of these mutations, Self et al (1998) noted that Myo7a is probably required for both stereocilia bundle formation and function. Furthermore, in constitutive Myo7a mutants, stereocilia exhibit abnormal elongation and disruption at P0 (Lefèvre et al., 2008). Ten years later, Corns et al (2018) used postnatal hair cell-specific deletion of Myo7a (using the Myo15 Cre driver) to demonstrate that Myo7a may have a role in mechano-electrical transduction, and furthermore that mechano-electrical transduction is required for the maintenance of postnatal IHC structure. Interestingly, the hair cell-specific Myo7a knockout exhibits normal IHC bundles that, although appearing similar to controls, have severely reduced MET channel currents at by P8 (OHCs were not investigated) (Corns et al., 2018). This pattern is somewhat similar to that reported in the three *Clrn2* mutants, whereby hair bundle abnormalities are present in global knockouts at neonatal/postnatal stages (though Myo7a mutants were not imaged after P0); and stereocilia appear morphologically normal but have reduced MET channel currents in the postnatal hair cell-specific knockout (i.e. when crossed to the Myo15 Cre driver). Conversely, constitutive sans knockout (Jackson shaker) mice exhibit disorganised bundles, that are

not U or V shaped, at P14 (Kitamura et al., 1992), but as previously mentioned, the hair cell-specific knockout is almost identical to the global *Clrn2* mutants (*clarinet* and *del629*) at P22 (Caberlotto et al., 2011b).

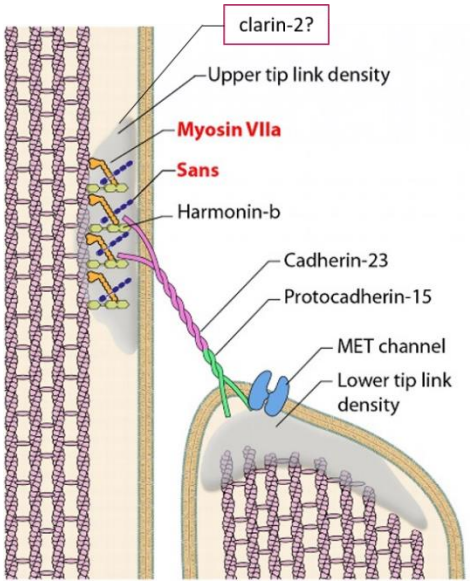

Figure 6.3: Schematic representation of the proposed MET channel complex, the tip link and the upper tip link density. The upper tip link density comprises Myo7a, sans and the harmonin-b isoform. My studies suggest clarin-2 may constitute, or interact with, the proteins that comprise the upper tip link density. Adapted from Grati and Kachar, 2011

As mentioned, Myo7a and sans both localise to the upper tip link density via cadherin 23. This complex is thought to anchor the tip link to the taller stereocilia and hence maintain its resting tension (Gillespie and Müller, 2009, Sakaguchi et al., 2009, Grati and Kachar, 2011). Furthermore, sans and Myo7a are reported to interact with harmonin (Boeda et al., 2002, Adato et al., 2004, Yan et al., 2010). Harmonin is a scaffold protein also part of the upper tip link density, that forms a complex with the upper tip link component cadherin 23 (Siemens et al., 2002) (Figure 6.3) and is crucial for mechano-electrical transduction (Grillet et al., 2009, Michalski et al., 2009). Mutations in harmonin underlie the USH1C phenotype (Bitner-Glindzicz et al., 2000, Verpy et al., 2000). Interestingly, harmonin is located much closer to the tips of the taller stereocilia in the *clarinet* mutant (when compared to controls), which might result from broken or absent tip links, leading to reduced gating of the MET channels (Dunbar

et al., 2019). Harmonin mislocalisation in this manner is also exhibited by mice lacking tip links (Lefèvre et al., 2008).

The hair bundle phenotype observed in *clarinet* mice (whereby transducing stereocilia are affected and MET channel current is reduced) combined with this mislocalisation of harmonin, therefore, could indicate that clarin-2 may constitute, or engage with, the upper tip link density, and interact with harmonin, sans and/or Myo7a. To confirm these proteins as interacting partners of clarin-2, their localisation could be investigated in *Clrn2* mutants and conversely, clarin-2 localisation should be investigated in Myo7a, harmonin and sans mutants, though this would be dependent on a working and reliable anti-clarin-2 antibody. An alternative *in vitro* approach could involve transiently transfecting tagged constructs for each candidate in a suitable system, and performing a co-immunoprecipitation experiment followed by mass spectrometry to identify interacting partners in an unbiased manner. In order to imitate the endogenous environment a ciliated cell line or a cell line with microvilli or filopodia projections may be required; additionally, generating a primary cell culture from tissue could be attempted, but this is associated with its own challenges (Zhang et al., 2019).

Numerous other mutants are reported to display a similar hair bundle phenotype, in which the shorter transducing stereocilia are affected. The genes responsible include TMC1/TMC2 (Kawashima et al., 2011), TMIE (Zhao et al., 2014) and LHFPL5 (Xiong et al., 2012); all genes whose encoded proteins are thought to form part of, or interact with, the elusive MET channel complex.

Research from Velez-Ortega et al (2017) provides insight into a potential contributor to the defect seen in *Clrn2* and other similar mutants. In this study, the authors used pharmacological channel blockers (amiloride or benzamil) to inhibit MET channel currents in immature murine models, which resulted in regression of the two shorter stereocilia rows and disruption of their tip links. Furthermore, through the treatment of organ of Corti explants with the membrane-permeable acetoxymethyl ester derivative BAPTA-AM, they demonstrated that Ca^{2+} influx might represent a critical component of the functional MET channel current, that influences the stability and maintenance of transducing

stereocilia. Interestingly, retracted stereocilia showed regrowth following washout of the channel blockers, though all these experiments could only be conducted in immature cochleae. In the context of my project, this research suggests that clarin-2 may be involved in maintenance of MET channel current, which may be through indirect interaction with the MET channel itself. Furthermore, the hair bundle defects in constitutive *Clrn2* mutants may be a consequence of disrupted MET channel current. However, as the experiments by Velez-Ortega et al could only be performed with explants cultured from postnatal tissue (aged P4-P6), it is unknown whether stereocilia regrowth is possible *in vivo* or at older ages. Regression of stereocilia following postnatal deletion of *Clrn2* in the *Clrn2^{fl};Myo15^{cre}* mutant may not occur because earlier *Clrn2* expression (up to the postnatal stages) is sufficient in beginning to establish the hair bundle and the MET channel current, although this is not sufficient in the long-term maintenance of the MET channel current at later stages.

6.4 The role of *CLRN2* in human hearing

Data from my studies have confirmed that *Clrn2* is critical for hearing in the mouse, and more specifically, has a role in maintenance of stereocilia structure into adulthood. Despite the strong implications that *CLRN2* is important for mammalian hearing, these studies have not involved the use of human participants or tissue and so we cannot conclude from these studies alone that *CLRN2* is involved in human hearing.

6.4.1 Human aged-related hearing difficulty may be associated with *CLRN2*

Data from the UK Biobank suggests that *CLRN2* may be associated aged-related hearing loss in humans. As discussed in 5.1, data from a GWAS undertaken into self-reported hearing difficulty identified several highly associated (i.e. common in the UK Biobank dataset) SNPs located in or very close to *CLRN2* on human chromosome 4 (Dunbar et al., 2019). Interestingly, the second most highly associated SNP (rs13147559) was located in *CLRN2*'s second exon, and likely represents a missense variant in the second transmembrane domain. Given the nonsense mutation that leads to a severely truncated protein (the *clarinet* mutant), and the entire deletion of exon 2 in the *del629* mutant both

lead to severe, early onset auditory phenotypes, it could be postulated that the SNP identified from the GWAS that results in a missense mutation is likely to result in mild hearing loss (or difficulty) that is neither congenital nor early-onset. As hearing difficulty was identified in a dataset which represents a middle-aged to elderly population, this correlates with data from my studies in Chapter 5, utilising the *Clrn2*^{fl}*;Myo15*^{cre} mouse, that suggests *Clrn2* is required into adulthood (or more specifically, up to at least P28). The association with mild hearing difficultly identified in the UK Biobank may represent heterozygous mutations, or SNPs, that are present and inherited in the general British population, which might explain why no cases of profound hearing difficulty caused by recessive *CLRN2* mutations have been reported in this cohort.

To meticulously investigate the effect of the coding *CLRN2* SNP identified in the UK Biobank cohort, a knockin mouse harbouring the specific mutation identified could be generated using CRISPR/Cas9 technology. Indeed, several recent studies have demonstrated that knockin mutants carrying known human deafness mutations are able to mimic the human auditory phenotype (Wang et al., 2019b, Wen et al., 2019, Chen et al., 2021). Given the 94% identity between human and mouse clarin-2 orthologous proteins (Figure 6.4), a heterozygous knock-in mutant for the coding SNP might recapitulate the human condition reported by UK Biobank participants, and provide further insight into the mechanisms underlying *CLRN2*-associated hearing difficulty. However, it should be noted that the coding SNP identified in this GWAS is not necessarily the underlying genetic lesion causing the observed phenotype; it is possible that currently unidentified alleles are in fact the cause. As whole

```
Query  1    MPGWFKKAWYGLASLLSFSSFILIIVALVVPHWLSGKILCQTGVDLVNATDRELVKFIGD  60
Sbjct  1    .......V.............L......SL.....................P........  60

Query  61   IYYGLFRGCKVRQCGLGGRQSQFTIFPHLVKELNAGLHVMILLLLFLALALALVSMGFAI  120
Sbjct  61   ........................................T.....................  120

Query  121  LNMIQVPYRAVSGPGGICLWNVLAGGVVALAIASFVAAVKFHDLTERIANFQEKLFQFVV  180
Sbjct  121  ..I........N.....................G..M.................R......  180

Query  181  VEEQYEESFWICVASASAHAANLVVVAISQIPLPEIKTKIEEATVTAEDILY  232
Sbjct  181  ........................................M......P.....  232
```

Figure 6.4: Human and mouse clarin-2 amino acid sequence alignment. Human and mouse clarin-2 proteins are 94% identical, and score 97% for positive (chemically similar) residues. Query – human clarin-2; Sbject (red) – mouse clarin-2. Both polypeptides comprise 232 residues. Dots represent identical residues. Assessed using the Basic Local Alignment Search Tool (BLAST) (https://blast.ncbi.nlm.nih.gov/).

genome sequencing of UK Biobank participants is underway, additional lesions in/around the *CLRN2* locus may identified as causative.

6.4.2 **Recessive *CLRN2* mutations in an Iranian family**

Very interestingly, mutations in the *CLRN2* gene has been identified as the cause of hearing loss in several members of an Iranian family. Recent studies undertaken by Vona et al (2021) identified this family (through a large and ethnically diverse rare disease study), in which three members (two siblings and their cousin) experience moderate-to-profound, bilateral, non-syndromic sensorineural hearing loss. The age of hearing loss onset was between two and three years of age for all three individuals, no vestibular or visual defects were identified and no issues were reported in speech and language development. The hearing loss phenotype was identified through reactive hearing tests. The affected individuals were found to harbour suspected pathogenic missense variants (c.494C > A) in the *CLRN2* gene, which were presumed to be homozygous and inherited in an autosomal recessive fashion, due to the parental consanguinity.

Furthermore, *in vitro* splicing analyses suggested the above variant results in either a mutant full-length protein (Thr165Lys), or a splice variant that results in a premature stop codon in the second intron (Gly146Lysfs*26). As previously discussed, the authors subsequently investigated *clrn2* function in zebrafish, and mouse (whereby some of the investigations I undertook into the *del629* mutant were included) and confirmed *Clrn2* mutation also results in auditory dysfunction in both species.

There are obvious differences in the auditory phenotypes investigated in the Iranian family and UK Biobank participants, with the former exhibiting a much earlier-onset and severe deficit. This could be explained by the nature of the mutation – affected individuals from the Iranian family harbour homozygous *CLRN2* mutations, most likely resulting from consanguinity as mentioned. Pathogenic heterozygous *CLRN2* mutations are likely the more common form in the UK Biobank demography, and given the rare occurrence of consanguinity in the population, there is little chance of two pathogenic alleles 'homozygosing'. As *clarinet* and *del629* heterozygotes exhibit normal hearing thresholds (which

are indistinguishable from wild type controls), it is unlikely that heterozygous mutations result in haploinsufficiency in this manner, in the UK Biobank cohort. However, any human *CLRN2* heterozygous mutations could result in haploinsufficiency through interaction with the environment – for example, by exposure to lifelong noise insult or a single traumatic noise event. The latter could be tested in heterozygous *Clrn2* mutant mice (see 6.5.3). Alternatively, a gain-of-function mutant allele could be acting in a dominant negative fashion against the wild type allele. This could result in mutant abnormal clarin-2 protein interfering with wild type protein, or preventing its normal function.

6.5 Future directions

My doctoral studies have provided the first insights into the requirement of *Clrn2* in the mammalian auditory system; however, questions regarding the temporal and spatial roles of clarin-2 remain to be answered.

6.5.1 Exploring the differential requirement of *Clrn2* in the two hair cell types

Conditional mouse models can be used to further explore the spatial and temporal requirement of *Clrn2* in the cochlea. As demonstrated in Chapter 5, the *Clrn2*^{fl} mouse can be crossed with Cre driver lines to generate conditional *Clrn2* knockout models. Investigations using the *Clrn2*^{fl}*;Myo15*^{cre} mutant, whose auditory phenotype progresses more slowly than constitutive *Clrn2* knockouts and retain three rows of stereocilia, suggest *Clrn2* is required for hearing after the postnatal stage, but not to maintain the structural integrity of the hair bundle. The *Clrn2*^{fl} mouse is due to be crossed to the inducible UBC-CreER^{T2} driver to allow temporal control over the ubiquitous expression of *Clrn2* (see 5.2.7 for details of the experimental regime), but the use of this particular Cre driver will not allow us to distinguish between any difference in the requirement or role of clarin-2 in the inner and outer hair cells. Crossing the *Clrn2*^{fl} mouse with an IHC- or OHC-specific Cre driver will, however, enable us to explore any differential role of clarin-2 in the two hair cell groups.

The *Clrn2*^{fl} mouse could be crossed with the inducible *Prestin-creER*^{T2} driver line (Fang et al., 2012). As prestin (*Slc26a5*) is only expressed in OHCs, dosing *Clrn2*^{fl}*;Prestin-creER*^{T2} mice with tamoxifen would

allow the controlled deletion of *Clrn2* in OHCs only, at chosen time points. This inducible Cre driver was recently employed in another study undertaken by colleagues (Chessum et al., 2018), and has demonstrated reliable Cre-mediated recombination upon tamoxifen dosing. Similar to the plans for the *Clrn2^{fl};UBC^{cre}* cohort, *Clrn2^{fl};Prestin-creER^{T2}* mice would undergo auditory phenotyping at P21 to establish baseline hearing function, before tamoxifen dosing between P35 and P42 (controls of the same genotype would receive vehicle only). Auditory phenotyping tests, including DPOAEs to specifically test OHC function, would be carried out from P56 before harvesting cochleae for SEM analyses. Because prestin is restricted to OHCs, IHCs will still express *Clrn2* following tamoxifen dosing and serve as a useful 'internal' control for any observed OHC phenotype.

6.5.2 Assessing localisation and interacting partners with a *Clrn2^{tag}* mouse

Confirming clarin-2's intracellular localisation is critical in understanding its role within the cochlea. As previously mentioned, there are several indirect methods available to investigate this. One approach would be to generate an *in vivo* tagged *Clrn2* mouse (*Clrn2^{tag}*) using CRISPR/Cas9 techniques, which an anti-tag antibody could be used to detect. Given clarin-2 is a relatively small protein (232 residues, approximately 25.5 kDa), a small tag would need to be attached to ensure it does not interfere with normal protein function (for example by preventing normal protein localisation or binding with partners); candidates include an HA-, Myc- or FLAG-tag (1.2, 1.1 and 1 kDa respectively; for comparison, GFP is approximately 27 kDa). Once normal hearing function is confirmed with auditory phenotyping, antibodies against the tag could be used to probe sub-dissected organ of Corti tissues in a variety of experiments including immunofluorescence labelling to assess localisation, and co-immunoprecipitation assays followed by mass spectrometry to identify endogenous interacting partners of wild type clarin-2. Some of these partners may be known deafness proteins such as sans, Myo7a and harmonin (as discussed in 6.3), while others may be proteins that are currently not associated with hearing loss. Genes encoding proteins in the latter group would, by association, become candidate hearing genes that could be investigated to further elaborate upon the genetic mechanisms underlying mammalian hearing.

6.5.3 **Noise challenging of *Clrn2* heterozygous mutants**

Data from the UK Biobank cohort suggests that *CLRN2* is associated with age-related hearing loss. As discussed previously (6.4.2), it is more likely that individuals heterozygous for *CLRN2* mutations are present at a higher frequency in the UK Biobank population than individuals homozygous for *CLRN2* mutations. It could, therefore, be hypothesised that individuals heterozygous for *CLRN2* mutations are more susceptible to lifetime environmental noise insult than those carrying two wild type alleles.

In order to assess the effect of the heterozygous *Clrn2* mutations on ageing mice, heterozygous animals, *Clrn2*$^{del629/+}$ animals (and their wild type littermates) could be allowed to age, with longitudinal ABRs conducted to monitor the progression of hearing loss. The *Clrn2*^{del629} cohort would need to be bred onto the repaired C57BL/6N background (Mianné et al., 2016) for this experiment; as they are currently maintained on the standard unrepaired background, they will develop aged-related hearing loss due to their *Cdh23*^{ahl} allele (see 1.6.2 for more details).

While a multitude of factors can contribute to aged-related hearing loss (such as diet, stress, infection and medications (Mills and Going, 1982)), traumatic noise exposure can be easily controlled in a laboratory setting. Furthermore, noise exposure in earlier life leaves the inner ear more vulnerable to age-related hearing loss in later life, in both human and mouse (Gates et al., 2000, Kujawa and Liberman, 2006). Therefore, to mimic the effect of noise damage inflicted from the environment, and to exacerbate aged-related hearing loss, mice heterozygous for *Clrn2* mutations (for example *Clrn2*$^{del629/+}$ mice) and wild type controls could be noise challenged. Aged sham-challenged *Clrn2*$^{del629/+}$ mice could also undergo ABR testing to assess how a lower level of environmental noise might interact with the heterozygous mutation.

This platform was not available at MRC Harwell Institute during my doctoral studies, but is currently being established to utilise in future investigations. Following an ABR to assess baseline hearing, mice will be exposed to a moderate noise exposure event. In wild type mice, this is expected to cause a temporary threshold shift, whereby ABR thresholds are transiently elevated as a result of

degeneration of the cochlear nerve (Kujawa and Liberman, 2009). If *Clrn2*$^{del629/+}$ animals are indeed more susceptible to noise damage, it could be hypothesised that they are slower to recover from a noise-induced temporary threshold shift (speculated to be associated with uncoupling of the OHCs to the tectorial membrane), or even experience a permanent threshold shift (thought to be due to hair cell death and nerve fibre degeneration (Nordmann et al., 2000).

6.6 Implications for therapeutic intervention

While my studies have contributed to the understanding of the involvement of *Clrn2* in the mammalian auditory system, implementation of therapeutic strategies to address *CLRN2*-assocaited hearing difficulty in the clinic is distant. As discussed in 1.5.3, current treatments for sensorineural hearing loss as a whole are extremely limited, and any therapeutic intervention must occur before the onset of hearing loss to preserve as much function as possible. There is unlikely to be the significant financial drive needed to address hearing loss caused by homozygous *CLRN2* mutations, given the suspected rarity of the condition. At least in the UK population, heterozygous *CLRN2* mutations that lead to mild hearing difficulty in later life are likely to be more frequent than homozygous mutations, and furthermore it is possible this hearing loss is already attenuated in individuals who wear hearing aids.

One possible avenue for the prevention of sensorineural hearing loss is gene replacement therapy, whereby the organ Corti is targeted via *in vivo* adeno-associated viral- (AAV) mediated gene delivery (Ren et al., 2019). Indeed, this has been achieved in *Clrn1* mutant mice (Dulon et al., 2018), whereby a *Clrn1* expression vector was transferred by microinjection into the round window of the cochlea in *Clrn1*$^{ex4fl/fl}$;*Myo15*$^{cre/+}$ neonates. This resulted in the prevention of synaptic defects and improved hearing function, and indicates the potential for similar strategies in *Clrn2* mutants.

In practice, the intervention window before the onset of hearing loss for a recessive condition is likely to be extremely small and would probably involve injection of AAV-packaged *CLRN2* into the developing fetus or baby, which is somewhat obstructed by practical and ethical issues. However, in

CLRN2-associated aged-related hearing difficulty (as identified by the UK Biobank), the therapeutic window is much longer, and so future gene replacement strategies to prevent *CLRN2*-associated hearing difficulty in later life are much more clinically relevant and feasible.

6.7 Concluding remarks

The data presented in my thesis has identified a critical role for the novel deafness gene, *Clrn2*, in the mammalian inner ear, and more specifically demonstrates how clarin-2 may have multiple different roles in development and maintenance of the hair bundle and hearing function. Besides investigating the requirement of *Clrn2,* and the clarin-2 protein, in the mammalian cochlea, my PhD project has further highlighted the value of using novel mouse models of hearing loss to continue to elaborate upon the genetic mechanisms underpinning the mammalian auditory system.

Chapter 7: References

ABRASHKIN, K. A., IZUMIKAWA, M., MIYAZAWA, T., WANG, C. H., CRUMLING, M. A., SWIDERSKI, D. L., BEYER, L. A., GONG, T. W. & RAPHAEL, Y. 2006. The fate of outer hair cells after acoustic or ototoxic insults. *Hear Res,* 218**,** 20-9.

ADACHI, N., YOSHIDA, T., NIN, F., OGATA, G., YAMAGUCHI, S., SUZUKI, T., KOMUNE, S., HISA, Y., HIBINO, H. & KURACHI, Y. 2013. The mechanism underlying maintenance of the endocochlear potential by the K+ transport system in fibrocytes of the inner ear. *J Physiol,* 591**,** 4459-72.

ADAMS, D. J. & VAN DER WEYDEN, L. 2008. Contemporary approaches for modifying the mouse genome. *Physiol Genomics,* 34**,** 225-38.

ADATO, A., LEFÈVRE, G., DELPRAT, B., MICHEL, V., MICHALSKI, N., CHARDENOUX, S., WEIL, D., EL-AMRAOUI, A. & PETIT, C. 2005. Usherin, the defective protein in Usher syndrome type IIA, is likely to be a component of interstereocilia ankle links in the inner ear sensory cells. *Hum Mol Genet,* 14**,** 3921-32.

ADATO, A., MICHEL, V., KIKKAWA, Y., REINERS, J., ALAGRAMAM, K. N., WEIL, D., YONEKAWA, H., WOLFRUM, U., EL-AMRAOUI, A. & PETIT, C. 2004. Interactions in the network of Usher syndrome type 1 proteins. *Human Molecular Genetics,* 14**,** 347-356.

ADATO, A., VREUGDE, S., JOENSUU, T., AVIDAN, N., HAMALAINEN, R., BELENKIY, O., OLENDER, T., BONNE-TAMIR, B., BEN-ASHER, E., ESPINOS, C., MILLAN, J. M., LEHESJOKI, A. E., FLANNERY, J. G., AVRAHAM, K. B., PIETROKOVSKI, S., SANKILA, E. M., BECKMANN, J. S. & LANCET, D. 2002. USH3A transcripts encode clarin-1, a four-transmembrane-domain protein with a possible role in sensory synapses. *Eur J Hum Genet,* 10**,** 339-50.

ALAGRAMAM, K. N., GOODYEAR, R. J., GENG, R., FURNESS, D. N., VAN AKEN, A. F., MARCOTTI, W., KROS, C. J. & RICHARDSON, G. P. 2011. Mutations in protocadherin 15 and cadherin 23 affect tip links and mechanotransduction in mammalian sensory hair cells. *PLoS One,* 6**,** e19183.

ANGELAKI, D. E. & CULLEN, K. E. 2008. Vestibular system: the many facets of a multimodal sense. *Annu Rev Neurosci,* 31**,** 125-50.

ANNIKO, M. 1983. Cytodifferentiation of cochlear hair cells. *American Journal of Otolaryngology,* 4**,** 375-388.

ANZALONE, A. V., RANDOLPH, P. B., DAVIS, J. R., SOUSA, A. A., KOBLAN, L. W., LEVY, J. M., CHEN, P. J., WILSON, C., NEWBY, G. A., RAGURAM, A. & LIU, D. R. 2019. Search-and-replace genome editing without double-strand breaks or donor DNA. *Nature,* 576**,** 149-157.

BAGULEY, D., MCFERRAN, D. & HALL, D. 2013. Tinnitus. *The Lancet,* 382**,** 1600-1607.

BARHA, C. K., NAGAMATSU, L. S. & LIU-AMBROSE, T. 2016. Basics of neuroanatomy and neurophysiology. *Handb Clin Neurol,* 138**,** 53-68.

BARIANI, P., DE CHIFFRE, L., HANSEN, H. N. & HORSEWELL, A. 2005. Investigation on the traceability of three dimensional scanning electron microscope measurements based on the stereo-pair technique. *Precision Engineering,* 29**,** 219-228.

BARR-GILLESPIE, P.-G. 2015. Assembly of hair bundles, an amazing problem for cell biology. *Molecular Biology of the Cell,* 26**,** 2727-2732.

BÉKÉSY, G. V. & WEVER, E. G. 1960. *Experiments in hearing,* New York, McGraw-Hill.

BERMINGHAM-MCDONOGH, O. & RUBEL, E. W. 2003. Hair cell regeneration: winging our way towards a sound future. *Curr Opin Neurobiol,* 13**,** 119-26.

BERMINGHAM, N. A., HASSAN, B. A., PRICE, S. D., VOLLRATH, M. A., BEN-ARIE, N., EATOCK, R. A., BELLEN, H. J., LYSAKOWSKI, A. & ZOGHBI, H. Y. 1999. Math1: an essential gene for the generation of inner ear hair cells. *Science,* 284**,** 1837-41.

BITNER-GLINDZICZ, M., LINDLEY, K. J., RUTLAND, P., BLAYDON, D., SMITH, V. V., MILLA, P. J., HUSSAIN, K., FURTH-LAVI, J., COSGROVE, K. E., SHEPHERD, R. M., BARNES, P. D., O'BRIEN, R. E., FARNDON, P. A., SOWDEN, J., LIU, X. Z., SCANLAN, M. J., MALCOLM, S., DUNNE, M. J., AYNSLEY-GREEN, A. & GLASER, B. 2000. A recessive contiguous gene deletion causing infantile

hyperinsulinism, enteropathy and deafness identifies the Usher type 1C gene. *Nat Genet,* 26**,** 56-60.

BOEDA, B., EL-AMRAOUI, A., BAHLOUL, A., GOODYEAR, R., DAVIET, L., BLANCHARD, S., PERFETTINI, I., FATH, K. R., SHORTE, S., REINERS, J., HOUDUSSE, A., LEGRAIN, P., WOLFRUM, U., RICHARDSON, G. & PETIT, C. 2002. Myosin VIIa, harmonin and cadherin 23, three Usher I gene products that cooperate to shape the sensory hair cell bundle. *EMBO J,* 21**,** 6689-99.

BONNET, C. & EL-AMRAOUI, A. 2012. Usher syndrome (sensorineural deafness and retinitis pigmentosa): pathogenesis, molecular diagnosis and therapeutic approaches. *Curr Opin Neurol,* 25**,** 42-9.

BOWL, M. R. & DAWSON, S. J. 2015. The Mouse as a Model for Age-Related Hearing Loss - A Mini-Review. *Gerontology,* 61**,** 149-157.

BRAMHALL, N. F., SHI, F., ARNOLD, K., HOCHEDLINGER, K. & EDGE, A. S. 2014. Lgr5-positive supporting cells generate new hair cells in the postnatal cochlea. *Stem Cell Reports,* 2**,** 311-22.

BRODY, S. A., DULAWA, S. C., CONQUET, F. & GEYER, M. A. 2004. Assessment of a prepulse inhibition deficit in a mutant mouse lacking mGlu5 receptors. *Molecular Psychiatry,* 9**,** 35-41.

BROSEL, S., LAUB, C., AVERDAM, A., BENDER, A. & ELSTNER, M. 2016. Molecular aging of the mammalian vestibular system. *Ageing Res Rev,* 26**,** 72-80.

BROWN, S. D., HARDISTY-HUGHES, R. E. & MBURU, P. 2008. Quiet as a mouse: dissecting the molecular and genetic basis of hearing. *Nat Rev Genet,* 9**,** 277-90.

BRYANT, C. D., ZHANG, N. N., SOKOLOFF, G., FANSELOW, M. S., ENNES, H. S., PALMER, A. A. & MCROBERTS, J. A. 2008. Behavioral differences among C57BL/6 substrains: implications for transgenic and knockout studies. *J Neurogenet,* 22**,** 315-31.

BURNS, J. C., COX, B. C., THIEDE, B. R., ZUO, J. & CORWIN, J. T. 2012. In vivo proliferative regeneration of balance hair cells in newborn mice. *J Neurosci,* 32**,** 6570-7.

BURNS, J. C. & STONE, J. S. 2017. Development and regeneration of vestibular hair cells in mammals. *Semin Cell Dev Biol,* 65**,** 96-105.

CABERLOTTO, E., MICHEL, V., BOUTET DE MONVEL, J. & PETIT, C. 2011a. Coupling of the mechanotransduction machinery and stereocilia F-actin polymerization in the cochlear hair bundles. *BioArchitecture,* 1**,** 169-174.

CABERLOTTO, E., MICHEL, V., FOUCHER, I., BAHLOUL, A., GOODYEAR, R. J., PEPERMANS, E., MICHALSKI, N., PERFETTINI, I., ALEGRIA-PREVOT, O., CHARDENOUX, S., DO CRUZEIRO, M., HARDELIN, J. P., RICHARDSON, G. P., AVAN, P., WEIL, D. & PETIT, C. 2011b. Usher type 1G protein sans is a critical component of the tip-link complex, a structure controlling actin polymerization in stereocilia. *Proc Natl Acad Sci U S A,* 108**,** 5825-30.

CACHEIRO, P., HAENDEL, M. A. & SMEDLEY, D. 2019. New models for human disease from the International Mouse Phenotyping Consortium. *Mamm Genome,* 30**,** 143-150.

CHAN, D. K. & CHANG, K. W. 2014. GJB2-associated hearing loss: Systematic review of worldwide prevalence, genotype, and auditory phenotype. *The Laryngoscope,* 124**,** E34-E53.

CHEN, X., ABAD, C., CHEN, Z. Y., YOUNG, J. I., GURUMURTHY, C. B., WALZ, K. & LIU, X. Z. 2021. Generation and characterization of a P2rx2 V60L mouse model for DFNA41. *Hum Mol Genet*.

CHESSUM, L., MATERN, M. S., KELLY, M. C., JOHNSON, S. L., OGAWA, Y., MILON, B., MCMURRAY, M., DRIVER, E. C., PARKER, A., SONG, Y., CODNER, G., ESAPA, C. T., PRESCOTT, J., TRENT, G., WELLS, S., DRAGICH, A. K., FROLENKOV, G. I., KELLEY, M. W., MARCOTTI, W., BROWN, S. D. M., ELKON, R., BOWL, M. R. & HERTZANO, R. 2018. Helios is a key transcriptional regulator of outer hair cell maturation. *Nature,* 563**,** 696-700.

CHIEN, W. W., MONZACK, E. L., MCDOUGALD, D. S. & CUNNINGHAM, L. L. 2015. Gene therapy for sensorineural hearing loss. *Ear Hear,* 36**,** 1-7.

CHUNG, D. Y., GANNON, R. P. & MASON, K. 1984. Factors affecting the prevalence of tinnitus. *Audiology,* 23**,** 441-52.

CIORBA, A., HATZOPOULOS, S., BIANCHINI, C., AIMONI, C., SKARZYNSKI, H. & SKARZYNSKI, P. H. 2015. Genetics of presbycusis and presbystasis. *Int J Immunopathol Pharmacol,* 28**,** 29-35.

CODNER, G. F., MIANNÉ, J., CAULDER, A., LOEFFLER, J., FELL, R., KING, R., ALLAN, A. J., MACKENZIE, M., PIKE, F. J., MCCABE, C. V., CHRISTOU, S., JOYNSON, S., HUTCHISON, M., STEWART, M. E., KUMAR, S., SIMON, M. M., AGIUS, L., ANSTEE, Q. M., VOLYNSKI, K. E., KULLMANN, D. M., WELLS, S. & TEBOUL, L. 2018. Application of long single-stranded DNA donors in genome editing: generation and validation of mouse mutants. *BMC Biology,* 16**,** 70.

COMMISSION ON HEARING LOSS, 2014. Final Report. page 13. [Online]. Available: https://ilcuk.org.uk/wp-content/uploads/2018/10/Hearing-loss-Commission-final-report-website.pdf [Accessed 03.04.2020].

COREY, D. P. & HUDSPETH, A. J. 1983. Kinetics of the receptor current in bullfrog saccular hair cells. *J Neurosci,* 3**,** 962-76.

CORNS, L. F., JOHNSON, S. L., KROS, C. J. & MARCOTTI, W. 2014. Calcium entry into stereocilia drives adaptation of the mechanoelectrical transducer current of mammalian cochlear hair cells. *Proc Natl Acad Sci U S A,* 111**,** 14918-23.

CORNS, L. F., JOHNSON, S. L., KROS, C. J. & MARCOTTI, W. 2016. Tmc1 Point Mutation Affects Ca2+ Sensitivity and Block by Dihydrostreptomycin of the Mechanoelectrical Transducer Current of Mouse Outer Hair Cells. *J Neurosci,* 36**,** 336-49.

CORNS, L. F., JOHNSON, S. L., ROBERTS, T., RANATUNGA, K. M., HENDRY, A., CERIANI, F., SAFIEDDINE, S., STEEL, K. P., FORGE, A., PETIT, C., FURNESS, D. N., KROS, C. J. & MARCOTTI, W. 2018. Mechanotransduction is required for establishing and maintaining mature inner hair cells and regulating efferent innervation. *Nat Commun,* 9**,** 4015.

CORVINO, V., APISA, P., MALESCI, R., LARIA, C., AULETTA, G. & FRANZÉ, A. 2018. X-Linked Sensorineural Hearing Loss: A Literature Review. *Curr Genomics,* 19**,** 327-338.

COX, B. C., CHAI, R., LENOIR, A., LIU, Z., ZHANG, L., NGUYEN, D. H., CHALASANI, K., STEIGELMAN, K. A., FANG, J., RUBEL, E. W., CHENG, A. G. & ZUO, J. 2014. Spontaneous hair cell regeneration in the neonatal mouse cochlea in vivo. *Development,* 141**,** 816-29.

CRAWLEY, J. N., BELKNAP, J. K., COLLINS, A., CRABBE, J. C., FRANKEL, W., HENDERSON, N., HITZEMANN, R. J., MAXSON, S. C., MINER, L. L., SILVA, A. J., WEHNER, J. M., WYNSHAW-BORIS, A. & PAYLOR, R. 1997. Behavioral phenotypes of inbred mouse strains: implications and recommendations for molecular studies. *Psychopharmacology,* 132**,** 107-124.

DABDOUB, A., PULIGILLA, C., JONES, J. M., FRITZSCH, B., CHEAH, K. S., PEVNY, L. H. & KELLEY, M. W. 2008. Sox2 signaling in prosensory domain specification and subsequent hair cell differentiation in the developing cochlea. *Proc Natl Acad Sci U S A,* 105**,** 18396-401.

DALLOS, P. 1992. The active cochlea. *J Neurosci,* 12**,** 4575-85.

DELPRAT, B., MICHEL, V., GOODYEAR, R., YAMASAKI, Y., MICHALSKI, N., EL-AMRAOUI, A., PERFETTINI, I., LEGRAIN, P., RICHARDSON, G., HARDELIN, J. P. & PETIT, C. 2005. Myosin XVa and whirlin, two deafness gene products required for hair bundle growth, are located at the stereocilia tips and interact directly. *Hum Mol Genet,* 14**,** 401-10.

DENK, W., HOLT, J. R., SHEPHERD, G. M. & COREY, D. P. 1995. Calcium imaging of single stereocilia in hair cells: localization of transduction channels at both ends of tip links. *Neuron,* 15**,** 1311-21.

DI PALMA, F., HOLME, R. H., BRYDA, E. C., BELYANTSEVA, I. A., PELLEGRINO, R., KACHAR, B., STEEL, K. P. & NOBEN-TRAUTH, K. 2001. Mutations in Cdh23, encoding a new type of cadherin, cause stereocilia disorganization in waltzer, the mouse model for Usher syndrome type 1D. *Nat Genet,* 27**,** 103-7.

DOUDNA, J. A. & CHARPENTIER, E. 2014. Genome editing. The new frontier of genome engineering with CRISPR-Cas9. *Science,* 346**,** 1258096.

DOUGHERTY, W. & KESSER, B. W. 2015. Management of Conductive Hearing Loss in Children. *Otolaryngol Clin North Am,* 48**,** 955-74.

DULON, D., PAPAL, S., PATNI, P., CORTESE, M., VINCENT, P. F., TERTRAIS, M., EMPTOZ, A., TLILI, A., BOULEAU, Y., MICHEL, V., DELMAGHANI, S., AGHAIE, A., PEPERMANS, E., ALEGRIA-PREVOT, O., AKIL, O., LUSTIG, L., AVAN, P., SAFIEDDINE, S., PETIT, C. & EL-AMRAOUI, A. 2018. Clarin-1

gene transfer rescues auditory synaptopathy in model of Usher syndrome. *J Clin Invest,* 128**,** 3382-3401.

DUNBAR, L. A., PATNI, P., AGUILAR, C., MBURU, P., CORNS, L., WELLS, H. R., DELMAGHANI, S., PARKER, A., JOHNSON, S., WILLIAMS, D., ESAPA, C. T., SIMON, M. M., CHESSUM, L., NEWTON, S., DORNING, J., JEYARAJAN, P., MORSE, S., LELLI, A., CODNER, G. F., PEINEAU, T., GOPAL, S. R., ALAGRAMAM, K. N., HERTZANO, R., DULON, D., WELLS, S., WILLIAMS, F. M., PETIT, C., DAWSON, S. J., BROWN, S. D., MARCOTTI, W., EL-AMRAOUI, A. & BOWL, M. R. 2019. Clarin-2 is essential for hearing by maintaining stereocilia integrity and function. *EMBO Molecular Medicine,* 11**,** e10288.

EFFERTZ, T., SCHARR, A. L. & RICCI, A. J. 2015. The how and why of identifying the hair cell mechano-electrical transduction channel. *Pflugers Arch,* 467**,** 73-84.

EHRET, G. 1974. Age-dependent hearing loss in normal hearing mice. *Naturwissenschaften,* 61**,** 506-7.

EHRET, G. & FRANKENREITER, M. 1977. Quantitative analysis of cochlear structures in the house mouse in relation to mechanisms of acoustical information processing. *Journal of comparative physiology,* 122**,** 65-85.

ELGOYHEN, A. B. 2020. Cochlear efferent innervation: function, development and plasticity. *Current Opinion in Physiology,* 18**,** 42-48.

FANG, J., ZHANG, W. C., YAMASHITA, T., GAO, J., ZHU, M. S. & ZUO, J. 2012. Outer hair cell-specific prestin-CreERT2 knockin mouse lines. *Genesis,* 50**,** 124-31.

FAY, J. P., PURIA, S. & STEELE, C. R. 2006. The discordant eardrum. *Proc Natl Acad Sci U S A,* 103**,** 19743-8.

FEKETE, D. M., MUTHUKUMAR, S. & KARAGOGEOS, D. 1998. Hair Cells and Supporting Cells Share a Common Progenitor in the Avian Inner Ear. *The Journal of Neuroscience,* 18**,** 7811-7821.

FETTIPLACE, R. 2016. Is TMC1 the Hair Cell Mechanotransducer Channel? *Biophys J,* 111**,** 3-9.

FLOCK, A. & CHEUNG, H. C. 1977. Actin filaments in sensory hairs of inner ear receptor cells. *Journal of Cell Biology,* 75**,** 339-343.

FORGE, A., LI, L., CORWIN, J. T. & NEVILL, G. 1993. Ultrastructural evidence for hair cell regeneration in the mammalian inner ear. *Science,* 259**,** 1616-9.

FRANCO, B. & MALGRANGE, B. 2017. Concise Review: Regeneration in Mammalian Cochlea Hair Cells: Help from Supporting Cells Transdifferentiation. *STEM CELLS,* 35**,** 551-556.

FUSTER-GARCÍA, C., GARCÍA-BOHÓRQUEZ, B., RODRÍGUEZ-MUÑOZ, A., ALLER, E., JAIJO, T., MILLÁN, J. M. & GARCÍA-GARCÍA, G. 2021. Usher Syndrome: Genetics of a Human Ciliopathy. *Int J Mol Sci,* 22.

GATES, G. A. & MILLS, J. H. 2005. Presbycusis. *Lancet,* 366**,** 1111-20.

GATES, G. A., SCHMID, P., KUJAWA, S. G., NAM, B. & D'AGOSTINO, R. 2000. Longitudinal threshold changes in older men with audiometric notches. *Hear Res,* 141**,** 220-8.

GÉLÉOC, G. G. S. & EL-AMRAOUI, A. 2020. Disease mechanisms and gene therapy for Usher syndrome. *Hearing Research***,** 107932.

GELLER, S. F., GUERIN, K. I., VISEL, M., PHAM, A., LEE, E. S., DROR, A. A., AVRAHAM, K. B., HAYASHI, T., RAY, C. A., REH, T. A., BERMINGHAM-MCDONOGH, O., TRIFFO, W. J., BAO, S., ISOSOMPPI, J., VASTINSALO, H., SANKILA, E. M. & FLANNERY, J. G. 2009. CLRN1 is nonessential in the mouse retina but is required for cochlear hair cell development. *PLoS Genet,* 5**,** e1000607.

GENG, R., GELLER, S. F., HAYASHI, T., RAY, C. A., REH, T. A., BERMINGHAM-MCDONOGH, O., JONES, S. M., WRIGHT, C. G., MELKI, S., IMANISHI, Y., PALCZEWSKI, K., ALAGRAMAM, K. N. & FLANNERY, J. G. 2009. Usher syndrome IIIA gene clarin-1 is essential for hair cell function and associated neural activation. *Hum Mol Genet,* 18**,** 2748-60.

GENG, R., MELKI, S., CHEN, D. H., TIAN, G., FURNESS, D. N., OSHIMA-TAKAGO, T., NEEF, J., MOSER, T., ASKEW, C., HORWITZ, G., HOLT, J. R., IMANISHI, Y. & ALAGRAMAM, K. N. 2012. The mechanosensory structure of the hair cell requires clarin-1, a protein encoded by Usher syndrome III causative gene. *J Neurosci,* 32**,** 9485-98.

GIBSON, F., WALSH, J., MBURU, P., VARELA, A., BROWN, K. A., ANTONIO, M., BEISEL, K. W., STEEL, K. P. & BROWN, S. D. M. 1995. A type VII myosin encoded by the mouse deafness gene shaker-1. *Nature,* 374**,** 62-64.

GILLESPIE, P. G. & MÜLLER, U. 2009. Mechanotransduction by Hair Cells: Models, Molecules, and Mechanisms. *Cell,* 139**,** 33-44.

GOLD, T. & GRAY, J. 1948. Hearing. II. The physical basis of the action of the cochlea. *Proceedings of the Royal Society B: Biological Sciences,* 135**,** 492-498.

GOPAL, S. R., CHEN, D. H., CHOU, S. W., ZANG, J., NEUHAUSS, S. C., STEPANYAN, R., MCDERMOTT, B. M., JR. & ALAGRAMAM, K. N. 2015. Zebrafish Models for the Mechanosensory Hair Cell Dysfunction in Usher Syndrome 3 Reveal That Clarin-1 Is an Essential Hair Bundle Protein. *J Neurosci,* 35**,** 10188-201.

GRATI, M., SHIN, J. B., WESTON, M. D., GREEN, J., BHAT, M. A., GILLESPIE, P. G. & KACHAR, B. 2012. Localization of PDZD7 to the stereocilia ankle-link associates this scaffolding protein with the Usher syndrome protein network. *J Neurosci,* 32**,** 14288-93.

GRATI, M. H. & KACHAR, B. 2011. Myosin VIIa and sans localization at stereocilia upper tip-link density implicates these Usher syndrome proteins in mechanotransduction. *Proceedings of the National Academy of Sciences,* 108**,** 11476-11481.

GRILLET, N., XIONG, W., REYNOLDS, A., KAZMIERCZAK, P., SATO, T., LILLO, C., DUMONT, R. A., HINTERMANN, E., SCZANIECKA, A., SCHWANDER, M., WILLIAMS, D., KACHAR, B., GILLESPIE, P. G. & MÜLLER, U. 2009. Harmonin mutations cause mechanotransduction defects in cochlear hair cells. *Neuron,* 62**,** 375-87.

GROVES, A. K. 2010. The challenge of hair cell regeneration. *Exp Biol Med (Maywood),* 235**,** 434-46.

GROVES, A. K., ZHANG, K. D. & FEKETE, D. M. 2013. The genetics of hair cell development and regeneration. *Annu Rev Neurosci,* 36**,** 361-81.

GUINAN, J. J. 1996. Physiology of Olivocochlear Efferents. *In:* DALLOS, P., POPPER, A. N. & FAY, R. R. (eds.) *The Cochlea.* New York, NY: Springer New York.

GURUMURTHY, C. B., GRATI, M., OHTSUKA, M., SCHILIT, S. L., QUADROS, R. M. & LIU, X. Z. 2016. CRISPR: a versatile tool for both forward and reverse genetics research. *Hum Genet,* 135**,** 971-6.

HALL, D. A. 2012. fMRI of the Central Auditory System. *In:* FARO, S. H., MOHAMED, F. B., LAW, M. & ULMER, J. T. (eds.) *Functional Neuroradiology: Principles and Clinical Applications.* Boston, MA: Springer US.

HARDISTY-HUGHES, R. E., PARKER, A. & BROWN, S. D. 2010. A hearing and vestibular phenotyping pipeline to identify mouse mutants with hearing impairment. *Nat Protoc,* 5**,** 177-90.

HARDY, S., LEGAGNEUX, V., AUDIC, Y. & PAILLARD, L. 2010. Reverse genetics in eukaryotes. *Biol Cell,* 102**,** 561-80.

HASSON, T., WALSH, J., CABLE, J., MOOSEKER, M. S., BROWN, S. D. & STEEL, K. P. 1997. Effects of shaker-1 mutations on myosin-VIIa protein and mRNA expression. *Cell Motil Cytoskeleton,* 37**,** 127-38.

HEFFNER, H. E. & HEFFNER, R. S. 2007. Hearing ranges of laboratory animals. *J Am Assoc Lab Anim Sci,* 46**,** 20-2.

HENRY, K. R. 1979. Auditory brainstem volume-conducted responses: origins in the laboratory mouse. *J Am Aud Soc,* 4**,** 173-8.

HUDSPETH, A. J. 1989. How the ear's works work. *Nature,* 341**,** 397-404.

INTERNATIONAL MOUSE PHENOTYPING CONSORTIUM. *Gene: Clrn2. MGI:3646230* [Online]. Available: https://www.mousephenotype.org/data/genes/MGI:3646230 [Accessed 29.06.2020].

JOHNSON, K. R., ERWAY, L. C., COOK, S. A., WILLOTT, J. F. & ZHENG, Q. Y. 1997. A major gene affecting age-related hearing loss in C57BL/6J mice. *Hear Res,* 114**,** 83-92.

JOHNSON, K. R., ZHENG, Q. Y. & NOBEN-TRAUTH, K. 2006. Strain background effects and genetic modifiers of hearing in mice. *Brain Res,* 1091**,** 79-88.

JOHNSTONE, B. M. & SELLICK, P. M. 1972. The peripheral auditory apparatus. *Q Rev Biophys,* 5**,** 1-57.

JONES, T. A., JONES, S. M., VIJAYAKUMAR, S., BRUGEAUD, A., BOTHWELL, M. & CHABBERT, C. 2011. The adequate stimulus for mammalian linear vestibular evoked potentials (VsEPs). *Hear Res,* 280**,** 133-40.

JUSTICE, M. J., NOVEROSKE, J. K., WEBER, J. S., ZHENG, B. & BRADLEY, A. 1999. Mouse ENU mutagenesis. *Hum Mol Genet,* 8**,** 1955-63.

KANE, K. L., LONGO-GUESS, C. M., GAGNON, L. H., DING, D., SALVI, R. J. & JOHNSON, K. R. 2012. Genetic background effects on age-related hearing loss associated with Cdh23 variants in mice. *Hear Res,* 283**,** 80-8.

KANTOR, A., MCCLEMENTS, M. E. & MACLAREN, R. E. 2020. CRISPR-Cas9 DNA Base-Editing and Prime-Editing. *Int J Mol Sci,* 21.

KAUR, G. & DUFOUR, J. M. 2012. Cell lines: Valuable tools or useless artifacts. *Spermatogenesis,* 2**,** 1-5.

KAWAMOTO, K., IZUMIKAWA, M., BEYER, L. A., ATKIN, G. M. & RAPHAEL, Y. 2009. Spontaneous hair cell regeneration in the mouse utricle following gentamicin ototoxicity. *Hear Res,* 247**,** 17-26.

KAWASHIMA, Y., GÉLÉOC, G. S., KURIMA, K., LABAY, V., LELLI, A., ASAI, Y., MAKISHIMA, T., WU, D. K., DELLA SANTINA, C. C., HOLT, J. R. & GRIFFITH, A. J. 2011. Mechanotransduction in mouse inner ear hair cells requires transmembrane channel-like genes. *J Clin Invest,* 121**,** 4796-809.

KAZMIERCZAK, P., SAKAGUCHI, H., TOKITA, J., WILSON-KUBALEK, E. M., MILLIGAN, R. A., MULLER, U. & KACHAR, B. 2007. Cadherin 23 and protocadherin 15 interact to form tip-link filaments in sensory hair cells. *Nature,* 449**,** 87-91.

KELSELL, D. P., DUNLOP, J., STEVENS, H. P., LENCH, N. J., LIANG, J. N., PARRY, G., MUELLER, R. F. & LEIGH, I. M. 1997. Connexin 26 mutations in hereditary non-syndromic sensorineural deafness. *Nature,* 387**,** 80-3.

KEMP, D. T. 1978. Stimulated acoustic emissions from within the human auditory system. *The Journal of the Acoustical Society of America,* 64**,** 1386-1391.

KIKKAWA, Y., SHITARA, H., WAKANA, S., KOHARA, Y., TAKADA, T., OKAMOTO, M., TAYA, C., KAMIYA, K., YOSHIKAWA, Y., TOKANO, H., KITAMURA, K., SHIMIZU, K., WAKABAYASHI, Y., SHIROISHI, T., KOMINAMI, R. & YONEKAWA, H. 2003. Mutations in a new scaffold protein Sans cause deafness in Jackson shaker mice. *Hum Mol Genet,* 12**,** 453-61.

KIKUCHI, T., KIMURA, R. S., PAUL, D. L., TAKASAKA, T. & ADAMS, J. C. 2000. Gap junction systems in the mammalian cochlea. *Brain Research Reviews,* 32**,** 163-166.

KILE, B. T. & HILTON, D. J. 2005. The art and design of genetic screens: mouse. *Nat Rev Genet,* 6**,** 557-67.

KIM, H., KIM, M., IM, S. K. & FANG, S. 2018. Mouse Cre-LoxP system: general principles to determine tissue-specific roles of target genes. *Lab Anim Res,* 34**,** 147-159.

KITAMURA, K., KAKOI, H., YOSHIKAWA, Y. & OCHIKUBO, F. 1992. Ultrastructural findings in the inner ear of Jackson shaker mice. *Acta Otolaryngol,* 112**,** 622-7.

KLEIN, J. O. 1994. Otitis media. *Clin Infect Dis,* 19**,** 823-33.

KLINKE, R. 1986. Neurotransmission in the inner ear. *Hearing Research,* 22**,** 235-243.

KOLLA, L., KELLY, M. C., MANN, Z. F., ANAYA-ROCHA, A., ELLIS, K., LEMONS, A., PALERMO, A. T., SO, K. S., MAYS, J. C., ORVIS, J., BURNS, J. C., HERTZANO, R., DRIVER, E. C. & KELLEY, M. W. 2020. Characterization of the development of the mouse cochlear epithelium at the single cell level. *Nat Commun,* 11**,** 2389.

KOMOR, A. C., KIM, Y. B., PACKER, M. S., ZURIS, J. A. & LIU, D. R. 2016. Programmable editing of a target base in genomic DNA without double-stranded DNA cleavage. *Nature,* 533**,** 420-4.

KREY, J. F., CHATTERJEE, P., DUMONT, R. A., O'SULLIVAN, M., CHOI, D., BIRD, J. E. & BARR-GILLESPIE, P. G. 2020. Mechanotransduction-Dependent Control of Stereocilia Dimensions and Row Identity in Inner Hair Cells. *Current Biology,* 30**,** 442-454.e7.

KROS, C. J., RUPPERSBERG, J. P. & RÜSCH, A. 1998. Expression of a potassium current in inner hair cells during development of hearing in mice. *Nature,* 394**,** 281-4.

KUBISCH, C., SCHROEDER, B. C., FRIEDRICH, T., LUTJOHANN, B., EL-AMRAOUI, A., MARLIN, S., PETIT, C. & JENTSCH, T. J. 1999. KCNQ4, a novel potassium channel expressed in sensory outer hair cells, is mutated in dominant deafness. *Cell,* 96**,** 437-46.

KUBOTA, M., SCHEIBINGER, M., JAN, T. A. & HELLER, S. 2021. Greater epithelial ridge cells are the principal organoid-forming progenitors of the mouse cochlea. *Cell Rep,* 34**,** 108646.

KUJAWA, S. G. & LIBERMAN, M. C. 2006. Acceleration of age-related hearing loss by early noise exposure: evidence of a misspent youth. *J Neurosci,* 26**,** 2115-23.

KUJAWA, S. G. & LIBERMAN, M. C. 2009. Adding insult to injury: cochlear nerve degeneration after "temporary" noise-induced hearing loss. *J Neurosci,* 29**,** 14077-85.

KURIMA, K., EBRAHIM, S., PAN, B., SEDLACEK, M., SENGUPTA, P., MILLIS, B. A., CUI, R., NAKANISHI, H., FUJIKAWA, T., KAWASHIMA, Y., CHOI, B. Y., MONAHAN, K., HOLT, J. R., GRIFFITH, A. J. & KACHAR, B. 2015. TMC1 and TMC2 Localize at the Site of Mechanotransduction in Mammalian Inner Ear Hair Cell Stereocilia. *Cell Rep,* 12**,** 1606-17.

KURIMA, K., PETERS, L. M., YANG, Y., RIAZUDDIN, S., AHMED, Z. M., NAZ, S., ARNAUD, D., DRURY, S., MO, J., MAKISHIMA, T., GHOSH, M., MENON, P. S., DESHMUKH, D., ODDOUX, C., OSTRER, H., KHAN, S., RIAZUDDIN, S., DEININGER, P. L., HAMPTON, L. L., SULLIVAN, S. L., BATTEY, J. F., JR., KEATS, B. J., WILCOX, E. R., FRIEDMAN, T. B. & GRIFFITH, A. J. 2002. Dominant and recessive deafness caused by mutations of a novel gene, TMC1, required for cochlear hair-cell function. *Nat Genet,* 30**,** 277-84.

LAKSO, M., SAUER, B., MOSINGER, B., JR., LEE, E. J., MANNING, R. W., YU, S. H., MULDER, K. L. & WESTPHAL, H. 1992. Targeted oncogene activation by site-specific recombination in transgenic mice. *Proc Natl Acad Sci U S A,* 89**,** 6232-6.

LE, T. N., STRAATMAN, L. V., LEA, J. & WESTERBERG, B. 2017. Current insights in noise-induced hearing loss: a literature review of the underlying mechanism, pathophysiology, asymmetry, and management options. *J Otolaryngol Head Neck Surg,* 46**,** 41.

LEFÈVRE, G., MICHEL, V., WEIL, D., LEPELLETIER, L. A., BIZARD, E., WOLFRUM, U., HARDELIN, J.-P. & PETIT, C. 2008. A core cochlear phenotype in USH1 mouse mutants implicates fibrous links of the hair bundle in its cohesion, orientation and differential growth. *Development,* 135**,** 1427-1437.

LEITNER, M. G. 2014. Zebrafish in auditory research: are fish better than mice? *J Physiol,* 592**,** 4611-2.

LELLI, A., ASAI, Y., FORGE, A., HOLT, J. R. & GÉLÉOC, G. S. 2009. Tonotopic gradient in the developmental acquisition of sensory transduction in outer hair cells of the mouse cochlea. *J Neurophysiol,* 101**,** 2961-73.

LEVY, S. & SHOHAM, T. 2005. Protein-protein interactions in the tetraspanin web. *Physiology (Bethesda),* 20**,** 218-24.

LI, C. W., VAN DE WATER, T. R. & RUBEN, R. J. 1978. The fate mapping of the eleventh and twelfth day mouse otocyst: an in vitro study of the sites of origin of the embryonic inner ear sensory structures. *J Morphol,* 157**,** 249-67.

LI, W., YOU, D., CHEN, Y., CHAI, R. & LI, H. 2016. Regeneration of hair cells in the mammalian vestibular system. *Front Med,* 10**,** 143-51.

LIM, D. J. 1980. Cochlear anatomy related to cochlear micromechanics. A review. *J Acoust Soc Am,* 67**,** 1686-95.

LIM, D. J. & ANNIKO, M. 1985. Developmental morphology of the mouse inner ear. A scanning electron microscopic observation. *Acta Otolaryngol Suppl,* 422**,** 1-69.

LIU, H., CHEN, L., GIFFEN, K. P., STRINGHAM, S. T., LI, Y., JUDGE, P. D., BEISEL, K. W. & HE, D. Z. Z. 2018. Cell-Specific Transcriptome Analysis Shows That Adult Pillar and Deiters' Cells Express Genes Encoding Machinery for Specializations of Cochlear Hair Cells. *Frontiers in Molecular Neuroscience,* 11.

LIU, H., PECKA, J. L., ZHANG, Q., SOUKUP, G. A., BEISEL, K. W. & HE, D. Z. Z. 2014. Characterization of Transcriptomes of Cochlear Inner and Outer Hair Cells. *The Journal of Neuroscience,* 34**,** 11085-11095.

LIVINGSTON, G., SOMMERLAD, A., ORGETA, V., COSTAFREDA, S. G., HUNTLEY, J., AMES, D., BALLARD, C., BANERJEE, S., BURNS, A., COHEN-MANSFIELD, J., COOPER, C., FOX, N., GITLIN, L. N., HOWARD, R., KALES, H. C., LARSON, E. B., RITCHIE, K., ROCKWOOD, K., SAMPSON, E. L., SAMUS, Q., SCHNEIDER, L. S., SELBAEK, G., TERI, L. & MUKADAM, N. 2017. Dementia prevention, intervention, and care. *Lancet,* 390**,** 2673-2734.

LONGO-GUESS, C. M., GAGNON, L. H., COOK, S. A., WU, J., ZHENG, Q. Y. & JOHNSON, K. R. 2005. A missense mutation in the previously undescribed gene Tmhs underlies deafness in hurry-scurry (hscy) mice. *Proc Natl Acad Sci U S A,* 102**,** 7894-9.

LUMPKIN, E. A., MARQUIS, R. E. & HUDSPETH, A. J. 1997. The selectivity of the hair cell's mechanoelectrical-transduction channel promotes Ca2+ flux at low Ca2+ concentrations. *Proceedings of the National Academy of Sciences,* 94**,** 10997-11002.

LUSH, M. E. & PIOTROWSKI, T. 2014. Sensory hair cell regeneration in the zebrafish lateral line. *Dev Dyn,* 243**,** 1187-202.

MAECKER, H. T., TODD, S. C. & LEVY, S. 1997. The tetraspanin superfamily: molecular facilitators. *Faseb j,* 11**,** 428-42.

MAEDA, R., KINDT, K. S., MO, W., MORGAN, C. P., ERICKSON, T., ZHAO, H., CLEMENS-GRISHAM, R., BARR-GILLESPIE, P. G. & NICOLSON, T. 2014. Tip-link protein protocadherin 15 interacts with transmembrane channel-like proteins TMC1 and TMC2. *Proc Natl Acad Sci U S A,* 111**,** 12907-12.

MAERKER, T., VAN WIJK, E., OVERLACK, N., KERSTEN, F. F., MCGEE, J., GOLDMANN, T., SEHN, E., ROEPMAN, R., WALSH, E. J., KREMER, H. & WOLFRUM, U. 2008. A novel Usher protein network at the periciliary reloading point between molecular transport machineries in vertebrate photoreceptor cells. *Hum Mol Genet,* 17**,** 71-86.

MAHENDRASINGAM, S., FETTIPLACE, R., ALAGRAMAM, K. N., CROSS, E. & FURNESS, D. N. 2017. Spatiotemporal changes in the distribution of LHFPL5 in mice cochlear hair bundles during development and in the absence of PCDH15. *PLoS One,* 12**,** e0185285.

MARCOTTI, W. 2012. Functional assembly of mammalian cochlear hair cells. *Exp Physiol,* 97**,** 438-51.

MARCOTTI, W., JOHNSON, S. L., HOLLEY, M. C. & KROS, C. J. 2003. Developmental changes in the expression of potassium currents of embryonic, neonatal and mature mouse inner hair cells. *J Physiol,* 548**,** 383-400.

MARCOTTI, W. & KROS, C. J. 1999. Developmental expression of the potassium current IK,n contributes to maturation of mouse outer hair cells. *J Physiol,* 520 Pt 3**,** 653-60.

MATHUR, P. & YANG, J. 2015. Usher syndrome: Hearing loss, retinal degeneration and associated abnormalities. *Biochim Biophys Acta,* 1852**,** 406-20.

MATSUBARA, A., LAAKE, J. H., DAVANGER, S., USAMI, S. & OTTERSEN, O. P. 1996. Organization of AMPA receptor subunits at a glutamate synapse: a quantitative immunogold analysis of hair cell synapses in the rat organ of Corti. *J Neurosci,* 16**,** 4457-67.

MBURU, P., MUSTAPHA, M., VARELA, A., WEIL, D., EL-AMRAOUI, A., HOLME, R. H., RUMP, A., HARDISTY, R. E., BLANCHARD, S., COIMBRA, R. S., PERFETTINI, I., PARKINSON, N., MALLON, A. M., GLENISTER, P., ROGERS, M. J., PAIGE, A. J., MOIR, L., CLAY, J., ROSENTHAL, A., LIU, X. Z., BLANCO, G., STEEL, K. P., PETIT, C. & BROWN, S. D. 2003. Defects in whirlin, a PDZ domain molecule involved in stereocilia elongation, cause deafness in the whirler mouse and families with DFNB31. *Nat Genet,* 34**,** 421-8.

MCGOVERN, M. M., RANDLE, M. R., CUPPINI, C. L., GRAVES, K. A. & COX, B. C. 2019. Multiple supporting cell subtypes are capable of spontaneous hair cell regeneration in the neonatal mouse cochlea. *Development,* 146**,** dev171009.

MCGRATH, J., ROY, P. & PERRIN, B. J. 2017. Stereocilia morphogenesis and maintenance through regulation of actin stability. *Semin Cell Dev Biol,* 65**,** 88-95.

MCINTURFF, S., BURNS, J. C. & KELLEY, M. W. 2018. Characterization of spatial and temporal development of Type I and Type II hair cells in the mouse utricle using new cell-type-specific markers. *Biol Open,* 7.

MCNULTY, J. A. & FOX, L. M. 1992. Pinealocyte synaptic ribbons and neuroendocrine function. *Microsc Res Tech,* 21**,** 175-87.

MELCHER, J. R. & KIANG, N. Y. S. 1996. Generators of the brainstem auditory evoked potential in cat III: identified cell populations. *Hearing Research,* 93**,** 52-71.

METZGER, D. & CHAMBON, P. 2001. Site- and time-specific gene targeting in the mouse. *Methods,* 24**,** 71-80.

MIANNÉ, J., CHESSUM, L., KUMAR, S., AGUILAR, C., CODNER, G., HUTCHISON, M., PARKER, A., MALLON, A.-M., WELLS, S., SIMON, M. M., TEBOUL, L., BROWN, S. D. M. & BOWL, M. R. 2016. Correction of the auditory phenotype in C57BL/6N mice via CRISPR/Cas9-mediated homology directed repair. *Genome Medicine,* 8**,** 16.

MICHALSKI, N., MICHEL, V., BAHLOUL, A., LEFÈVRE, G., BARRAL, J., YAGI, H., CHARDENOUX, S., WEIL, D., MARTIN, P., HARDELIN, J. P., SATO, M. & PETIT, C. 2007. Molecular characterization of the ankle-link complex in cochlear hair cells and its role in the hair bundle functioning. *J Neurosci,* 27**,** 6478-88.

MICHALSKI, N., MICHEL, V., CABERLOTTO, E., LEFÈVRE, G. M., VAN AKEN, A. F., TINEVEZ, J. Y., BIZARD, E., HOUBRON, C., WEIL, D., HARDELIN, J. P., RICHARDSON, G. P., KROS, C. J., MARTIN, P. & PETIT, C. 2009. Harmonin-b, an actin-binding scaffold protein, is involved in the adaptation of mechanoelectrical transduction by sensory hair cells. *Pflugers Arch,* 459**,** 115-30.

MICHANSKI, S., SMALUCH, K., STEYER, A. M., CHAKRABARTI, R., SETZ, C., OESTREICHER, D., FISCHER, C., MÖBIUS, W., MOSER, T., VOGL, C. & WICHMANN, C. 2019. Mapping developmental maturation of inner hair cell ribbon synapses in the apical mouse cochlea. *Proceedings of the National Academy of Sciences,* 116**,** 6415-6424.

MICHEL, V., BOOTH, K. T., PATNI, P., CORTESE, M., AZAIEZ, H., BAHLOUL, A., KAHRIZI, K., LABBE, M., EMPTOZ, A., LELLI, A., DEGARDIN, J., DUPONT, T., AGHAIE, A., OFICJALSKA-PHAM, D., PICAUD, S., NAJMABADI, H., SMITH, R. J., BOWL, M. R., BROWN, S. D., AVAN, P., PETIT, C. & EL-AMRAOUI, A. 2017. CIB2, defective in isolated deafness, is key for auditory hair cell mechanotransduction and survival. *EMBO Mol Med,* 9**,** 1711-1731.

MILLS, J. H. & GOING, J. A. 1982. Review of environmental factors affecting hearing. *Environ Health Perspect,* 44**,** 119-27.

MITCHEM, K. L., HIBBARD, E., BEYER, L. A., BOSOM, K., DOOTZ, G. A., DOLAN, D. F., JOHNSON, K. R., RAPHAEL, Y. & KOHRMAN, D. C. 2002. Mutation of the novel gene Tmie results in sensory cell defects in the inner ear of spinner, a mouse model of human hearing loss DFNB6. *Human Molecular Genetics,* 11**,** 1887-1898.

MORESCO, E. M., LI, X. & BEUTLER, B. 2013. Going forward with genetics: recent technological advances and forward genetics in mice. *Am J Pathol,* 182**,** 1462-73.

MORSLI, H., CHOO, D., RYAN, A., JOHNSON, R. & WU, D. K. 1998. Development of the mouse inner ear and origin of its sensory organs. *J Neurosci,* 18**,** 3327-35.

MOUNTAIN, D. C. & HUBBARD, A. E. 1989. Rapid force production in the cochlea. *Hear Res,* 42**,** 195-202.

NOBEN-TRAUTH, K., ZHENG, Q. Y. & JOHNSON, K. R. 2003. Association of cadherin 23 with polygenic inheritance and genetic modification of sensorineural hearing loss. *Nat Genet,* 35**,** 21-3.

NOEBELS, J. L., QIAO, X., BRONSON, R. T., SPENCER, C. & DAVISSON, M. T. 1990. Stargazer: a new neurological mutant on chromosome 15 in the mouse with prolonged cortical seizures. *Epilepsy Research,* 7**,** 129-135.

NORDMANN, A. S., BOHNE, B. A. & HARDING, G. W. 2000. Histopathological differences between temporary and permanent threshold shift. *Hear Res,* 139**,** 13-30.

NOUVIAN, R., BEUTNER, D., PARSONS, T. D. & MOSER, T. 2006. Structure and function of the hair cell ribbon synapse. *J Membr Biol,* 209**,** 153-65.

OGUN, O. & ZALLOCCHI, M. 2014. Clarin-1 acts as a modulator of mechanotransduction activity and presynaptic ribbon assembly. *J Cell Biol,* 207**,** 375-91.

OHLEMILLER, K. K., JONES, S. M. & JOHNSON, K. R. 2016. Application of Mouse Models to Research in Hearing and Balance. *J Assoc Res Otolaryngol,* 17**,** 493-523.

OHYAMA, T., BASCH, M. L., MISHINA, Y., LYONS, K. M., SEGIL, N. & GROVES, A. K. 2010. BMP signaling is necessary for patterning the sensory and nonsensory regions of the developing mammalian cochlea. *J Neurosci,* 30**,** 15044-51.

OHYAMA, T., GROVES, A. K. & MARTIN, K. 2007. The first steps towards hearing: mechanisms of otic placode induction. *Int J Dev Biol,* 51**,** 463-72.

ORBAN, P. C., CHUI, D. & MARTH, J. D. 1992. Tissue- and site-specific DNA recombination in transgenic mice. *Proc Natl Acad Sci U S A,* 89**,** 6861-5.

PAIGEN, K. 2003. One hundred years of mouse genetics: an intellectual history. II. The molecular revolution (1981-2002). *Genetics,* 163**,** 1227-35.

PAN, B., GELEOC, G. S., ASAI, Y., HORWITZ, G. C., KURIMA, K., ISHIKAWA, K., KAWASHIMA, Y., GRIFFITH, A. J. & HOLT, J. R. 2013. TMC1 and TMC2 are components of the mechanotransduction channel in hair cells of the mammalian inner ear. *Neuron,* 79**,** 504-15.

PERKINS, R. E. & MOREST, D. K. 1975. A study of cochlear innervation patterns in cats and rats with the Golgi method and Nomarski optics. *Journal of Comparative Neurology,* 163**,** 129-158.

PICKETT, S. B. & RAIBLE, D. W. 2019. Water Waves to Sound Waves: Using Zebrafish to Explore Hair Cell Biology. *Journal of the Association for Research in Otolaryngology,* 20**,** 1-19.

PICKLES, J. O., COMIS, S. D. & OSBORNE, M. P. 1984. Cross-links between stereocilia in the guinea pig organ of Corti, and their possible relation to sensory transduction. *Hear Res,* 15**,** 103-12.

POTTER, P. K., BOWL, M. R., JEYARAJAN, P., WISBY, L., BLEASE, A., GOLDSWORTHY, M. E., SIMON, M. M., GREENAWAY, S., MICHEL, V., BARNARD, A., AGUILAR, C., AGNEW, T., BANKS, G., BLAKE, A., CHESSUM, L., DORNING, J., FALCONE, S., GOOSEY, L., HARRIS, S., HAYNES, A., HEISE, I., HILLIER, R., HOUGH, T., HOSLIN, A., HUTCHISON, M., KING, R., KUMAR, S., LAD, H. V., LAW, G., MACLAREN, R. E., MORSE, S., NICOL, T., PARKER, A., PICKFORD, K., SETHI, S., STARBUCK, B., STELMA, F., CHEESEMAN, M., CROSS, S. H., FOSTER, R. G., JACKSON, I. J., PEIRSON, S. N., THAKKER, R. V., VINCENT, T., SCUDAMORE, C., WELLS, S., EL-AMRAOUI, A., PETIT, C., ACEVEDO-AROZENA, A., NOLAN, P. M., COX, R., MALLON, A. M. & BROWN, S. D. 2016. Novel gene function revealed by mouse mutagenesis screens for models of age-related disease. *Nat Commun,* 7**,** 12444.

RAMÍREZ-CAMACHO, R., GARCÍA-BERROCAL, J. R., TRINIDAD, A., GONZÁLEZ-GARCÍA, J. A., VERDAGUER, J. M., IBÁÑEZ, A., RODRÍGUEZ, A. & SANZ, R. 2006. Central role of supporting cells in cochlear homeostasis and pathology. *Medical Hypotheses,* 67**,** 550-555.

RANUM, P. T., GOODWIN, A. T., YOSHIMURA, H., KOLBE, D. L., WALLS, W. D., KOH, J.-Y., HE, D. Z. Z. & SMITH, R. J. H. 2019. Insights into the Biology of Hearing and Deafness Revealed by Single-Cell RNA Sequencing. *Cell Reports,* 26**,** 3160-3171.e3.

REINERS, J., MÄRKER, T., JÜRGENS, K., REIDEL, B. & WOLFRUM, U. 2005. Photoreceptor expression of the Usher syndrome type 1 protein protocadherin 15 (USH1F) and its interaction with the scaffold protein harmonin (USH1C). *Mol Vis,* 11**,** 347-55.REIS, L. R. & ESCADA, P. 2016. Presbycusis: do we have a third ear? *Braz J Otorhinolaryngol,* 82**,** 710-714.

REN, Y., LANDEGGER, L. D. & STANKOVIC, K. M. 2019. Gene Therapy for Human Sensorineural Hearing Loss. *Frontiers in Cellular Neuroscience,* 13.

RIAZUDDIN, S., BELYANTSEVA, I. A., GIESE, A. P., LEE, K., INDZHYKULIAN, A. A., NANDAMURI, S. P., YOUSAF, R., SINHA, G. P., LEE, S., TERRELL, D., HEGDE, R. S., ALI, R. A., ANWAR, S., ANDRADE-ELIZONDO, P. B., SIRMACI, A., PARISE, L. V., BASIT, S., WALI, A., AYUB, M., ANSAR, M., AHMAD, W., KHAN, S. N., AKRAM, J., TEKIN, M., RIAZUDDIN, S., COOK, T., BUSCHBECK, E. K., FROLENKOV, G. I., LEAL, S. M., FRIEDMAN, T. B. & AHMED, Z. M. 2012. Alterations of the CIB2 calcium- and integrin-binding protein cause Usher syndrome type 1J and nonsyndromic deafness DFNB48. *Nat Genet,* 44**,** 1265-71.

ROBERTS, L. E., EGGERMONT, J. J., CASPARY, D. M., SHORE, S. E., MELCHER, J. R. & KALTENBACH, J. A. 2010. Ringing Ears: The Neuroscience of Tinnitus. *The Journal of Neuroscience,* 30**,** 14972-14979.

ROBLES, L. & RUGGERO, M. A. 2001. Mechanics of the mammalian cochlea. *Physiol Rev,* 81**,** 1305-52.

ROCHE, J. P. & HANSEN, M. R. 2015. On the Horizon: Cochlear Implant Technology. *Otolaryngol Clin North Am,* 48**,** 1097-116.

ROSENTHAL, N. & BROWN, S. 2007. The mouse ascending: perspectives for human-disease models. *Nat Cell Biol,* 9**,** 993-9.

ROYAL NATIONAL INSTITUTE FOR DEAF PEOPLE. *Facts and Figures* [Online]. Available: https://www.actiononhearingloss.org.uk/about-us/our-research-and-evidence/facts-and-figures/ [Accessed 03.04.2020].

ROYAL NATIONAL INSTITUTE FOR DEAF PEOPLE. 2014. *Hearing Matters Report* [Online]. Available: https://www.actiononhearingloss.org.uk/about-us/our-research-and-evidence/research-reports/hearing-matters-report/ [Accessed 19.03.2020].

RUSSELL, W. L., KELLY, E. M., HUNSICKER, P. R., BANGHAM, J. W., MADDUX, S. C. & PHIPPS, E. L. 1979. Specific-locus test shows ethylnitrosourea to be the most potent mutagen in the mouse. *Proc Natl Acad Sci U S A,* 76**,** 5818-9.

SAKAGUCHI, H., TOKITA, J., MÜLLER, U. & KACHAR, B. 2009. Tip links in hair cells: molecular composition and role in hearing loss. *Curr Opin Otolaryngol Head Neck Surg,* 17**,** 388-93.

SANDER, J. D. & JOUNG, J. K. 2014. CRISPR-Cas systems for editing, regulating and targeting genomes. *Nature Biotechnology,* 32**,** 347-355.

SAWADA, I., KITAHARA, M. & YAZAWA, Y. 1994. Swimming test for evaluating vestibular function in guinea pigs. *Acta Otolaryngol Suppl,* 510**,** 20-3.

SCHNEIDER, M. E., BELYANTSEVA, I. A., AZEVEDO, R. B. & KACHAR, B. 2002. Rapid renewal of auditory hair bundles. *Nature,* 418**,** 837-838.

SCHUKNECHT, H. F. 1964. FURTHER OBSERVATIONS ON THE PATHOLOGY OF PRESBYCUSIS. *Arch Otolaryngol,* 80**,** 369-82.

SCHWANDER, M., KACHAR, B. & MÜLLER, U. 2010. Review series: The cell biology of hearing. *J Cell Biol,* 190**,** 9-20.

SELF, T., MAHONY, M., FLEMING, J., WALSH, J., BROWN, S. D. & STEEL, K. P. 1998. Shaker-1 mutations reveal roles for myosin VIIA in both development and function of cochlear hair cells. *Development,* 125**,** 557-566.

SHEARER, E. H., M.; SMITH, R. 1999. *Hereditary Hearing Loss and Deafness Overview* [Online]. Available: https://www.ncbi.nlm.nih.gov/books/NBK1434/#_ncbi_dlg_citbx_NBK1434 [Accessed 11th January 2021].

SHI, L., CHANG, Y., LI, X., AIKEN, S., LIU, L. & WANG, J. 2016. Cochlear Synaptopathy and Noise-Induced Hidden Hearing Loss. *Neural Plast,* 2016**,** 6143164.

SIEMENS, J., KAZMIERCZAK, P., REYNOLDS, A., STICKER, M., LITTLEWOOD-EVANS, A. & MÜLLER, U. 2002. The Usher syndrome proteins cadherin 23 and harmonin form a complex by means of PDZ-domain interactions. *Proceedings of the National Academy of Sciences,* 99**,** 14946-14951.

SIEMENS, J., LILLO, C., DUMONT, R. A., REYNOLDS, A., WILLIAMS, D. S., GILLESPIE, P. G. & MULLER, U. 2004. Cadherin 23 is a component of the tip link in hair-cell stereocilia. *Nature,* 428**,** 950-5.

SLEPECKY, N. B., HENDERSON, C. G. & SAHA, S. 1995. Post-translational modifications of tubulin suggest that dynamic microtubules are present in sensory cells and stable microtubules are present in supporting cells of the mammalian cochlea. *Hear Res,* 91**,** 136-47.

SMITH, C. A., LOWRY, O. H. & WU, M.-L. 1954. The electrolytes of the labyrinthine fluids. *The Laryngoscope,* 64**,** 141-153.

SORUSCH, N., BAUß, K., PLUTNIOK, J., SAMANTA, A., KNAPP, B., NAGEL-WOLFRUM, K. & WOLFRUM, U. 2017. Characterization of the ternary Usher syndrome SANS/ush2a/whirlin protein complex. *Hum Mol Genet,* 26**,** 1157-1172.

STAECKER, H. & THOMPSON, J. 2013. Central Auditory System, Anatomy. *In:* KOUNTAKIS, S. E. (ed.) *Encyclopedia of Otolaryngology, Head and Neck Surgery.* Berlin, Heidelberg: Springer Berlin Heidelberg.

STAHL, S. M. 2017. Does treating hearing loss prevent or slow the progress of dementia? Hearing is not all in the ears, but who's listening? *CNS Spectr,* 22**,** 247-250.

SUDLOW, C., GALLACHER, J., ALLEN, N., BERAL, V., BURTON, P., DANESH, J., DOWNEY, P., ELLIOTT, P., GREEN, J., LANDRAY, M., LIU, B., MATTHEWS, P., ONG, G., PELL, J., SILMAN, A., YOUNG, A., SPROSEN, T., PEAKMAN, T. & COLLINS, R. 2015. UK biobank: an open access resource for identifying the causes of a wide range of complex diseases of middle and old age. *PLoS Med,* 12**,** e1001779.

SUN, S., BABOLA, T., PREGERNIG, G., SO, K. S., NGUYEN, M., SU, S. M., PALERMO, A. T., BERGLES, D. E., BURNS, J. C. & MULLER, U. 2018. Hair Cell Mechanotransduction Regulates Spontaneous Activity and Spiral Ganglion Subtype Specification in the Auditory System. *Cell,* 174**,** 1247-1263.e15.

TASAKI, I. & SPYROPOULOS, C. S. 1959. Stria vascularis as source of endocochlear potential. *J Neurophysiol,* 22**,** 149-55.

TAWFIK, K. O., KLEPPER, K., SALIBA, J. & FRIEDMAN, R. A. 2019. Advances in understanding of presbycusis. *J Neurosci Res*.

THARPE, A. M. & GUSTAFSON, S. 2015. Management of Children with Mild, Moderate, and Moderately Severe Sensorineural Hearing Loss. *Otolaryngol Clin North Am,* 48**,** 983-94.

THOMSON, S. & MADANI, G. 2014. The windows of the inner ear. *Clin Radiol,* 69**,** e146-52.

TIAN, G., ZHOU, Y., HAJKOVA, D., MIYAGI, M., DINCULESCU, A., HAUSWIRTH, W. W., PALCZEWSKI, K., GENG, R., ALAGRAMAM, K. N., ISOSOMPPI, J., SANKILA, E. M., FLANNERY, J. G. & IMANISHI, Y. 2009. Clarin-1, encoded by the Usher Syndrome III causative gene, forms a membranous microdomain: possible role of clarin-1 in organizing the actin cytoskeleton. *J Biol Chem,* 284**,** 18980-93.

TILNEY, L. G., TILNEY, M. S. & DEROSIER, D. J. 1992. Actin filaments, stereocilia, and hair cells: how cells count and measure. *Annu Rev Cell Biol,* 8**,** 257-74.

TOS, M. 1984. Epidemiology and natural history of secretory otitis. *Am J Otol,* 5**,** 459-62.

TURNER, J. G., PARRISH, J. L., HUGHES, L. F., TOTH, L. A. & CASPARY, D. M. 2005. Hearing in laboratory animals: strain differences and nonauditory effects of noise. *Comp Med,* 55**,** 12-23.

UCHIDA, Y., SUGIURA, S., NISHITA, Y., SAJI, N., SONE, M. & UEDA, H. 2019. Age-related hearing loss and cognitive decline — The potential mechanisms linking the two. *Auris Nasus Larynx,* 46**,** 1-9.

VAN DER HEIJDEN, M., LORTEIJE, J. A., PLAUŠKA, A., ROBERTS, M. T., GOLDING, N. L. & BORST, J. G. 2013. Directional hearing by linear summation of binaural inputs at the medial superior olive. *Neuron,* 78**,** 936-48.

VAN HEERBEEK, N., INGELS, K. J. A. O., RIJKERS, G. T. & ZIELHUIS, G. A. 2002. Therapeutic improvement of Eustachian tube function: a review. *Clinical Otolaryngology & Allied Sciences,* 27**,** 50-56.

VELEZ-ORTEGA, A. C., FREEMAN, M. J., INDZHYKULIAN, A. A., GROSSHEIM, J. M. & FROLENKOV, G. I. 2017. Mechanotransduction current is essential for stability of the transducing stereocilia in mammalian auditory hair cells. *Elife,* 6.

VENEKAMP, R. P., MICK, P., SCHILDER, A. G. & NUNEZ, D. A. 2018. Grommets (ventilation tubes) for recurrent acute otitis media in children. *Cochrane Database Syst Rev,* 5**,** Cd012017.

VERPY, E., LEIBOVICI, M., ZWAENEPOEL, I., LIU, X.-Z., GAL, A., SALEM, N., MANSOUR, A., BLANCHARD, S., KOBAYASHI, I., KEATS, B. J. B., SLIM, R. & PETIT, C. 2000. A defect in harmonin, a PDZ domain-containing protein expressed in the inner ear sensory hair cells, underlies Usher syndrome type 1C. *Nature Genetics,* 26**,** 51-55.

VOGEL, C. & MARCOTTE, E. M. 2012. Insights into the regulation of protein abundance from proteomic and transcriptomic analyses. *Nature Reviews Genetics,* 13**,** 227-232.

VONA, B., MAZAHERI, N., LIN, S.-J., DUNBAR, L. A., MAROOFIAN, R., AZAIEZ, H., BOOTH, K. T., VITRY, S., RAD, A., RÜSCHENDORF, F., VARSHNEY, P., FOWLER, B., BEETZ, C., ALAGRAMAM, K. N., MURPHY, D., SHARIATI, G., SEDAGHAT, A., HOULDEN, H., PETREE, C., VIJAYKUMAR, S., SMITH, R. J. H., HAAF, T., EL-AMRAOUI, A., BOWL, M. R., VARSHNEY, G. K. & GALEHDARI, H. 2021. A biallelic variant in CLRN2 causes non-syndromic hearing loss in humans. *Human Genetics*.

WANG, D. T., RAMAKRISHNAIAH, R. & KANFI, A. 2019a. Sensorineural Hearing Loss Through the Ages. *Semin Roentgenol,* 54**,** 207-214.

WANG, J., SHEN, J., GUO, L., CHENG, C., CHAI, R., SHU, Y. & LI, H. 2019b. A humanized mouse model, demonstrating progressive hearing loss caused by MYO6 p.C442Y, is inherited in a semi-dominant pattern. *Hear Res,* 379**,** 79-88.

WARR, W. B. 1992. Organization of Olivocochlear Efferent Systems in Mammals. *In:* WEBSTER, D. B., POPPER, A. N. & FAY, R. R. (eds.) *The Mammalian Auditory Pathway: Neuroanatomy.* New York, NY: Springer New York.

WATERSTON, R. H., LINDBLAD-TOH, K., BIRNEY, E., ROGERS, J., ABRIL, J. F., AGARWAL, P., AGARWALA, R., AINSCOUGH, R., ALEXANDERSSON, M., AN, P., ANTONARAKIS, S. E., ATTWOOD, J., BAERTSCH, R., BAILEY, J., BARLOW, K., BECK, S., BERRY, E., BIRREN, B., BLOOM, T., BORK, P., BOTCHERBY, M., BRAY, N., BRENT, M. R., BROWN, D. G., BROWN, S. D., BULT, C., BURTON, J., BUTLER, J., CAMPBELL, R. D., CARNINCI, P., CAWLEY, S., CHIAROMONTE, F., CHINWALLA, A. T., CHURCH, D. M., CLAMP, M., CLEE, C., COLLINS, F. S., COOK, L. L., COPLEY, R. R., COULSON, A., COURONNE, O., CUFF, J., CURWEN, V., CUTTS, T., DALY, M., DAVID, R., DAVIES, J., DELEHAUNTY, K. D., DERI, J., DERMITZAKIS, E. T., DEWEY, C., DICKENS, N. J., DIEKHANS, M., DODGE, S., DUBCHAK, I., DUNN, D. M., EDDY, S. R., ELNITSKI, L., EMES, R. D., ESWARA, P., EYRAS, E., FELSENFELD, A., FEWELL, G. A., FLICEK, P., FOLEY, K., FRANKEL, W. N., FULTON, L. A., FULTON, R. S., FUREY, T. S., GAGE, D., GIBBS, R. A., GLUSMAN, G., GNERRE, S., GOLDMAN, N., GOODSTADT, L., GRAFHAM, D., GRAVES, T. A., GREEN, E. D., GREGORY, S., GUIGO, R., GUYER, M., HARDISON, R. C., HAUSSLER, D., HAYASHIZAKI, Y., HILLIER, L. W., HINRICHS, A., HLAVINA, W., HOLZER, T., HSU, F., HUA, A., HUBBARD, T., HUNT, A., JACKSON, I., JAFFE, D. B., JOHNSON, L. S., JONES, M., JONES, T. A., JOY, A., KAMAL, M., KARLSSON, E. K., et al. 2002. Initial sequencing and comparative analysis of the mouse genome. *Nature,* 420**,** 520-62.

WAYNE, R. V. & JOHNSRUDE, I. S. 2015. A review of causal mechanisms underlying the link between age-related hearing loss and cognitive decline. *Ageing Res Rev,* 23**,** 154-66.

WEIL, D., BLANCHARD, S., KAPLAN, J., GUILFORD, P., GIBSON, F., WALSH, J., MBURU, P., VARELA, A., LEVILLIERS, J., WESTON, M. D. & ET AL. 1995. Defective myosin VIIA gene responsible for Usher syndrome type 1B. *Nature,* 374**,** 60-1.

WEIL, D., EL-AMRAOUI, A., MASMOUDI, S., MUSTAPHA, M., KIKKAWA, Y., LAINÉ, S., DELMAGHANI, S., ADATO, A., NADIFI, S., ZINA, Z. B., HAMEL, C., GAL, A., AYADI, H., YONEKAWA, H. & PETIT, C. 2003. Usher syndrome type I G (USH1G) is caused by mutations in the gene encoding SANS, a protein that associates with the USH1C protein, harmonin. *Hum Mol Genet,* 12**,** 463-71.

WEINSTEIN, B. E. & VENTRY, I. M. 1982. Hearing Impairment and Social Isolation in the Elderly. *Journal of Speech, Language, and Hearing Research,* 25**,** 593-599.

WELLS, H. R. R., FREIDIN, M. B., ZAINUL ABIDIN, F. N., PAYTON, A., DAWES, P., MUNRO, K. J., MORTON, C. C., MOORE, D. R., DAWSON, S. J. & WILLIAMS, F. M. K. 2019. GWAS Identifies 44 Independent Associated Genomic Loci for Self-Reported Adult Hearing Difficulty in UK Biobank. *Am J Hum Genet,* 105**,** 788-802.

WEN, Z., ZHU, H., LI, Z., ZHANG, S., ZHANG, A., ZHANG, T., FU, X., SUN, D., ZHANG, J. & GAO, J. 2019. A knock-in mouse model of Pendred syndrome with Slc26a4 L236P mutation. *Biochem Biophys Res Commun,* 515**,** 359-365.

WIJSHAKE, T., BAKER, D. J. & VAN DE SLUIS, B. 2014. Endonucleases: new tools to edit the mouse genome. *Biochimica et Biophysica Acta (BBA) - Molecular Basis of Disease,* 1842**,** 1942-1950.

WOODS, C., MONTCOUQUIOL, M. & KELLEY, M. W. 2004. Math1 regulates development of the sensory epithelium in the mammalian cochlea. *Nature Neuroscience,* 7**,** 1310-1318.

WORLD HEALTH ORGANISATION, Grades of Hearing Impairment [Online]. Available: https://www.who.int/pbd/deafness/hearing_impairment_grades/en/ [Accessed 20.06.20]

XIONG, W., GRILLET, N., ELLEDGE, H. M., WAGNER, T. F., ZHAO, B., JOHNSON, K. R., KAZMIERCZAK, P. & MULLER, U. 2012. TMHS is an integral component of the mechanotransduction machinery of cochlear hair cells. *Cell,* 151**,** 1283-95.

XIONG, W., WAGNER, T., YAN, L., GRILLET, N. & MÜLLER, U. 2014. Using injectoporation to deliver genes to mechanosensory hair cells. *Nat Protoc,* 9**,** 2438-49.

YAN, J., PAN, L., CHEN, X., WU, L. & ZHANG, M. 2010. The structure of the harmonin/sans complex reveals an unexpected interaction mode of the two Usher syndrome proteins. *Proc Natl Acad Sci U S A,* 107**,** 4040-5.

YANG, J., LIU, X., ZHAO, Y., ADAMIAN, M., PAWLYK, B., SUN, X., MCMILLAN, D. R., LIBERMAN, M. C. & LI, T. 2010. Ablation of whirlin long isoform disrupts the USH2 protein complex and causes vision and hearing loss. *PLoS Genet,* 6**,** e1000955.

YANG, Y., MOHAND-SAID, S., DANAN, A., SIMONUTTI, M., FONTAINE, V., CLERIN, E., PICAUD, S., LEVEILLARD, T. & SAHEL, J. A. 2009. Functional cone rescue by RdCVF protein in a dominant model of retinitis pigmentosa. *Mol Ther,* 17**,** 787-95.

ZAHNERT, T. 2011. The differential diagnosis of hearing loss. *Dtsch Arztebl Int,* 108**,** 433-43; quiz 444.

ZALLOCCHI, M., MEEHAN, D. T., DELIMONT, D., ASKEW, C., GARIGE, S., GRATTON, M. A., ROTHERMUND-FRANKLIN, C. A. & COSGROVE, D. 2009. Localization and expression of clarin-1, the Clrn1 gene product, in auditory hair cells and photoreceptors. *Hear Res,* 255**,** 109-20.

ZALLOCCHI, M., MEEHAN, D. T., DELIMONT, D., RUTLEDGE, J., GRATTON, M. A., FLANNERY, J. & COSGROVE, D. 2012. Role for a novel Usher protein complex in hair cell synaptic maturation. *PLoS One,* 7**,** e30573.

ZHANG, L. W., CANG, X. H., CHEN, Y. & GUAN, M. X. 2019. In vitro culture of mammalian inner ear hair cells. *J Zhejiang Univ Sci B,* 20**,** 170-179.

ZHAO, B., WU, Z., GRILLET, N., YAN, L., XIONG, W., HARKINS-PERRY, S. & MULLER, U. 2014. TMIE is an essential component of the mechanotransduction machinery of cochlear hair cells. *Neuron,* 84**,** 954-67.

ZHENG, Q. Y., JOHNSON, K. R. & ERWAY, L. C. 1999. Assessment of hearing in 80 inbred strains of mice by ABR threshold analyses. *Hear Res,* 130**,** 94-107.